online issn: 1307-6892

irc 2021

XV. international research conference

proceedings

open science index 15 2021

september 16-17, 2021 amsterdam netherlands

international scholarly and scientific research & innovation

Open Science

Open Science Philosophy

Open science encompasses unrestricted access to scientific research articles, access to data from public research, and collaborative research enabled by information and communication technology tools, models, and incentives. Broadening access to scientific research publications and data is at the heart of open science. The objective of open science is to make research outputs and its potential benefits available to the entire world and in the hands of as many as possible:

- Open science promotes a more accurate verification of scientific research results. Scientific inquiry and discovery can be sped up by combining the tools of science and information technologies. Open science will benefit society and researchers by providing faster, easier, and more efficient availability of research outputs.
- Open science reduces duplication in collecting, creating, transferring, and re-using scientific material.
- Open science increases productivity in an era of tight budgets.
- Open science results in great innovation potential and increased consumer choice from public research.
- Open science promotes public trust in science. Greater citizen engagement leads to active participation in scientific experiments and data collection.

Open Science Index

The Open Science Index (OSI) currently provides access to over thirty thousand full-text journal articles and is working with member and non-member organizations to review policies to promote and assess open science. As part of the open science philosophy, and by making open science a reality; OSI is conducting an assessment of the impact of open science principles and restructuring the guidelines for access to scientific research. As digitalization continues to accelerate science, Open science and big data hold enormous promise and present new challenges for policymakers, scientific institutions, and individual researchers.

OSI is helping the global scientific research community discover, evaluate, and access high-quality research output. Renowned for its editorially curated and refereed collection of the highest-quality publications, OSI has always been and will remain free-of-charge.

OSI provides an efficient and thorough discovery process to the open science research database and provides links and free access to full-text articles. There are 50 open access journal categories that are curated and refereed by international scientific committees, the in-house editorial team, and trusted partners. Since its inception in 2007, OSI has made more than thirty thousand peer-reviewed open access full-text journal articles (PDF versions) freely available online without cost, barriers, or restrictions.

Open Science Access

With the Open Science Index, researchers can discover and access trusted peer-reviewed open access full-text scientific research articles with confidence. OSI helps researchers find appropriate non-profit open access journals to publish their work.

OSI gives one-click access to online full-text PDFs and expands the reach to global society by giving users free access from anywhere around the globe. Through cutting-edge open science collaboration, in an innovative public partnership, the non-profit OSI is devoted to making science open and reusable.

To learn more, visit online at waset.org

Open Science

Open Society

An open society allows individuals to change their roles and to benefit from corresponding changes in status. Open science depends to a greater or lesser extent on digital technologies and innovations in structural processes by an open society. When realized, open science research and innovation can create investment opportunities for new and better products and services and therefore increase competitiveness and employment. Open science research and innovation is a key component of thematic open science priorities. Central to the open science digital infrastructure is enabling industry to benefit from digital technology and to underpin scientific advances through the development of an open society. Open science research and innovation can also contribute to society as a global actor because scientific relations can flourish even where global relations are strained. Open science has a critical role across many areas of decision making in providing evidence that helps understand the risks and benefits of different open science choices. Digital technology is making the conduct of open science and innovation more collaborative, more global, and more open to global citizens. Open society must embrace these changes and reinforce its position as the leading power for science, for new ideas, and for investing sustainably in the future.

It is apparent in open society that the way science works is fundamentally changing, and an equally significant transformation is taking place in how organizations and societies innovate. The advent of digital technology is making research and innovation more open, collaborative, and global. These exchanges are leading open society to develop open science and to set goals for research and innovation priority. Open science goals are materializing in the development of scientific research and innovation platforms and greater acceptance of scientific data generated by open science research. Open science research and innovation do not need help from open society to come up with great ideas, but the level of success ideas ultimately reach is undoubtedly influenced by regulation, financing, public support, and market access. Open society is playing a crucial role in improving all these success factors.

Open Science

Open science represents a new approach to the scientific process based on cooperative work and new ways of diffusing knowledge by using digital technologies and collaborative tools. These innovations capture a systemic change to the way science and research have been carried out for the last fifty years. Science is shifting from the standard practice of publishing research results in scientific publications after the research and reviews are completed. The shift is towards sharing and using all available knowledge at an earlier stage in the research process. Open science is to science what digital technology is to social and economic transactions: allowing end users to be producers of ideas, relations, and services and in doing so, enabling new working models, new social relationships and leading to a new modus operandi for science. Open science is as important and disruptive as e-commerce has been for the retail industry. Just like e-commerce, the open science research paradigm shift affects the whole business cycle of doing science and research. From the selection of research subjects to the carrying out of research, to its use and re-use, to the role of universities, and that of publishers are all dramatically changed. Just as the internet and globalization have profoundly changed the way we do business, interact socially, consume culture, and buy goods, these changes are now profoundly impacting how one does research and science.

The discussion on broadening the footprint of science and on novel ways to produce and spread knowledge gradually evolved from two global trends: Open Access and Open Source. The former refers to online, peer-reviewed scholarly outputs, which are free to read, with limited or no copyright and licensing restrictions, while open source refers to software created without any proprietary restriction and which can be accessed and freely used. Although open access became primarily associated with a particular publishing

or scientific dissemination practice, open access already sought to induce a broader practice that includes the general re-use of all kinds of research products, not just publications or data. It is only more recently that open science has coalesced into the concept of a transformed scientific practice, shifting the focus of researchers' activity from publishing as fast as possible to sharing knowledge as early as possible. Open science is defined as the idea that scientific knowledge of all kinds should be openly shared as early as is practical in the discovery process. As a result, the way science is done in the future will look significantly different from the way it is done now. Open science is the ongoing evolution in the modus operandi of doing research and organizing science. This evolution is enabled by digital technology and is driven by both the globalization of the scientific community and increasing public demand to address the societal challenges of our times. Open science entails the ongoing transitions in the way research is performed, researchers collaborate, knowledge is shared, and science is organized.

Open science impacts the entire research cycle, from the inception of research to its publication, and on how this cycle is organized. The outer circle reflects the new interconnected nature of open science, while the inner circle shows the entire scientific process, from the conceptualization of research ideas to publishing. Each step in the scientific process is linked to ongoing changes brought about by open science, including the emergence of alternative systems to establish a scientific reputation; changes in the way quality and impact of research are evaluated; the growing use of scientific blogs; open annotation; and open access to data and publications. All institutions involved in science are affected, including research organizations, research councils, and funding bodies. The trends are irreversible, and they have already grown well beyond individual projects. Theses changes predominantly result from a bottom-up process driven by a growing number of researchers who increasingly employ social media in their research and initiate globally coordinated research projects while sharing results at an early stage in the research process.

Open science is encompassed in five schools of thought:

- the infrastructure school, concerned with technological architecture
- the public school, concerned with the accessibility of knowledge creation
- the measurement school, concerned with alternative impact assessment
- the democratic school, concerned with access to knowledge
- the pragmatic school, concerned with collaborative research

According to the measurement school, the reputation and evaluation of individual researchers are still mainly based on citation-based metrics. The h-index is an author-level metric that attempts to measure both the productivity and citation impact of the publications of a scientist or scholar. The impact factor is a measure reflecting the average number of citations to articles published in an academic journal and is used as a proxy for the relative importance of a journal.

Numerous criticisms have been made of citation-based metrics, primarily when used, and often misused, to assess the performance of individual researchers. These metrics:

- are often not applicable at the individual level
- do not take into account the broader social and economic function of scientific research
- are not adapted to the increased scale of research
- cannot recognize new types of work that researchers are performing

Web-based metrics for measuring research output, popularized as altmetrics, have recently received much attention: some measure the impact at the article level, others make it possible to assess the many outcomes of research in addition to the number of scientific articles and references. The current reputation and evaluation system has to adapt to the new dynamics of open science and acknowledge and incentivize

engagement in open science. Researchers engaging in open science have growing expectations that their work, including intermediate products such as research data, will be better rewarded or taken into account in their career development. Vice-versa, the use, and reuse of open data will require appropriate codes of conduct requiring, for example, the proper acknowledgment of the original creator of the data.

These ongoing changes are progressively transforming scientific practices with innovative tools to facilitate communication, collaboration, and data analysis. Researchers that increasingly work together to create knowledge can employ online tools and create a shared space where creative conversation and collaboration can occur. As a result, the problem-solving process can be faster, and the range of problems that can be solved can be expanded. The ecosystem underpinning open science is evolving very rapidly. Social network platforms for researchers already attract millions of users and are being used to begin and validate more research projects.

Furthermore, the trends towards open access are redefining the framework conditions for science and thus have an impact on how open innovation is produced by encouraging a more dynamic circulation of knowledge. It can enable more science-based startups to emerge thanks to the exploitation of openly accessible research results. Open science, however, does not mean free science. It is essential to ensure that intellectual property is protected before making knowledge publicly available in order to subsequently attract investments that can help translate research results into innovation. If this is taken into account, fuller and broader access to scientific publications and research data can help to accelerate innovation. Investments that boost research and innovation in open science would benefit society with fewer barriers to knowledge transfer, open access to scientific research, and greater mobility of researchers. In this context, open access can help overcome the barriers that innovative organizations face in accessing the results of research funded by the public.

Open innovation

An open society is the largest producer of knowledge, but the phenomenon of open science is changing every aspect of the scientific method by becoming more open, inclusive, and interdisciplinary. Ensuring open society is at the forefront of open science means promoting open access to scientific data and publications alongside the highest standards of research integrity. There are few forces in this globe as engaging and unifying as science. The universal language of science maintains open channels of communication globally. Open society can maximize its gains through maintaining its presence at the highest level of scientific endeavor, and by promoting a competitive edge in the knowledge society of the information age. The ideas and initiatives described in this publication can stimulate anyone interested in open science research and innovation. It is designed to encourage debate and lead to new ideas on what and open society should do, should not do, or do differently.

An open society can lead to a research powerhouse; however, open society rarely succeeds in turning research into innovation and in getting research results to the global market. Open society must improve at making the most of its innovation talent, and that is where open innovation comes into play. The basic premise of open innovation is to open up the innovation process to all active players so that knowledge can circulate more freely and be transformed into products and services that create new markets while fostering a stronger culture of entrepreneurship. Open innovation is defined as the use of purposive inflows and outflows of knowledge to accelerate internal innovation. This original notion of open innovation was primarily based on transferring knowledge, expertise, and even resources from one company or research institution to another. This notion assumes that firms can and should use external ideas as well as internal ideas, and internal and external paths to market, as they seek to improve their performance. The concept of open innovation is continually evolving and is moving from linear, bilateral transactions and collaborations

towards dynamic, networked, multi-collaborative innovation ecosystems. This means that a specific innovation can no longer be seen as the result of predefined and isolated innovation activities but rather as the outcome of a complex co-creation process involving knowledge flows across the entire economic and social environment. This co-creation takes place in different parts of the innovation ecosystem and requires knowledge exchange and absorptive capacities from all the actors involved, whether businesses, academia, financial institutions, public authorities, or citizens.

Open innovation is a broad term, which encompasses several different nuances and approaches. Two main elements underpin the most recent conceptions of open innovation: the users are in the spotlight and invention becomes an innovation only if users become a part of the value creation process. Notions such as user innovation emphasize the role of citizens and users in the innovation processes as distributed' sources of knowledge. This kind of public engagement is one of the aims of open science research and innovation. The term 'open' in these contexts has also been used as a synonym for 'user-centric'; creating a well-functioning ecosystem that allows co-creation and becomes essential for open innovation. In this ecosystem, relevant stakeholders are collaborating along and across industry and sector-specific value chains to co-create solutions for socio-economic and business challenges. One important element to keep in mind when discussing open innovation is that it cannot be defined in absolutely precise terms. It may be better to think of it as a point on a continuum where there is a range of context-dependent innovation activities at different stages, from research to development through to commercialization, and where some activities are more open than others. Open innovation is gaining momentum thanks to new large-scale trends such as digitalization and the mass participation and collaboration in innovation that it enables. The speed and scale of digitalization are accelerating and transforming the way one designs, develops, and manufactures products, the way one delivers services, and the products and services themselves. It is enabling innovative processes and new ways of doing business, introducing new cross-sector value chains and infrastructures.

Open society must ensure that it capitalizes on the benefits that these developments promise for citizens in terms of tackling societal challenges and boosting business and industry. Drawing on these trends, and with the aim of helping build an open innovation ecosystem in open society, the open society's concept of open innovation is characterized by:

- combining the power of ideas and knowledge from different actors to co-create new products and find solutions to societal needs
- creating shared economic and social value, including a citizen and user-centric approach
- capitalizing on the implications of trends such as digitalization, mass participation, and collaboration

In order to encourage the transition from linear knowledge transfer towards more dynamic knowledge circulation, experts agree that it is essential to create and support an open innovation ecosystem that facilitates the translation of knowledge into socio-economic value. In addition to the formal supply-side elements such as research skills, excellent science, funding and intellectual property management, there is also a need to concentrate on the demand side aspects of knowledge circulation, making sure that scientific work corresponds to the needs of the users and that knowledge is findable, accessible, interpretable and reusable. Open access to research results aims to make science more reliable, efficient, and responsive and is the springboard for increased innovation opportunities, e.g. by enabling more science-based startups to emerge. Prioritizing open science does not, however, automatically ensure that research results and scientific knowledge are commercialized or transformed into socio-economic value. In order for this to happen, open innovation must help to connect and exploit the results of open science and facilitate the faster translation of discoveries into societal use and economic value.

Open Science

Collaborations with global partners represent important sources of knowledge circulation. The globalization of research and innovation is not a new phenomenon, but it has intensified in the last decade, particularly in terms of collaborative research, international technology production, and worldwide mobility of researchers and innovative entrepreneurs. Global collaboration plays a significant role both in improving the competitiveness of open innovation ecosystems and in fostering new knowledge production worldwide. It ensures access to a broader set of competencies, resources, and skills wherever they are located, and it yields positive impacts in terms of scientific quality and research results. Collaboration enables global standard-setting, allows global challenges to be tackled more effectively, and facilitates participation in global value chains and new and emerging markets.

To learn more, visit online at waset.org

Open Science

Scholarly Research Review

The scholarly research review is a multidimensional evaluation procedure in which standard peer review models can be adapted in line with the ethos of scientific research, including accessible identities between reviewer and author, publishing review reports and enabling greater participation in the peer review process. Scholarly research review methods are employed to maintain standards of quality, improve performance, provide credibility, and determine suitability for publication. *Responsible Peer Review Procedure:* Responsible peer review ensures that scholarly research meets accepted disciplinary standards and ensures the dissemination of only relevant findings, free from bias, unwarranted claims, and unacceptable interpretations. Principles of responsible peer review:

• Honesty in all aspects of research
• Accountability in the conduct of research
• Professional courtesy and fairness in working with others
• Good stewardship of research on behalf of others

The responsibilities of peer review apply to scholarly researchers at all stages of peer review: Fairness, Transparency, Independence, Appropriateness and Balance, Participation, Confidentiality, Impartiality, Timeliness, Quality and Excellence, Professionalism, and Duty to Report.

Scholarly Research Review Traits:
• Scholarly Research Review Identities: Authors and reviewers are aware of each other's identity

• Scholarly Research Review Reports: Review reports are published alongside the relevant article

• Scholarly Research Review Participation: The wider academic community is able to contribute to the review process

• Scholarly Research Review Interaction: Direct reciprocal discussion between author(s) and reviewers, and/or between reviewers, is allowed and encouraged

• Scholarly Research Pre-review Manuscripts: Manuscripts are made immediately available in advance of any formal peer review procedures

• Scholarly Research Review Final-version Reviewing: Editorial revision of the language and format is conducted on the final version of the manuscript for publication

• Scholarly Research Review Platforms: The scholarly research review process is independent of the final publication of the manuscript and it is facilitated by a different organizational entity than the venue of publication

All submitted manuscripts are subject to the scholarly research review process, in which there are three stages of evaluation for consideration: pre-review manuscripts, chair-review presentation, and final-review manuscripts. All submitted full text papers, that may still be withstand the editorial review process, are presented in the conference proceedings. Manuscripts are tracked and all actions are logged by internal and external reviewers according to publication policy. External reviewers' editorial analysis consists of the evaluation reports of the conference session chairs and participants in addition to online internal and external reviewers' reports. Based on completion of the scholarly research review process, those manuscripts meeting the publication standards are published 10 days after the event date.

To learn more, visit online at waset.org

TABLE OF CONTENTS

Preparation of Papers - Good Governance: An Effective Public Participation Approach for Urban Development of City Centres

Okacha, Lojaine M.

***Abstract*—** In the past half-century, researchers started paying attention to enhancing the performance of urban spaces. Their idea of performance comprised urban climate performance, space synthesis, economic performance, and enhancing the quality of life in space. However, they all agreed that the key to achieving any of the previously mentioned development projects is good governance. Having good governance allows citizens to participate freely in the urbanization or development projects within cities. Consequently, using the city resources and assets as efficiently as possible, and ensures the fulfillment of the users' needs and requests.

This paper aims to propose an effective participation framework to help citizens have their voices heard and participate in the decisions that will affect their living situation. The framework allows governments to use their public resources to their best. However, This study focuses on public participation in third world countries with unitary decentralized governance systems such as Egypt. It summarizes the challenges facing the participation practices, identifies the keys to a successful participation process, and draws on dominant effective participation practice lying on the relationship between the levels of participation, stakeholders participating, the urban development stages, the city-systems, and participation process. These components are integrated to create a real-world effective participation Framework. The results of the analysis were incredible and produced a functional and progressive approach for effective public participation to introduce to the governments. The model itself is combined with additional principles allowing the best practice to the process. The framework is finally compared with a real case of urban development.

***Keywords*—**Public participation, Good Governance, Urban development, city systems .

Lojaine Okacha is with the Alexandria Universty, Egypt (e-mail: lojaina.okacha@alexu.edu.eg).

Tunable Crystallinity of Zinc Gallogermanate Nanoparticles via Organic Ligand-Assisted Biphasic Hydrothermal Synthesis

Sarai Guerrero, Lijia Liu

Abstract -- Zinc gallogermanate (ZGGO) is a persistent phosphor that can emit in the near infrared (NIR) range once dopped with Cr^{3+} enabling its use for *in-vivo* deep-tissue bio-imaging. Such a property also allows for its application in cancer diagnosis and therapy. Given this, work into developing a synthetic procedure that can be done using common laboratory instruments and equipment as well as understanding ZGGO overall, is in demand. However, the ZGGO nanoparticles must have a size compatible for cell intake to occur while still maintaining sufficient photoluminescence. The nanoparticle must also be made biocompatible by functionalizing the surface for hydrophilic solubility and for high particle uniformity in the final product. Additionally, most research is completed on doped ZGGO, leaving a gap in understanding the base form of ZGGO. It also leaves a gap in understanding how doping affects the synthesis of ZGGO. In this work, the first step of optimizing the particle size via the crystalline size of ZGGO was done with undoped ZGGO using the organic acid, oleic acid (OA) for organic ligand-assisted biphasic hydrothermal synthesis. The effects of this synthesis procedure on ZGGO's crystallinity were evaluated using Powder X-Ray Diffraction (PXRD). OA was selected as the capping ligand as experiments have shown it beneficial in synthesizing sub-10 nm zinc gallate (ZGO) nanoparticles as well as palladium nanocrystals and magnetite (Fe_3O_4) nanoparticles. Later it is possible to substitute OA with a different ligand allowing for hydrophilic solubility. Attenuated Total Reflection Fourier-Transform Infrared (ATR-FTIR) was used to investigate the surface of the nanoparticle to investigate and verify that OA had capped the nanoparticle. PXRD results showed that using this procedure led to improved crystallinity, comparable to the high-purity reagents used on the ZGGO nanoparticles. There was also a change in the crystalline size of the ZGGO nanoparticles. ATR-FTIR showed that once capped ZGGO cannot be annealed as doing so will affect the OA. These results point to this new procedure positively affecting the crystallinity of ZGGO nanoparticles. There are also repeatable implying the procedure is a reliable source of highly crystalline ZGGO nanoparticles. With this completed, the next step will be working on substituting the OA with a hydrophilic ligand. As these ligands effect the solubility of the nanoparticle as well as the pH that the nanoparticles can dissolve in, further research is needed to verify which ligand is best suited for preparing ZGGO for bio-imaging.

***Keywords*—** biphasic hydrothermal synthesis, crystallinity, oleic acid, zinc gallogermanate

S. Guerrero is with the University of Western Ontario, London, ON N6K1W8 Canada (e-mail: sguerre2@uwo.ca).

L. Liu is with the University of Western Ontario, London, ON N6K1W8 Canada (e-mail: lijia.liu@uwo.ca).

6D Posture Estimation of Road Vehicles from Color Images

Yoshimoto Kurihara, Tad Gonsalves

***Abstract*—**Currently, in the field of object posture estimation, there is research on estimating the position and angle of an object by storing a 3D model of the object to be estimated in advance in a computer and matching it with the model. However, in this research, we have succeeded in creating a module that is much simpler, smaller in scale, and faster in operation. Our 6D pose estimation model consists of two different networks – a classification network and a regression network. From a single RGB image, the trained model estimates the class of the object in the image, the coordinates of the object, and its rotation angle in 3D space. In addition, we compared the estimation accuracy of each camera position, i.e., the angle from which the object was captured. The highest accuracy was recorded when the camera position was 75°, the accuracy of the classification was about 87.3%, and that of regression was about 98.9%.

***Keywords*—**AlexNet, Deep learning, image recognition, 6D posture estimation.

I. Introduction

THE 6D posture estimation of objects is a very important technology in the field of robotics, automatic driving and nursing care robots. The 6D posture estimation of an object is a technique to estimate the position of the object to be estimated, i.e., the coordinates in the x, y, and z axes, and the direction of the object to be estimated, i.e., the rotation angle around the x, y, and z axes, when a point in the image is set as the origin. If this estimation becomes possible, robots will be able to estimate more than humans, and will be able to predict the next moment's situation from the direction of other vehicles or pedestrians in an automatic driving situation [1], [2] or to grasp an object accurately even with a thin arm [3]. Moreover, it also has tremendous applications in augmented reality [4].

The 6D pose estimation is easier for objects with texture. However, the estimation of untextured objects poses a challenging task [5]. Various methods have been proposed for estimating the posture of an object by matching it with a 3D model stored beforehand in a computer, but the latest methods are all computationally very expensive, and take a long time to estimate the posture [6]. Brachmann et al. have demonstrated the feasibility of 6D pose estimation from a single RGB image [7]. This has motivated us to experiment 6D pose estimation from single RGB images, because of lower computational load and faster response.

Since AlexNet [8] won the ILSVRC (International Large Scale Visual Recognition Challenge) in 2012 by a large margin over the accuracy of the second-ranked networks, which contained manually tuned parameters, the use of CNNs has become common in image recognition. Currently, CNNs are used for various image recognition applications including camera images [9]-[11], and various networks have been proposed as the successor of AlexNet. The accuracy of CNNs is constantly improving. Hence, this study uses AlexNet to estimate the posture of 3D objects. Its greatest advantage is that it requires relatively less computational resources and runs faster than other existing models.

The contribution of our 6D model is in the area of autonomous or self-driving land vehicles. In the autonomous driving technology, the positioning of the visual camera is extremely important to gather the most relevant information for driving. As demonstrated by our deep learning model, if the front camera is placed at an angle of 75° with respect to the vehicle plane, the classification as well as pose estimation accuracy of objects in front of the driving vehicle is optimal.

This paper is organized as follows: Section II introduces related studies on 6D pose estimation, Section III describes our deep learning network model. Section IV explains the creation of dataset and the experimental setup, while Section V discusses the experimental results. The paper closes with a brief conclusion, indicating points for further research.

II. Related Works

There are many studies on 6D pose recognition of objects found in literature. For example, PoseCNN and DeepIM are two of the recent methods. Fundamental to PoseCNN model is a CNN model which estimates the 3D co-ordinates of an object. The 3D rotation of the object is estimated by means of regression [12], [13]. DeepIM [14] is a model that estimates the pose of an object by storing a 3D model of the object in the computer in advance, rendering images of the object viewed from various angles, and repeatedly matching these images with the pose of the detected object in the observed images. In addition to these, there is research on posture estimation using template matching which considers images and their gradients to detect objects, making them suitable for detecting untextured objects. They can directly provide a coarse estimation of the object pose which is especially important for robots interacting with their environment [15]-[18].

Other methods include posture estimation by detecting feature points of objects using deep neural networks and linking them to the PnP problem [19]. In addition, there is research that uses RGB-D images for pose estimation [7], [20], [21]. One method often used is to estimate the reference pose of an object

Y. Kurihara is with the Dept. of Information & Communication Sciences, Sophia University, Tokyo, Japan (e-mail: y-kurihara-8u6@eagle.sophia.ac.jp).

T. Gonsalves, PhD, is with the Dept. of Information & Communication Sciences, Sophia University, Tokyo, Japan (corresponding author; e-mail: t-gonsal@ sophia.ac.jp).

from a color image, and then repeat the process of position and pose estimation by selecting the nearest neighbor points in each point cloud, using ICP and other methods [22].

III. Network Model

The network constructed in this study is shown in Fig. 1. The network simultaneously learns two models: a model for classifying objects, whose output is the type of object (hereinafter referred to as the classification model), and a model for pose estimation, whose output is the coordinates in the x, y, and z axes and the rotation angle around the x, y, and z axes (hereinafter referred to as the regression model). Specifically, the camera images described in Section 4 *A* are input to the two models, and the necessary parts are extracted from the text file described in Section 4 *A* and correspond to the output of each model in the network. Both the classification model and the regression model are based on AlexNet. The loss function is NLL Loss for the classification model, and RMSE Loss for the regression model.

For simplicity, we use up to nine objects for detection, but it is possible to estimate the pose of many objects by increasing the number of output nodes.

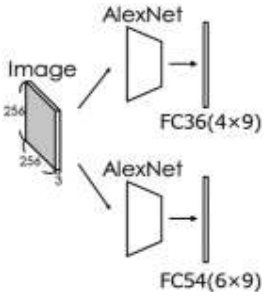

Fig. 1 Network model for 6D pose estimation

IV. ML Experiment

A. Creation of Dataset

The dataset was created using the game development platform Unity. Three types of objects (white vehicle, truck, and tank truck) are placed at random positions on the road at the bottom of Fig. 2, and the camera is fixed at a point on the arc in the figure. The image which the camera shot was output to an external file. At the same time, the name of the object, the relative coordinates of the object with the center of the arc in Fig. 2 as the origin (hereinafter referred to as the coordinates of the object), and the rotation angles around the x-, y-, and z-axes (hereinafter referred to as the posture of the object) were output to a text file. Using this text file and the camera images as a set of data, 30,000 data records were created for each of the camera positions of 0°, 15°, 30°, 45°, 60°, 75°, and 90°. Here, "when the camera position is x°" means "when the angle between the direction of the camera's line of sight and the horizon is x°", and the same expression is used hereafter.

Figs. 3-5 are examples of input images. Since it is difficult to understand the disparity for each camera position with these images alone, Figs. 6-8 are images taken by fixing the position of the object and moving only the camera position.

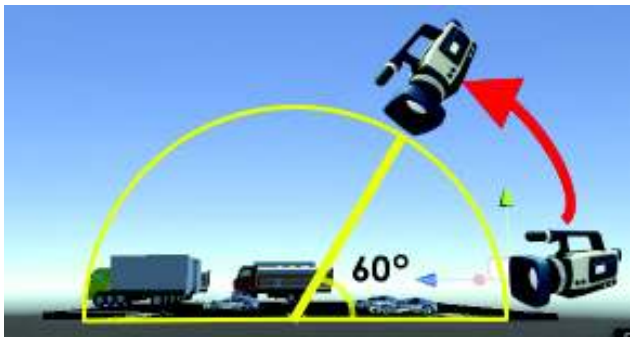

Fig. 2 Data set creation setting

Fig. 3 Input image (camera position: 0°)

Fig. 4 Input image (camera position: 75°)

Fig. 5 Input image (camera position: 90°)

Fig. 6 Image visibility (camera position: 0°)

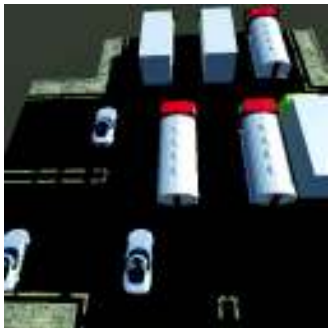

Fig. 7 Image visibility (camera position: 75°)

Fig. 8 Image visibility (camera position: 90°)

B. Experimental Setup

The batch size was 256, the number of epochs was 20, and the learning coefficients were 1.0×10^{-7} for classification, 1.0×10^{-4} for regression, and 5.0×10^{-4} for weight decay. We chose this value for the learning coefficient because the learning converges very quickly when the learning coefficient is large, and the weights tend to fall into local optima when the learning coefficient is smaller than this value.

The experimental environment used in this study is shown in Table I.

TABLE I
EXPERIMENTAL ENVIRONMENT IN THIS STUDY

CPU	AMD® Ryzen threadripper 2990wx 32-core processor × 64
GPU	NVIDIA GeForce GTX 1080 Ti/PCIe/SSE2
Main memory	62.8 GB
Programming language	Python3.6
Framework	pytorch

V. RESULTS

For reasons of space, only results that are considered important are described below. Figs. 9-11 show the graphs of the change in accuracy per epoch for the classifications at 0°, 75°, and 90°, respectively, and Figs. 12-14 show the change in loss per epoch for the classifications, respectively, Figs. 15-17 show the change of loss per epoch in regression, respectively.

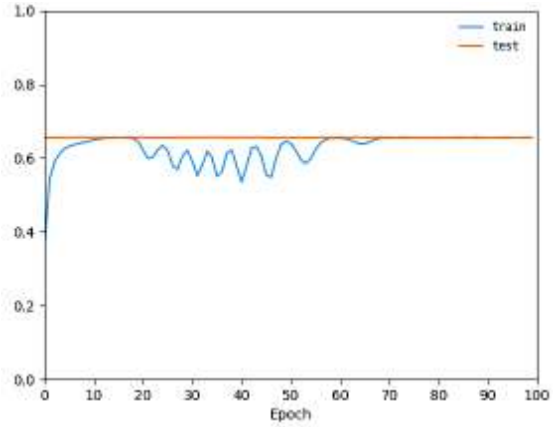

Fig. 9 Changes in accuracy for each epoch in the classification (camera position: 0°)

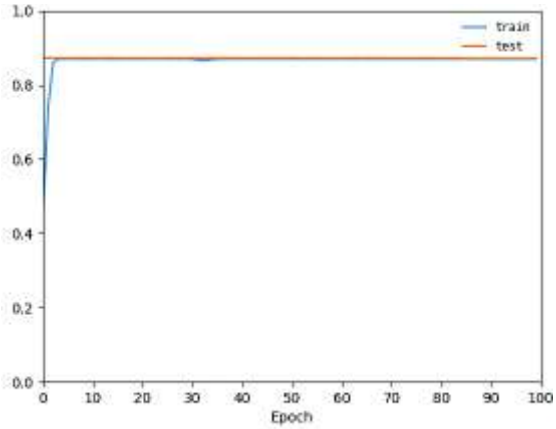

Fig. 10 Changes in accuracy for each epoch in the classification (camera position: 75°)

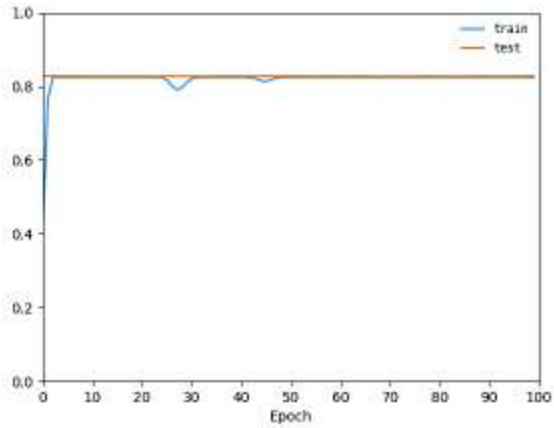

Fig. 11 Changes in accuracy for each epoch in the classification (camera position: 90°)

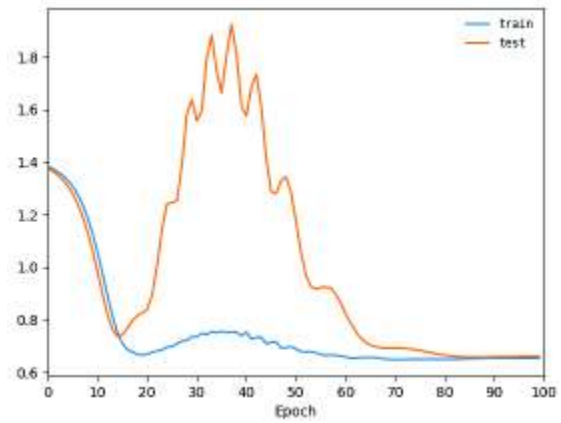

Fig. 12 Changes in loss per epoch in classifications (camera position: 0°)

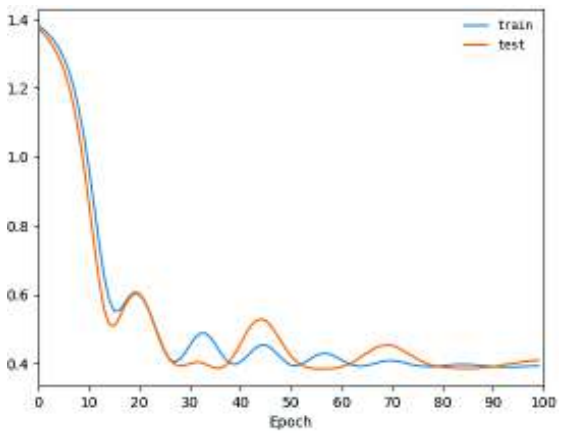

Fig. 13 Changes in loss per epoch in classifications (camera position: 75°)

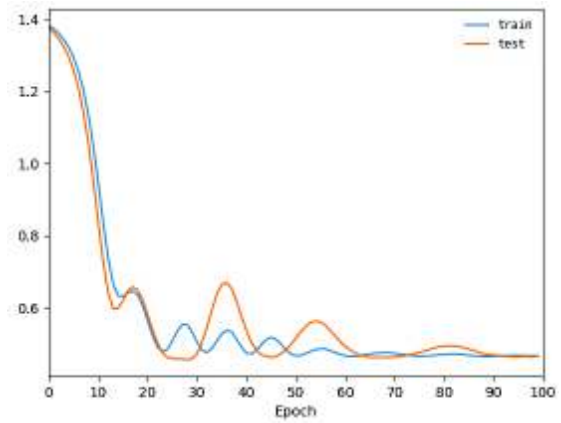

Fig.14 Changes in loss per epoch in classifications (camera position: 90°)

Figs. 18-20 summarize the best result for each angle. Fig. 18 is a graph of the highest accuracy of accuracy for class classification, Fig. 19 is a graph of the highest accuracy of loss for class classification, and Fig. 20 is a graph of the highest accuracy of loss for each epoch for regression.

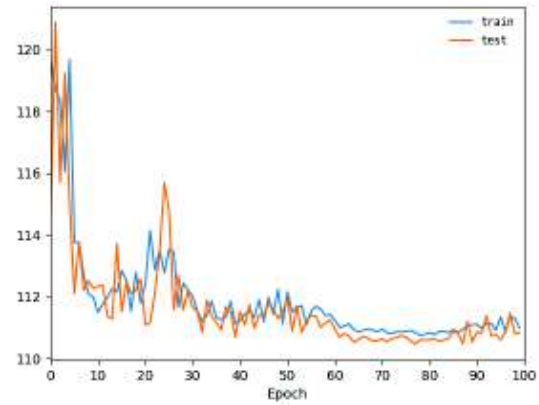

Fig. 15 Change in loss per epoch in regression (camera position: 0°)

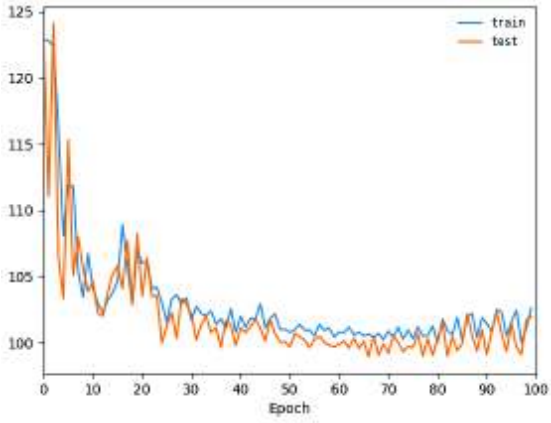

Fig. 16 Change in loss per epoch in regression (camera position: 75°)

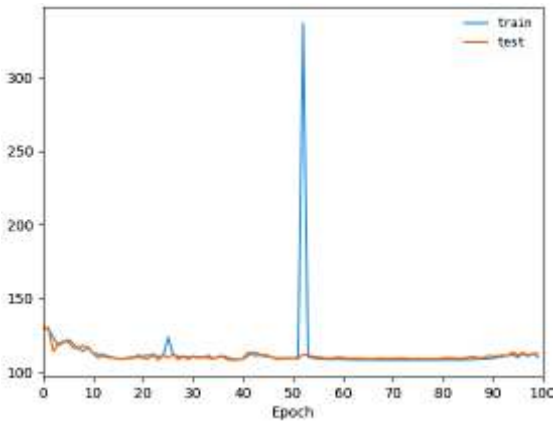

Fig. 17 Change in loss per epoch in regression (camera position: 90°)

The highest accuracy was recorded when the camera position was 75°, the accuracy of the classification was about 87.3%, the loss of the classification was about 0.392, and the loss of the regression was about 98.9.

VI. Conclusion

For the dataset used in this study, the highest accuracy is obtained when the camera is positioned at 75° resulting in an accuracy of 87.3% for classification and about 98.9% for

regression.

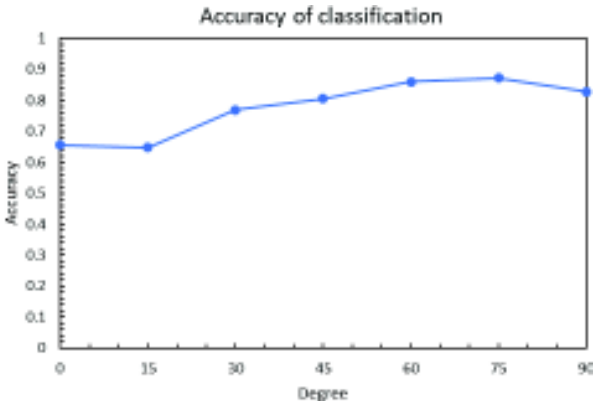

Fig. 18 Comparison of the accuracy of classifications for each angle

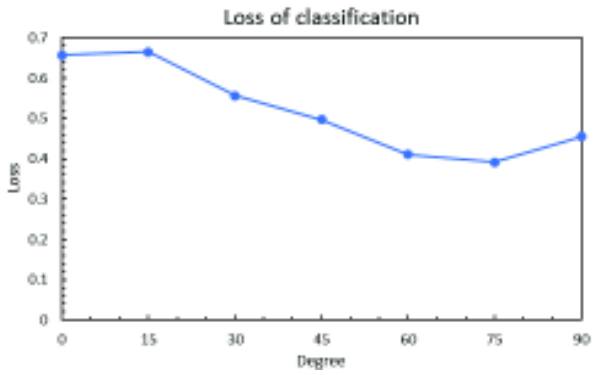

Fig. 19 Comparison of the loss of classifications for each angle

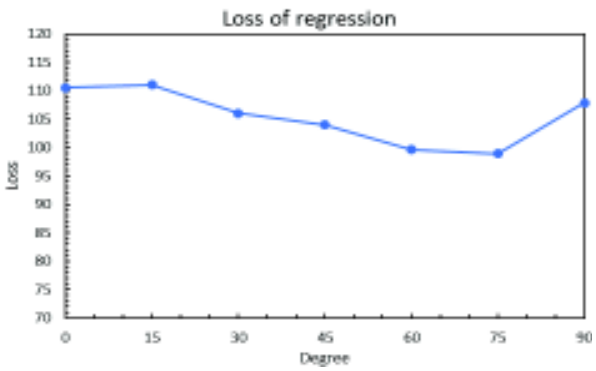

Fig. 20 Comparison of the loss of regression for each angle

In this study, we adopted AlexNet because of its simplicity in implementation; accuracy concerns were secondary in this preliminary study. In the future, we would like to improve the accuracy by adopting relatively new networks such as ResNet. Further, we used the Unity automobile asset to create a dataset necessary for training automated driving-related technologies, but we believe the same results can be obtained by using other assets. For example, when we apply the network to the research of garbage sorting robots, we can obtain the same results by using the assets of plastic bottles and cans.

REFERENCES

[1] X. Chen, H. Ma, J. Wan, B. Li and T. Xia, "Multi-view 3D Object Detection Network for Autonomous Driving," 2017 IEEE Conference on Computer Vision and Pattern Recognition (CVPR), 2017, pp. 6526-6534, doi: 10.1109/CVPR.2017.691.

[2] D. Wu, Z. Zhuang, C. Xiang, W. Zou and X. Li, "6D-VNet: End-To-End 6DoF Vehicle Pose Estimation from Monocular RGB Images," 2019 IEEE/CVF Conference on Computer Vision and Pattern Recognition Workshops (CVPRW), 2019, pp. 1238-1247, doi: 10.1109/CVPRW.2019.00163.

[3] Menglong Zhu, Konstantinos G Derpanis, Yinfei Yang, Samarth Brahmbhatt, Mabel Zhang, Cody Phillips, Matthieu Lecce, and Kostas Daniilidis. Single image 3d object detection and pose estimation for grasping. In 2014 IEEE International Conference on Robotics and Automation (ICRA), pages 3936–3943. IEEE, 2014.

[4] F. Tang, Y. Wu, X. Hou and H. Ling, "3D Mapping and 6D Pose Computation for Real Time Augmented Reality on Cylindrical Objects," in IEEE Transactions on Circuits and Systems for Video Technology, vol. 30, no. 9, pp. 2887-2899, Sept. 2020, doi: 10.1109/TCSVT.2019.2950449.

[5] C. Wu, L. Chen, Z. He and J. Jiang, "Pseudo-Siamese Graph Matching Network for Textureless Objects' 6D Pose Estimation," in IEEE Transactions on Industrial Electronics, doi: 10.1109/TIE.2021.3070501.

[6] A. Doumanoglou, R. Kouskouridas, S. Malassiotis and T. Kim, "Recovering 6D Object Pose and Predicting Next-Best-View in the Crowd," 2016 IEEE Conference on Computer Vision and Pattern Recognition (CVPR), 2016, pp. 3583-3592, doi: 10.1109/CVPR.2016.390.

[7] E. Brachmann, F. Michel, A. Krull, M. Y. Yang, S. Gumhold and C. Rother, "Uncertainty-Driven 6D Pose Estimation of Objects and Scenes from a Single RGB Image," 2016 IEEE Conference on Computer Vision and Pattern Recognition (CVPR), 2016, pp. 3364-3372, doi: 10.1109/CVPR.2016.366.

[8] Alex Krizhevsky, Ilya Sutskever and Geoffrey E. Hinton, "ImageNet Classification with Deep Convolutional Neural Networks". NIPS12, VoL1, pp-1097-1105, (2012).

[9] Komatsu R, Gonsalves T. Comparing U-Net Based Models for Denoising Color Images. AI. 2020; 1(4):465-486. https://doi.org/10.3390/ai1040029

[10] Simonyan, K.; Zisserman, A. Very Deep Convolutional Networks for Large-Scale Image Recognition. arXiv 2014, arXiv:1409.1556. Available online: https://arxiv.org/abs/1409.1556 (accessed on 1 May 2020).

[11] Galea, C.; Farrugia, R.A. Matching Software-Generated Sketches to Face PhotographsWith a Very Deep CNN, Morphed Faces, and Transfer Learning. IEEE Trans. Inf. Forensics Secur. 2017, 13, 1421–1431.

[12] Yu Xiang, Tanner Schmidt, Venkatraman Narayanan, Dieter Fox, "PoseCNN: A Convolutional Neural Network for 6D Object Pose Estimation in Cluttered Scenes", arXiv preprint arXiv: 1711.00199, (2019).

[13] Alirezazadeh, P., Yaghoubi, E., Assunção, E., Neves, J. C., & Proença, H. (2019, September). Pose Switch-based Convolutional Neural Network for Clothing Analysis in Visual Surveillance Environment. In 2019 International Conference of the Biometrics Special Interest Group (BIOSIG) (pp. 1-5). IEEE.

[14] Yi Li, Gu Wang, Xiangyang Ji, Yu Xiang, Dieter Fox, "DeepIM: Deep Iterative Matching for 6D Pose Estimation", arXiv preprint arXiv: 1804.00175, (2019).

[15] S. Hinterstoisser, V. Lepetit, S. Ilic, P. Fua, and N. Navab, "Dominant Orientation Templates for Real-Time Detection of Texture-Less Objects," in IEEE Conference on Computer Vision and Pattern Recognition, 2010.

[16] Muja, M., Rusu, R. B., Bradski, G., & Lowe, D. G. (2011, May). Rein-a fast, robust, scalable recognition infrastructure. In 2011 IEEE international conference on robotics and automation (pp. 2939-2946). IEEE.

[17] Hinterstoisser S, Cagniart C, Ilic S, Sturm P, Navab N, Fua P, Lepetit V, "Gradient response maps for real-time detection of texture less objects.", IEEE Transactions on Pattern Analysis and Machine Intelligence (TPAMI) 34(5):876-888 (2012)

[18] E. Muñoz, Y. Konishi, C. Beltran, V. Murino and A. Del Bue, "Fast 6D pose from a single RGB image using Cascaded Forests Templates," 2016 IEEE/RSJ International Conference on Intelligent Robots and Systems (IROS), 2016, pp. 4062-4069, doi: 10.1109/IROS.2016.7759598.

[19] Tremblay J, To T, Sundaralingam B, Xiang Y, Fox D,Birchfield S, "Deep object pose estimation for semantic robotic grasping of household

objects.", In: Conference on Robot Learning, pp 306-316, (2018)

[20] V. L. Tran and H. -Y. Lin, "3D Object Detection and 6D Pose Estimation Using RGB-D Images and Mask R-CNN," 2020 IEEE International Conference on Fuzzy Systems (FUZZ-IEEE), 2020, pp. 1-6, doi: 10.1109/FUZZ48607.2020.9177601.

[21] L. Peng, Y. Zhao, S. Qu, Y. Zhang and F. Weng, "Real Time and Robust 6D Pose Estimation of RGBD Data for Robotic Bin Picking," 2019 Chinese Automation Congress (CAC), 2019, pp. 5283-5288, doi: 10.1109/CAC48633.2019.8996450.

[22] Zeng A, Yu KT, Song S, Suo D, Walker E, Rodriguez A, Xiao J, "Multi-view self-supervised deep learning for 6D pose estimation in the amazon picking challenge.", IEEE International Conference on Robotics and Automation (ICRA), pp 1386-1383, (2017)

Traffic Signs Recognition Based on Convolutional Neural Networks Model for the use of Autonomous Cars

Said Gadri

***Abstract*—** Autonomous cars provide many benefits for humanity, such as reduction of deaths and injuries in road accidents, reduction of air pollution, increasing the quality of car control. For this purpose, some cameras or sensors are placed on the car, and an efficient control system must be setup, this system allows to receive images from different cameras and/or sensors in real time especially those representing traffic signs and process them to allows high autonomous control and driving of the car. Among the most promising algorithms used in this field are convolutional neural networks (CNN). The present study has proposed a CNN model composed of many convolutional layers, maxpooling layers, and full connected layers. As programming tools, this study has used python, Tensorflow and Keras which are currently the most used in the field.

***Keywords*—** machine learning, deep learning, traffic signs recognition, Convolutional Neural Networks, autonomous driving, self-driving cars.

Said Gadri is with the University Mohamed Boudiaf of M'sila, Algeria (e-mail: said.kadri@univ-msila.dz).

Compact Microstrip Ultra-Wideband Bandstop Filter with Quasi-Elliptic Function Response

Faris H. Almansour
Innovation and Industrial Development Institute
King Abdulaziz City for Science and Technology (KACST)
Riyadh, 11442, Saudi Arabia
falmansour@kacst.edu.sa

Hussein N. Shaman
Communications & Information Technology Research Institute
King Abdulaziz City for Science and Technology (KACST)
Riyadh, 11442, Saudi Arabia
hshaman@kacst.edu.sa

***Abstract*—This paper proposes a modified optimum bandstop filter with ultra-wideband stopband. The filter consists of three shunt open-circuited stubs and two non-redundant unit elements. The proposed bandstop filter is designed with unequal electrical lengths of the open-circuited stubs at the mid-stopband. Therefore, the filter can exhibit a quasi-elliptic function response that improves the selectivity and enhances the rejection bandwidth. The filter is designed to exhibit a fractional bandwidth of about 114% at a mid-stopband frequency of 3.0 GHz. The filter is successfully realized in theory, simulated, fabricated and measured. An excellent agreement is obtained between calculated, simulated and measured. The fabricated filter has a compact size with a low insertion loss in the passbands, high selectivity and good attenuation level inside the desired stopband.**

Keywords—Microstrip filter; lowpass filter; UWB filter, transmission line filter;

I. INTRODUCTION

Bandstop filters with steep skirt, high attenuation and wideband stopband characteristics are always in demand for blocking undesired signals or to suppress the unwanted spurious harmonics. Recently, various structures of bandstop filters have been proposed to achieve these objectives [1]-[10]. In [1]-[2], a cross-coupling between two nonadjacent transmission lines is introduced, using pair of symmetrical parallel coupled-lines and a capacitive load, to enhance the stopband performance by generating new transmission zeros inside the stopband leading to elliptic/quasi-elliptic response. However, a tight input/output coupling is required to achieve a wide-stopband and the attenuation across the stopband is limited. A further performance enhancement can be achieved by replacing the symmetrical parallel coupled-lines with a stepped-impedance coupled line which generates additional transmission zeros [3]. Bandstop filters with elliptic/quasi-elliptic response can also be built by using hybrid microstrip/ coplanar waveguide (CPW)-defected ground structure (DGS) with via-hole connection [4] or using tap coupled open-loop resonators [5] for a limited stopband with FBW of less than 35%. Moreover, stub-enclosed stepped-impedance resonator (SE-SIR) [6] or defected microstrip structure (DMS) [7] can be implemented to obtain dual or triple stopband responses but with limited FBWs. A common filter design for wideband realization is based on a standard conventional filters with quarter-wavelength shunt open-circuited stubs separated by quarter-wavelength connecting lines (unit elements) [8]. The unit elements of conventional filter are redundant and therefore, their filtering properties are not implemented. In order to enhance the performance of the conventional bandstop filter, the unit elements can be designed as non-redundant element as an optimum filter [9]. Both conventional and optimum bandstop filters using quarter-wavelength open-circuited stubs exhibit only one transmission zero at the mid-stopband. This is because all of their circuit elements have the same electrical length which is a quarter-wavelength at the mid-stopband frequency. Therefore, these types of filters require more elements in order to enhance their performances. Alternatively, a cross coupling is introduced by adding a quarter wavelength parallel-coupled line section that coupled the input and output of the optimum bandstop filter to provide a quasi-elliptic function response [10]. As a result, the filter shows two additional transmission zeros inside the stopband that enhance the selectivity and increase the 30-dB bandwidth of the stopband by more than 32% over the optimum bandstop filter.

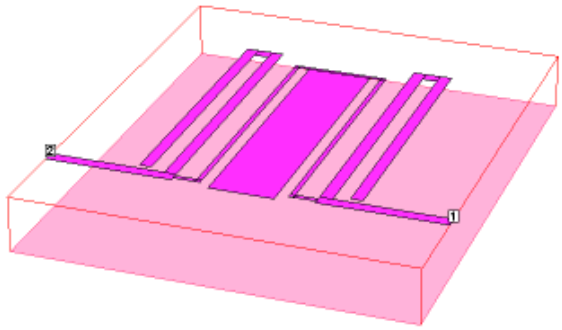

Fig. 1. Configuration of the proposed microstrip bandstop filter with ultra-wide stopband.

In this paper, we propose a new design of a bandstop filter with an ultra-wide stopband. The proposed bandstop filter is designed to have three shunt open-circuited stubs separated by non-redundant unit elements as demonstrated in Figure 1. The proposed filter is designed to have unequal electrical lengths of the open-circuited stubs. Therefore, the filter can exhibit a ripple stopband which effectively improves the filter selectivity and enhances the rejection bandwidth. The filter is realized on Roger

RT5880 microstrip substrate with a relative dielectric constant of (2.2) and with a thickness of (0.254 mm). The theoretical analysis, simulation, and experiment results are demonstrated.

.

II. Design and Analysis

Figure 1 illustrates the microstrip structure of the proposed filter. The filter design is based on a general circuit model for an optimum bandstop filter with two non-redundant unit elements and three shunt open-circuited stubs as displayed in Figure 2 [11]. The open-circuited stubs have characteristic impedances of Z_1, Z_2 and Z_3 with $Z_1 = Z_3$. The connecting lines have characteristic impedances Z_{12} and Z_{23}, where $Z_{12} = Z_{23}$. The electrical lengths of the shunt open-circuited stubs are represented by θ_1, θ_2 and θ_3. The electrical length of the unit element is denoted by θ_c and the terminal impedance is denoted by Z_O.

The general transfer function of the optimum bandstop filter with n open-circuited stubs and $n-1$ connecting lines can be written as follows [11]:

$$S_{21}(f)^2 = \frac{1}{1+\varepsilon^2 F_N{}^2(f)} \tag{1}$$

where ε is the ripple constant of passband and (F_N) is the filtering function defined as follows:

$$F_N(f) = T_n(\frac{t}{t_c})T_{n-1}(\frac{t\sqrt{1-t_c{}^2}}{t_c\sqrt{1-t^2}}) - U_n(\frac{t}{t_c})U_{n-1}(\frac{t\sqrt{1-t_c{}^2}}{t_c\sqrt{1-t^2}}) \tag{2}$$

in which $T_n(x)$ and $U_n(x)$ are the Chebyshev functions and t is the Richard's transform variable given by:

$$t = j\tan(\frac{\pi f}{2f_o}),\ t_c = j\tan[\ \frac{\pi}{4}(2-\mathrm{FBW})\ ] \tag{3}$$

where f_o and FBW are the mid-stopband frequency and the fractional bandwidth respectively, and can be defined by:

$$FBW = \frac{f_2 - f_1}{f_o},\ f_o = \frac{f_2 + f_1}{2} \tag{4}$$

f_1 and f_2 are the stopband lower and upper cut-off frequencies, respectively. The element values for the optimum bandstop filter, with $\theta_1 = \theta_2 = \theta_3 = \theta_c = \lambda l4$, are available in [11] for very wide range of fractional bandwidths. The standard optimum bandstop filter is designed to exhibit an ultra-wide stopband with a FBW of about 150% at a mid-stopband frequency of 3.0 GHz. The characteristic impedances of the unit elements and the open-circuited stubs of the circuit model,

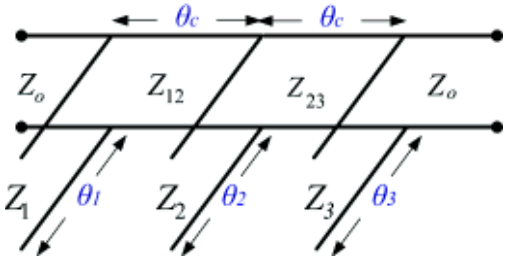

Fig. 2. Circuit model for proposed UWB bandstop filter.

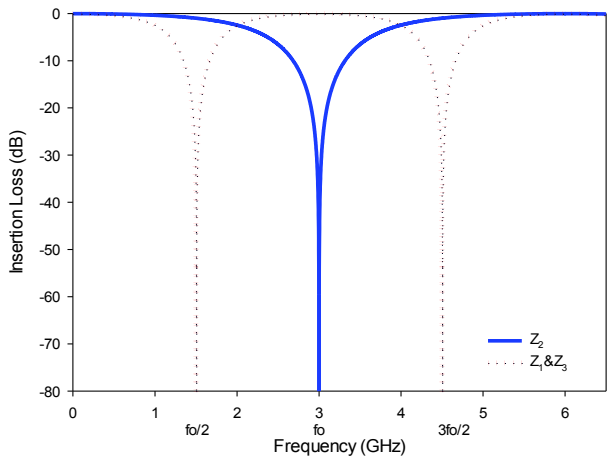

Fig. 3. Calculated insertion loss of Z_2 ($\theta_2 = \lambda/4$ at f_o) and Z_1 & Z_3 ($\theta_1 = \theta_3 = \lambda/4$ at $f_o/2$) shunt connected to a 50 Ohm line .

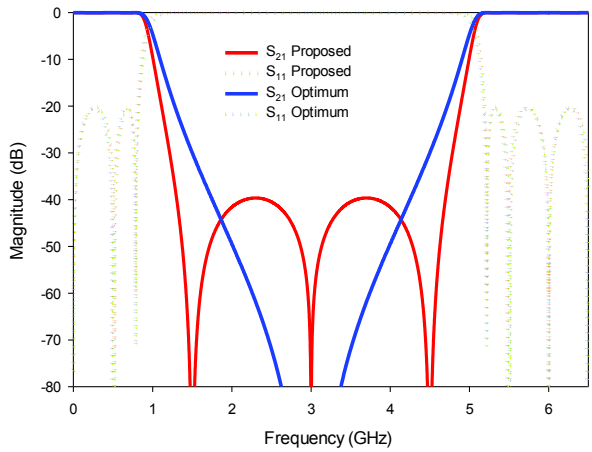

Fig. 4. A comparison between the standard optimum filter for $Z_1 = Z_3 = 24.15\Omega$, $Z_2 = 13.16\Omega$, $Z_{12} = Z_{23} = 160\Omega$ and $\theta_1 = \theta_2 = \theta_3 = \theta_c = \lambda l4$ at $3.0GHz$ with the proposed filter for $Z_1 = Z_3 = 51.7\Omega$, $Z_2 = 12.28\Omega$, $Z_{12} = Z_{23} = 162.9\Omega$, $\theta_1 = \theta_3 = \lambda l4$ at $1.5GHz$, and $\theta_2 = \theta_c = \lambda l4$ at $3.0GHz$.

displayed in Figure 2 with $\theta_1 = \theta_2 = \theta_3 = \theta_c = \lambda l 4$ at a mid-stopband frequency of 3.0 GHz, are calculated and found to be as follows: $Z_1 = Z_3 = 24.15\Omega$, $Z_2 = 13.16\Omega$ and $Z_{12} = Z_{23} = 160\Omega$. In order to increase the selectivity of the optimum bandstop filter, transmission zeros inside the stopband can be introduced which increase the bandwidth and also sharpen the filter selectivity. This can be achieved by changing the electrical lengths of the first and last open-circuited stubs to be $\lambda l 4$ at $f_o / 2$ as shown in Figure 3. As can be noticed in Figure 3, the second stub contributes a single transmission zero at the mid-stopband frequency (f_o) while the first and last stubs (Z_1 & Z_3) contribute two transmission zeros at ($f_o / 2$) and ($3f_o / 2$). A comparison between the computed s-parameters response for the standard optimum bandstop filter and the proposed filter is demonstrated in Figure 4. As can be noticed in Figure 4, both filters have identical performance inside the two passbands but different performance inside the stopband. Since all the open-circuited stubs are a quarter-wavelength at $f_o = 3.0$ GHz, the standard optimum bandstop filter only shows a single transmission zero at 3.0GHz (f_o). However, the proposed filter exhibits additional transmission zeros inside the desired stopband at 1.5 GHz ($f_o / 2$) and at 4.5 GHz ($3f_o / 2$). Since the open-circuited stubs of the proposed filter resonates at three different frequencies ($f_o / 2, f_o, 3f_o / 2$), the proposed filter shows elliptic function response with ripples in both stopband and passband. Thus, the selectivity of the proposed filter is effectively enhanced and the 40-dB rejection bandwidth is extended by more than 36% compared to the optimum filter with the same number of stubs.

III. Implementation Experiment

The design of the proposed bandstop filter is realized on a Roger RT5880 substrate with a thickness of 0.254 mm and a relative dielectric constant of 2.2. The microstrip layout with the physical lengths of the filter design is depicted Figure 5. The first and third open-circuited stubs and the unit elements are folded to shrink the size of the layout. The microstrip layout of the filter design is simulated using commercially available tool [12]. Figure 6 displays the calculated and the full-wave EM simulated insertion and return losses of the proposed filter, where excellent agreement is attained. Using print-circuit-board (PCB) technology, the microstrip filter layout is fabricated. The fabricated filter which is photographed in Figure 7, including 5.0 mm feed line at the input and the output, occupies a small size of 19.4 mm by 18.9 mm. The fabricated prototype is measured where the measurement performance is compared to the simulated result as shown in Figure 8. Excellent agreement is obtain where both simulated and measured results show three transmission zeros at the wanted stopband. The filter prototype shows an ultra-wide stopband with a 40-dB fractional bandwidth of approximately 114% at a mid-band frequency of 3.0 GHz with a very high selectivity. The measured insertion loss is found to be 0.5 dB at the mid-band frequency of the first passband and less than 1.3 dB at the mid-band frequencies of the upper passband.

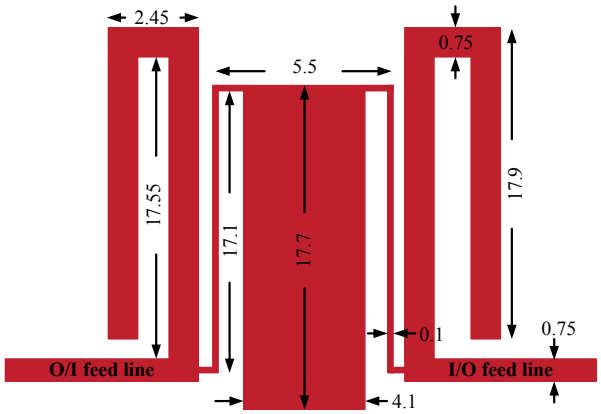

Fig. 5. Microstrip layout of the ultra-wideband bandstop filter. (Unit: mm).

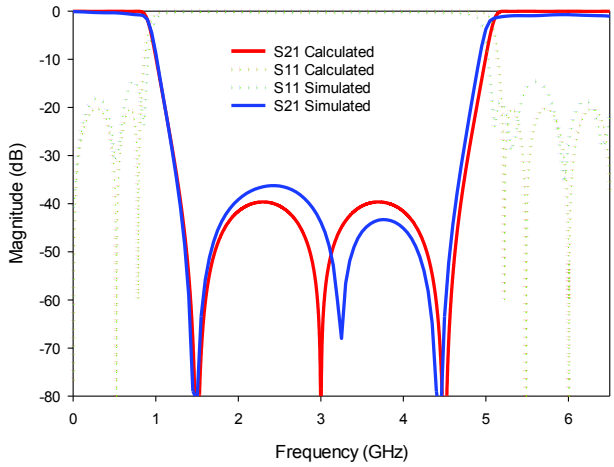

Fig. 6. A comparison between the calculated and full-wave EM simulated magnitude responses.

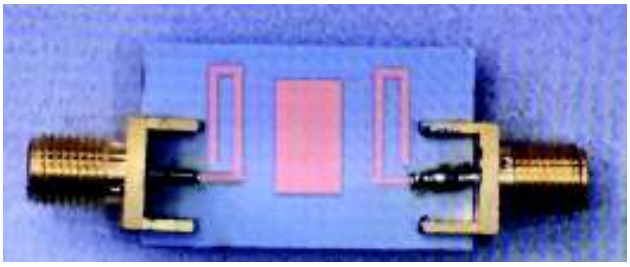

Fig. 7. A photograph of the prototype filter.

IV. Conclusion

A bandstop filter with an ultra-wide stopband has been proposed and presented in this paper. The proposed bandstop filter comprises of two non-redundant unit elements and three shunt open-circuited stubs. The proposed bandstop filter has been successfully realized in theory, simulated, fabricated and measured. It has been shown that the proposed filter can exhibit a ripple stopband which effectively improves the filter selectivity and enhances the rejection bandwidth. It has been verified that the proposed technique not only enhances the filter selectivity, but it also widens the 40-dB bandwidth by more than 36% over that of the optimum design. The fabricated filter has the advantages of low insertion loss, small size and ultra-wide rejection band.

Acknowledgment

This work is sponsored by King Abdulaziz City for Science and Technology (KACST).

References

[1] Hsieh MY, Wang SM. Compact and wideband microstrip bandstop filter. IEEE Microwave and Wireless Component Letter 2005;15 (7):472–474.

[2] Li R, Kim DI, Choi CM. Compact structure with three attenuation poles for improving stopband characteristics. Microwave and Wireless Component Letter 2006;16(12):663–665.

[3] Ren S, Wu L, Peng H, Mao J. Quasi-Elliptic Wideband Bandstop Filter Using Stepped-Impedance Coupled Line. IEEE Microwave Wireless Components Letter 2015;25(6):364-366.

[4] Chen H, Jiang D, Chen X. Wideband bandstop filter using hybrid microstrip/CPW-DGS with via-hole connection. IEEE Microwave Wireless Components Letter 2016;51(17):1469–1470.

[5] Yeo KSK, Vijaykumar P. Quasi-elliptic Microstrip Bandstop Filter Using Tap Coupled Open-loop Resonators. Progress In Electromagnetics Research C Letters 2013;35:1-11.

[6] Koirala GR, Shrestha B, Kim N-Y. Compact Dual-Wideband Bandstop Filter Using a Stub-Enclosed Stepped-Impedance Resonator. AEU-Int J Electron C 70 (2016) 198–203.

[7] Xiao J-K, Zhu Y-F. Multi-band bandstop filter using inner T-shaped defectedmicrostrip structure (DMS). AEU-Int J Electron C 2014;68:90–6.

[8] Schiffman B, Matthaei G. Exact design of band-stop microwave filters. IEEE Transactions on Microwave Theory and Techniques 1964;12:6-15.

[9] Horton M, Menzel R. General theory and design of optimum quarter wave TEM filters. IEEE Transactions on Microwave Theory and Techniques 1965;13:316-327.

[10] Shaman H, Hong JS. Wideband bandstop filter with cross-coupling. IEEE Transactions on Microwave Theory and Techniques 2007;55(8):1780–1785.

[11] Hong JS, Lancaster MJ. Microstrip Filters for RF/Microwave Applications. New York: Wiley, 2001.

[12] Sonnet Software Inc., EM User's Manual,Ver. 12, NY 2005

Technical, Environmental, and Financial Assessment for the Optimal Sizing of a Run-of-River Small Hydropower Project: A Case Study in Colombia

David Calderón Villegas, Thomas Kalitzky

***Abstract*—**Run-of-river (RoR) hydropower projects represent a viable, clean, and cost-effective alternative to dam-based plants and provide decentralized power production. However, RoR schemes' cost-effectiveness depends on the proper selection of site and design flow, which is a challenging task because it requires multivariate analysis. In this respect, this study presents the development of an investment decision support tool for assessing the optimal size of an RoR scheme considering the technical, environmental, and cost constraints. The net present value (NPV) from a project perspective is used as an objective function for supporting the investment decision. The tool has been tested by applying it to an actual RoR project recently proposed in Colombia. The obtained results show that the optimum point in financial terms does not match the flow that maximizes energy generation from exploiting the river's available flow. For the case study, the flow that maximizes energy corresponds to a value of 5.1 m^3/s. In comparison, an amount of 2.1 m^3/s maximizes the investors NPV. Finally, a sensitivity analysis is performed to determine the NPV as a function of the debt rate changes and the electricity prices and the CapEx. Even for the worst-case scenario, the optimal size represents a positive business case with an NPV of 2.2 USD million and an internal rate of return (IRR) 1.5 times higher than the discount rate.

***Keywords*—**Small hydropower, renewable energy, RoR schemes, optimal sizing, financial analysis.

I. Introduction

In the last decades, awareness about the need for the responsible use of fossil reserves and increasing penetration of renewable energy sources has favored the development of hybrid energy systems, mainly based on renewable energy sources. In developing countries, the exploitation of renewable sources represents an excellent opportunity for increasing the number of people having access to electricity with an adequate degree of availability and reliability [1]. Hydropower is one of the most used renewable sources of electricity, accounting for more than 16% of the world's net electricity production and more than 71% of net global renewable electricity production. As compared to other renewable energy sources, hydropower is reliable, economical, highly efficient, has a low maintenance cost, and has a large storage capacity [2], [3]. Notwithstanding, dam-based plant construction and operation are costly, can damage and disrupt the upstream and downstream ecosystem, and have catastrophic effects on downriver settlements and infrastructure [4]. Thereof, legislation in many countries, prohibits further construction of such plants [5].

Considering the current environmental and economic restrictions mentioned above, it is of prime importance to find a way that hydropower, as an electricity source, can be carried out through more reliable, more cost-effective, and safer engineering and financial mechanisms. Small hydropower projects (SHP) can serve this purpose. These are viable, clean, and cost-effective alternatives to dam-based plants and provide decentralized power production. Their relatively low operation and maintenance cost, long life spans, and negligible socioeconomic impacts are highly desirable and have propelled SHP to the center stage of the energy debate [6]. Nevertheless, an investment in an SHP entails a certain number of expenses, extended over the life of the project, and procures some revenues also distributed over the same period. The costs include a fixed component -the capital cost, insurance, taxes other than the income taxes, etc.- and a variable part -operation and maintenance expenses.

In pursuing widespread renewable energy sources in the increasing energy infrastructure, it is essential to address the optimal sizing of an SHP quantitatively. Thus, it is crucial to develop an investment decision support tool that quickly verifies the hydroelectric potential, performing a rapid optimization based on the technical parameters and financial values. In that context, this study analyzes which technical, environmental, and financial aspects need to be considered and how can they be integrated into an investment decision tool that optimizes the design of SHP to maximize investors NPV.

II. Literature Review

The basic principle of hydropower generation is impulse-momentum. Water potential is converted into mechanical energy by rotating the turbine, and mechanical energy is further converted into electrical energy using a generator. The definition of a SHP varies significantly from one country to another. There are three types of SHP. I) Dam-reservoirs, II) Pumped-storage and III) RoR, where water from the natural runoff generates electricity directly; therefore, there is no storage associated with it [7]. This research focuses on the analysis of this type of projects.

In small hydropower RoR schemes, water is diverted from the river by a structure located across the river, called the diversion weir. Water is then passed through the power channel

David Calderon is with Integral Ingenieros, Colombia (e-mail: dcalderon@integral.com.co).

up to the forebay tank [8]. A pressure pipe, called a penstock, conveys the water from the forebay to the turbine [9]. Water carried by the penstock directly strikes the turbine blade, followed by the guide vanes to rotate the turbine runner. The turbine's runner is coupled with the shaft, connected with the generator to produce electricity [10]. During the past three decades, research studies on an RoR have been devoted to the plant's optimal design, operation, and performance [11]. Within that research, a primary category is distinguished, which is the focus of the present study; Assessment of the optimal sizing of a RoR small hydropower plant.

The optimization of an RoR has been examined in various studies and it has been framed into three broad sub-categories: A) technical assessment, B) environmental assessment, and C) economic and financial indexes for assessing optimal size. The main contributions in each sub-category are explained below.

A. Technical Assessment

Given that the electro-mechanical equipment (turbines) represents an extensive contribution to the project's economic breakdown, most studies carried out have focused on determining the optimal size of them. Voros et al. [12] present an empirical short-cut design method for selecting the nominal flow rate of hydraulic turbines. Montanari et al. [13] also analyze and develop a model for optimizing a type of turbine through the exploitation of water resources in places with low head. Other studies have considered some other components and the turbine characteristics to determine the plant's optimal size. Almeida et al. [14] introduce a novel methodology where an economic and financial simulation model is used to analyze the project's risk and market variability. Basso et al. [15] proposes an analytical framework to describe the energy production and economic profitability of small RoR power plants based on the underlying streamflow regime.

B. Environmental Assessment

Most RoR hydropower projects commonly adopted the approach to enhance their environmental flow (e-flow), defined as the minimum flow required in the dewatered section of the river to maintain its ecological condition [16]. Magaju et al. [17] presented a model that can potentially integrate e-flows computed according to topographic or hydrologic criteria based on the flow duration curve (sub-basin surface, percentage of the design discharge, or similar). Blanco et al. [18] perform a sensitivity analysis regarding power generation's effect, considering a variable environmental flow, both for low water and floods.

C. Economic and Financial Indexes for Optimal Size Assessment

The evaluation of small hydropower plants' investment is made from the base economic criteria, represented by the proposed acquisition's economic indicators. These are static criteria such as the payback time, and the ROI offers only a general view of the value of the planned investment. On the other hand, there are dynamic criteria such as NPV. In these criteria, the time value of money is considered. Most of the studies consider the NPV of the plant as the primary financial indicator for optimization, since it represents the net difference between all revenues received from the produced electricity and the lifetime cost of the SHP.

III. METHODOLOGY

As explained in the previous section, this study presents the development of a robust computational model of an investment decision support tool that allows evaluating feasibility to determine the optimum size of the SHP. The energy system modeling is made through the combination of empirical and conceptual models [19]. Furthermore, a hybrid approach, meaning the combination of top-down and bottom-up approaches [20], is used to evaluate technical, environmental, and economic parameters. Moreover, the general model itself refers to an optimization model whereby the size of the RoR is optimized by means of an objective function. Fig. 1 summarizes the methodology.

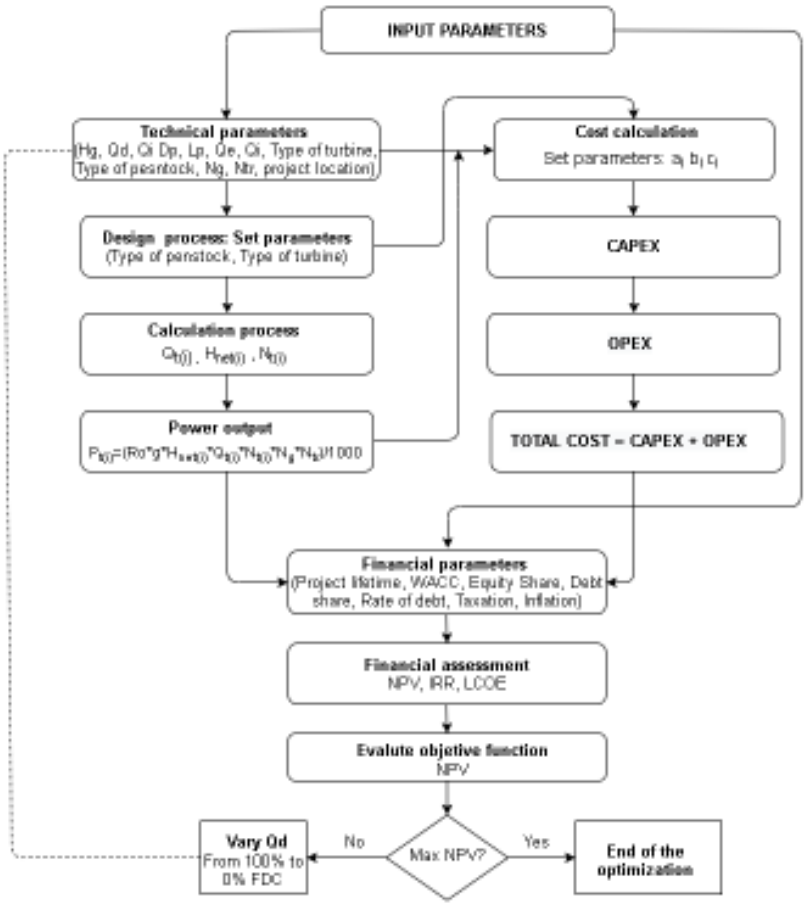

Fig. 1 Flow chart of the optimization process with the technical, cost, and financial models

The optimization process follows three steps

- find the installed capacity and the electricity output for a particular design flow,
- calculate the yearly benefits of all the different design flows, and
- select a set of power plants that maximize the NPV based on a combination of the cited constraints.

As a key differentiating element, this study conducts the calculations considering explicitly the turbine efficiency, the hydraulic losses, and the penstock diameter. In like manner, the river's environmental flow is considered and discounted from the disposable flow. This directly impacts the power output of the system. Moreover, static, and dynamic economic indexes are considered for financial optimization. Fig. 1 shows that the optimization model comprises three main blocks: A) Technical-Environmental model, B) The cost model, and C) The financial model. Below a detailed explanation of each block is presented.

A. Technical-Environmental Model

Energy production from hydropower plants is computed daily, considering the environmental flow and technical limitations due to the turbine's technical features. The power output of the hydropower plant, P, in kilowatt (kW), for an instant t, is calculated using (1):

$$P_{t(i)} = \left(\rho_w * g * H_{net(i)} * Q_{t(i)} * \eta_{t(i)} * \eta_g * \eta_{tr}\right)/1000 \qquad (1)$$

where $\rho_w, g, \eta_g, \eta_{tr}$ are constants and represent the density of water (kg/m^3), the gravitational acceleration (m/s), the generator, and the transformer efficiency. On the other hand, $H_{net(i)}, Q_{t(i)}, \eta_{t(i)}$ represent the net head or effective water pressure at the bottom of the penstock, the turbine inflow, and the turbine efficiency, respectively.

The turbine inflow is time-dependent and fluctuates according to the natural streamflow, the flow design, the environmental flow, and the minimal technical turbine flow. Likewise, the net head and the turbine efficiency are time-dependent and depend or vary as a function of the turbine inflow, the penstock diameter, and the design flow. Furthermore, turbine efficiency depends on the type of turbine (e.g., Pelton or Francis). As it is possible to elucidate, (2) has boundary conditions dynamically. Therefore, it cannot be solved analytically. In this respect, numerical integration is applied by constructing an N-vector of mean daily turbine inflows with a fixed daily integration time step. The series of mathematical formulations used to solve (1) is described step by step below.

- Turbine inflow calculation: The process for calculating the turbine inflow is described mathematically by means of (2)-(10). The turbine operates when the water flow is

between a minimum and a design flow (Qmin, Qd). Both limits depend on the type of turbine and are specified by the manufacturer. As a rule of thumb, for a Francis turbine, the lower limit is set in 55% of the flow design, while for a Pelton turbine, the limit is set at 35% of the nominal flow rate [21].

$$Q_{u(i)} = Q_{intake(i)} - Q_{environmental} \quad (2)$$

$$if\ Type\ of\ turbine = Pelton \quad (3)$$

$$Q_{min} = 0.15Q_d \quad (4)$$

$$else: Q_{min} = 0.5Q_d \quad (5)$$

$$if\ Q_{u(i)} \leq Q_{min} \quad (6)$$

$$Q_{t(i)} = 0 \quad (7)$$

$$elif\ Q_{u(i)} < Q_d \quad (8)$$

$$Q_{t(i)} = Q_{u(i)} \quad (9)$$

$$else: Q_{t(i)} = Q_d \quad (10)$$

- Net head calculation: The net head is involved in (1). It can be calculated by subtracting the system's hydraulic losses (hf) that correspond to the flow rate ($Q_{t(i)}$,) conducted to the turbines from the gross head (Hg). The singular losses are related to the enlargement and narrowing, respectively at the entrance and the exit of the forebay tank and to the bend at the beginning of the penstock. These local losses are linked with the motion of the fluid and can be neglected for long pipes [22]. The hydraulic losses (hf) are a function of the length (Lp) and diameter (Dp) of the penstock, the flow velocity (Vt(i)) at the penstock, which is a function of the turbine inflow, and the friction factor (f). The latter is a function of the type of material (e.g., steel or GRP) and the flow regime inside the pipe (e.g., laminar or turbulent flow).

Generally, the friction factor (f) can be computed by the well-known White-Colebrook equation for a specific flow Reynolds number and a given pipe wall roughness. It is not convenient to use, because its implicit expression in f requires iteration. Since power generation analysis is done for a series of flows over 39 years, with the daily resolution, this iterative process generates a considerable computational cost. For this reason, several approximate explicit counterparts have been proposed. For this study, the equation proposed by [23] is implemented.

As previously introduced, hydraulic losses and flow rates are a function of speed within the penstock. Since the flow depends on the river's conditions and the type of turbine, the pipeline's diameter is a fundamental variable since it determines the speed of the flow. From an economic and construction point of view, it is better to have a small diameter pipe. However, this implies higher flow velocity and, therefore, higher hydraulic losses. The latter translates into a reduction in the electricity generated. On the other hand, a substantial diameter is useful for electricity generation. However, the costs of the pipe increase quadratically with the diameter. Therefore, doubling the diameter implies a 4-fold increase in prices. In this study, for each design flow analyzing and depending on the pipeline's material, the required diameter is calculated to calculate the pipe's maximum velocity below the upper limit. The limits were set based on the author's experience in the feasibility study of hydropower projects and specialized literature. For GRP, the maximum flow velocity is set as 3 m/s, and for steel, the maximum flow velocity is set as 5 m/s [24], [25]. The process for calculating the net head (Hnet) is described mathematically by means of (11)-(24)

$$if\ Type\ of\ penstock = Steel: \quad (11)$$

$$V_{max} = 5\ m/s \quad (12)$$

$$Else: Vmax = 3\ m/s \quad (13)$$

$$A_P = \frac{Q_d}{V_{max}} \quad (14)$$

$$D_p = \sqrt{\frac{4*A_p}{3.1416}} \quad (15)$$

$$if\ Type\ of\ penstock = Steel: \quad (16)$$

$$e = 0.000045\ m \quad (17)$$

$$Else\ e = 0.000029\ m \quad (18)$$

$$e_R = \frac{e}{D_p} \quad (19)$$

$$V_{p(i)} = \frac{Q_t}{A_p} \quad (20)$$

$$R_{e(i)} = \frac{\rho_w * V_{p(i)} * D_p}{\mu_w} \quad (21)$$

$$f_i = 1.613 * \left[ln\left(0.234 * {e_R}^{1.1007} - \frac{60.525}{{R_{e(i)}}^{1.1105}} + \frac{56.291}{{R_{e(i)}}^{1.0712}}\right)\right]^{-2} \quad (22)$$

$$h_{f(i)} = f_i \frac{L_p}{D_p} \frac{{V_{p(i)}}^2}{2g} \quad (23)$$

$$H_{Net(i)} = H_{gross} - h_{f(i)} \quad (24)$$

- Turbine efficiency calculation: The turbine's performance is characterized by its nominal flowrate, Qr, which is an explicit indication of its size. Likewise, turbine efficiency depends on the working fluid flow rate and actual turbine characteristics. Voros et al. [12] present an expression that allows calculating Pelton and Francis turbines' efficiency, considering the relationship of the turbine inflow and the design flow. As a novelty, they introduce two characteristic turbine parameters Qmin and Qmax, representing the fraction of its nominal flowrate corresponding the lower and upper extreme working flowrates, respectively. The

empirical expression is proposed for describing the turbine efficiency characteristic curve. Excellent fits to actual experimental data were detected when the proposed expression was used as real turbine data. For each type of turbine (Pelton or Francis), there are maximum efficiencies, design and minimum flow rates, and constants specific to each turbine's efficiency curves. All the technical values are described within [12]. The process for calculating the turbine efficiency (η_t) is described mathematically by means of (25)-(27)

$$if\ Type\ of\ turbine = Pelton: \tag{25}$$

$$\eta_t = \eta_{tmax}\left(-0.224\left(\frac{Q_{t(i)}}{Q_d}\right)^2 + 0.483\left(\frac{Q_{t(i)}}{Q_d}\right) + 0.741\right) \tag{26}$$

$$else: \eta_t = \eta_{tmax}\left(-0.537\left(\frac{Q_{t(i)}}{Q_d}\right)^2 + 1.047\left(\frac{Q_{t(i)}}{Q_d}\right) + 0.49\right) \tag{27}$$

By coupling the previously described steps, (2) is solved using numerical integration for each intake flow. Thus, power output is calculated. The system's rated power is reached when the design flow (Qd) is derived through the penstock. For this flow, the maximum efficiency of the turbine is achieved. And therefore, the full output power is created. This outcome is one of the primary inputs of the next block. It is the cost model, where the cost of the main components is calculated.

B. Cost Model

The costs of any SHP framed as an RoR project are divided into two categories: capital and variable costs [26]. In the first category, two main components should be considered. I) construction of civil works and, II) electromechanical equipment. The second category refers to the operating and maintenance costs of the two components mentioned above. These can be assumed either as a fixed percentage of the capital expenditures or variables during the project's lifetime.

The maximum power output calculated before is used as an input along with other established variables, such as the system's gross head. Combining those variables, the project's total cost is estimated through the aggregation of capital expenditures (CapEx) and the operational expenses (OpEx). A non-linear statistical relationship, proposed by [27] and showed through (28) is used for this calculation:

$$CapEx = a * P(MW)^b * H(m)^c \tag{28}$$

where C is the component cost, P means the rated power and H means the gross head. The constants a,b and c are correlation constants which vary depending on the region.

C. Financial Model

The financial evaluation is performed by maximizing an objective function. Therefore, the unknown variable is set as the design flow, and the constraints are the environmental flow, the type of turbine, and the maximum velocity regarding the kind of penstock used. The main inputs are the electricity output integrated in time and the total cost. The NPV method is used to analyze the profitability of investment in an RoR project. Thus, financial evaluation is performed using the discounted cash flow method from a project perspective. The NPV is the sum of the present values of each period's cash flow, plus the initial investment (CapEx). Mathematically, this latter discussion could be described by (29):

$$NPV = CapEx + \sum_{i=0}^{T} \frac{C_i}{(1+WACC)^t} \tag{29}$$

where C_i means the cash flow at year i, T represents the horizon time (discussed in the case-study), t the analyzed year and $WACC$ the weighted average cost of capital. The projects with negative NPV will be rejected since this means the discounted benefits during the project's lifetime period cannot cover the initial costs invested for the expected risk associated with the project. In comparing a group of projects, the project with the most significant positive NPV is the best one.

IV. Case Study

The case study involves the analysis of a proposed RoR project in Colombia. The proposed project should exploit the stream flows of a small tributary of the Porce River. The catchment area at the intake of the RoR is about 79 km^2.

The hydrological data consist of 39 consecutive years of mean daily flow data from 1973 until 2011. The mean daily flow data are used to characterize the river's flow regime and constructs the flow duration curve (Fig. 2). At the intake, the discharge fluctuates moderately between values of 0 to 10.5 m^3/s, with a mean flow of about 3.11 m^3/s. The environmental flow (e-flow) is set as 0.51 m^3/s. The gross hydraulic head (Hg) available is set as the difference between the intake and powerhouse. For the case study, it represents a value of 235 m. the GRP pipe on the bench and with an overpass has a length of 1,720 m. The powerhouse is of the superficial type and is equipped with Pelton turbines. The transformer and generator efficiencies are assumed as constants and with values of 0.972 and 0.992, respectively. Fig. 3 shows a schematic plan view of the project.

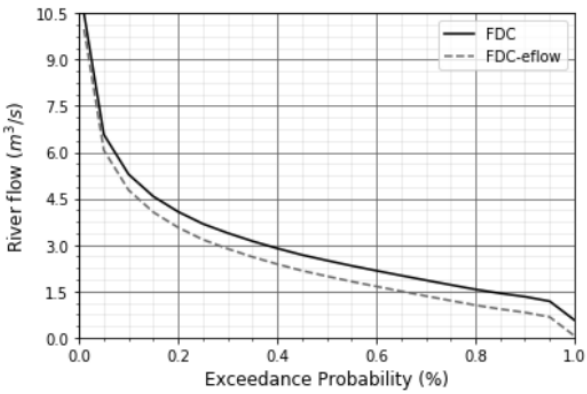

Fig. 2 Flow duration curve of the analyzed river

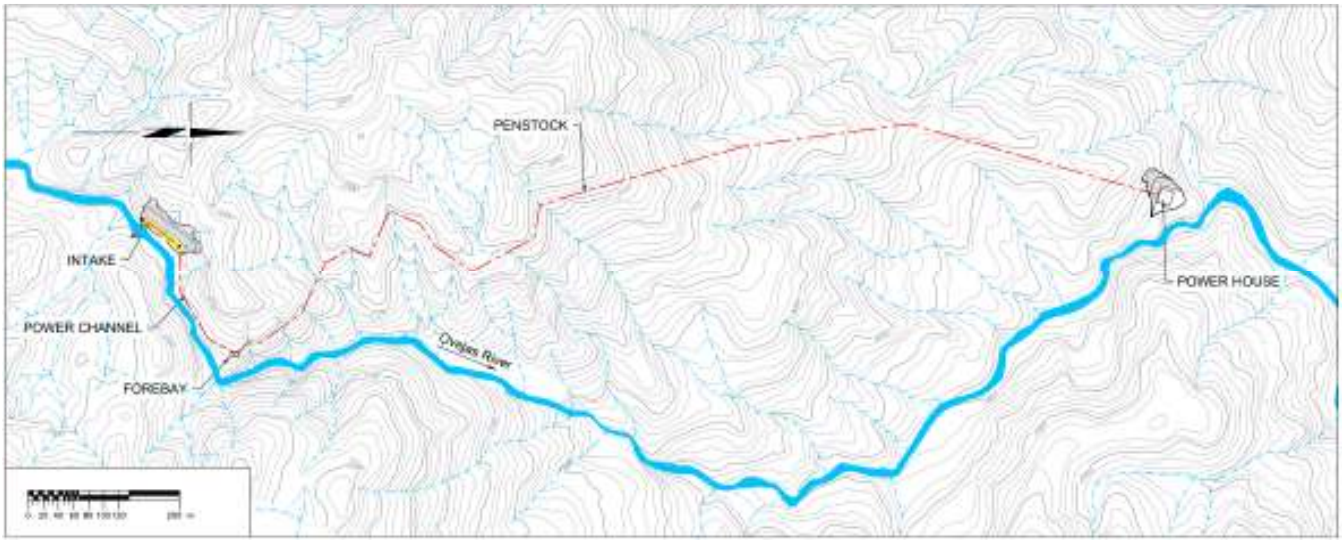

Fig. 3 Top view of the proposed SHP for the case study

The financial evaluation is carried out by constructing the net flows of funds for the project. The tangible benefits associated with electricity sales are considered. A feed-in tariff scheme is assumed. For the complete assessment of the project, additional financial and fiscal parameters are introduced, like the construction period, tax rate, annual operation and maintenance cost, inflation rate, electricity prices, and project lifetime. For this project, the capital structure is composed of 70% debt and 30% equity. The income statement construction was made considering a depreciation horizon of 10 years and a tax rate of 19%. Besides, regarding the debt, the debt horizon and the rate of debt are assumed as ten years and 7.5 %, respectively.

For the analysis, both CapEx and OpEx are considered. The CapEx was considered the sum of the main components, such as civil works, electro-mechanical equipment, and transmission costs. The OpEx is fixed and represents a 4%/year of the CapEx. To calculate the Weighted Average Cost of Capital (WACC), it is necessary to know the Risk-free return, beta, and ERP. Those values are obtained according to different specialized sources. For the first two variables, a value of 1.07 and 6% are used.

To calculate the incomes, the wholesale electricity price (USD/MWh) is essential. However, the possible fluctuations of those prices are complicated to estimate due to social and political reasons, the increase in renewable energy in the primary grid, and the possible subsidies. Considering that the project's lifetime is 30 years, an initial value, at 2020 of 45 USD/MWh (based on the Colombian Market) is used for the wholesale electricity price. A simple linear interpolation is used to estimate an inflation ratio, which is applied to both variables at each year of the project evaluation. An inflation value of 3.5% is fixed for all the years

V. Results

A. Preliminary Results

The initial picture of the plant performance is shown in Fig. 4. Graph (a) from it shows the behavior of the installed capacity (primary Y-axis), and the capacity factor (secondary Y-axis) of the evaluated points are illustrated, depending on the design flow. The total variation interval, expressed in terms of the plant capacity, plant factor, ranges from 0 MW to 20.7 MW and from 0.18 to 1, respectively. As expected, due to the linear relationship among the variables, the higher the flow, the bigger the plant's power. However, the capacity factor behavior is inversely proportional because of the water resource's depletion at the source to serve the plant's high capacities. Capacity factors represent the ratio between the annual output and the nominal capacity. For a RoR project, plant factors more significant than 0.50 and less than 0.80 are considered adequate [28]. Thus, it is expected that the optimal flow is in the range of 1.9 m^3/s to 4.7 m^3/s. Graph (b) from Fig 4 shows the behavior of the electricity output (primary Y-axis) and the capacity factor (secondary Y-axis) of the evaluated points are illustrated, depending on the rated power.

Graph (b) shows that neither of the two variables has a linear dependency. Energy production increases as installed capacity increases because the more significant the installed capacity, the larger the turbines and, therefore, the river's high flow regime is exploited more efficiently. However, the curve exhibits an inflection point where electricity production begins to decrease. The turbines' installed capacity is such that it cannot operate during low flows period since the flow to be derived far from the minimum turbine inflow that guarantees safe and reliable operation of the equipment.

The maximum electricity output of 36975 MWh/year is reached when the design flow is equal to 5.3 m^3/s, representing a rated power of 10.40 MW and a capacity factor of 0.41. As will be discussed below, the flow implies the highest energy generation does not mean the plant's optimum point.

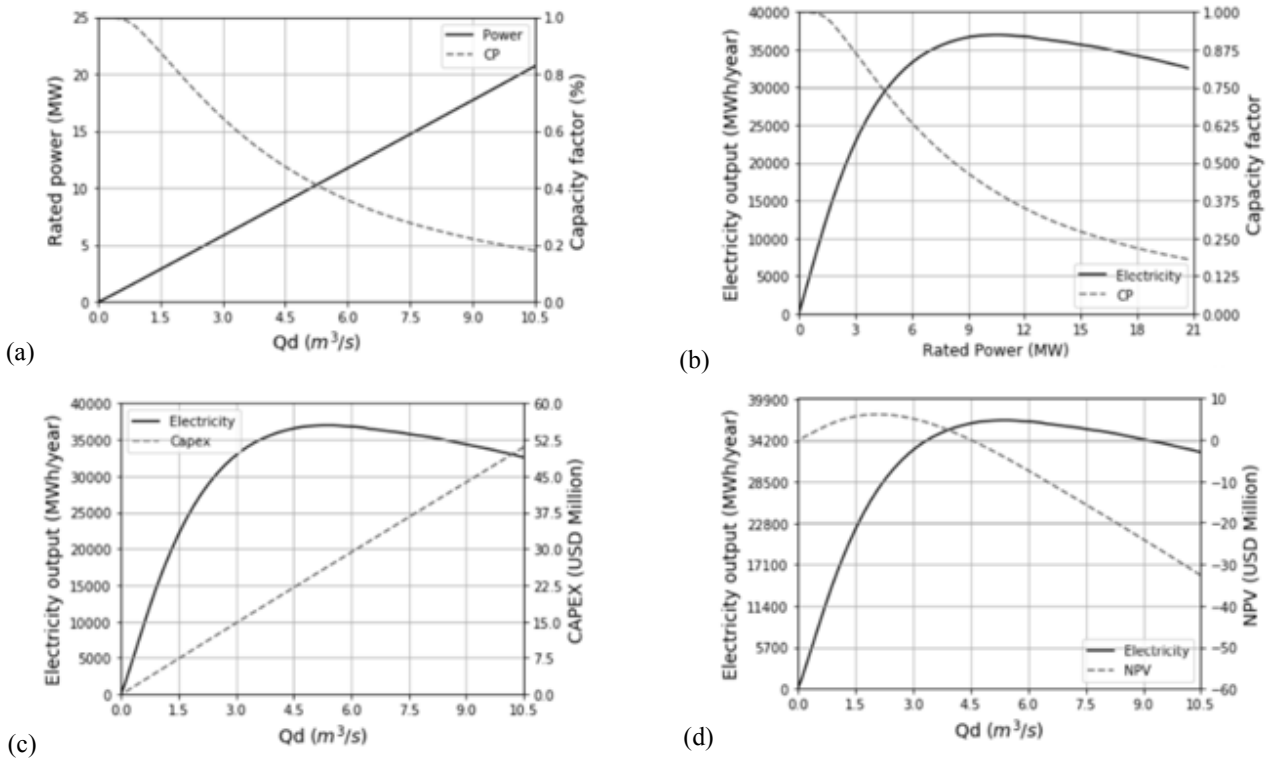

Fig. 4 Primary optimization results

Graph (c) of Fig. 4 compares the electricity output (primary Y-axis) and the CapEx (secondary Y-axis) depending on the design flow. While the cost of capital (CapEx) decreases as the installed capacity is reduced, which occurs due to the reduction of the design flow, the generation of energy has an inverse behavior. For a flow range between 10.5 m^3/s and 5.3 m^3/s electricity production increases. However, from the lower limit of the previous range, the generation begins to fall with a gradual slope until it reaches a value of 2 m^3/s, representing an installed capacity of 3.6 MW and an electricity generation of 25,915 MWh/year. From this point on, the electricity generation decreases considerably, which means there is a non-optimal exploitation of the plant's water resource.

Graph (d) from Fig. 4 shows the behavior of the electricity output (primary Y-axis) and the investor NPV (secondary Y-axis) depending on the design flow. The NPV curve also shows nonlinear behavior. From the investors point of view, the range of flows in which the project begins to be financially attractive coincides with the range previously identified. The plant factors fluctuate between values considered adequate according to the literature. These cover a range of flows between 1.9 and 4.3 m^3/s, which correspond to values between 35% and 143% of the multi-annual average flow. From a design flow of 10.5 m^3/s, representing the maximum flow of the river duration curve, to the upper limit of the range described above, the electricity production only marginally increases while adding extra cost to the construction and the O&M of the project. That means that both capital and operational expenditures for the higher rated power exceed the revenues from the incremental power production.

B. Selected Design Flow

The selected design flow is the streamflow that maximizes the objective function (the investors NPV). The corresponding optimal design flow is equal to 2.1 m^3/s, a streamflow that is exceeded 60% of the time. Thus, the degree of exploitation of the available water resources allowed by the optimal design flow is very high, as evidenced by the capacity factor obtained, with a value of 0.78. For this flow of 2.1 m^3/s, the rated power of the RoR is 4 MW, and the annual electricity output reaches a value of 27,567 MWh. Regarding the economic values, the reached NPV is USD 6.4 million, the IRR is 18%, and the payback time is eight years.

Given the NPV of USD 6.4 million, it is possible to conclude that the analyzed case is a positive or profitable business model. Besides, the IRR is 2.5 times higher than the WACC. In respect thereof, the optimized RoR project represents a desirable rate of return for investors. Fig. 5 shows the behavior of the comparison between the free cash flow of the project and the cumulative cash flow.

Regarding Fig. 5, it is essential to highlight that the project is in the execution stage during the first three years. Thus, this initial stage represents a negative cash flow. However, as of the fourth year, when electricity generation begins, a constant, growing, and positive cash flow is presented. Since the operation's marginal costs are meager given that the primary

fuel is water, which is free and renewable, the investment and initial capital injection is recovered in year 8, where the breakeven is reached (from a pay-back time perspective). From this point, the project only leaves profits for the investors.

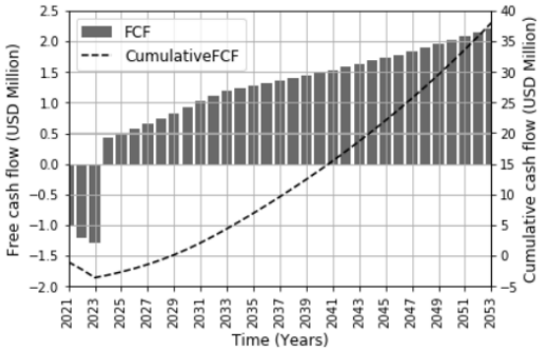

Fig. 5 Comparison between the FCF and the Cumulative FCF of the investors

C. Sensitivity Analysis

For the current case, capital incomes are due to electricity sales. Contrarily, expenses are associated with the initial investment (CapEx) and Operational costs (OpEx). A sensitivity analysis is performed to determine the impact of the change in some of the variables and its effect on the project's profitability. The used methodology consists of simultaneously changing both variables, where one of the variables is related to the income (electricity sales) and the other to the operational costs (CapEx). Then the leading financial indicator (NPV) is calculated for each possible combination. Both variables are sensed up to 15% above and below the current price in every combination. This latter is done with intervals of 5% up and down.

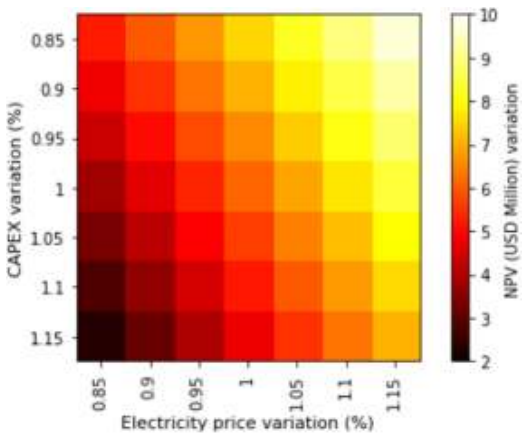

Fig. 6 Relationship among NPV, Electricity and CapEx value fluctuation

Based on the results shown on Fig. 6, it is essential to mention that even for both variables' most unfavorable combinations, the NPV is positive. If the electricity price is 15% below the expected market value and the CapEx investments are 15% higher than the used values, the NPV is still positive, i.e., USD 2.33 million. This latter means that the investment risk is covered in the worst of conditions since the IRR value is 1.5 higher than WACC. On the contrary, if the variables analyzed are inverted, the price of energy increases by 15%, and the initial cost of the investment decreases in the same proportion, the business case rises considerably, and the value of the NPV is USD 9.67 million.

The levelized cost of electricity (LCOE) is the current total cost value of building and operating a power-generating facility over its entire useful life [29]. Lately, the LCOE has become a commonly used tool for cost comparison and has been useful to government and investors in their decision-making processes.

As discussed, hydropower is capital-intensive and has low O&M costs and no fuel costs. Thus, LCOE and NPV are very sensitive to investment costs and interest rates. Since the project capital structure is fixed, the only way to vary the discount rate (WACC for the present analysis) is by changing the cost of debt. To understand the previous discussion's impact, a sensitivity analysis is carried out, varying the cost of debt from a value of 3% to 10% with intervals of 0.5%.

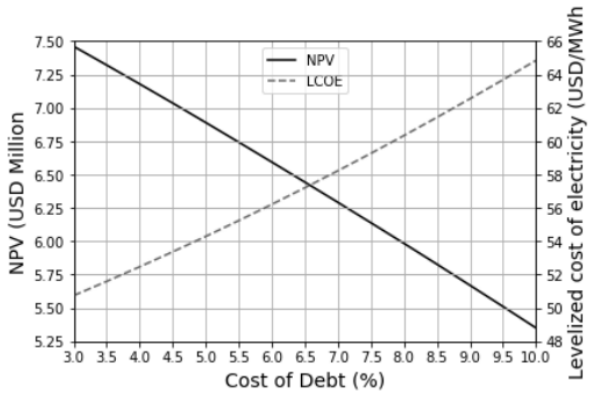

Fig. 7 Sensitivity of the NPV and LCOE to different debt costs

Fig. 7 shows that the lower the cost of debt the higher the NPV and the lower the LCOE. For the scenario where the debt cost is equal to 3%, the NPV and the LCOE obtained are USD 7.85 million and 50.7 USD/MWh, respectively. In the extreme case in which the debt cost value is 10%, the NPV decreases to USD 5.35 million and the LCOE reaches a value of 65 USD/MWh

VI. Conclusion

The present research develops an investment decision support tool to assess the optimal size of RoR scheme. The methodology and the tool itself are applicable and scalable through regions and economies. Its flexibility and generality make it a useful tool for selecting the optimal design flow in practical applications as demonstrated by the case study presented in the research.

It is concluded that the acquisition and cost of debt depend on the specific project and the country where it is deployed. In emerging countries such as the one exposed the cost of debt can considerably affect the competitiveness (measured via the LCOE) of the electricity source, and therefore the project´s financial viability. Furthermore, the results of this research

study allow to show that it is paramount to consider the turbine efficiency, the hydraulic losses, and the penstock diameter to assess the economic feasibility of an RoR project, before spending substantial sums of money. Finally, the present analysis was performed for a typical case where the RoR project is connected to the primary grid. However, the optimal design flow's main outcome could change if the analysis is performed for a non-grid connected project. Therefore, as part of the ongoing research, it is recommended to analyze this kind of scenario in the short-term.

REFERENCES

[1] Cavazzini G, Santolin A, Pavesi G, Ardizzon G. Accurate estimation model for small and micro hydropower plants costs in hybrid energy systems modelling. Energy (Internet). 2016;103:746–57. Available from: http://dx.doi.org/10.1016/j.energy.2016.03.024

[2] Mishra S, Singal SK, Khatod DK. Optimal installation of small hydropower plant - A review. Renew Sustain Energy Rev (Internet). 2011;15(8):3862–9. Available from: http://dx.doi.org/10.1016/j.rser.2011.07.008

[3] Liu J, Zuo J, Sun Z, Zillante G, Chen X. Sustainability in hydropower development - A case study. Renew Sustain Energy Rev (Internet). 2013;19:230–7. Available from: http://dx.doi.org/10.1016/j.rser.2012.11.036

[4] Zarfl C, Lumsdon AE, Berlekamp J, Tydecks L, Tockner K. A global boom in hydropower dam construction. Aquat Sci. 2014;77(1):161–70.

[5] Paish O. Small hydro power: Technology and current status. Vol. 6, Renewable and Sustainable Energy Reviews. 2002. p. 537–56.

[6] Edenhofer O, Pichs-Madruga R, Sokona Y, Seyboth K, Eickemeier P, Matschoss P, et al. IPCC, 2011: Summary for Policymakers. In: IPCC Special Report on Renewable Energy Sources and Climate Change Mitigation (Internet). Cambridge University Press. 2011. 246 p. Available from: http://srren.ipcc-wg3.de/report

[7] Bernhard Pelikan. Guide on How to Develop a Small Hydropower Plant. Eur Small Hydropower Assoc (Internet). 2004;296. Available from: http://citeseerx.ist.psu.edu/viewdoc/download?doi=10.1.1.172.1731&rep=rep1&type=pdf

[8] Mishra S, Singal SK, Khatod DK. Costing of a Small Hydropower Projects. Int J Eng Technol. 2012;4(3):239–42.

[9] Campbell RJ. CRS Report for Congress Small Hydro and Low-Head Hydro Power Technologies and Prospects Specialist in Energy Policy. 2010; Available from: http://nepinstitute.org/get/CRS_Reports/CRS_Energy/Renewable_Fuels/Small_hydro_and_Low-head_hydro_power.pdf

[10] Singh VK, Singal SK. Operation of hydro power plants-a review. Renew Sustain Energy Rev (Internet). 2017;69(November 2016):610–9. Available from: http://dx.doi.org/10.1016/j.rser.2016.11.169

[11] Yildiz V, Vrugt JA. A toolbox for the optimal design of run-of-river hydropower plants. Vol. 111, Environmental Modelling and Software. 2019. p. 134–52.

[12] Voros NG, Kiranoudis CT, Maroulis ZB. Short-cut design of small hydroelectric plants. Renew Energy. 2000;19(4):545–63.

[13] Montanari R. Criteria for the economic planning of a low power hydroelectric plant. Renew energy. 2003;28(13):2129–45.

[14] de Almeida JL, Lejeune AGH, Marques JAAS, Cunha MC. OPAH a model for optimal design of multipurpose small hydropower plants. Adv Eng Softw. 2006;37(4):236–47.

[15] Basso S, Botter G. Streamflow variability and optimal capacity of run-of-river hydropower plants. 2012;48(August):1–13.

[16] Boodoo KS, Mcclain ME, Julia J, Lucia O, Lo O. Ecohydrology & Hydrobiology Impacts of implementation of Colombian environmental flow methodologies on the flow regime and hydropower´ River, Colombia production of the Chinchina. 2014;14:267–84.

[17] Magaju D, Cattapan A, Franca M. Energy for Sustainable Development Identi fi cation of run-of-river hydropower investments in data scarce regions using global data. Energy Sustain Dev (Internet). 2020;58:30–41. Available from: https://doi.org/10.1016/j.esd.2020.07.001

[18] Carvajal CR, García-Muñiz AS, Cuartas BM. Assessing socioeconomic impacts of integrating distributed energy resources in electricity markets through input-output models. Energies. 2019;12(23):1–21.

[19] Kokkonen T, Koivusalo H, Karvonen T. A semi-distributed approach to rainfall-runoff modelling — a case study in a snow affected catchment. 2001;16(5):481–93.

[20] Ringkjøb HK, Haugan PM, Solbrekke IM. A review of modelling tools for energy and electricity systems with large shares of variable renewables. Renew Sustain Energy Rev (Internet). 2018;96(July):440–59. Available from: https://doi.org/10.1016/j.rser.2018.08.002

[21] Anagnostopoulos JS, Papantonis DE. Optimal sizing of a run-of-river small hydropower plant. Vol. 48, Energy Conversion and Management. 2007. p. 2663–70.

[22] Garegnani G, Sacchelli S, Balest J, Zambelli P. GIS-based approach for assessing the energy potential and the financial feasibility of run-off-river hydro-power in Alpine valleys. Appl Energy (Internet). 2018;216(February):709–23. Available from: https://doi.org/10.1016/j.apenergy.2018.02.043

[23] Fang X, Xu Y, Zhou Z. New correlations of single-phase friction factor for turbulent pipe flow and evaluation of existing single-phase friction factor correlations. 2011;241:897–902.

[24] Edition S. Fiberglass Pipe Design.

[25] Design TCSP, Bambei JH. Steel Penstocks: Second Edition (Internet). American Society of Civil Engineers; 2012. (ASCE Manuals and Reports on Engineering Practice). Available from: https://books.google.com.br/books?id=SpUjebFpyC0C

[26] Hatata AY, El-Saadawi MM, Saad S. A feasibility study of small hydro power for selected locations in Egypt. Energy Strateg Rev (Internet). 2019;24(April 2018):300–13. Available from: https://doi.org/10.1016/j.esr.2019.04.013

[27] Davitti A. Project cost modelling for hydropower schemes in. 2019; (February).

[28] 2017 Hydropower Market Report.pdf.

[29] Kost C, Shammugam S, Jülch V, Nguyen H, Schlegl T. Levelized Cost of Electricity- Renewable Energy Technologies. 2018;(March).

MATLAB Model to Predict the Effect of Temperature Polarization in Direct Contact Membrane Distillation for Graphene Oxide Surface Modified Membranes

Radwan Alfahel, Alaa AlHawari

***Abstract*—** Desalination and brine management is one of the main concerns on the last decades. Membrane distillation showed promising results in operating high feed salinity. Direct contact membrane distillation (DCMD) gain the most attention among other configurations due to its simplicity. This study is applied to predict the performance of DCMD when graphene oxide (GO) is used for membrane surface modification. MATLAB software was used to predict the temperature polarization coefficient and the flux of DCMD.

***Keywords*—**Membrane Distillation, Graphene Oxide, Temperature Polarization, Brine

Radwan Alfahel, Qatar University – Department of Civil & Architectural Engineering, College of Engineering, P.O. Box 2713, Doha, Qatar (e-mail: ra1404482@qu.edu.qa)

Alaa AlHawari Qatar University – Department of Civil & Architectural Engineering, College of Engineering, P.O. Box 2713, Doha, Qatar (e-mail: a.hawari@qu.edu.qa)

Insight On Consumer Psychology in Driving Green and Conscious Purchasing Towards a Circular Economy

Dahanayake I. D, Koodamangalath R, Wijayasundara M, Perera N

***Abstract*—**Textile and clothing industries one of the most polluting industries globally with a high environmental footprint associated with production. Adding to that, post-consumption waste from the clothing industry mostly end up in landfills, with recycling rates reporting low. Consumerism and high underutilization are other reported trends in the industry, leading to increased waste that reach landfills. Aiming to reduce purchases far in excess of utilized levels and to drive consumer purchasing towards greener alternatives, this paper looks at consumer psychology associated with consumerism and green purchasing. The paper reviews strategies adopted to disrupt such patterns and discusses the application of those relevant to clothing purchasing. The insights of the paper would be valuable for creating effective purchasing conditions and strategies in driving green purchasing in the clothing industry, in line with the principles of circular economy.

***Keywords*—**Textile, Clothing, Green purchasing, Consumer behavior.

Rahul Dev Koodamangalath is with the Deakin University, Australia (e-mail: seerahuldev@gmail.com).

Method for Tuning Level Control Loops Based on IMC and Closed Loop Step Test Data

Arnaud Nougues

Arnaud Nougues is with the Yokogawa Europe Solutions, Netherlands (e-mail: arnaud.nougues@nl.yokogawa.com).

***Abstract*—**This paper describes a two-stage methodology derived from IMC (Internal Model Control) for tuning a PID (Proportional-Integral-Derivative) controller for levels or other integrating processes in an industrial environment. Focus is ease of use and implementation speed which are critical for an industrial application. Tuning can be done with minimum effort and without the need of time-consuming open-loop step tests on the plant.

The first stage of the method applies to levels only: the vessel residence time is calculated from equipment dimensions and used to derive a set of preliminary PI (Proportional-Integral) settings with IMC. The second stage, re-tuning in closed-loop, applies to levels as well as other integrating processes: a tuning correction mechanism has been developed based on a series of closed-loop simulations with model errors. The tuning correction is done from a simple closed-loop step test and application of a generic correlation between observed overshoot and integral time correction. A spin-off of the method is that an estimate of the vessel residence time (levels) or open-loop process gain (other integrating process) is obtained from the closed-loop data.

***Keywords*—**Closed-loop model identification, IMC-PID tuning method, integrating process control, on-line PID tuning adaptation.

I. Introduction

Base Layer Controls in general, and PID loops in particular are critical to maintain stable, safe and profitable operating conditions of plants in the process industries. Achieving optimum performance for these loops depend on a number of factors, including instrumentation in good operating condition (sensors as well as control valves), proper control strategy and last but not least adequate tuning. As an illustration, a set of case studies can be found in [1] with typical examples of control loop issues for various process industries. Additional information about practical aspects of loop tuning in an industrial environment and the economic incentive to improve the control loops performance can be found in [3], [4] and [5].

Industrial Automation companies such as Yokogawa have developed a wide range of systems, tools and methods to help get the most of the base layer controls. This paper focuses on loop tuning and specifically on loop tuning for integrating processes such as levels.

PID controllers for integrating processes is of special importance for a number of reasons:

1) It is a fairly wide class of control loops, not just tank levels but also many pressure control loops and even a number of temperature control loops,
2) These loops have a major impact on the overall plant stability: a mistuned, oscillatory level control causes oscillations on the rest of the downstream process equipment,
3) Tuning of integrating process loops is difficult and time consuming when done according to the traditional "open-loop" method. It is then required to operate the loop in manual mode while step tests are applied to the control valve. The data is then used to characterize the process response; this model in turn is used to derive the PID parameters. The step test in open-loop is troublesome to Process Operators, as special attention is required since integrating processes are by nature unstable in open-loop.
4) How to tune integrating process loops is quite different from tuning self-regulating loops; it is counter-intuitive in some aspects and very often misunderstood. For instance, increasing the PID proportional action for a level control generally reduces the response overshoot, quite the opposite effect compared to a self-regulating process.

The paper presents a two-stage methodology for tuning level control loops. In stage 1, equipment dimension data, readily available in the process documentation, is used to characterize the open-loop response in terms of the residence time. The residence time is used to derive the PI tuning parameters by application of the standard IMC tuning rules for an integrating process. This gives a theoretical, preliminary set of tuning parameters. In stage 2, the preliminary tuning parameters are applied to the loop; a closed-loop setpoint step test is executed in order to fine-tune the loop, according to the actually observed process response. The methodology has then been extended to integrating processes other than levels.

The paper provides the details of the method so that it can be used in practice for tuning integrating process PID loops. The method has been widely applied in an industrial environment as part of actual projects. The paper is also helpful to get a good understanding of the specificities of integrating process PID control.

II. Equipment Dimension Method for Tuning a Level Controller

Level control loops can be pre-tuned based on the vessel dimensions and the instruments characteristics. The data requirements are:

1) Vessel dimensions, obtained from P&ID's or mechanical diagrams: vessel type (horizontal or vertical), diameter, length.
2) Level instrument span (length in mm) obtained from level data sheets,
3) Flow data: if LC to valve loop: design flow and design valve information, obtained from control valve data sheets;

if LC-FC cascade loop: FC instrument range.

4) Stream density if the valve data sheet or flow meter information is on a mass flow basis.

To illustrate the concept, a simple example is given here of a vertical cylindrical vessel.

- Vessel diameter: D = 4.6 m
- Level gauge height: H = 6 m
- Flowmeter range: Fmax = 20 m^3/min

The vessel residence time is then calculated as follows:

- Useful volume for level control:

$$V = \pi H D^2 / 4 \quad (1)$$

- Residence Time:

$$RT = V / Fmax = \pi H D^2 / (4 Fmax) \quad (2)$$

For the given numerical values, the resulting Residence Time is 4.986 minutes, therefore approximately 5 minutes.

Interpretation: Assuming as starting condition a stable level with equal inlet and outlet flows, a vessel residence time of 5 minutes implies that if the inlet flow is increased by 1 % of the flowmeter range, then the level will ramp up at a steady rate of 1 % in 5 minutes.

The inverse of the residence time is called the ramp process open-loop gain; in this case:

$$\text{Open-Loop Gain} = 1/5 = 0.2 \text{ min}^{-1} \quad (3)$$

The calculations in case of a horizontal vessel follow the same principles as given above for a vertical vessel; they are somewhat more complicated because of the presence of hemispherical or ellipsoidal heads at both ends of the cylindrical vessel. It should also be noted that strictly speaking, the residence time for a horizontal vessel is not fixed and depends on the level itself, since the liquid surface varies with the level. This effect is however in general neglected and the residence time calculated at a 50% level.

After calculating the vessel residence time, the IMC method is used to derive the PID controller settings.

IMC tuning is widely documented in the literature; see for instance one of the original publications [2]. The IMC tuning formulae for a level are given further in this article in equations (6) and (7). Three important points should be kept in mind:

1) IMC tuning relies on specifying one single parameter, the desired closed-loop time constant, that determines the speed of the controller response. In the variant of IMC used in this study, a dimensionless Loop Tuning Factor is used instead of the closed-loop time constant.
2) It is assumed in this paper that the open-loop response is an integrating process with no or negligible time delay. IMC then results in a set of P and I parameters, with 0 derivative action. So a PI controller as opposed to PID.
3) The PID controller structure is the "classical" one, also referred to as "standard".

III. IMC TUNING PROPERTIES FOR AN INTEGRATING PROCESS

Before explaining the second part of the tuning procedure, it is useful to point out the special properties of IMC tuning for integrating processes.

Table I below summarizes the results of a series of simulations of a PI level controller for an integrating process in closed-loop, tuned with IMC.

Assumptions:

1) The process is a "pure" integrator, with negligible time delay and negligible first order dynamics.
2) Variables that have been tested at different values:
   - Integrator Gain i.e. inverse of the vessel residence time in case of a level; the gain is expressed in %PV per minute / % MV);
   - IMC Loop Tuning Factor: 0.5, 1 and 2. The loop tuning factor in IMC sets the desired closed-loop speed of response. A larger loop tuning factor gives a longer closed-loop response time.
3) Two scenarios are considered:
   - Application of setpoint step change,
   - Application of load step change.

TABLE I
IMC TUNING AS A FUNCTION OF PROCESS GAIN AND LOOP TUNING FACTOR

			IMC PI parameters		Setpoint step change		Load disturbance step 1%	
Process Gain	Process Residence Time	Loop Tuning Factor	Controller Gain	Ti	Overshoot	Time when PV at max	Max. PV disturbance	Time when PV disturbance is maximum
(%PV per min / %MV)	*(min)*			*(min)*	*(%)*	*(min)*	*(%)*	*(min)*
0.1	10	0.5	2.67	15	13.8	14.4	0.28	7.4
0.1	10	1	1.33	30	13.8	28.5	0.56	14.3

0.1	10	2	0.67	60	13.8	57.0	1.11	28.5
0.2	5	0.5	2.67	7.5	13.7	7.2	0.28	3.6
0.2	5	1	1.33	15	13.8	14.4	0.56	7.4
0.2	5	2	0.67	30	13.8	28.5	1.11	14.3
0.4	2.5	0.5	2.67	3.75	13.7	3.7	0.28	1.9
0.4	2.5	1	1.33	7.5	13.7	7.2	0.56	3.6
0.4	2.5	2	0.67	15	13.8	14.4	1.11	7.4

For illustration, the simulated IMC responses to a setpoint step change and load step change are shown in Figures 1 and 2 below. This is for the case Process Gain = 0.2, Loop Tuning Factor = 1.

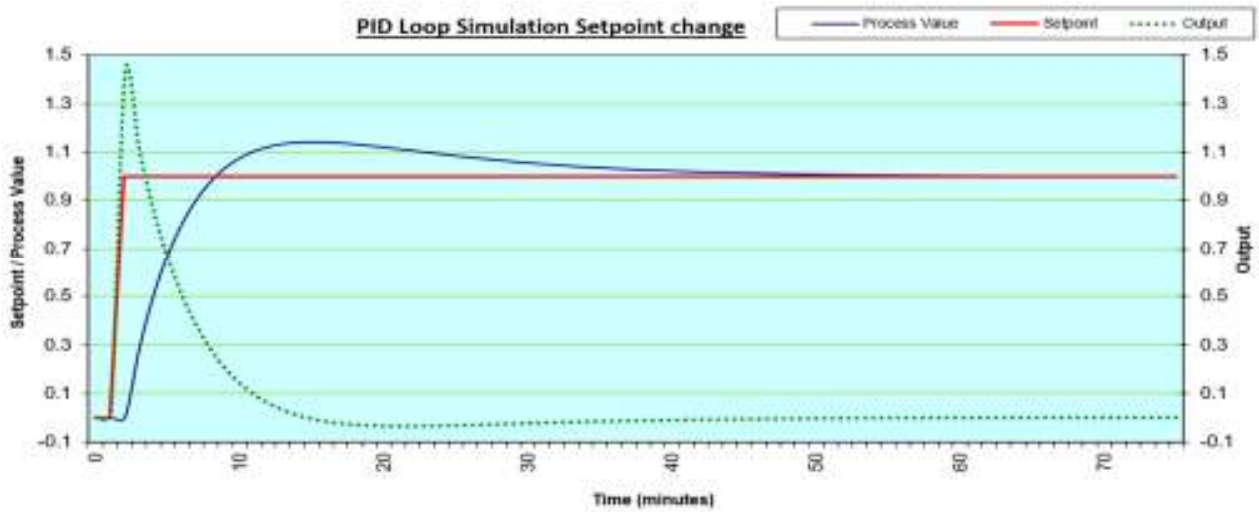

Fig. 1 Closed-loop setpoint change response with IMC tuning

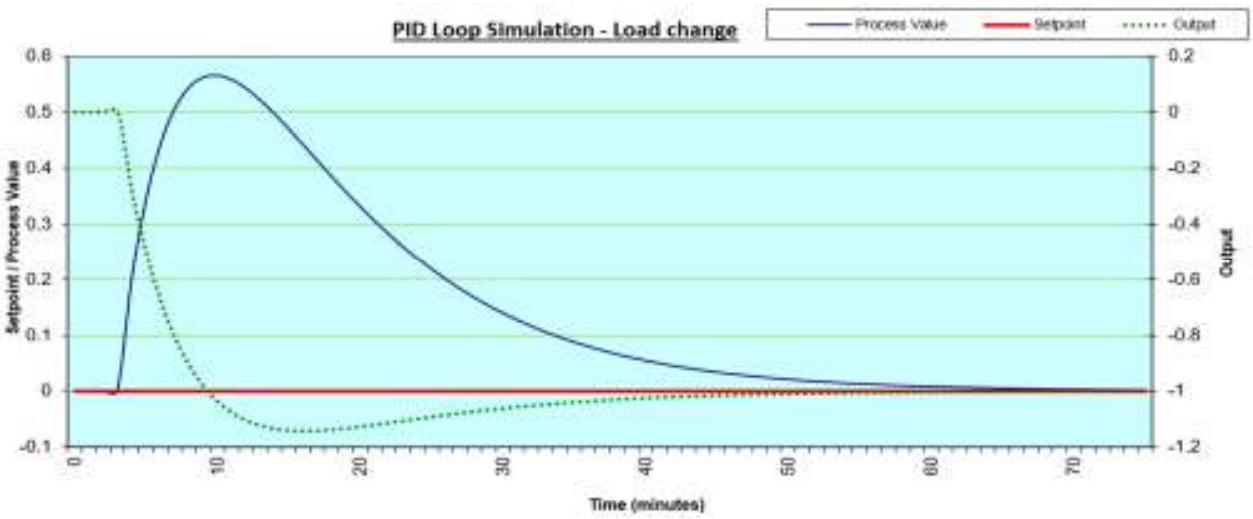

Fig. 2 Closed-loop load change response with IMC tuning

The results in Table I illustrate a number of key properties of IMC for an integrating process:

1) IMC tuning always gives an overshoot of about 14% for the PV response to a setpoint step change, independently of the process gain and of the loop tuning factor.

2) There is a one-to-one relationship between Loop Tuning Factor and controller gain, independently of the process gain. **In other words, whatever the process open-loop gain, the controller gain can be set according to the desired closed-loop speed of response**, say 0.5 for a fast response, 1 for an average speed response and 2 for a slow

response.

3) The difficulty is setting the integral action Ti; this latter parameter depends on the desired speed as well as the process characteristic i.e. the open-loop process gain.
4) The Loop Tuning Factor determines the closed-loop speed of response in terms of:
   - how fast the PV reaches its maximum value in response to a setpoint change,
   - how fast a load disturbance is compensated for and how large the maximum level disturbance is.
5) In first approximation, the IMC Integral Time Ti is equal to the time when the PV reaches its maximum in response to a setpoint change.

IV. Practical procedure for PI tuning of a level controller

Pre-tuning the level controller based on the vessel dimensions and the instruments characteristics as explained in Section II will give a reasonable preliminary tuning with which the controller can be operated in automatic mode. It is however not sufficient. The residence time calculation is in general not accurate, in particular in case of a LC loop direct to the control valve because of the significant valve non-linearity. Fine-tuning the loop is therefore almost always necessary.

In this method, fine tuning is done based on executing a closed-loop step test, characterizing the observed response in terms of percent overshoot and applying a generic correction of the controller integral time parameter. In summary, the advocated tuning method for a level controller is a two-stage procedure as follow:

Stage 1: Preliminary tuning via Equipment dimension method and application of IMC tuning rules.

1) P or the Proportional Band (=100/P) only depends on the desired Loop Tuning Factor, whatever the Residence Time is.
2) Ti on the other hand depends on the Residence Time as well as the chosen Loop Tuning Factor. It is therefore necessary to have at least a rough estimate of the Residence Time to determine Ti.
3) The Residence time of the vessel can be calculated using the Equipment dimensions method described earlier; then the IMC tuning rules can be applied.

Stage 2: Re-tuning in closed-loop.

1) A closed-loop step test should be performed in order to check the performance of the preliminary IMC settings. Re-tuning / fine-tuning is done by application of a tuning correction graph described in section V,
2) Re-tuning in principle only concerns Ti; P can be kept constant since it only depends on the chosen Loop Tuning Factor.
3) Re-tuning Ti is completed when the closed-loop response to a setpoint change matches the IMC characteristics, i.e.:
   - Overshoot 14%, and
   - Ti about equal to the time of the first PV maximum.
4) A generic correlation between observed overshoot and integral time correction has been developed to make it easy to re-tune Ti based on the closed-loop step response. This is presented in the next section.

V. Integral action correction and residence time estimation from closed-loop test

A. Ti tuning correction in Closed-Loop

The Ti tuning correction mechanism has been developed based on a series of closed-loop simulations with a model error for the vessel residence time.

Principle of the simulations:

1) Reference case: Process Gain = 0.2; reference IMC tuning calculated with Loop Tuning Factor = 1. This gives Controller Gain = 1.333 and Ti = 15 minutes;
2) The Process Gain is then changed by increments from 0.015 to 1.5 and closed-loop setpoint step test simulations are run for all the cases **while keeping the controller settings the same**;
3) For each case:
   - the corresponding PV overshoot is recorded,
   - the IMC-Ti value is calculated for the Process Gain, with Loop Tuning Factor kept at 1.
4) This gives the Ti Correction Factor = IMC-Ti / Reference IMC-Ti.

The results are given in Table II.

TABLE II
Closed-loop simulation results with Process Gain model Error

		Setpoint step change			
Process Gain	Process Residence Time	Overshoot	Time when PV at max	Ti-Corrected	Ti-Corrected / Ti
(%PV per min / %MV)	*(min)*	*(%)*	*(min)*	*(min)*	

0.015	66.7	47.6	70.0	200	13.3
0.0175	57.1	45.7	67.2	171	11.4
0.02	50.0	43.6	62.0	150	10.0
0.027	37.0	39.1	52.2	111	7.4
0.035	28.6	35.2	44.5	86	5.7
0.05	20.0	30.0	35.7	60	4.0
0.1	10.0	21.0	23.1	30	2.0
0.2	5.0	13.8	14.4	15	1.0
0.3	3.3	10.4	10.5	10	0.67
0.4	2.5	8.5	8.4	8	0.50
0.5	2.0	7.2	7.0	6	0.40
0.75	1.3	5.2	4.9	4	0.27
1	1.0	4.1	3.9	3	0.20
1.5	0.7	3.0	2.1	2	0.13

A graph that gives the Ti correction factor as a function of the observed overshoot has then been derived from Table II and is shown in Figure 3. A logarithmic scale has been used for Ti - Corrected / Ti in order to give a proper resolution below 1.

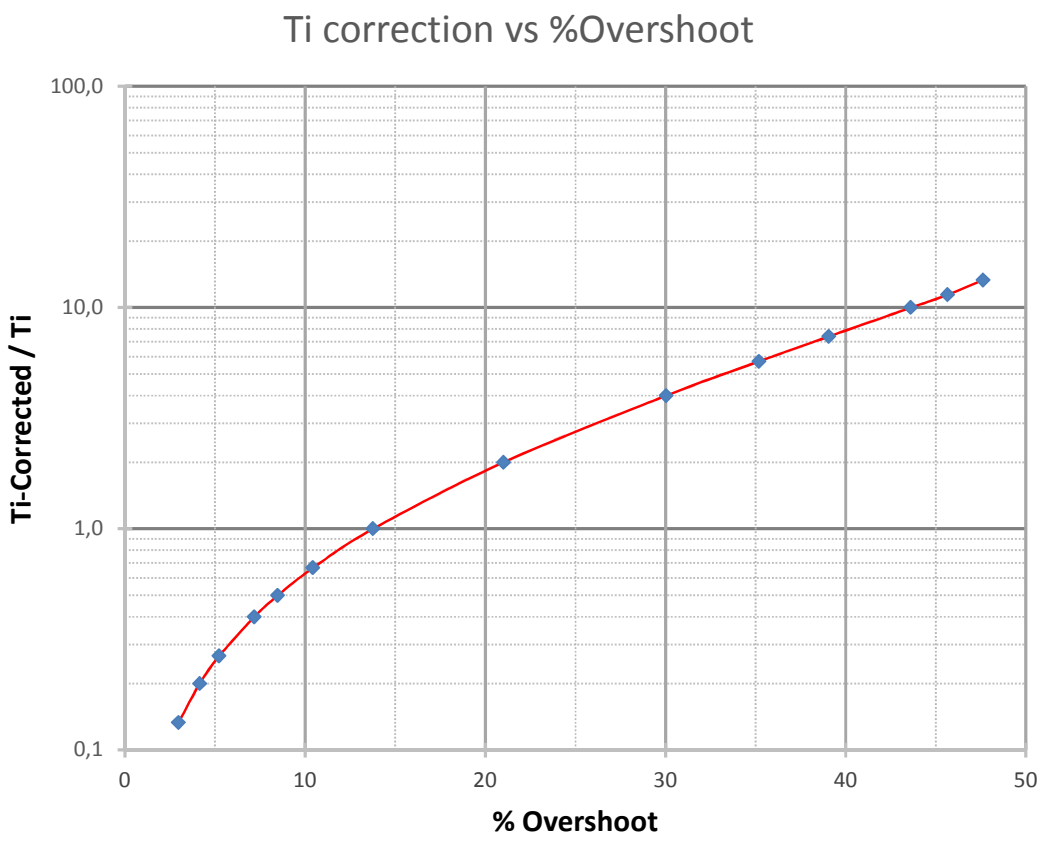

Fig. 3 IMC Ti Correction Graph

As a check that the results are generic, two other sets of simulations have been run with a different reference case; these give the same results in terms of Ti-Corrected / Ti :

- Process Gain 0.2, Loop Tuning Factor 2,
- Process Gain 0.3, Loop Tuning Factor 1.

B. Practical use of the IMC Ti Correction Graph

It is assumed that the level controller has been pre-tuned, preferably via IMC, based on a preliminary estimation of the Vessel Residence Time. The PI tuning parameters are denoted Gain, Ti.

With the controller in AUTO mode, apply a step test on the setpoint when the level is stable. Determine the observed overshoot and time of the first maximum.

If the overshoot is about 14%, no need to correct Ti; the loop response already matches an IMC response.

If overshoot different from 14% (too large or too small), then change Ti according to:

$$\text{Corrected Ti} = \text{Ti Correction Factor} * \text{Ti} \quad (4)$$

where the Ti Correction Factor is read from the IMC Ti Correction Graph in Figure 3.

Repeat setpoint step test and verify that the overshoot is now close to 14%. The time of the first PV maximum should also be roughly equal to the corrected Ti.

C. Vessel Residence time estimation

An additional outcome of the closed-loop step test is that it can also give an estimate of the Vessel Residence time. The IMC Ti Correction Graph can therefore also be used for the closed-loop model estimation of the integrating process characteristic, with the following formula:

$$\text{Vessel Residence Time} = \text{Controller Gain} * \text{Ti Correction Factor} * \text{Ti} / 4 \quad (5)$$

Where:
- Vessel Residence Time (min)
- Controller Gain (%MV / %PV)
- Ti (min)

The formula is applicable whatever the original PI settings are, whether calculated via IMC or not; it is applicable to levels as well as other integrating processes.

Derivation of the formula for the Vessel Residence Time estimation:

Notations:
- RT: Residence time (min)
- G: Controller Gain (%MV / %PV)
- Ti: Controller Integral Time before correction (min)
- Corrected-Ti: Controller Integral Time after correction (min)
- LTF: IMC Loop Tuning Factor
- TCF: Ti Correction Factor

IMC tuning rules for level control, assuming no time delay between controller output and level PV:

$$G = 2 / (1.5 * LTF) \quad (6)$$

$$\text{Corrected Ti} = 3 * RT * LTF \quad (7)$$

Combining equations (6) and (7):

$$G * \text{Corrected Ti} = 4 * RT \quad (8)$$

Ti correction based on closed-loop set point step test:

$$\text{Corrected-Ti} = TCF * Ti \quad (9)$$

Combining equations (8) and (9):

$$G * \text{Corrected-Ti} = G * TCF * Ti = 4 * RT \quad (10)$$

Therefore:

$$RT = G * TCF * Ti / 4 \quad (11)$$

VI. Application of Methodology to a Non-Level Integrating Process

Not only levels are integrating processes. Other variables such as pressure or temperature (e.g. tray temperature in special distillation columns) also can have an integrator behavior. The same method is applicable in these cases.

The difference is that strictly speaking there is no physical vessel and no "residence time" for such variables. Instead it more appropriate to use the Process Gain, equal to the inverse of the residence time.

Assuming that the integrating variable controller has been pre-tuned by whatever method with given values for the PI parameters, the second part of the method can then be applied as follows:

1) Conduct closed-loop setpoint step test,
2) Observe PV overshoot,
3) Use IMC Ti Correction Graph to get the Ti Correction Factor,
4) Apply Process Gain estimation formula derived from equation (11):

$$\text{Process Gain (\%PV per min / \% MV)} = 4 / (G * TCF * Ti) \quad (12)$$

5) Apply IMC based on the estimated Process Gain.

VII. Examples from Actual Loop Tuning Project

Two examples are given in this section of control loops from an industrial process, that have been tuned by application of the presented methodology as part of a Loop Tuning and Base Layer Control improvement project. The tag names have been changed for confidentiality reasons.

A. Level control loop

The preliminary tuning for this loop is:
- Gain = 2
- Ti = 2.5 min

The controller behavior, including a setpoint step test is shown in Figure 4.

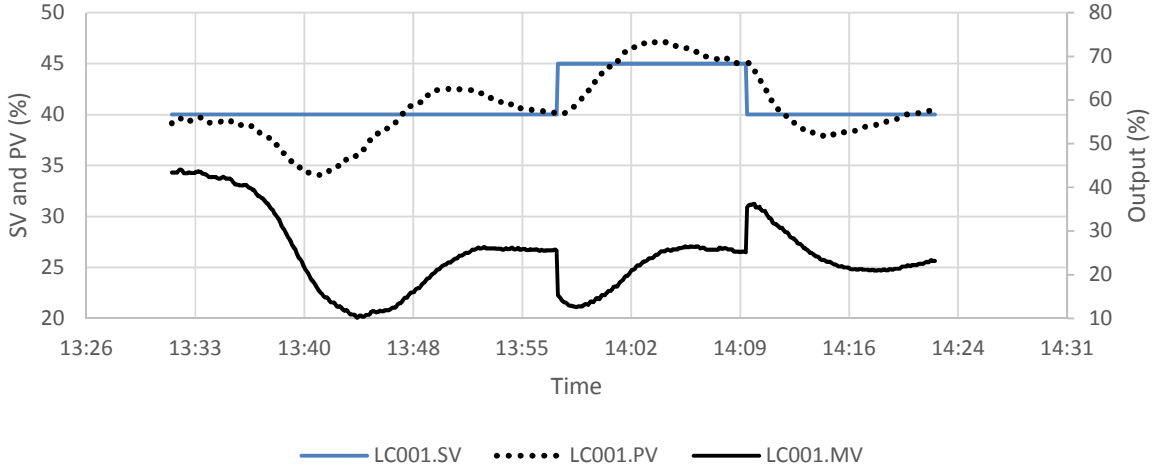

Fig. 4 Preliminary loop response; Gain = 2, Ti =2.5 min

The average PV overshoot resulting from the setpoint changes is excessive, about 43%. By application of the Ti correction graph, the Ti multiplicative factor is 9. Therefore, the corrected Ti value is 2.5 * 9 = 22.5 min.

The controller behavior with the new settings Gain = 2, Ti = 22.5 min is shown in Figure 5.

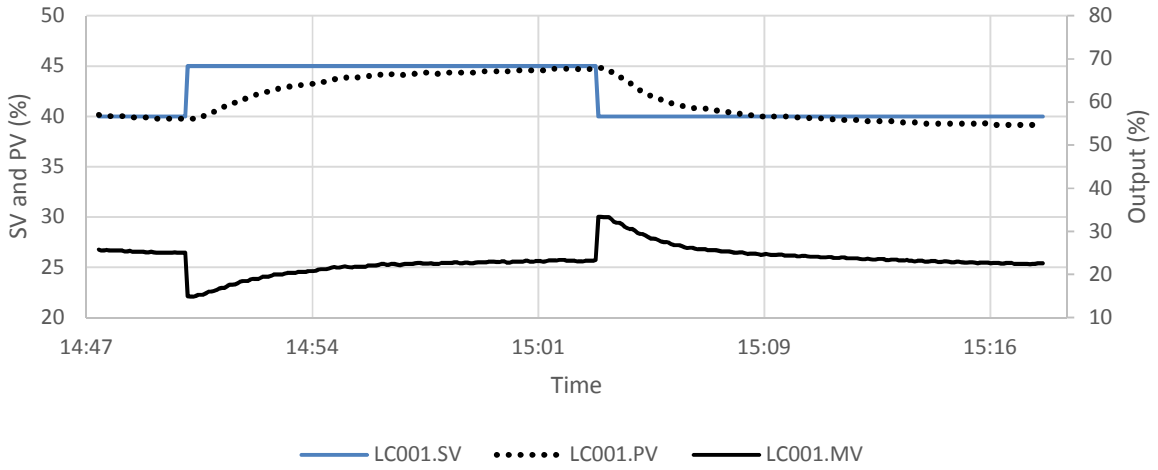

Fig. 5 Loop response after correction; Gain = 2, Ti =22.5 min

The residence time estimation gives the following result:

RT = G * TCF * Ti / 4 = 2 * 9 * 2.5 / 4 = 11.25 min

Faster tuning has been tested, by application of IMC using the estimated residence time, and desired closed loop speed twice as fast. This give a controller gain multiplied by 2 and Ti divided by 2, therefore: Gain = 4, Ti = 11.25 min. The corresponding controller behavior is shown in Figure 6.

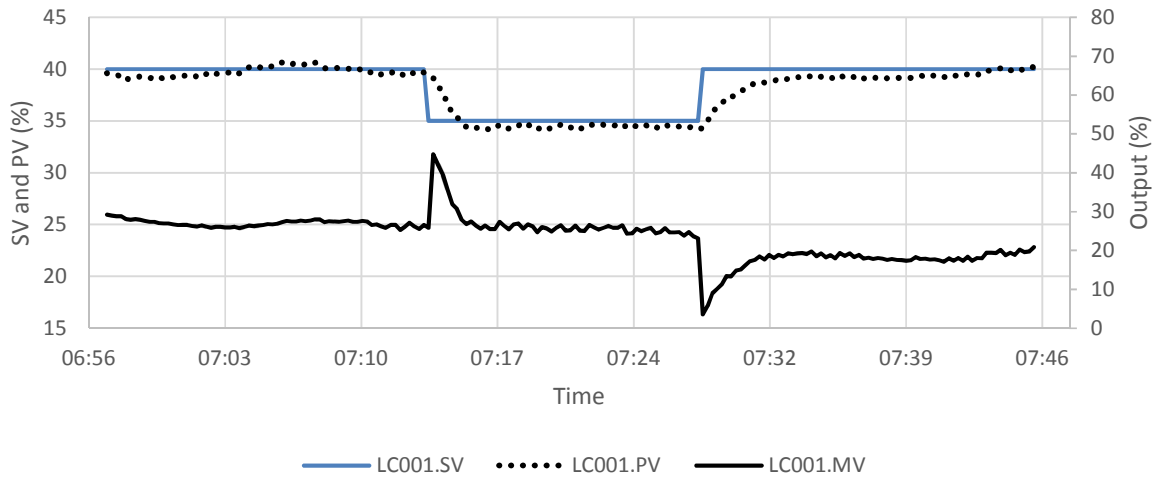

Fig. 6 Loop response with fast tuning; Gain = 4, Ti =11.25 min

B. Pressure control loop

In this case, a total of 4 setpoint steps have been applied. The first two steps with the preliminary PI settings and the last two steps with the corrected Ti.

TABLE III
PRESSURE CONTROL STEP TESTS RESULTS

Step #	Step Size (barg)	Controller Gain	Controller Ti (min)	Overshoot (%)
1	0.1	10	10	36
2	0.1	10	10	26
3	0.2	10	42	14
4	0.2	10	42	7

The corresponding trends are given in Figure 7. It should be noted that steps 3 and 4 are twice as large as steps 1 and 2. So it can be seen that the PV response % overshoot has been reduced as expected, although on the graph the absolute values of the overshoot appear to be similar.

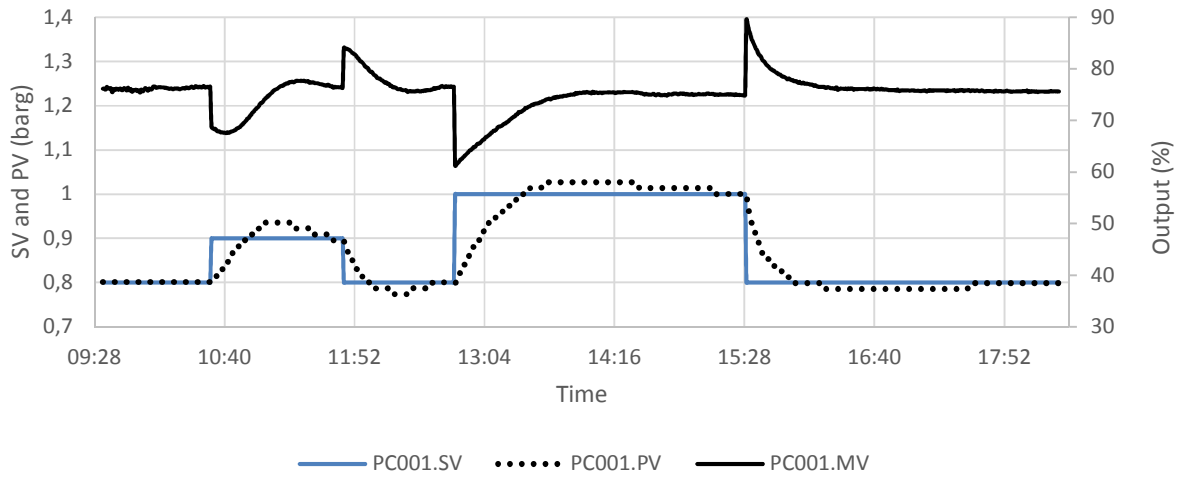

Fig. 7 Pressure controller trends before and after Ti correction

VIII. CONCLUSION

Integrating process control loops, including levels as well as many pressure loops and also a number of temperature loops, form a wide class of controllers in the process industry for which proper tuning is critical to stabilize operation and operate the plant safer and more profitably.

The method developed in this paper to tune PI loops for integrating processes is summarized as follows:

For levels: two stage procedure with first stage of

preliminary tuning based on exploiting equipment dimension data and application of the IMC tuning rules; re-tuning as a second stage via correction of the integral action from a closed-loop step test and use of graph in Figure 3 to determine the Ti correction factor.

For non-level integrating processes: Assuming any initial PI settings, conduct a closed-loop step test; use the process gain estimation formula from equation (12) and apply IMC with the estimated gain via equations (6) and (7).

The method is easy to use and applicable with minimum effort; it avoids the time consuming and troublesome open-loop test required in a traditional tuning approach.

REFERENCES

[1] Bernardo Soares Torres, Fábio Barros de Carvalho, Marcos de Oliveira Fonseca, Constantino Seixas Filho, *Performance assessment of control loops*, 2006 IFAC.

[2] D. E. Rivera, M. Morari, S. Skogestad (1986), *Internal Model Control, 4. PID controller design*, Ind. Eng. Chem. Res. 25(1), 252-265.

[3] Patwardhan R. S. and Ruel M., *Best Practices for Monitoring your PID Loops – The Key to Optimizing Control Assets*, Proceedings of the ISA EXPO 2008, Houston,TX, November 2008

[4] Brisk M. L., *Process Control: Potential Benefits and Wasted Opportunities*, 5th Asian Control Conference, vol. 1, 2004, pp.20-23

[5] Ruel, Loop Optimization: *Before You Tune - Troubleshooting - How to Tune a Loop*, Control Magazine, March/April/May 1999

Arnaud Nougues is Principal Consultant with Yokogawa Europe Solutions B. V., Amersfoort, The Netherlands (e-mail: arnaud.nougues@nl.yokogwa.com), for Process Control, Advanced Process Control, Process Optimization and energy saving solutions. He has over 35 years of experience in process control and supply chain optimization, with previous jobs with Shell, Profimatics and Honeywell. He graduated as engineer from Télécom ParisTech and holds a MS in Statistics (Texas A&M University, 1980).

Estimating CO_2 Storage Capacity under Geological Uncertainty Using 3D Geological Modeling of Unconventional Reservoir Rocks in Block nv32, Shenvsi Oilfield, China

Ayman Mutahar Alrassas, Shaoran Ren, Renyuan Ren, Hung Vo Thanh, Mohammed Hail Hakimi, Zhenliang Guan

***Abstract*—** The significant effect of CO_2 on global climate and the environment has gained more concern worldwide. Enhance oil recovery (EOR) associated with sequestration of CO_2 particularly into the depleted oil reservoir is considered the viable approach under financial limitations since it improves the oil recovery from the existing oil reservoir and boosts the relation between global-scale of CO_2 capture and geological sequestration. Consequently, practical measurements are required to attain large-scale CO_2 emission reduction. This paper presents an integrated modeling workflow to construct an accurate 3D reservoir geological model to estimate the storage capacity of CO_2 under geological uncertainty in an unconventional oil reservoir of the Paleogene Shahejie Formation (Es1) in the block Nv32, Shenvsi oilfield, China. In this regard, geophysical data, including well logs of twenty-two well locations and seismic data, were combined with geological and engineering data and used to construct a 3D reservoir geological modeling. The geological modeling focused on four tight reservoir units of the Shahejie Formation (Es1-x1, Es1-x2, Es1-x3, and Es1-x4). The validated 3D reservoir models were subsequently used to calculate the theoretical CO_2 storage capacity in the block Nv32, Shenvsi oilfield. Well logs were utilized to predict petrophysical properties such as porosity and permeability, and lithofacies and indicate that the Es1 reservoir units are mainly sandstone, shale, and limestone with a proportion of 38.09%, 32.42%, and 29.49, respectively. Well log-based petrophysical results also show that the Es1 reservoir units generally exhibit 2–36% porosity, 0.017 mD to 974.8 mD permeability, and moderate to good net to gross ratios. These estimated values of porosity, permeability, lithofacies, and net to gross were up-scaled and distributed laterally using Sequential Gaussian Simulation (SGS) and Simulation Sequential Indicator (SIS) methods to generate 3D reservoir geological models. The reservoir geological models show there are lateral heterogeneities of the reservoir properties and lithofacies, and the best reservoir rocks exist in the Es1-x4, Es1-x3, and Es1-x2 units, respectively. In addition, the reservoir volumetric of the Es1 units in block Nv32 was also estimated based on the petrophysical property models and fund to be between 0.554368.

***Keywords*—** CO_2 storage capacity, 3D geological model, geological uncertainty, unconventional oil reservoir, block Nv32

Ayman M AlRassas, PhD at China University of Petroleum (East China), Qingdao, 266555 China (+8613129966925).

Shaoran Ren, Professor at China University of Petroleum (East China), Qingdao, 266555 China (+86-532-86981882).

Renyuan Sun, Professor at China University of Petroleum (East China), Qingdao, 266555 China (+86-532-86981882).

Hung Vo Thanh, Post-doctoral at Seoul National University, 08826 Korea (82-2-880-8692).

Mohammed Hail Hakimi, Professor at Taiz University, 6803 Yemen (+967736375367).

Zhenliang Guan, Professor at China University of Geosciences (Wuhan), 430074 China (86-27-67883283).

Developing an Optimisation Model for Repairable Spares Stocks in Telecommunications Networks

Michael MacDonnell, Samir Mirdad

***Abstract*—**An optimization model has been developed for the management of repairable aircraft spares, known as rotables. These assets are tracked, high-value items that can be maintained and returned to stock for future service. The pool of rotables held in support of an airline fleet forms a closed-loop supply chain, as items may be maintained for the lifespan of the system (aircraft fleet). The optimization model applies a service level goal for the system, which is the aggregate of service level thresholds for a large number of line items. The inventory holding is optimized for minimal total asset cost while meeting a system service level target. By skewing inventory in favor of lower-value items, it is possible to maintain the overall system service level target with a large reduction in total inventory value when compared with inventory calculations performed at the individual line-item level. Savings of up to 40% in asset value have been demonstrated, compared with conventional inventory planning algorithms. The optimization model comprises a large-scale linear programming solution using stochastic parameters and has high computational intensity. The model has been validated using simulation and by successful operational use by aircraft operators and maintenance, repair and overhaul operators. It is proposed to apply this model to an analogous application in telecommunications networks, where valuable network equipment assets may be defined in a closed-loop supply chain, whereby spares inventory is maintained and held in stock for the lifespan of the operating network. Using known reliability metrics (mean time to failure) for individual inventory items and by setting service level targets at the system level, it is proposed to develop a stochastic-deterministic, computationally intensive optimization model to calculate an inventory set that achieves minimal inventory investment while maintaining system service levels. This project combines supply chain development (closed-loop supply chain) with a computationally-intensive business analytics application to improve an operations management problem (repairable spares inventory management) in an evolving field of telecommunications networking technology. Inputs required from the industry partner comprise a set of inventory data for suitable high-value spares used in support of a network, together with reliability data and service level targets.

***Keywords*—**inventory**,** optimisation, repairables, telecommunications

Michael MacDonnell, University College Dublin, michael@ucd.ie
Samir Mirdad, University College Dublin, samir.mirdad@gmail.com

The Functional Roles of Right Dorsolateral Prefrontal Cortex and Ventromedial Prefrontal Cortex in Risk-Taking Behavior

Aline Dantas, Teresa Schuhmann, Elisabeth Bruggen, Peiran Jiao, Alexander Sack

***Abstract*—** Many of our daily decisions involve some form of risk, may it be investing in stocks, gambling in a casino or trying a new cuisine. This risk-taking behavior is part of a decision process that has been associated with activity changes in specific prefrontal regions of the brain, including the ventromedial prefrontal (VMPFC) and the dorsolateral prefrontal cortex (DLPFC) (Fecteau et al., 2007; Gianotti et al., 2009), likely activated by the involved sub processes of valuation (DMPFC) and executive control (DLPFC) (Berkman, 2018; Clark et al., 2017; Gallagher et al., 2009)

Using non-invasive brain stimulation methods (NIBS), the functional role of the DLPFC in risk-taking behavior consistently revealed that inhibition of the DLPFC leads to an increase in risk taking behavior (Boggio et al., 2010; Fecteau et al., 2007; Gilmore et al., 2018). In contrast, the specific, potentially different role of the VMPFC for risk taking behavior is less well established. Although many brain imaging studies take the activity of these two prefrontal areas as indicators of different functions during risky choices (Hare et al., 2009; Hutcherson et al., 2012), this differential functional contribution is yet to be confirmed.

Here, we used continuous theta burst stimulation (cTBS) to inhibit either the VMPFC or DLPFC during the execution of the computerized Maastricht Gambling Task (MGT - Dantas et al., 2021), allowing us to estimate participants' risk-taking behavior. This enables us to investigate the specific and differential effects of TMS-induced inhibition of the DLPFC and VMPFC on both, risk-taking behavior as a whole, and the valuation process in particular.

We hypothesized that, compared to sham stimulation, VMPFC inhibition would lead to a reduction in risk-taking behavior by reducing the participants' choice of average values, whereas the TMS-induced inhibition of the right DLPFC (rDLPFC) would lead to an increase in risk taking due to a reduction in cognitive control (Knoch et al., 2006).

In a within-subject design, 33 participants were asked to complete the MGT before and after receiving either VMPFC, rDLPFC or sham stimulation in separate, counterbalanced sessions. Transcranial magnetic stimulation (TMS) was applied with a MagPro X100 stimulator using a double cone coil (Magventure, Denmark) at 100% resting motor threshold.

Stimulation of both the rDLPFC and the VMPFC led to an increase in risk-taking behavior (beta = -0.47, $t(8847) = -2.98$, $p < .01$beta = -0.45, 95%, $t(8847) = -3.01$, $p < .01$; respectively). We also found a significant medium positive increase in the average valuation after both DLPFC (beta = 0.67, $t(8847) = 2.63$, $p < .01$) and VMPFC stimulation (beta = 0.71, $p < .01$).

Inhibition of DLPFC and VMPFC both increased risk-taking behavior as well as choice valuation, compared to sham, not showing the expected difference in functional roles of those brain regions in risk-taking. SIMNIBS simulations confirmed distinct stimulation areas (using our methodology) when targeting DLPFC and VMPFC, suggesting that we have successfully targeted both regions distinctively. Therefore, our results indicate that inhibiting them separately leads to no differential effects in risk taking behavior or valuation. The strong anatomical and functional interconnection of the VMPFC and DLPFC has already been stated in numerous studies (Figner et al., 2010; Hare et al., 2009; Hutcherson et al., 2012; Rudorf & Hare, 2014). The here presented rTMS results indicate that these two areas are also intrinsically working together during the processing of risk and valuation.

***Keywords*—** TMS, DLPFC, VMPFC, risk-taking behavior.

Aline Dantas is with the Maastricht University, Netherlands (e-mail: a.dantas@maastrichtuniversity.nl).

A Gut Feeling: How Your Gut and Brain Determine Your Choices

Aline M. Dantas, Peiran Jiao, Alexander T. Sack, Elisabeth Bruggen, Teresa Schuhmann

***Abstract*—** Recent research has shown that gut microbiota can influence the interaction between the central and the enteric nervous system via the gut-brain axis (GBA). Neural activity in brain regions linked to basic emotional as well as cognitive processes have already been shown to be affected by manipulations of the gut microbiota. Whether such gut microbiota manipulations also affects human decision making, however, remains largely unknown. Based on previous studies in animal models and indications from neuroimaging studies, we here test the effects of the gut-brain axis on decision-making under risk and intertemporal choices.

In a placebo-controlled double-blinded design, with two sessions separated by 28 days, during which participants received daily doses of probiotics (or placebo), we investigated whether the prolonged and controlled intake of probiotics affects risk-taking behavior and intertemporal choices using incentivized games.

We found a significant decrease in risk-taking behavior and increase in future-oriented choices in the probiotics group, as compared to placebo. These findings provide first direct experimental evidence for the functional role of the microbiota-gut-brain axis on decision-making, creating a path for potential clinical applications and allowing for a better understanding of the underlying neural mechanisms of risk-taking behavior and intertemporal choices.

***Keywords*—** gut-brain, probiotics, risk, intertemporal choice.

Aline Dantas is with the Maastricht University, Netherlands (e-mail: a.dantas@maastrichtuniversity.nl).

Is Biodiversity Conservation Properly Valued? Impact of the Embedding Effect

Vásquez-Lavín, F., Dávila, J., Orihuela, C., Lavado, K.

Jose Davila is with the ESAN University, Peru (e-mail: 20181461@lamolina.edu.pe).

***Abstract*—** The limitations of stated preference (SP) methods for properly estimating the willingness to pay (WTP) for the non-use value of environmental goods are well known. One of them is the potential appearance of insensitivity to scope that is part of embedding effect (EE) whose presence leads to conflicts with rationality in the consumer's choice, generating WTP that are not very useful to efficiently assign the public resources destined to their conservation. This is important in the case of biodiversity conservation, whose valuation based on SP mostly uses questionable representations that would potentially generate the emergence of the EE, not fulfilling NOAA requirements to be taken into account as public policies. A review of SP studies shows that the vast majority of them suffer from some type of defect that makes them not recommended to apply.

***Keywords*—** biodiversity conservation, embedding effect, sensitivity scope, plausibility, stated preferences.

1. Introduction

Biodiversity conservation may be considered as a public good, that is a good for which there is no rivalry or exclusion in its consumption (Boyle et al., 1998). Public goods lack of markets that could provide information regarding its relative scarcity (Arrow et al., 1996), making it difficult to evaluate policies orientated to its conservation. Biodiversity is an essential input for many ecosystem services, and therefore, the economic value of biodiversity could be derived through the value of those ecosystem services. Nevertheless, there have been several attempts to value biodiversity on its own (Jacobsen et al., 2008; Jacobsen et al, 2011; Bakhtiari et al, 2013; Remoundou et al., 2015). In these studies, biodiversity is usually treated as a source of non-use value, whose estimation relies on stated preferences (SP) techniques, such as contingent valuation (CV) or choice experiments (CE). SP require the implementation of surveys that create hypothetical markets to respondents aiming to capture people's preferences for changes in the quantity or quality levels of some biodiversity proxies (Kahneman & Knetsch, 1992; Constanza et al., 1997; Hanemann, 1999; Rolfe & Windle, 2012; Martin-Ortega et al., 2015). These preferences are then translated into monetary terms to construct welfare measures with

which various public policy proposals in favor of conservation can be evaluated (Rudd, 2009; Lew et al., 2010; Wallmo & Lew, 2016; Spencer-Cotton et al., 2018).

There are so far numerous applications of CV and CE on biodiversity valuation (Jorgensen et al., 2001; Olar et al., 2007; Jin et al., 2010; Bakhtiari et al., 2013; Borzykowski et al., 2017; Vedogbeton et al., 2020). These techniques have been criticized because of their potential to generate results inconsistent with the economic theory of rational consumer choice (Diamond et al., 1993; Adams et al., 2008; Nijkamp et al., 2008; Szabó, 2011; Ferrini & Turner, 2018). These critics are not exclusive to biodiversity's valuation, but they are especially relevant in this context. These allegedly inconsistencies can be grouped into three groups (Hoevenagel, 1996; Czajkowski & Hanley, 2009): inadequate survey design, "warm glow" effect[1], and embedding effect (EE).

Hanemann (1994) indicates that the EE includes three effects: sequence, additivity, and sensitivity to scope; Carson & Mitchell (1995) facilitate advances in sensitivity to scope, identifying two types of nested goods: i) "quantitative nesting" that occurs when the goods in a list, say A, B and C are distinguished only by the magnitude of one argument in a multivariate utility function; and ii) "qualitative nesting" that occurs when the goods are distinguished by changes in more than one argument in a multivariate utility function. Bateman et al. (2004) add two aspects not considered: i) "inclusive list" when goods are presented as additions or subtractions from any good versus "exclusive list" when goods are presented as alternatives to any other goods given; and ii) the visible choice set that is related with the study design and consists in the full extent of purchase options which will be made available in the course of that exercise for the respondents.

Although some researchers claim that the EE's presence generates a conflict with behavioral economic theory and weakens the results of SP studies (Loomis et al, 1993; Pouta, 2005; Ojea & Loureiro, 2009; Morse-Jones et al., 2012), others argue that this is not the case (Jorgensen et al., 2001; Olar et al., 2007; Ressurreição et al., 2012). In that sense, the insensitivity to scope can be explained by the reduction of marginal utility as a sign of satiety (Rollins & Lyke, 1998; Wheeler & Damania, 2001; Olar et al., 2007; Jacobsen et al., 2011; Lew & Wallmo, 2011), or could appear in a certain point as a threshold (i.e., a minimum viable population for a species) (Ojea & Loureiro, 2009).

For example, the interviewee expresses interest in protecting the first 100 ha of zone Z. From then on, and there may be little or no interest in increasing the protected area since he considers that 100 ha is sufficient. In the extreme, conserving an additional 100 ha could even lead to

[1] The "warm glow" effect occurs when interviewees engage in altruistic behavior in their responses to an asset (Martin-Ortega et al.,2015)

losses in their well-being. Also, a drastic reduction in marginal utility can be explained by the fact that the interviewees are willing to make few transactions of money and environmental goods (Amiran & Hagen, 2010). That is, interviewees may be willing to exchange money for the first increases in the environmental good, not for additional increases; that is that Utility Marginal soon would be equal or near to zero.

The insensitivity to scope, under certain circumstances, seems to fit in a rational behavior of the interviewee or consumer, and its presence should not question the results. These two arguments in favor of insensitivity to CV studies' scope have been strongly challenged by Burrows et al. (2017), who found that many CV-based articles did not perform both requirements suggested by the NOAA panel in 1993: i) Pass the test of sensitivity to scope, and ii) "Plausibility" that is a measure of WTP elasticity [$(\Delta WTP / WTP_0) / (\Delta Q / Q_0)$]. It should be noted that although NOAA panel indicates that the results must fulfill "plausibility", it does not indicate the measure and value that should be taken account as a decision indicator. Some authors as Whitehead (2016) take an elasticity of 0.20 and others as Burrows et al. (2017) take a value of 0.50, so the value is not defined and could be denominated as an arbitrary value. One aspect to take into account is that Burrows et al. (2017) only take account studies that use tests of external consistency (split samples); they assume consistency for internal tests (non-split samples) because they point that it is the same person who chose in different moments respect the same valuation.

Even though, insensitivity to scope is present in many assessment studies based on CV, its presence in biodiversity conservation valuations seem to be even more widespread. The problem appears to be exacerbated by biodiversity representation in SP studies (Nunes & van den Bergh, 2001; Jacobsen et al., 2008; Bartkowski et al. 2015).

Species and habitats representations as quantitative terms can be conducive to the interviewee's understanding of biodiversity; however, the problem is that the former term is equivalent to a single component of biodiversity, while the latter can be very broad and unspecific (Ring et al., 2010; Bartkowski et al., 2015), generating assets that are indistinguishable from the perspective of the interviewee so, it could be a source of insensitivity to scope.

For example, representations of biodiversity from uncharismatic and unrecognized species can make variations in the property equally perceptible to interviewees and can generate insensitivity to scope (Boyle et al., 1998; Jacobsen et al., 2008; Ojea & Loureiro, 2009; Morse-Jones et al., 2012). Likewise, interviewees may perceive that biodiversity conservation is only a task for the government, avoiding the actual declaration of their WTP (Jin et al., 2010). In addition, if conservation actions have a negative effect on employment and economic activity in an area, this may negatively affect people's preferences (Pouta, 2005). Failures in the adequate

appreciation of biodiversity and its hypothetical market by the interviewees may translate into zero or even negative marginal utility (which would be reflected in the insensitivity to scope), and thus even to making decisions against welfare (Carson & Mitchell, 1995; Morrison, 2014; Mwebaze et al., 2018).

Functionality is an uncommon representation as qualitative and quantitative proxy of biodiversity, which goes beyond an isolated group of species or areas, and is equivalent to the interrelation of agents that generate stability and resilience in ecosystems, and may represent in a better way the changes and impacts on human well-being (Bartkowski et al., 2015). This could be a better option to represent biodiversity (Bartkowski, 2017); however, interviewees may not be very familiar with functionality (Ring et al., 2010; Bakhtiari et al., 2013; Bartkowski et al., 2015, Jordano, 2016), although there is evidence to suggest otherwise (Rajmis et al. 2009).

Not all the countries have the same kind and richness of biodiversity. In fact, exist a group of countries which possess at less 70% of biodiversity on the planet; these countries are known as Megabiodiversity Countries (MC). This point should not go unnoticed, because it is not the same to use Specie and Habitat representations in a small area where live just a small quantity of species, than in an area of thousands or millions hectares where live hundreds or thousands species, that is the case of MC. In that sense, it is not the same to lose 10 species in a Non-MC than lose 10 species in a MC; in the latter the loss could be less perceived than in the formers.

If SP methods are tools for biodiversity conservation valuation, then they must be applied appropriately and provide results consistent with economic theory. The presence of EE due to insensitivity to scope and the questionable representation of biodiversity would limit the potential for biodiversity studies to be seriously considered in decision making.

Therefore, it is proposed to identify the fulfill of NOAA panel requirements and recognize whether insensitivity to scope in SP studies is linked to representation and richness biodiversity.

2. Methodology

The first step was to compile the studies on the economic valuation of biodiversity based on indexed journals using SP (CV and CE). The second step was to identify the presence of sensitivity to scope; then we estimate “plausibility” results. Third, we classify the studies by method used and according to the proxy that represents biodiversity in the following way: species (S), habitat (H) and functionality (Fx).

For both methods, we represent the results of sensitivity to scope with letters. Studies that pass the scope tests are marked with a “P”, those that fail the scope test are marked with an “F”, and

those with mixed[2] results are marked with an "M". When possible, we estimate the plausibility and mark with a square (■) if the study was developed in a MB country. We identify if the study used Split or Non-Split samples.

With this information we summarize the information in bar graphs and tables, for each technique.

3. Results and discussion

Contingent Valuation

We identified 78 studies that applied Contigent Valuation (CV) for valuing biodiversity conservation from two types of representations: Species (S) and Habitat (H). Studies that represent biodiversity from Species not use always the same kind and number of species of animals and/or plants. In some cases, authors use "flagship" and "very known" species, with which respondents feels closely identified, as: fishes (McDaniels et al., 2003), mammals (Tanguay et al., 1993; White et al., 2001; Giraud & Valcic, 2004; Boxall et al., 2012; Frontuto et al., 2017), while others use conservation situation of species (Veisten et al., 2004[a], Poe et al., 2005; Stithou & Scarpa, 2012).

We identified that "S" representation, in the majority of cases (29 studies) represent small quantities of species of the valued place and probably of the country. That is the case of migratory birds whose conservation has been valued many times in USA (Desvousges et al., 1992; Boyle et al., 1994) but only from two species and up to 200,000 birds that represent only 20% of all bird populations that fly over that air corridor. Jakobsson & Dragun (2001) and Vargas & Díaz (2014) valued conservation programs for Australia and Colombia, respectively using only one of hundred species that represent less of the 5% of animals that inhabit those places.

On the other hand, we find studies (30) that represent biodiversity with a place characterized mainly by its size (hectares, square kilometers, square miles, or an iconic place) denominated as "Habitat"; for example: wilderness areas (Gilbert et al., 1991; Diamond et al., 1993; McFadden & Leonard, 1993; McFadden, 1994), rivers (Brown & Duffield, 1995), wetlands (Powe & Bateman, 2004; Whitehead et al., 2009; Pattison et al., 2011), and forests (Adams et al., 2008; Borzykowski et al., 2017).

[2] It is considered a mixed result when sensitivity to scope is detected in one part and insensitivity to scope in another part of the same study when the same scenario or attribute is used. Some studies with this type of result are Veisten et al. (2004a), Olar et al. (2007), Jin et al. (2010), Boxall et al. (2012), Cerda et al. (2013), and Spencer-Cotton et al. (2018).

In other cases (19) both representations "Species + Habitat" were used together to explain scenarios to interviewees (Berrens et al., 1996; Lehtonen et al., 2003; Baral et al., 2007; Khai & Yabe, 2014).

We found that 15 studies passed sensitivity to scope test, and 20 studies showed mixed results. However, we found 43 studies that: i) not passed sensitivity test (Desvousges et al., 1992, Diamond et al., 1993; McFadden, 1994; Brown et al., 1995; Loomis & Ekstrand, 1997) and/or ii) authors did not take account sensitivity to scope tests in their papers (Bergstrom & Stoll, 1987; Samples & Hollyer, 1990; Moran, 1994; White et al., 1997).

From the 15 studies that passed sensitivity to scope test (6 use "E", 4 use "H", and 5 use "E+H"). We could measure the "adequacy" or "plausibility" in 14 of them. Reasons why we cannot measure "plausibility" are: we do not have data or a base situation to do an estimation. In some cases, "status quo" and levels have categorical values as: "minor-major" (Carson & Mitchell, 1995), "types of program conservation" (Kontoleon & Swanson, 2003; Lehtonen et al., 2003; Nunes & Schokkaert, 2003).

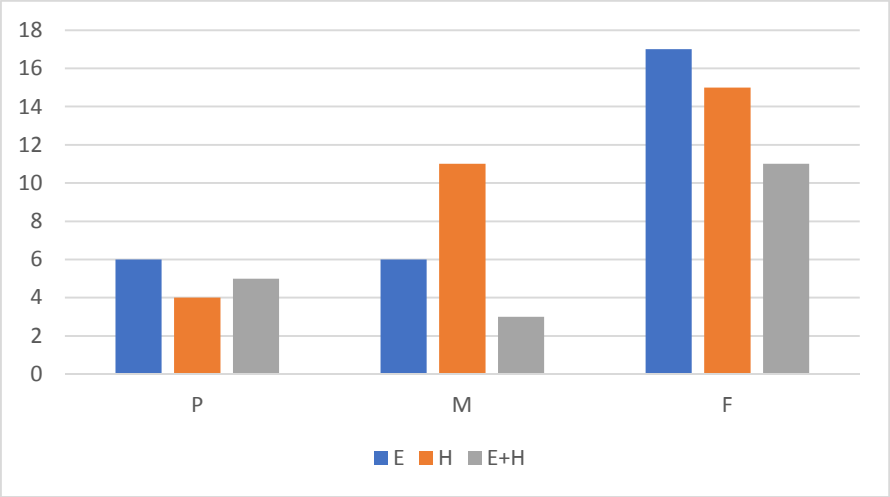

Following to Whitehead (2016) and Burrows et al. (2017) we found 10 studies in which there have sensitivity to scope and "plausible" results at less in part of them, from: "S" (Carson et al., 1994; Carson & Mitchell, 1995; Jakobsson & Dragun, 2001; Stanley, 2005; Boxall et al., 2012; Forbes et al., 2015), "H" (Blomquist & Whitehead, 1998; Alvarez-Farizo et al., 1999; Powe & Bateman, 2004; Brouwer et al., 2016), and "S+H" (Berrens et al., 1996; Berrens et al., 2000; Kontoleon & Swanson, 2003; McDaniels et al., 2003; Tonin, 2019). It is important to mention that a plausibility result higher than 0.50 not ensure to pass sensitivity test; as we identify in White et al. (2001), Lehtonen et al. (2003), and Black et al. (2010).

Unlike what was proposed by Burrows et al (2017), we reviewed both types of test consistency, and found that most of the results come from Split samples (65).

	P	M	F
Split	14	20	31
Non-Split	1	0	12

Retaking the studies that passed sensitivity and plausibility test, we noted that none of them was developed in a Megabiodiverse Country (MC). We found 9 studies developed in MC, but none of them fulfill any of NOAA requirements; only in Svedsäter (2001) and Adams et al. (2008) we identified a plausibility near to 0.20 but it did not fulfill sensitivity test.

Choice Experiment

We identified 102 studies that used Choice Experiments (CE) for valuing biodiversity conservation. Unlike CV studies, in this group appears in addition to "S" and "H", some cases that represent biodiversity from Functionality (Fx). According to Bartkowski et al. (2015) and Jordano (2013), Fx is the interrelations between species which not all the species have the same importance; there are key species -no populations of them- with more important roles than others, contributing to the stability and resilience of biodiversity.

Similar to CV analysis, we identified CE cases where authors study: only one or a small quantity of species (Hanley et al., 2003; Olar et al., 2007; Hoyos et al., 2012; Yao et al., 2014), iconic or flagship species (Christie et al., 2006; Christie et al., 2007; Morse-Jones et al., 2010; Cerda & Losada, 2013; Hausmann et al., 2015), or categorical levels in general (Carlsson et al., 2003; Birol et al., 2006; Eggert & Olson, 2009; Mc Vittie & Morán, 2010; Jacobsen et al., 2011).

On the other hand, habitats are presented as: different size areas (Rolfe et al., 2000; Rolfe & Windle, 2012; Rogers et al., 2013; Shoyama et al., 2013; Estifanos et al., 2019), and/or places where live species (Meyerhoff et al., 2009; Thiene et al. 2012; Hausmann et al., 2015; He et al., 2016; Pakalniete et al., 2017).

The third representation Functionality appears in six studies (Czajkowski et al., 2009; Czajkowski & Hanley, 2009; Cerda et al., 2012; Bakhtiari et al., 2013; Rambonilaza & Brahic, 2016; Bakhtiari et al., 2018) and it is related with the definition that we mentioned earlier.

Summarizing, we identified 56 cases that use only "S", 2 cases that use only "H", and none that use exclusively "Fx". Moreover, we found some cases in which authors used more than one representation of biodiversity: "E+H" (38), "E+Fx" (3), and "E+H+Fx" (3). It is important to say that 31 cases used "Split" simples and 71 cases used "Non-Split" samples.

Only 14 passed sensitivity to scope test, and 12 showed mixed results -showing in two cases signs of sensitivity to scope for Fx attribute-. For these 26 studies, we found three kind of

situations: i) authors estimate sensitivity to scope tests (Olar et al., 2007; Lew & Wallmo, 2011; Spencer-Cotton et al., 2018); ii) authors that mention existence of sensitivity to scope (Lehtonen et al., 2003; Chhun et al., 2013; Grilli & Notaro, 2019); iii) authors who do not estimate sensitivity test, but whose results shows sensitivity to scope from confidence intervals (Christie et al., 2007; Borger et al., 2015; Boeri et al., 2020).

On the other hand, we found 76 cases in which there was no sensitivity signs due to: i) they did not pass internal consistency tests (Czajkowski & Hanley, 2012; Jacobsen et al., 2012; Pakalniete et al., 2017; Tan et al., 2018), contrary to what is stated by Burrows et al. (2017); and ii) cases that were only valuing a specific situation, leaving aside NOAA requirements (Horne et al., 2005; Do & Bennett, 2008; Veríssimo et al., 2009).

From the 14 studies that passed sensitivity to scope test (10 use "S", 2 use "H", and 2 use "E+H"), we could estimate the "adequacy" or "plausibility" at less in part of each all cases; having that in 8 and 6 cases used internal and external consistency tests, respectively.

We had some inconvenient, the same of CV cases, to estimate "plausibility". In some cases, in addition, we found "status quo" situations had a willingness to pay (WTP) USD 0, so we decided to put a WTP of USD 1 to operate mathematically and estimate the elasticity that represents "plausibility". In other cases, results could be questioned, since the values of qualitative levels could be assumed or accommodated by researchers and decision makers, to obtain expected results.

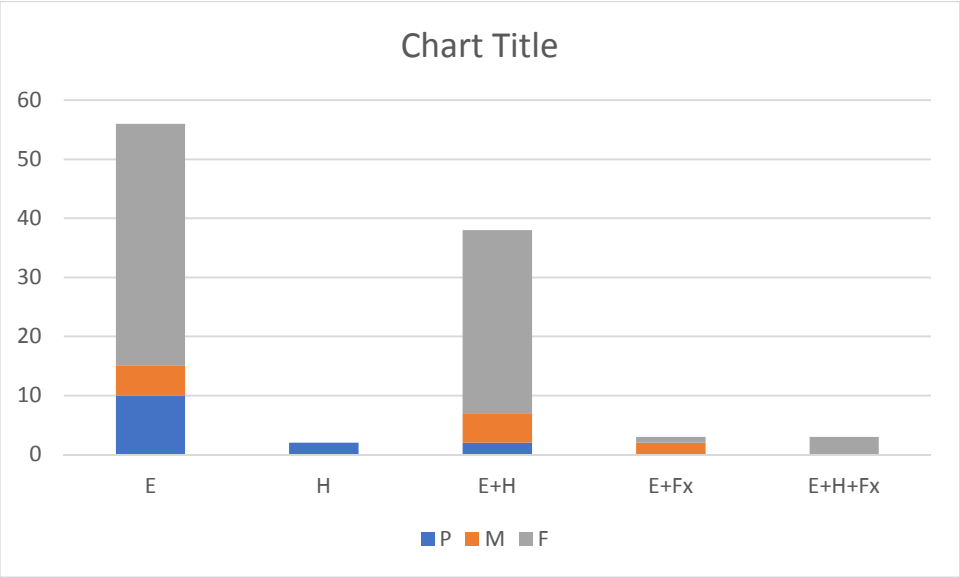

Following CV analysis, we identified 13 studies developed in a MC using "E" (8), and "E+H" (5) representations, one from a "Split" sample and 12 from "Non-Split" samples. Only in Wang

et al. (2014) applied in China and Estifanos et al. (2019) applied in Ethiopia, we found signs of sensitivity to scope and plausibility, both from "Non-Split" samples, and using "S" and "S+H", respectively.

	P	**M**	**F**
Split	6	7	18
Non Split	8	5	58

An important issue that we noted is that in some CE studies, the authors analyzed not only biodiversity conservation but other attributes, proposing final scenarios to evaluate policy impacts. For example, Dechasa et al. (2020) and Hou et al. (2020) did not apply sensitivity to scope tests to every attribute, however after their analysis they propose scenarios with significative attributes and levels. In this sense, scenarios could be designed with levels that fulfill NOAA requirements, to evaluate them and finally develop public policies.

4. Conclusions

Based on a review of studies that economically value biodiversity conservation, it was found that, in those based on CV, only a small fraction (19%) satisfactorily fulfilled the scope tests. Most of the studies conducted in CE did not pass sensitivity to scope tests (75%); in 97% of them appear exclusively "Habitat" and "Species" as biodiversity proxies, which has been questioned in the literature as potential sources of insensitivity to scope and, therefore, of the embedding effect. Moreover, just 16% of the studies (from SP methods) fulfill NOAA requirements (sensitivity to scope and plausibility). This indicates that most of the results of these studies are questionable and therefore of limited scope in decision making.

Few studies (3%) have used the functionality as a biodiversity proxy. Apparently, its use should offer a better image and information to interviewees and thus, satisfy the sensitivity to scope, fitting the results to the economic theory of consumer choice. Although it is true that all studies that used this proxy passed the sensitivity to scope tests its still limited application in the literature does not allow us to ensure that such a proxy always provides adequate results. Nevertheless, it is recommended that future researches based on SP incorporate quantitative measures to facilitate the evaluation of the scope effect and plausibility.

We think that CE could be a good method to value biodiversity conservation, but not only considering one representation but the three we mentioned in this paper, and not only from "Split" samples. Special attention deserves cases that develop in places with a large number of habitats and species (MC).

In that sense, we need to carefully define the levels of the attributes with the support of a multidisciplinary team, and point out that the valuation is exclusively for biodiversity conservation. We believe that it is necessary that the attributes (Species, Habitat and Functionality) fulfill NOAA requirements separately, and then together in order to elaborate public policies whose objective is to maximize well-being.

All this suggests that, despite decades of experience in applying SP in the economic valuation of biodiversity conservation, much work remains to be done so that studies of this type can be considered methodologically sound and valid for decision making.

Acknowledgements. This research has been made possible by the Grant Agreement 200-2015-FONDECYT and UNALM.

Table 3.1: Economic valuation studies of biodiversity conservation based on CV

Lista

Table 3.2: Economic valuation studies of biodiversity conservation based on CE

Lista

EN UN MAPA ASI MARCARIAMOS!!!!!????

The Prerequisites of Direct-to-Consumer Strategies of Established Consumer Goods Manufacturers

S. Lienhard, M. Schoegel

***Abstract*—** Established consumer goods manufactures are increasingly pursuing a direct-to-consumer (D2C) strategy, which means selling directly to the customers. In 2014, 56% of the manufactures in the UK had D2C strategies in place whereas this share increased to 73% in 2019. Going direct and bypassing intermediaries belongs to the channel selection strategies of vertical integration, namely forward integration. It is linked with a decrease in transaction-related costs, can lead to higher profits for manufacturers and addresses the double marginalization problem. D2C strategies also expand a manufacturer's understanding of consumers and their behaviour. On the other hand, D2C strategies also have disadvantages including channel conflicts and the need for new competencies. Moreover, the addition of channels does not automatically lead to an increase in company value. Previous research showed that launching a D2C strategy is not the major obstacle for consumer goods manufacturers, but rather the development afterwards. Difficulties may be the lack of financial resources to drive traffic to their stores, a loyal customer base and brand awareness. Consequently, many D2C strategies do not generate a lot of revenue yet, but rather are pause in the start-up stage. However, some manufacturers like Nespresso, Omega or Nike have been capable to increase D2C revenues significantly over the last years. The conditions required to achieve the desired revenue growth are unknown. Moreover, as the perspective of managers of consumer goods manufacturers is decisive, the investigation of prerequisites they consider as necessary to grow the revenues of D2C strategies is of great interest. Therefore, this study conducted eight first-round interviews followed by 2 x 8 interviews with the same participants to deepen and validate the first-round results (total 24). Commitment, capabilities, culture and customer transformation management (i.e., switching from a Business to a Consumer focus) were revealed as crucial prerequisite dimensions. These four dimensions correspond to certain company levels: Commitment is mainly required from the top management, capabilities and customer transformation management are middle management related dimensions and culture is a company-wide one. These findings contribute to the literature stream about D2C strategies. They improve the understanding of the conditions required for revenue growth of this strategic option for consumer goods manufacturers. The managerial implications of these findings come in different ways. The prerequisite dimensions can be used by managers as guidance either when considering to go direct, to assess existing implemented D2C strategies or to figure out potential fields of improvement.

***Keywords*—** consumer goods manufacturers, direct-to-consumer strategy, prerequisite, vertical integration.

Severin Lienhard is with the University of St. Gallen, Switzerland (e-mail: severin.lienhard@unisg.ch).

International Sales Agent Management: A Mixed-Method Approach to Identify Drivers and Barriers of Export Performance in German Manufacturing SMEs (Research in Progress)

Fabienne Ruoss, Hartmut H. Holzmüller

***Abstract*—** To reduce uncertainties evolving from a lack of foreign business knowledge and make export more cost-efficient, small- and medium-sized enterprises (SME) tend to develop an export strategy involving overseas sales agents. In regard to the coordination of the relationship to sales agents, manufacturers face numerous problematic aspects and challenges. Therefore, the guidance and management of sales agents in export markets are assumed to be a central success factor. This study identifies factors influencing the success of export relationships between German-based manufacturing SMEs and their independent sales agents. The theoretical foundation of the research is the principal-agent problem. Hence, a special focus lies on the identification of measures, that are used to control and motivate sales agents, due to the geographic and cultural distance, that causes information asymmetry and misunderstandings. While motivation research in the export-import ((E-I) literature generally lacks in the context of cross-border relationships, only little attention has been given to the effects of control measures on export performance in the SME context. Furthermore, the study assumes, that export-related processes are different in an SME context compared to investigations with larger firms. This is due to the fact, that SMEs oftentimes encounter resource inadequacies. Thus, this study aims to contribute to the E-I research stream by highlighting differences in-factors, that influence export success depending on firm size. A mixed-method research design, comprising qualitative interviews with CEOs and export managers of German manufacturing SMEs and data from an online survey, are employed to address these topics. Due to the prominent practical relevance, the study intends to provide extensive recommendations for action and measures to implement a feasible international sales agent management system in manufacturing SMEs. Special attention will be paid to control and motivation measures, that are applicable for resource-poor SMEs.

***Keywords*—**Export Management, Exporter-Importer Relationships, Independent Sales Agents, Small and Medium Enterprises

F. Ruoss is with the Department of Marketing, TU Dortmund University, Germany, (e-mail: fabienne.ruoss@tu-dortmund.de).

H. H. Holzmüller is with the Department of Marketing, TU Dortmund University, Germany, (e-mail: fabienne.ruoss@tu-dortmund.de).

Digital Marketing: Analysis in Social Media Platform and Content Analysis: Qualitative Content Analysis Case Study Brand XYZ in Indonesia

Meutia Arsanti, Rizal Edy

***Abstract*—** Technology are emerging and Internet user increasing rapidly and now the use of Social Media also expanding not only for personal use but also for company Brand. Now Marketing specialist this days also believe that using Social Media is effectively to boost its Company Brand with more effectively than conventional way. Indonesia is one of a country that have rapid user in interner user and third largest population in the world. With so many social media platform that serve the end customer, The objectives of the study is to analyze the use of social media platform that customer use related to a brand and content that trigger their behavior using a case study of XYZ Brand. Fresh fruits industry were categorize as impulsive product and heavily depends on offline marketing strategy to engage to the customer and XYZ Brand were market leader in fresh fruit in Indonesia market. Since the industry characteristic were quality are important factor not in retail and customer, XYZ brand need to find another way to communicate the brand to digital. As the current situation of 'New Normal' caused by the Pandemic, offline marketing strategy may not as effective as before to attract customer to come and buy in store. The study will provide a suggestion of digital strategy plan for XYZ Brand by maximize the potential tool for social media platform and content that trigger the customer behavior in engaging a brand. with many platform serve as tool for Brand in communicating their product or services XYZ Brand need to optimize it resources and focus to build in digital plan to create loyal community. Primary data will be gathered using Single Case Study and Qualitative methodology through interview from social media user and XYZ brand management to identify their needs and insight about behavior in using social media and brand information and secondary data also will be gathered from company records on social media. The data process will be using content analysis approach to analysis the result of interview and answer the objective of the study. Using framework of customer decision making journey, that from the case study were found that each platform serve specific purpose for the customer and they only using one or two main social media in following the brand and look for information. Specific platform such as Instagram and Twitter are main source of platform customer used in following a brand or gather information for user in Indonesia. And with the emerge of e-commerce that integrated from Brand social media platform and integrate to the e-commerce channel become a convenient way for the customer to make a purchase. The limitation of the study are specifically based from the XYZ Brand in Fresh Fruits Industry thus hopefully this study can be as start for qualitative research to understand the Fresh Fruit Consumer in Indonesia and more specific about the content in Digital Social Media use relatively to a Brand and being looked by the customer and their behavior in digital social media..

***Keywords*—** digital marketing, social media, qualitative content analysis, fresh fruits.

Meutia Arsanti is with the Faculty of Economic and Business, University of Indonesia, Indonesia (e-mail: Rafiyani.meutia@gmail.com).

Shaping of Metal-Organic Frameworks for Water Vapor Adsorption

Tsung-Lin Hsieh, Jiun-Jen Chen, Yuhao Kang

***Abstract*—**Metal-organic frameworks (MOFs) have drawn scientists' attention for decades due to its high specific surface area, tunable pore size and relatively low temperature for regeneration. Bearing with those mentioned properties, MOFs has been widely used in various applications, such as adsorption/separation and catalysis. However, the current challenge for practical use of MOFs is to effectively shape these crystalline powder material into controllable forms such as pellets, granules and monoliths with sufficient mechanical and chemical stability, while maintaining the excellent properties of MOFs powders. Herein, we have successfully synthesized an Al-based MOF powder which exhibits a high water capacity at relatively low humidity conditions and relatively low temperature for regeneration. Then the synthesized Al-MOF was shaped into granules with particle size of 2-4 mm by (1) tumbling granulation, (2) High shear mixing granulation and (3) Extrusion techniques. Finally, the water vapor adsorption rate and crush strength of Al-MOF granules by different shaping techniques were measured and compared.

***Keywords*—**granulation, granules, metal-organic frameworks, water vapor adsorption.

Tsung-Lin Hsieh is with the Industrial Technology Research Institute, Hsinchu, Taiwan (e-mail: itriA70459@itri.org.tw).

Jiun-Jen Chen is with the Industrial Technology Research Institute, Hsinchu, Taiwan (e-mail: derekkang@itri.org.tw).

Yuhao Kang is with the Industrial Technology Research Institute, Hsinchu, Taiwan (e-mail: JiunJenChen@itri.org.tw).

Synthesis and Optimization of Bio Metal-Organic Framework with Permanent Porosity

Tia Kristian Tajnšek, Matjaž Mazaj, Nataša Zabukovec Logar

***Abstract*—** Metal-organic frameworks (MOFs) with their specific properties and the possibility of tuning the structure represent excellent candidates for use in the biomedical field. Their advantage lies in large pore surfaces and volumes, as well as the possibility of using bio-friendly or bioactive constituents. So-called bioMOFs are representatives of MOFs which are constructed from at least one biomolecule (metal, a small bioactive molecule in metal clusters and/or linker) and are intended for bio-application (usually in the field of medicine; most commonly drug delivery). When designing a bioMOF for biomedical applications, we should adhere to some guidelines for an improved toxicological profile of the material. Such as (i) choosing an endogenous/nontoxic metal, (ii) GRAS (generally recognized as safe) linker, and (iii) nontoxic solvents. Design and synthesis of bioNICS-1 (bioMOF of National Institute of Chemistry Slovenia – 1) consider all these guidelines. Zinc (Zn) was chosen as an endogenous metal with an agreeable recommended daily intake (RDI) and LD_{50} value, and ascorbic acid (Vitamin C) was chosen as a GRAS and active linker. With these building blocks, we have synthesized a bioNICS-1 material. The synthesis was done in ethanol using a solvothermal method. The synthesis protocol was further optimized in three separate ways. Optimization of (i) synthesis parameters to improve the yield of the synthesis, (ii) input reactant ratio, and addition of specific modulators for production of larger crystals and (iii) differing of the heating source (conventional, microwave and ultrasound) to produce nano-crystals. With optimization strategies, the synthesis yield was increased. Larger crystals were prepared for structural analysis with the use of a proper species and amount of modulator. Synthesis protocol was adjusted to different heating sources, resulting in the production of nano-crystals of bioNICS-1 material. BioNICS-1 was further activated in ethanol and structurally characterized, resolving the crystal structure of new material.

***Keywords*—** ascorbic acid, bioMOF, MOF, optimization, synthesis, zinc ascorbate

T.K.T. is with the National Institute of Chemistry, Hajdrihova ulica 19, 1000 Ljubljana, Slovenia (tia.tajnsek@ki.si) and University of Ljubljana, Faculty of Chemistry and Chemical Technology, Večna pot 113, 1000 Ljubljana

M. M. is with the National Institute of Chemistry, Hajdrihova ulica 19, 1000 Ljubljana, Slovenia (matjaz.mazaj@ki.si)

N. Z. L. is with the National Institute of Chemistry,Hajdrihova ulica 19, 1000 Ljubljana, Slovenia and University of Nova Gorica, Vipavska cesta, 5000 Nova Gorica, Slovenia (natasa.zabukovec@ki.si)

Effect of Aluminium Content on Bending Properties and Microstructure of Al_xcocrfeni Alloy Fabricated by Induction Melting

Marzena Tokarewicz, Małgorzata Grądzka-Dahlke

***Abstract*—** High-entropy alloys (HEAs) have gained significant attention due to their great potential as functional and structural materials. HEAs have very good mechanical properties (in particular, alloys based on CoCrNi). They also show the ability to maintain their strength at high temperatures, which is extremely important in some applications. AlCoCrFeNi alloy is one of the most studied high-entropy alloys. Scientists often study the effect of changing the aluminium content in this alloy, because it causes significant changes in phase presence and microstructure, and consequently affects its hardness, ductility and other properties. Research conducted by the authors also investigates the effect of aluminium content in Al_xCoCrFeNi alloy on its microstructure and mechanical properties. Al_xCoCrFeNi alloys were prepared by vacuum induction melting. The obtained samples were examined for chemical composition, microstructure and microhardness. Three-point bending method was carried out to determine the bending strength, bending modulus and conventional bending yield strength. The obtained results confirm the influence of aluminium content on the properties of Al_xCoCrFeNi alloy. Most studies on Al_xCoCrFeNi alloy focus on the determination of mechanical properties in compression or tension, much less in bending. The achieved results provide valuable information on the bending properties of Al_xCoCrFeNi alloy and lead to interesting conclusions.

***Keywords*—** bending properties, high-entropy alloys, induction melting, microstructure

M. Tokarewicz is with the Faculty of Mechanical Engineering, Bialystok University of Technology ul. Wiejska 45 C, 15-351 Bialystok, Poland (e-mail: m.tokarewicz@doktoranci.pb.edu.pl)

M. Grądzka-Dahlke is with the Department of Materials and Biomedical Engineering, Bialystok University of Technology, ul. Wiejska 45 C, 15-351 Białystok, Poland (e-mail: m.dahlke@pb.edu.pl)

The Visibility of Metal-Organic Framework Technologies by Atomic Layer Deposition - A review

Omotayo Sanni, Jianwei Ren, Tien-Chien Jen

***Abstract*—**Over the past decades of research and development, metal-organic frameworks (MOFs) are gradually coming out of the laboratories to solve real-world problems with unlimited applications. However, their powdered condition presents difficulty in utilizing them widely in actual practices. Depending on the envisioned applications, MOFs will be desired to integrate as an application-oriented form for example thin films into a microelectronic device to achieve the desired performance. Hence, atomic layer deposition (ALD) as a gas-phase technique was designed to coat thin films of numerous materials onto any target substrates. ALD produced films with excellent controls on film thickness, composition, conformity, very low pinhole, and particle levels on planar substrates even on the high aspect-ratio structures. Given these excellent properties, the ALD technique has been used worldwide as a reliable tool to coat films or fabricate membranes in different fields of applications. In this regard, ALD promises to deposit MOFs films onto the target substrates and assist the visibility of MOFs technologies by facilitating MOFs devices integration. In this review, the past ALD research efforts towards MOFs films growth, post-synthetic functionalization, and devices integration will be summarized. In this context, the parallel advancements such as lessons or concepts from other technologies to be beneficial were also drawn to guide further optimization and improvement of applications based on MOFs-enabled technologies. The overview from the literature on the current technology readiness level (TRLs) of MOFs technologies indicated the up-to-date MOFs research, development, and innovation (RD&I) are still between TRL3 and TRL4. Taking technology from laboratory pieces to device integration is always a challenge, and their progression towards higher TRLs needs collective advancements from other technologies.

***Keywords*—** Atomic layer deposition, Metal-organic frameworks, Technology readiness levels, Visibility of MOFs technologies

.

Omotayo Sanni is with the Department of Mechanical Engineering Science, University of Johannesburg, Cnr Kingsway and University Roads, Auckland Park, 2092, Johannesburg, South Africa (e-mail: tayo.sanni@yahoo.com).

Jianwei Ren is with the Department of Mechanical Engineering Science, University of Johannesburg, Cnr Kingsway and University Roads, Auckland Park, 2092, Johannesburg, South Africa (e-mail: jren@uj.ac.za).

Tien-Chien Jen is with the Department of Mechanical Engineering Science, University of Johannesburg, Cnr Kingsway and University Roads, Auckland Park, 2092, Johannesburg, South Africa (e-mail: tjen@uj.ac.za).

Recycling PET to Fe-MOF Nanocrystals for Elimination of Heavy Metals

A. Nqombolo, B. Sartowska, W. Starosta, J. Ren, P. N. Nomngongo

***Abstract*—** In this work, polyethylene-based MOFs have been synthesized and used as an adsorbent in the removal of Cd, Pb and Cr from wastewater and acid mine effluents using adsorption batch system. X-Ray Diffraction, Fourier transform infrared spectroscopy, Brunnuer-Emmet-Teller and transmission electron microscope were used for structural, morphological and surface characteristics of MIL-101(Fe). The concentration of heavy metal ions in water samples was measured by inductively coupled plasma optical emission spectrometry. Different experimental factors/variables (such as contact time, shaking speed or sonication, dosage, temperature and pH) affecting the adsorption of metals were optimized using multivariate optimisation. The nature of the adsorption process was investigated using Langmuir, Freundlich and Temkin isotherm models. Furthermore, the adsorption mechanism was investigated using five kinetic models, that is, pseudo-first order, pseudo-second order, intraparticle diffusion, Elovich model and Boyd model.

***Keywords*—**About four key words or phrases in alphabetical order, separated by commas.

A. Nqombolo is with the Department of Chemical Sciences, University of Johannesburg, Doornfontein Campus, P.O. Box 17011, Johannesburg, 2028, South Africa, 2028, South Africa and Department of Science and Innovation (DSI)/National Research Foundation (NRF) South African Research Chair Initiative (SARChI): Nanotechnology for Water, University of Johannesburg, Doornfontein 2028, South Africa (email: azilenqombolo@gmil.com)

B. Sartowska is with the Laboratory of Materials Research, Institute of Nuclear Chemistry and Technology, Dorodna 16, 03-195 Warsaw, Poland (email: b.sartowska@ichtj.waw.pl)

W. Starosta is with the Laboratory of Materials Research, Institute of Nuclear Chemistry and Technology, Dorodna 16, 03-195 Warsaw, Poland (email: (email: b.sartowska@ichtj.waw.pl)

J. Ren is with the Department of Mechanical Engineering Science, University of Johannesburg, Cnr Kingsway and University Roads, Auckland Park, 2092, Johannesburg, South Africa (email: jren@uj.ac.za).

P.N. Nomngongo is with the Department of Chemical Sciences, University of Johannesburg, Doornfontein Campus, P.O. Box 17011, Johannesburg, 2028, South Africa, 2028, South Africa and Department of Science and Innovation (DSI)/National Research Foundation (NRF) South African Research Chair Initiative (SARChI): Nanotechnology for Water, University of Johannesburg, Doornfontein 2028, South Africa (email: pnnomngongo@uj.ac.za)

Preparation and Characterization of Pb-Ge-Te Nanocrystals as a Candidate for Ferroelectric and Solar Energy Applications

Iman A. Mahdy, A. M. El-Khodary, S. M. El Sheikh

***Abstract*—** The class of IV-VI semiconductor nanocrystals, among them germanium and lead tellurides, have a great potential for mid-infrared optoelectronic devices, such as photon detectors and laser emitters, in addition to energy conversion systems, such as solar cells, owing to their narrow bandgap energy. Moreover, their ability to undergo a structural ferroelectric phase transition qualifies them for ferroelectric random-access memory (FRAM). The present study is aiming to investigate the structural, morphological, optical, and ferroelectric properties of $Pb_{50-x}Ge_xTe_{50}$ (at different values of x) nanocrystals, with a deep focus on increasing the ferroelectric phase transition temperature to overcome the first barrier of applying them to memory storage devices. Results of atomic force microscopy give an indication of the decrement of particle size with increasing Ge content as like as obtained from XRD results. The optical band gap evaluated shows decrement from 1.53 to 1.45 eV with increasing Ge content from 15 at. % to 30 at. %, which is considered the optimum optical gap for the solar absorber. Ferroelectric properties P-E characteristics show symmetric hysteresis loop with increasing coercive field with increasing applied frequency from 200 Hz to 2 kHz.

Acknowledgment: This study has been funded by the American University in Cairo AUC (SSE-PHYS-S.E.-FY17- FY18- FY19-RG(20)-2016-Feb-10-08-45-59.

***Keywords*—** ferroeelectric nanocrystal, non-volatile memory applications, solar energy applications, IV-VI semiconductors.

Iman A. Mahdy is with the Ph ysics Department, Faculty of Science (Girls), Al-Azhar University, 11753, Nasr City, Cairo, Egypt(e-mail: imanmahdy@azhar.edu.eg).

A. M. El-Khodary is with the British University in Cairo, El Sherouk City, 11837.

S. M. El Sheikh is with the Physics Department, Faculty of Science& Engineering, American University in Cairo, 11835, New Cairo, Egypt.

A Modeling Study of Early COVID-19 Pandemic Suppression and Mitigation Strategies in Ghana

N.K.Frempong, T.Acheampong, J.H. Amuasi

***Abstract*—**This paper uses publicly available data and various statistical models to estimate the basic reproduction number (R_0) and other disease parameters for the early COVID-19 pandemic outbreak in Ghana. We also test the effectiveness of government imposition of public health measures to reduce the risk of transmission and impact of the pandemic, especially in the early phase. R_0 is estimated from the statistical model as 3.21 using a 0.147 estimated growth rate [95% C.I.: 0.137-0.157] and a 15-day time to recovery after COVID-19 infection. This estimate of the initial R_0 is consistent with others reported in the literature from other parts of Africa, China and Europe. Our results also indicate that COVID-19 transmission reduced consistently in Ghana after the imposition of public health interventions - such as border restrictions, intra-city movement, quarantine and isolation - during the first phase of the pandemic from March to May 2020. However, the time-dependent reproduction number (Rt) beyond mid-May 2020 does not represent the true situation given there was not consistent testing regime in place. This was also confirmed by the Jack-knife bootstrap estimates which show that the positivity rate over-estimates the true incidence rate from mid-May 2020. Given concerns about virus mutations, delays in vaccination and a possible new wave of the pandemic, there is a need for systematic testing of a representative sample of the population to monitor the reproduction number. There is also an urgent need to increase the availability of testing for the general population to enable early detection, isolation and treatment of infected individuals to reduce progression to severe disease and mortality.

***Keywords*—**COVID 19,Public health, Statistical Models, Reproduction Number

Nana Kena Frempong is with the Kwame Nkrumah University of Science and Technology, Ghana (e-mail: nkf.cos@gmail.com).

Optimal Design of the Flexure in Two-axis Fast Steering Mirror by Design of Experiment Technique

Long Kim Vu, Ban Dang Nguyen

***Abstract*—** Flexure is a crucial component in the fast steering mirror (FSM) to provide the capability of passive vibration isolation for the system. In this paper, the optimal method is utilized to design the flexure satisfying the objective function of mode shape and the constraint of fatigue. First, the structure of the flexure is determined by 7 design parameters. Then, the Design of Experiment (DOE) technique is applied to analyze the influence of 5 dominant factors to the characteristics of the flexure. Finally, the finite element method (FEM) with modal analysis is carried to virtually investigate the performance of the optimal flexure with the passive isolation feature. The results show that the designed FSM with optimal flexure meet the requirement of mechanical performance.

***Keywords*—**DOE, flexure, modal analysis, optimal design.

Long Vu Kim is with the Viettel High Technology Industries Corporation, Vietnam (e-mail: longvk1@viettel.com.vn).

Historic Fire Occurrence in Hemi-Boreal Forests: Exploring Natural and Cultural Scots Pine Multi-Cohort Fire Regimes in Lithuania

Charles Ruffner, Michael Manton, Gintautas Kibirkstis, Gediminas Brazaitas, Vitas Marozas, Ekaterine Makrickiene, Rutile Pukiene, Per Angelstam

***Abstract*—** In dynamic boreal forests, fire is an important natural disturbance, which drives regeneration and mortality of living and dead trees, and thus successional trajectories. However, current forest management practices focusing on wood production only have effectively eliminated fire as a stand-level disturbance. While this is generally well studied across much of Europe, in Lithuania, little is known about the historic fire regime and the role fire plays as a management tool towards the sustainable management of future landscapes. Focusing on Scots pine forests, we explore; i) the relevance of fire disturbance regimes on forestlands of Lithuania; ii) fire occurrence in the Dzukija landscape for dry upland and peatland forest sites, and iii) correlate tree-ring data with climate variables to ascertain climatic influences on growth and fire occurrence. We sampled and cross-dated 132 Scots pine samples with fire scars from 4 dry pine forest stands and 4 peatland forest stands, respectively. The fire history of each sample was analyzed using standard dendrochronological methods and presented in FHAES format. Analyses of soil moisture and nutrient conditions revealed a strong probability of finding forests that have a high fire frequency in Scots pine forests (59%), which cover 34.5% of Lithuania's current forestland. The fire history analysis revealed 455 fire scars and 213 fire events during the period 1742-2019. Within the Dzukija landscape, the mean fire interval was 4.3 years for the dry Scots pine forest and 8.7 years for the peatland Scots pine forest. However, our comparison of fire frequency before and after 1950 shows a marked decrease in mean fire interval. Our data suggest that hemi-boreal forest landscapes of Lithuania provide strong evidence that fire, both human and lightning-ignited fires, has been and should be a natural phenomenon and that the examination of biological archives can be used to guide sustainable forest management into the future. Currently, fire use is prohibited by law as a tool for forest management in Lithuania. We recommend introducing trials that use low-intensity prescribed burning of Scots pine stands as a regeneration tool towards mimicking natural forest disturbance regimes.

***Keywords*—** biodiversity conservation, cultural burning, dendrochronology, forest dynamics, forest management, succession

Charles Ruffner is with the School of Forestry and Horticulture, Southern Illinois University-Carbondale, Ill 62901-4411 (e-mail: ruffner@siu.edu).

Michael Manton, Gediminas Brazaitas, Vitas Marozas, Ekaterina Makrickiene are with the Vytautas Magnus University, Faculty of Forest Science and Ecology, Studentu 13, LT-53362 Akademija, Kauno r., Lithuania.

Gintautas Kibirkštis, Rūtilė Pukienė are with the Nature Research Centre, Akademijos str. 2, LT–08412 Vilnius, Lithuania.

Per Angelstam is with the Inland Norway University of Applied Sciences, Faculty of Applied Ecology, Agricultural Sciences and Biotechnology, Department of Forestry and Wildlife Management, Campus Evenstad, N-2480 Koppang, Norway.

Geographic Information Systems (GIS) and a Breath of Opportunities for Supply Chain Management: Results from a Systematic Literature Review

Author Ms Anastasia Tsakiridi (MSc, BSc, GIS Specialist)

Abstract**—**Geographic Information Systems (GIS) have been utilized in numerous spatial problems, such as site research, land suitability, and demographic analysis. Besides, GIS have been applied in scientific fields like geography, health and economics. In business studies GIS have been used to provide insights and spatial perspectives in demographic trends, spending indicators and network analysis. To date, the information regarding the available usages of GIS in Supply Chain Management (SCM) and how these analyses can benefit businesses is limited. A systematic literature review (SLR) of the last 5-year peer-reviewed academic literature was conducted, aiming to explore the existing usages of GIS in SCM. The searches were performed in 3 databases (Web of Science, ProQuest, and Business Source Premier) and reported using the Preferred Reporting Items for Systematic Reviews and Meta-Analyses (PRISMA) methodology. The analysis resulted in 79 papers. The results indicate that the existing GIS applications used in SCM were in the following domains: a) Network/ transportation analysis (in 53 of the papers), b) Location – Allocation Site Search/ Selection (Multiple-criteria decision analysis) (in 45 papers), c) Spatial analysis (demographic or physical) (in 34 papers), d) combination of GIS and Supply Chain/network optimization tools (in 32 papers), and e) Visualization/ monitoring or Building Information Modeling applications (in 8 papers). An additional categorization of the literature was conducted by examining the usage of GIS in the Supply Chain (SC) by the business sectors, as indicated by the volume of the papers. The results showed that GIS are mainly being applied in the SC of the Biomass Biofuel/Wood industry (33 papers). Other industries that are currently utilizing GIS in their SC were the Logistics industry (22 papers), the Humanitarian/ Emergency/ Health Care sector (10 papers), the Food/ Agro-Industry sector (5 papers), the Petroleum/ Coal/ Shale Gas sector (3 papers), the Faecal Sludge sector (2 papers), the Recycle and product footprint industry (2 papers), and the Construction sector (2 papers). The results were also presented by the geography of the included studies and the GIS software used, to provide critical business insights and suggestions for future research. The results showed that research case studies of GIS in SCM were conducted in 26 countries (mainly in the USA) and that the most prominent GIS software provider was Environmental Systems Research Institute's ArcGIS (in 51 of the papers). This study is a systematic literature review of the usage of GIS in SCM. The results showed that the GIS capabilities could offer substantial benefits in SCM decision making, by providing key insights to cost minimization, supplier selection, facility location, SC network configuration and asset management. However, as presented in the results only eight industries/sectors are currently using GIS in their SCM activities. These findings may offer essential tools to SC managers who seek to optimize the SC activities and/or minimize logistic costs, and to consultants and business owners that want to make strategic SC decisions. Furthermore, the findings may be of interest to researchers aiming to investigate unexplored research areas where GIS may improve SCM.

Keywords**—** Supply Chain Management, Logistics, Systematic Literature Review, GIS

Author is with the Alliance Manchester Business School, Booth St W, Manchester M15 6PB (e-mail: natasa.tsakiridi@gmail.com)

Making Vulnerable Road Users More Visible to Radar : A Communications Inspired Approach

Saeid K.Dehkordi, Giuseppe Caire, *Fellow, IEEE*

***Abstract*—Intelligent reflecting surfaces (IRS) are a novel technology envisaged to significantly improve the performance of next generation wireless communication networks, utilizing passive reflecting elements arranged in planar arrays to reconfigure the wireless propagation environment. This study investigates the use of Intelligent Reflecting Surfaces for Vulnerable Road Users (VRU) such as pedestrians, bicycles, and wheelchair users. This can be made possible by recent advances in IRS technology and can significantly improve the radar visibility of VRUs. In this work we propose a potential use case for IRS which aims to improve the detection of traffic users by automotive radar irrespective of the object's orientation which may severely impact its observable radar cross section. Furthermore, this approach can be extended to form a network where multiple radar sensors can become aware of a VRU's presence even in cases where the users have not been directly observed by the respective sensor. Numerical results are provided to show the proposed approach can enhance the radar detection capability of VRUs and make the orientation-dependent radar cross section of targets a less significant challenge.**

***Index Terms*—Joint Radar-Communications, Intelligent reflecting surfaces, V2X, VRU**

I. Introduction

In the context of automated driving systems and Vehicle-to-Everything (V2X) communications envisioned in 5G and beyond systems, radar sensors are one the key enabling technologies [7]. State-of-the-art automotive radars are mostly based on techniques such as frequency-modulated continuous waves (FMCW) e.g. Chirp Sequence (CS) while more recently, much research has been dedicated to the integration of dual function radar and communications systems commonly referred to as *RadCom*, which combine target estimation capability with communication networks in a single system [6]. The work in [1] considers a joint radar estimation and communication system utilizing multi-carrier digital formats based on an orthogonal time frequency space (OTFS) principle. As compared to other sensing techniques such as lidar and vision sensors, radar systems offer a unique solution for target tracking in that they can directly estimate the Doppler velocity of objects. However the Radar Cross Section (RCS) of an object can vary significantly depending on a multitude of parameters including physical size, composition material and object orientation w.r.t to the radar transmitter. In contrast to communications devices, radar technology operates on a passive regime i.e. the radar receiver collects the reflected transmit signal from the object of interest and estimates the target's parameters from the received echo. Modern automotive radars typically estimate range, Doppler velocity and angle of arrival and can produce an estimate of the target reflection intensity proportional to the RCS [2]. One of the main challenges with current automotive radar is the detection of objects referred to as Vulnerable Road Users (VRU) such as pedestrians and animals which have weak reflection properties. The detection of VRU's poses a great challenge for automotive radar and has been one the key performance indicators to ensure a widespread roll-out of highly automated driving systems. A common approach among industrial manufacturers is to enhance the radar hardware capability by increasing the electrical aperture size, which proportionally increases the angular resolution or to increase the sensitivity of the radar receiver to detect weaker signatures, and given that most of today's vehicles with automated driving capability are equipped with multiple radar sensors, including short, medium and long range sensors,this adds up to a prohibitive increase in hardware cost.

On the other hand, in next generation mobile communications network architectures, significant interest in developing *reconfigurable* propagation environments has been shown [4] [5]. A number of technologies that show promise in achieving this goal are intelligent reflecting surfaces (IRS) [3], software-controlled metasurfaces, and re-configurable intelligent surfaces [5], which work on the principle of controlling the reflection of impinging EM waves. In this work we are particularly interested in IRS where the common assumption is that the elements in an array similar to that of patch antenna arrays, can perform passive beamforming via creating individual phase shifts on the impinging wave. Although in communication systems, IRS assisted networks can be though of as an extension to the already well developed relay concepts such as Amplify-and-Forward (AF), in this work we propose a different use case for IRS which to the best of the authors' knowledge has yet not been proposed at the time of writing. Given the assumption that the IRS can receive information about the automobile's position through the mobile device from the user as explained in the sections that follow, the proposed approach can be applied for any radar system including CS. However, with the advancement of RadCom systems, where the resources including the transmit/receive array and frequency band used are common among the two systems and therefore the IRS can be deployed as a passive device for target detection enhancement, we focus our study on such systems. In section II a brief mathematical description of IRS and their working principle are described. Section III-B provides a description of the system model. In section IV

Saeid K.Dehkordi and Giuseppe Caire are with the Communications and Information Theory Group, Technische Universität Berlin, Berlin, Germany e-mail: s.khalilidehkordi@tu-berlin.de .

numerical results are presented to showcase the viability of the proposed methodology.

II. Background

A. Intelligent Reflecting Surfaces

The hardware implementation of IRS are based on the concept of metasurfaces discussed in [8], where a metasurface is described as a two dimensional planar array of metamaterials (i.e. the thickness of the material is negligible) of which properties can be digitally controlled. This metasurface would typically entail a large number of array elements and the controllable properties include an induced phase shift and amplitude change of the impinging wave to create a desired reflection. From a practical perspective such as the work in [11], electronic device components such as field-effect transistors (FETs), positive intrinsic-negative diodes(PIN) and micro-electromechanical system (MEMS) switches have recently been employed to achieve this goal.

III. Mathematical Modeling

A. IRS Model

In mathematical terms, for an IRS with N elements, the reflected signal by the nth, $n \in \{1, 2, .., N\}$ element of the IRS, denoted by y_n, is given by multiplying the corresponding incident signal, denoted by x_n, by a complex coefficient, i.e. $y_n = \beta_n e^{j\phi_n}$ where $\beta_n \in [0, 1]$ and $\phi_n \in [-\pi, \pi]$ specify the reflection coefficient and control the reflected signal's amplitude (or attenuation due to passive reflection) and phase shift, respectively. The IRS array can control the reflection direction of the incoming wave through setting the values in matrix $\mathbf{\Phi}$ which is defined as :

$$\mathbf{\Phi} = \text{diag}(\beta_1 e^{j\phi_1}, ..., \beta_N e^{j\phi_N}) \tag{1}$$

where in recent studies [13] due to the progress made in developing lossless metasurfaces which provide perfect reflection magnitude with an arbitrary adjustable reflection phase, it can be assumed that all the coefficients β_i are equal to 1.

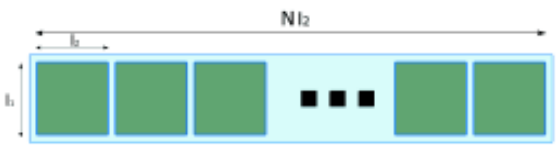

Fig. 1: IRS array composed of N uniformly placed elements.

B. System Model

Consider the scenario in fig.3 where a User Equipment (UE) is communicating with an automobile. The automobile is equipped with a ULA of L elements serving as a joint RadCom system. The RadCom communicates with the mobile UE with ULA of M elements. In this work we consider the RadCom system described in [1] where the mono-static fullduplex radar, conveys a message to its targeted receiver while estimating parameters of interest related to the same receiver from the backscattered signal. Note that the IRS has no sensory capability however it includes a smart controller which can in practice be implemented using field-programmable gate arrays (FPGA) connected to a control circuit board responsible for the adjustment of the reflection amplitude and phase shifts (β_n, ϕ_n) of the N array elements described in the previous section. Through the same HW the IRS can communicate with other mobile devices such as the mobile UE. This connection maybe established through a wireless connection such as a Bluetooth. The complete system process is represented in diagram2.

In order to provide the required reflection angle for the IRS, we assume that the Comm. module of the automobiles and UE can gain an estimate of their respective positions via protocols such as the IEEE 802.11p standard or other beam alignment techniques such as the method developed in [10], which relies on compressive sensing techniques to reduce overhead. In the context of V2X, the known standard of IEEE 802.11p operates by periodically broadcasting a *ping* signal to indicate the automobile's presence. The UEs are equipped with an 802.11p type receiver which pick up the beacon signal of the car which contains also its position. Therefore the UE knows that a car is approaching along with information about its direction. This information is then shared via a Bluetooth connection to the IRS to configure the phase and amplitude coefficients accordingly. This process is carried out dynamically via a control loop since the user is moving and its relative position may change over time. This method can be expanded within a connected network where multiple approaching cars some of which may not be able to directly observe the VRU in their sensory FoV, as depicted in fig.3 are present. In this case, assuming that all these beacon signals can be decoded by the UE, since 802.11p is a collision protocol such that the signals are received without collision or alternatively the position of other cars can be transmitted to the UE directly via the car to which it communicates (since multiple cars are connected, either directly or through a Base Station (BS)), then the IRS can switch its reflection coefficients in a time divided manner such that the impinging radar signal from a specific car is directed also towards other cars. In this way each car can obtain it's own estimate of the target (including Doppler velocity, accurate DoA).

C. IRS-Aided System Performance

Given the system model above, the aim is to show how the detected signal SNR is affected. In the case of the IRS-free RadCom system the same array is used for sensing and communication and the SNR for the radar system is given [1]:

$$\text{SNR}_{\text{RC}} = \frac{G_{TX} G_{RX} \sigma_{rcs} \lambda^2}{(4\pi)^3 r^4 \sigma_n^2} P_{\text{TX,avg}} \tag{2}$$

In eq.2 σ_{rcs} is the target RCS, G_{TX} and G_{RX} are the transmitter and receiver gain, respectively which in the case of the RadCom system will be equal. Note that in many automotive radar systems, transmit beamforming is non-existent or that the receive and transmit gains are not the same. λ is the

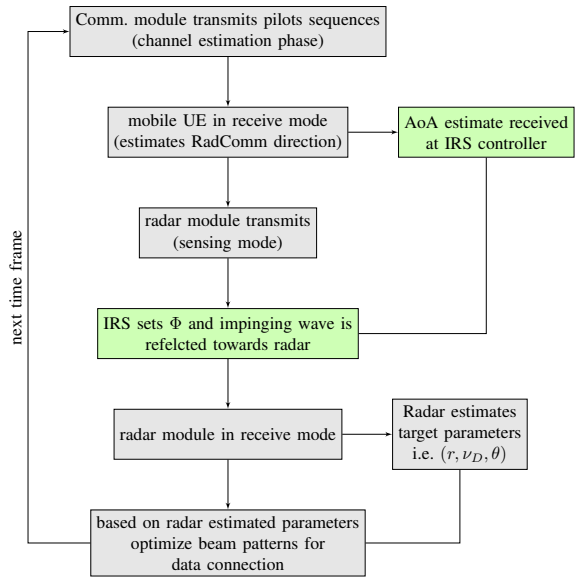

Fig. 2: Flowchart of the IRS assisted Radar-Comm system. The green blocks indicate the IRS functions.

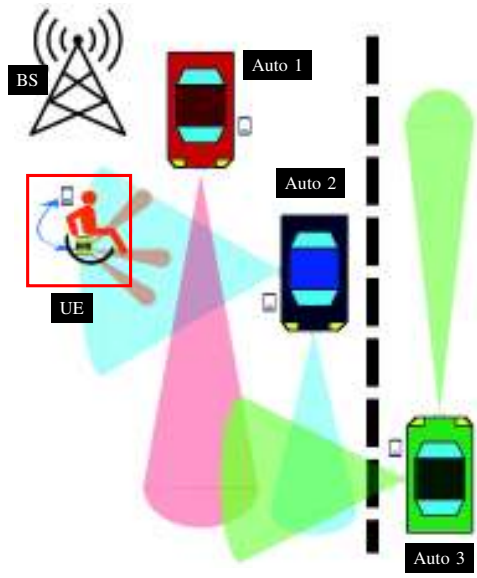

Fig. 3: Traffic scenario with possible use case of a Radar-Comm-IRS network. The automobiles' Comm. units intercommunicates with the mobile equipment of the VRU which in turn can communicate with the mounted IRS panels through a low-rate connection such as Bluetooth. In addition the BS can transmit to and receive from any of the users. The vehicles may be equipped with multiple radar sensors with different FoVs and ranges.

wavelength at the transmitted RF frequency, r is the distance between transmitter and receiver and the system noise variance is given $awgn \sim \mathcal{N}(0, \sigma_n^2)$. $P_{\text{TX,avg}}$ is the average transmitted power. When an IRS is present, the estimated direction of the transmitter ϕ_i is sent to the IRS control and consequently the IRS adjusts Φ to the desired angle. The SNR only from the reflected wave off the IRS in this case is [12]:

$$\text{SNR}_{\text{IRS}} = \beta_{\text{IRS}} \frac{P_{\text{TX,avg}}}{\sigma_n^2} \tag{3}$$

and the pathloss β_{IRS} at the far-field distance can be approximated as:

$$\beta_{\text{IRS}}(r_1, r_2, \phi_r) = \frac{G_{TX} G_{RX}}{(4\pi)^2} \left(\frac{N l_1 l_2}{r_1 r_2}\right)^2 cos^2(\phi_i) \tag{4}$$

with l_1, l_2 representing the physical dimensions of a rectangular array element as in fig.1, r_1, r_2 are the distance to and from the IRS from the TX/RX module, where in the case of a mono-static radar they are set as equal. ϕ_i and ϕ_r are the angle of incidence and desired reflection angle. Note that since the physical dimension of the IRS array as presented in sectionIV are relatively insignificant as compared to real life VRUs, particularly in the mmWave frequency bands of interest. Therefore the total reflected power approximately is the linear combination of the power reflection resultant from the VRU's observed RCS and the reflected (and beamformed) signal from the IRS. However in this work we assume the extreme to be true such that the observed RCS is very small due to effects such as orientation of the object or the material type. The challenge set by orientation angle however is not problematic for the IRS, in the sense that this would translate to a different angle of incidence as covered in [12], and with information about the target position the IRS can modify the amplitude/phases of elements accordingly.

IV. Simulation and Numerical Results

For the simulations in this section we consider a RadCom system consisting of a $L = 64$ ULA, a UE with $M = 1$ single isotropic element. The IRS device considered, consists of an array of N linear elements each with a physical size of $l_1 \times l_2$ such that they are smaller than a wavelength, here we set $l_1, l_2 = \lambda/2$. The RCS value of humans and bicycles has been extensively studied at the two common automotive radar frequency bands of 24 and 77 GHz in [14]. Figure 4 shows the measured RCS of a human at 77GHz with different rotation angles. It's clearly visible that the RCS values can significantly fluctuate and hinder radar detection depending on the orientation and clothing type. We choose the RCS values for humans according to tableI, where the maximum measured value is assumed. In order to demonstrate the improvement in detection capability we compare the obtained SNR values over range for the proposed system with SNR values obtained based on RCS dependent reflection of the conventional RadCom system. For $G_{\text{TX}}, G_{\text{RX}}$ the assumption is that the transmitted signal is directed towards the target and that the maximum beamforming gain of the RadCom ULA is achieved. Additionally a curve is presented showing the SNR where no transmit beamforming is present (i.e. $G_{\text{TX}} = 1$).

In fig.6 the dependence of path loss component of the IRS is shown as the angle of incidence varies. It can be seen that a change of incidence from 0 to 50° only changes very steadily within a region of less than 4 dB whereas the measurements in [14] show that for very minor changes in orientation of the human body a sharp drop of up to 15dB can occur. As an alternative to linear arrays, the plots in fig.7 compare the SNR gain when addition elements are stacked in the vertical dimension. It is observed that in the case of using $N = 128$ as in the simulations, the physical aperture size at the frequency of interest is around 25cm which can very easily be mounted on wearable items or rigid frames such bicycles and wheelchairs.

TABLE I: Measured RCS values for common VRUs

	Frequency Range/ Type		
	76-81 Bicycle	***76-81 Adult***	***76-81 Child***
RCS(dBsm)	-4	-5	-11

The values are maximum of average values provided in [14].

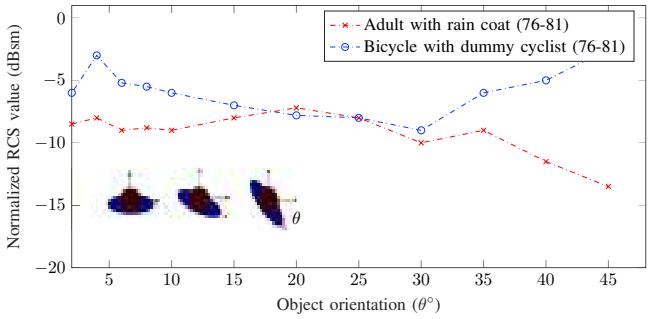

Fig. 4: Fluctuations of a measured human and dummy cyclist RCS in the 77 GHz band as suggested in [14]. The schematic below the curve shows the orientation angle of the object.

V. CONCLUSIONS

IRS-aided wireless networks are an emerging research topic and practical use cases of these systems remain unexplored and therefore the hope is that this work has successfully identified a future direction of research for this technology. In particular, we believe that single user case of IRS in this work can be integrated into V2X systems to provide information to the user through communicating automobiles and create awareness of the VRU even in cases were other connected automobiles may not be able to directly observe the user with their respective sensors.

REFERENCES

[1] L. Gaudio, M. Kobayashi, G. Caire and G. Colavolpe, "On the Effectiveness of OTFS for Joint Radar Parameter Estimation and Communication," in IEEE Transactions on Wireless Communications, vol. 19, no. 9, pp. 5951-5965, Sept. 2020, doi: 10.1109/TWC.2020.2998583.

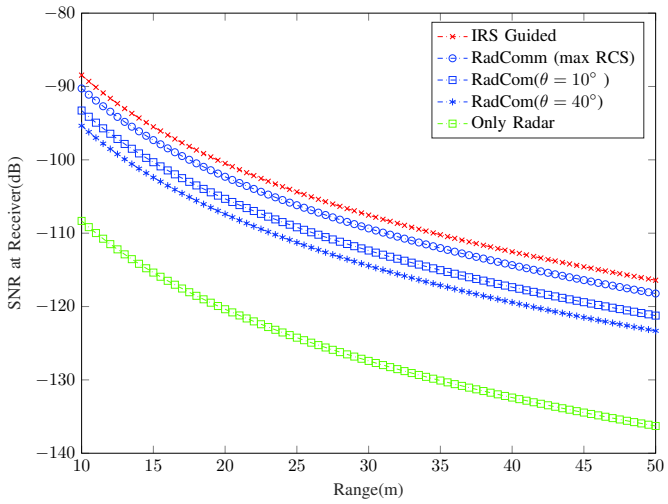

Fig. 5: Comparison of the expected SNR values at the receiver of the RadCom system with and without IRS with $N = 128$ at 77 GHz. The curve *Only radar* implies the case where no transmit beamforming (gain) is present.

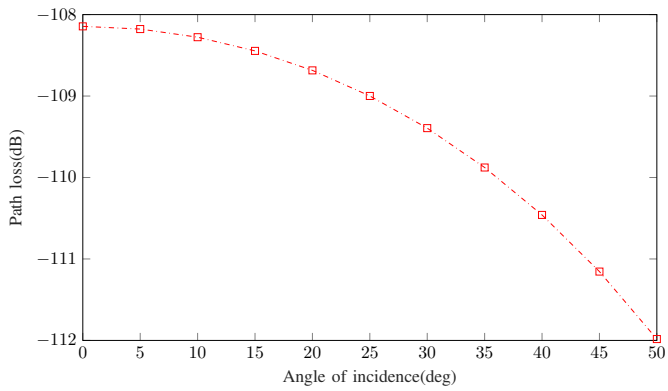

Fig. 6: Path loss value β_{IRS} of an IRS Vs. the incidence angle of the impinging wave.

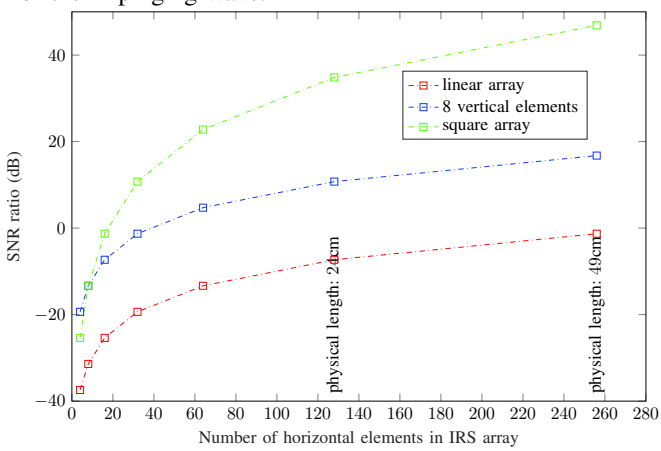

Fig. 7: The curves depict the gained value $\frac{\text{SNR}_{\text{IRS}}}{\text{SNR}_{\text{RC}}}$ at 77GHz. The two top curves consider linear rectangular arrays instead of ULAs.

[2] S. K. Dehkordi, N. Appenrodt, J. Dickmann and C. Waldschmidt, ”Region of Interest Based Adaptive High Resolution Parameter Estimation with Applications in Automotive Radar,” 2018 19th International Radar Symposium (IRS), Bonn, 2018, pp. 1-10, doi: 10.23919/IRS.2018.8448115.

[3] Q. Wu and R. Zhang, ”Towards Smart and Reconfigurable Environment: Intelligent Reflecting Surface Aided Wireless Network,” in IEEE Communications Magazine, vol. 58, no. 1, pp. 106-112, January 2020, doi: 10.1109/MCOM.001.1900107.

[4] E. Bjoernson, L. Sanguinetti, H. Wymeersch, J. Hoydis, and T. L. Marzetta, “Massive MIMO is a reality—What is next? Five promising research directions for antenna arrays,” Digit. Signal Process., vol. 94, pp. 3–20, Nov. 2019.

[5] M. D. Renzo et al., “Smart radio environments empowered by reconfigurable AI meta-surfaces: An idea whose time has come,” EURASIP J. Wireless Commun. Netw., vol. 2019, p. 129, May 2019.

[6] L. Zheng, M. Lops, Y. C. Eldar, and X. Wang, “Radar and Communication Co-existence: an Overview: a Review of Recent Methods,” IEEE Signal Process. Mag., vol. 36, no. 5, pp. 85–99, Sep. 2019.

[7] S. Chen, J. Hu, Y. Shi, Y. Peng, J. Fang, R. Zhao, and L. Zhao, “Vehicle-to-everything (V2X) services supported by LTE-based systems and 5G,” IEEE Communications Standards Magazine, vol. 1, no. 2, pp. 70–76, 2017.

[8] V. S. Asadchy, M. Albooyeh, S. N. Tcvetkova, A. Díaz-Rubio, Y. Ra’di, and S. A. Tretyakov, “Perfect control of reflection and refraction using spatially dispersive metasurfaces,” Phys. Rev. B, Condens. Matter, vol. 94, Aug. 2016, Art. no. 075142.

[9] C. Sturm and W. Wiesbeck, “Waveform Design and Signal Processing Aspects for Fusion of Wireless Communications and Radar Sensing,” Proc. IEEE, vol. 99, no. 7, pp. 1236–1259, July 2011.

[10] X. Song, S. Haghighatshoar and G. Caire, ”A Scalable and Statistically Robust Beam Alignment Technique for Millimeter-Wave Systems,” in IEEE Transactions on Wireless Communications, vol. 17, no. 7, pp. 4792-4805, July 2018, doi: 10.1109/TWC.2018.2831697.

[11] X. Tan, Z. Sun, D. Koutsonikolas, and J. M. Jornet, “Enabling indoor mobile millimeter-wave networks based on smart reflect-arrays,” IEEE Conference on Computer Communications (IEEE INFOCOM), pp. 270–278, April 2018.

[12] Ö. Özdogan, E. Björnson and E. G. Larsson, ”Intelligent Reflecting Surfaces: Physics, Propagation, and Pathloss Modeling,” in IEEE Wireless Communications Letters, vol. 9, no. 5, pp. 581-585, May 2020, doi: 10.1109/LWC.2019.2960779.

[13] A. Daz-Rubio, V. Asadchy, A. Elsakka, and S. Tretyakov, “Metasurfaces for perfect control of reflection,” in 2017 International Workshop on Antenna Technology: Small Antennas, Innovative Structures, and Applications (iWAT), March 2017, pp. 3–5.

[14] J. Fortuny-Guasch, J. Chareau,”Radar Cross Section Measurements of Pedestrian Dummies and Humans in the 24/77 GHz Frequency Bands,” JRC Scientific and policy reports, EU 2013.

IPG CarMaker Plug-In Controller Based Automated Vehicle Simulation Using Malaysian Environment

Vimal R. Aparow, Cheok J. Hong, Ahmad M. H. Ismail, Tomas H. Maul

***Abstract*—**In most of developing counties, high traffic intensity causes road traffic accidents which increases the damage to the society and lead to injuries or even deaths. Based on statistics analysis by Malaysian Institute Road Safety and Research (MIROS), most of the vehicle crash fatalities are due to run-off-road incidents and driver failure to avoid obstacles in front of them. This issues mainly happen in near collision situation where the driver fails to provide required steering inputs to avoid the collisions or delay in providing the braking inputs. Therefore, autonomous vehicle using advanced driver assistance system called Autonomous Emergency Braking, Adaptive Cruise Control, Lane Keeping Assist System were developed by automotive developers to overcome the shortcomings. These systems are activated based on the need and emergency to avoid the road accidents. However, a proper virtual simulation testing is required to evaluate the effectiveness of the ADAS system based on the environment, in this case is Malaysian road and traffic environment. Therefore, this research is focused on the evaluation of the autonomous vehicle in virtual testing platform using selected Malaysian road and traffic environments. Meanwhile, 2nd Malaysian national, Myvi vehicle is designed as the autonomous vehicle model for this evaluation which is equipped with 4 camera sensor modules.

***Keywords*—**Camera sensor, autonomous vehicle, IPG CarMaker, Malaysian Road and Environment, Perodua Myvi.

I. Introduction

IT has been reported that road traffic injuries has resulted in the death of about 1.2 million people each year around the world and this shows that road traffic accident is becoming one of the serious social problems [1]. Meanwhile, Malaysia has been recorded as one of the top countries with the highest rate in accidents and death. The World Health Organization (WHO) [2] indicates that Malaysia is one of the emerging countries with the hazardous roads after Thailand, Indonesia and South Africa which are prone to the road accidents [3]. Based on this report, it is noted that road accident is a major cause of death and injuries to humans in Malaysia. Meanwhile, a statistics report issued by the Malaysian Institute of Road Safety Research (MIROS) and Polis Di Raja Malaysia (PDRM) between the 2010 until 2018 shows a significant increase in the number of road traffic crashes, from 414,421 cases to 548,621 cases [4]. Moreover, the total death cases resulted from road accidents approaches more than 6000 every year. Based on statistical analysis, there are three major factors contributing to road crashes, namely human, vehicle's performance as well as road and environment have been identified [5]. Additionally, various studies have revealed that driver factor accounts for over 80% of all fatal and injury cases, thus prompting human-related issues to gain traction among the research fraternity [6].

Rear-end and forward collisions are responsible for a large number of crashes in most of the countries. These types of road accidents normally occurred at speed up to 30-50 km/h in city traffic conditions in most of the developing countries [7]-[9]. One of the main contributing factors to traffic accidents could be that the distance between the two vehicles are too close while traveling. In the phase of non-free flow driving conditions, most of the drivers always avoid from being lag the preceding vehicle and try to follow as close as possible [10]-[13]. However, most drivers are oblivious of vehicle safety where collision could take place if the driver is unable to provide the required brake torque if the front vehicle suddenly stops. If there is enough safe distance between two cars, the driver of the following vehicle will have enough time to respond based on the speed changes of the front vehicle. Then, the driver can implement emergency measures when the vehicle ahead suddenly brakes [10], [11]. Meanwhile, the other contributing factor is the driver's incorrect judgment for braking safety distance because they cannot estimate the suitable distance between their cars from the front car. Due to these factors, they could not take immediate action. Another factor of the collision is the road and environmental effect, such as raining or slippery road that can affect the braking performance of the vehicle which is unable to maintain a safe distance. It can be observed that a proper safety testing platform is highly required to investigate the performance of an autonomous vehicle before deploying in developing countries, such as Malaysia. In order to overcome these drawbacks, an adequate virtual testing platform is required before deploying autonomous vehicle in Malaysia. The testing platform should have focused on five important elements such as vehicle dynamics model, road network model, traffic conditions, sensor modules and control algorithm. Therefore, this project is focused on the development of a testing platform for safety assessment of autonomous vehicles within a virtual environment using Malaysian road and vehicle model. The testing platform that is aimed to be developed can be used to supervise autonomous vehicles to adapt on Malaysian roads and traffic scenarios and also to evaluate the capability of an autonomous vehicle to perform emergency braking and obstacles avoidance autonomously to minimize road accidents. Thus, in this study, IPG CarMaker is used as the platform to develop the safety testing procedure for autonomous vehicle using Malaysian road, vehicle dynamic, traffic and sensors configuration. The controller design using Autonomous Emergency Braking and Adaptive Cruise Control

Vimal Rau Aparow is with the University of Nottingham Malaysia, Malaysia (e-mail: Vimal.Rau@nottingham.edu.my).

are connected via Simulink Plug-In. Various scenarios are designed to evaluate the performance of autonomous vehicle in Malaysian virtual road.

II. CO-SIMULATION IPG CARMAKER WITH SIMULINK

In this study, co-simulation between IPG CarMaker and Simulink is configured for the evaluation purposes. Therefore, a few elements need to be configured in the IPG CarMaker and Simulink to conduct the virtual testing. Firstly, the model configuration between IPG CarMaker and Simulink Plug-In is ESTABLISHED IN ORDER THE CO-SIMULATION CAN BE PERFORMED. THE controller for the autonomous vehicle such as AEB and ACC is developed using the Simulink Plug-In. Then, environment model is designed based on selected road network in Malaysia and 2nd national vehicle model is configured in the IPG CarMaker. As for the sensor modules, camera sensor and object sensor modules are selected for the obstacle detection. Then, the traffic objects are configured based for the test cases. The detail explanation is given in the following section.

A. IPG CarMaker Simulink Plug-In

There are few methods that can be used to develop model integration between IPG CarMaker and 3rd party tool for co-simulation process. One of the methods that used in this study is using CarMaker for Simulink (CarMaker4SL). This method is known as the approach that implement the CarMaker fully in the Simulink allowing researchers to integrate models directly on Simulink level. However, executing the virtual testing for many variations of test cases using both Simulink and IPG CarMaker required high computational time and this will slow down the simulation process. Thus, IPG CarMaker Simulink Plug-In is used in this study.

The connection between IPG CarMaker and Simulink can be established by creating the CarMaker Plug-In model as shown in Figure 1. Figure 1 shows the configuration to setup the plug-in whereby the model is created by assigning the model type which is “VehicleControl” and create the model name as “ACC_AEB” to represents as longitudinal control for both Adaptive Cruise Control and Autonomous Emergency Braking system. Once the template is created, the a few important input and output ports are identified using the “IF_In_Selector” and “IF_Out_Selector” where the output ports will be connected back to the IPG CarMaker as shown in Figure 2.

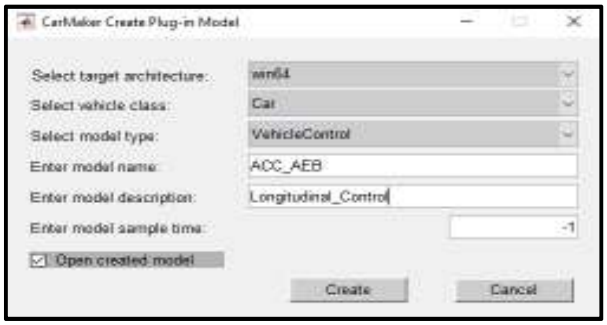

Fig. 1 CarMaker Create Plug-in Model

Once the required inputs and output ports are selected, the ACC and AEB control algorithm is developed which will be explained in following sections. Then, the template will be “Build” through the Simulink Coder. During the build process, the model will be added to the current project’s source code. Then, a new executable CarMaker file is generated where this file is located at the “src folder”. The executable file need to be apply in the IPG CarMaker’s Application section. Then, the newly build template model can be extracted at the “Vehicle Control” section by selecting the template name “ACC_AEB”.

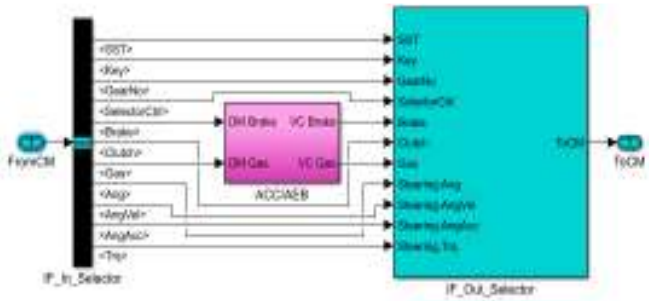

Fig.2 ACC_AEB model template

B. Vehicle Control Configuration

In this study, longitudinal controllers are explored to implement the speed control using ACC and distance control using AEB as shown in Figure 3. The ACC model is used mainly to control the vehicle longitudinal speed based on desired set speed or reference with front vehicle speed to maintain the gap between the ego-vehicle and traffic vehicle. It controls the longitudinal acceleration of the vehicle by changing the position of the brake and gas pedal. If ACC is deactivated there is no manipulation of the pedal position by the controller. The controller distinguishes two cases such as

(a) If there is no target detected, the velocity will be controlled.

(b) If there is a relevant target detected, the distance will be controlled.

Meanwhile, the AEB system is used to produce required brake to halt the ego-vehicle to avoid vehicle rear-end collision and frontal accidents during pedestrian crossing. The AEB is activated if the obstacle is detected suddenly in the sensor range and decelerate safely the ego-vehicle to the velocity of the target object ahead. In order to activate the AEB system, it compares the time-to-collision with a time-threshold-brake to decide if a braking intervention is required.

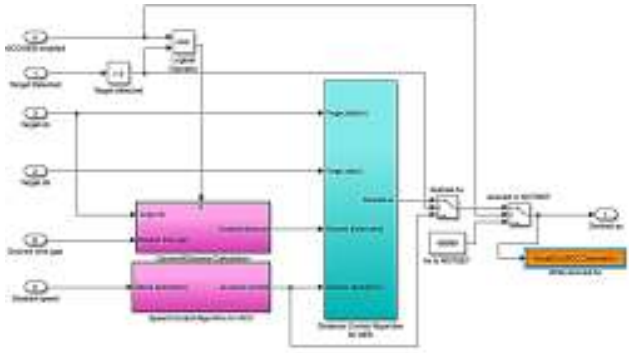

Fig. 3 ACC and AEB activation control mode

For the ACC control module, object sensor module is used as the feedback inputs to control the throttle input for the vehicle. Meanwhile, for the AEB, the feedback from camera sensor which is placed at the dashboard mirror is used to identify the obstacles. The ACC and AEB controllers are designed in Simulink using sensors information as the inputs. After processing the information, the controllers provide control signal to the IPG CarMaker's GUI through the CarMaker Plug-In model. The developed controller is interface under "VehicleControl" mode in order to actuate the ego-vehicle in terms of throttling or braking responses as shown in Figure 4.

Fig.4 Controller integration using Plug-In Mode

C. Vehicle dynamic configuration

Vehicle dynamic configuration plays an important role in developing the virtual testing platform for autonomous vehicle. In this virtual testing process, Malaysian 2nd national vehicle, Perodua model called Myvi 1.3L X model using Automatic Transmission gearbox system is used as the ego-vehicle as shown in Figure 5. In the vehicle model configuration, the powertrain, steering, brake and suspension systems are updated based on the actual vehicle.

(a) Actual Myvi Vehicle

(b) Virtual Myvi vehicle model

Fig. 5(a). Actual Myvi Vehicle; Fig. 5(b). Actual and Virtual model of Perodua Myvi 1.3L X

Based on actual vehicle configuration, this ego-vehicle model is configured in the IPG CarMaker starting with the powertrain system. The driveline for this vehicle is front wheel drive with engine model based on conventional ICE with maximum torque of 4200 Nm. The brake system is using the conventional hydraulic brake meanwhile the steering configuration is configured using electronic power steering system. The tire and wheel configuration are 185/55 R15 and the front suspension is designed using MacPherson Strut while the rear suspension is designed using Torsion Beam type. In terms of steering system, Electronic Power Steering (EPS) configuration is used for the vehicle model based on steering mechanism.

D. Sensor module configurations

Sensor module selection and configuration is one of the crucial elements in developing autonomous vehicle using virtual testing platform. Sensor modules used to measure the behavior of the vehicle responses and gather surrounding information which will be used as the input for the controller development stages. Various types of sensor modules have been included in IPG CarMaker for the virtual testing purposes. However, most crucial sensor modules have been implemented in the ego-vehicle due to the cost of implementation in real life vehicle. In order to measure the lateral and longitudinal behavior of the ego-vehicle, inertial and slip angle sensor module have been used in the vehicle. These sensor modules are implemented at the center of gravity (CG) of the ego-vehicle. Meanwhile, the road sensor is used to obtain the desired travel path of the ego-vehicle inside the campus. This path information is used in the Matlab Simulink for localization of the ego-vehicle before initiating the simulation and also to provide the desired steering angle, throttle and brake responses to the ego-vehicle.

Meanwhile, other sensor modules have been selected and configured for the ego-vehicle by considering the real-life cost implementation. Based on that consideration, a few sensors have been selected. Firstly, object sensor is used in the ego-vehicle to use as a radar sensor. This sensor is used to detect the speed of frontal vehicle which is used in the development of ACC system. The Object sensor provides object list with quantities for each traffic obstacle relative to the view of the sensor. The object sensor provides observation area, position and orientation of the traffic object relatives to the to the sensor view. Next, one camera sensor module has been placed at the dashboard reverse mirror to capture the scenario through the frontal wind screen. Meanwhile, two camera sensor modules have placed at the side mirror to detect the obstacles in the blind spot region. These sensors mainly used to detect pedestrians, cyclist and motorbike users approaching towards the ego-vehicle from blind spot region, especially in urban area driving. The configuration of the sensors for the Myvi vehicle model is shown in Figure 6.

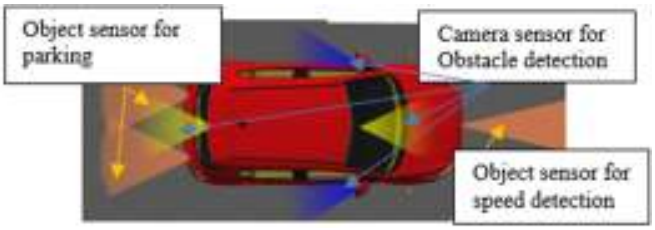

Fig. 6. Sensor configuration for Myvi

III. Scenario Identifications

In this study, urban area of driving has become one of the crucial area due to large number of road users. In Malaysia, there are many locations populated with large numbers of road users whom depends on the public transportation, using pedestrians walk way, cyclist and motorbikes. Therefore, it is quite crucial to test autonomous vehicle in location with large numbers of road user. In this study, a few locations have been identified for the testing such University of Nottingham Malaysia Campus's pedestrian zebra crossing, car parking area nearby the shopping mall area, housing area near campus locations and shop lots area. The details of the locations are described in the following sub-section.

A. Location A: Inside University of Nottingham Malaysia

This location has been selected as one of the priority area to test the performance of ego-vehicle because this location is highly populated with road users such as pedestrians (undergraduate and postgraduate students, workers and etc), cyclist and e-bike scooters, motorbikes and vehicles. The location of the zebra crossing inside University of Nottingham Malaysia is shown in Figure 7. This zebra crossing is nearby to the main guard house of the campus which is also connected pathway to the Trent Building of the campus.

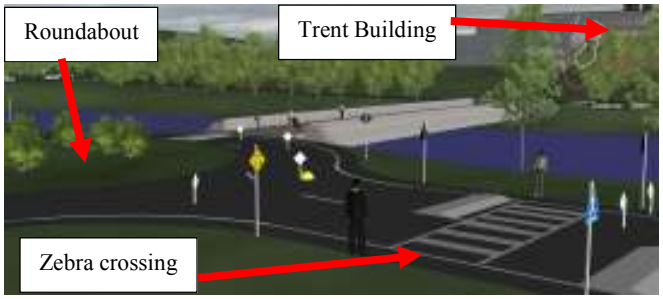

Fig. 7 Zebra crossing in University of Nottingham Malaysia

B. Location B: Car parking area

Location B is focused at the car park nearby the shopping lot area. This location is located at the Jalan Semenyih area opposite the Tesco building. This is one of the important aspects need to be considered for the testing because of the pedestrian movement to the shop lots. This area also will be encountered with vehicle driving out or driving into the parking area. Therefore, this location is selected as one of the testing areas for ego-vehicle as shown in Fig. 8.

Tesco mall

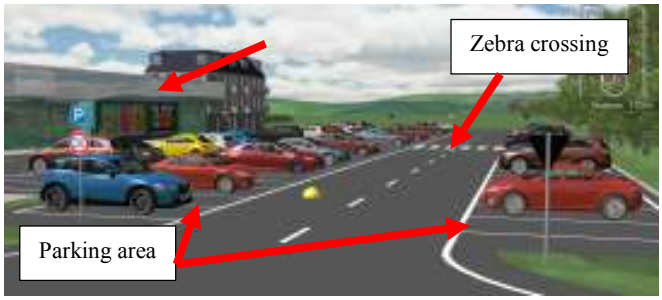

Fig. 8 Car Parking area nearby shopping lots

C. Location C: Housing area

Housing area is one of the important scenarios need to be focused since this area could be one of potential area to deploy ego-vehicle, especially as the public transportation in urban cities. Therefore, it is very crucial to test in this area since this location is highly populated with pedestrians such as kids playing outside of their housing area. The pedestrian's movement will be very random since their moving pattern is scattered around this housing area and quite unpredictable. Figure 9 shows the housing area for based on the housing area located nearby the University of Nottingham Malaysia campus.

Fig. 9 Housing area nearby to university campus location

D. Location D: Shopping mall area

This last location focusing on the shopping mall area located at Jalan Semenyih area as shown in Fig. 9. This location also consists of other buildings such as restaurants and groceries shops. Therefore, a lot of road users such as pedestrians (with various ages), motorbikes and cyclist moving in this location. Thus, this location become one of the critical areas to investigate the performance of an ego-vehicle.

Fig. 10 Shopping mall area with other shop lots

IV. Test Case Development

As part of the test case development, this study focused mainly on performance evaluation of an ego-vehicle in urban cities which involve more road users such as pedestrians, cyclist and motorbikes. The performance of the ego-vehicle is

evaluated based capability to identify the dynamic obstacles (road user motion) in the vehicle path and respond based on the nearest obstacle in the path of the autonomous vehicle. The ego-vehicle should be able to reduce the vehicle speed and maintain the safest gap between road users and ego-vehicle to avoid road accidents. Therefore, a few road users have been defined as the traffic objects using the traffic module in IPG CarMaker as shown in Figure 11. The details of the type of road users, starting point, speed of the road users (walking, running or static) and the trajectory path. This information will be projected during the simulation process.

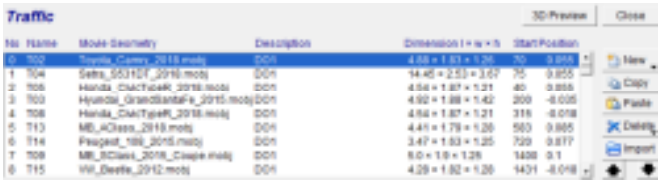

Fig. 11 Road user's behavior configuration using traffic module

V. Simulation Testing

In this section, a complete simulation testing for all four scenarios have been conducted. All the scenarios have been tested with various obstacles (dynamic or static) to evaluate the behavior of ego-vehicle react to the environment while driving in these locations. The details for each scenario are explained in the following section.

A. Test Case 1: Pedestrian and E-Scooter Crossing

In the first test case, the behavior of the ego-vehicle is evaluated while driving inside University of Nottingham Malaysia as shown in Figure 12. The ego-vehicle is driving inside campus at maximum speed of 15 km/h to 20 km/h. In this stage, the ego-vehicle is following the desired speed based on the frontal vehicle and at the same time, the ego-vehicle able to maintain the shortest stopping distance to avoid the accidents with road users nearby the zebra crossing area. It can be observed the camera vision sensor able to capture the dynamic and static objects. The static object information in terms of object ID and trajectory profile is provided to the AEB controller. Based on this information, the AEB controller provide the control signal to brake system once detect the obstacles near in ego-vehicle's path.

Fig. 12 Test Case 1 inside campus

B. Pedestrian Jay-Walking at Zebra Crossing

In the second test case, the ego-vehicle is driving in the car park area nearby the Tesco building as shown in Figure 13. In this test case, a jay-walking pedestrian is walking across the road to move towards the building. Once observe the sudden appearance of the dynamic obstacle, the ego-vehicle will change the driving model from ACC to AEB controller and apply sudden brake to maintain the safest distance to avoid hitting the pedestrian. In this case, the dynamic obstacle (pedestrian) was walking from the hidden area (unable to locate the dynamic object). Thus, the ego-vehicle has to apply sudden brake instead of applying slow response braking using ACC.

Fig. 13 Test Case 2 nearby the Tesco area

C. Pedestrians(kids) random Jay-Walking at Housing Area

For the third test case, random Jay-Walking by pedestrians is explored as shown in Figure 14. The pedestrian in this test case is the kids playing in front of the housing area. The motion of these types of pedestrians are set to be random movement (running or walking) to observe the response of the ego-vehicle to maintain safest distance and at the same time does not increase the vehicle speed since this area is housing area. It can be observed that in this test case, the ego-vehicle minimize the speed up to 10 km/h only to avoid any road casualties until the path is cleared from the pedestrian's movement.

Fig. 14 Test Case 3 Housing area nearby campus

D. Pedestrian random Jay-Walking at Shopping Mall

In the last test case, the ego-vehicle is evaluated at the shopping mall area which is surrounded by other shopping lots. Generally, this location is selected as one of the test case location because most of the time this area is crowded with people whom working in the mall, or people who would like to go for shopping or for dining. The ego-vehicle performance needs to be tested in this location since a lot of random road user's movement can be observed in this location with different ages (adult and kids). In this type of situation, the ego-vehicle should maintain the driving speed not more than 20 km/h to 25 km/h only to avoid unwanted road casualties and the controller should be ready for switching from ACC to AEB mode to halt

the vehicle.

Fig. 15 Test Case 4 nearby the shopping mall

VI. Simulation Analysis

From the simulation, it can be observed that the ego-vehicle operates in the range of 15 km/h to 40 km/h only depending on the location and involvement of road users in a particular area. From the simulation analysis, it can be noted that the ego-vehicle minimized the vehicle speed in the housing area, campus and shopping mall area since these locations are highly populated with road users with different kind of ages. The AEB controller reacts based on object ID and its classification based on road user's trajectory profile. This prediction is mainly required to predict the movement of road users towards the ego-vehicle's driving path. Table 1 shows the comparison of vehicle speed and shortest distance maintain each time the ego-vehicle encounter with road users.

TABLE I Automated Vehicle Performance Comparison

Scenario	*Initial Ego-vehicle speed*	*Type of obstacle*	*Road user trajectory pattern*	*Road user maxi mum speed*	*Distance between Ego-vehicle and nearest dynamic object*
Test Case 1	15.5 km/h	Pedestrian	Lateral movement	7.6 km/h	1.5 meter
		Traffic Vehicle	Longitudinal motion	20 km/h	1.3 meter
Test Case 2	23.2 km/h	Pedestrian	Lateral movement	8.2 km/h	0.76 meter
Test Case 3	13.8 km/h	Pedestrian	Random movement in lateral & longitudinal	4.8 km/h - 5.3 km/h	1.67 meter
Test Case 4	25.2 km/h	Pedestrian	Random movement in lateral & longitudinal	4.8 km/h - 8 km/h	1.24 meter
		Traffic Vehicle	Longitudinal motion	25 km/h	1.47 meter

VII. Conclusion

As a conclusion, it can be noted that Simulink Plug-In controller based automated vehicle can be used to test the ego-vehicle performance in urban areas. The ego-vehicle is tested in various location which involve random movement of road users. These types of scenarios are very important to be used as the test cases to evaluate the performance of an automated vehicle before can proceed with on-road testing. This is mainly to verify the validated of the controller performance of ACC and AEB to adapt with urban city environment in developing countries such as Malaysia.

Acknowledgment

This work is the preliminary work on testing performance of automated vehicle in selected areas in Malaysia. This work is supported by the University of Nottingham Malaysia through faculty funding for purchasing the vehicle dynamic simulation tool namely IPG CarMaker. I also would like to thank the Head of Department Electrical and Electronics, Mr Anandan Shanmugam for his continuous support to conduct research in the department. This financial and moral support are gratefully acknowledged.

References

[1] N.I. P. Jabo, *Safety distance awareness system for Malaysian driver*, (Doctoral dissertation, Universiti Tun Hussein Onn Malaysia), 2013.

[2] World Health Organization, Global status report on road safety: time for action, 2017, Gevena.

[3] A.S. M. Nasir, H.H. Husainizam, N. S. Halim, A. I. Malek, and A. H. Malek, "Modelling road accidents in Malaysia," *ESTEEM Academic Journal*, 14, pp.66-76, 2018.

[4] PDRM, *Laporan Tahunan PDRM* (Royal Malaysia Police Annual Report (2018). Royal Malaysia, Police, Ed. Kuala Lumpur, Malaysia.

[5] M.S. Solah, A. Hamzah, A.H. Ariffin, N.F. Paiman, I.A. Hamid, M.A. Wahab, Z.M. Jawi, and M.R. Osman. "Private vehicle roadworthiness in Malaysia from the vehicle inspection perspective." Journal of the Society of Automotive Engineers Malaysia 1.3, 2017.

[6] R.W. Cuerden, M.J. Edwards, and M.B. Pittman, *Effect of vehicle defects in road accident*. (Published project report, PPR565). Berks, UK: Transport Research Laboratory (TRL), 2011.

[7] B. Canis, *Issues in Autonomous Vehicle Testing and Deployment* (No. R45985), Congressional Research Service, 2019.

[8] A.A. Provisions, *Uniform provisions concerning the approval of motor vehicle headlamps equipped with gas-discharge light sources*. Regulation No 98 of the Economic Commission for Europe of the United Nations (UN/ECE), 2010.

[9] S.S. Shadrin, and A.I. Anastasiia "Analytical Review of Standard Sae J3016 «Taxonomy And Definitions For Terms Related To Driving Automation Systems For On-Road Motor Vehicles» With Latest Updates." *Avtomobil'. Doroga. Infrastruktura*. Vol. 3, No.21, 2019.

[10] P. Zíta, *Simulation of AEB system testing, Diploma Thesis, Faculty of Mechanical Engineering*, Czech Technical University in Prague, 2017.

[11] A. Arcidiacono, *ADAS virtual validation: ACC and AEB case study with IPG CarMaker*, Doctoral dissertation, Politecnico di Torino, 2018.

[12] J. Kim, Y.J. Woo, S.Kwon, and Y. Kim, "Performance test of autonomous emergency braking system based on commercial radar." *In 2016 5th IIAI International Congress on Advanced Applied Informatics (IIAI-AAI)*, pp. 1211-1212. IEEE, 2016.

[13] H. Matthias, M. Dziennus, T. Hesse, A. Schieben, C. Brunken, C. Löper, J. Kelsch, and M. Baumann. "Interaction design of automatic steering for collision avoidance: challenges and potentials of driver decoupling." *IET intelligent transport systems*. Vol. 9, No. 1, pp. 95-104, 2014.

The Role of Synthetic Data in Aerial Object Detection

Ava Dodd, Jonathan Adams

***Abstract*—**The purpose of this study is to explore the characteristics of developing a machine learning application using synthetic data. The study is structured to develop the application for the purpose of deploying the computer vision model. The findings discuss the realities of attempting to develop a computer vision model for practical purposes, and detail the processes, tools and techniques that were used to meet accuracy requirements. The research reveals that synthetic data represent another variable that can be adjusted to improve the performance of a computer vision model. Further, a suite of tools and tuning recommendations are provided.

***Keywords*—**Computer vision, machine learning, synthetic data, YOLOv4.

I. Introduction

THE purpose of this study is to explore the question of whether machine learning can be successfully undertaken using only a machine learning computer and media that is readily available. This research attempts to understand the challenges associated with high failure rates [11] for companies seeking to implement machine learning. Some research suggests that many solutions found in the current literature are developed in simulated environments, making the results "not close enough to what is expected in real-life applications" [15]. Further, the study sought to understand whether synthetic imagery has the potential to substitute for authentic images and mitigate pervasive human labeling errors noted in research literature [5]. The project goal is to employ available resources to train YOLO4 to detect sharks, as a means to improve human-shark interactions in recreational settings.

The completed pipeline included a detailed production specification for 3D artwork, tools for managing the datasets, and potential strategies to optimize the performance of the model were investigated [19]. The synthetic images used in this study are sourced from publicly available 3D models, which are processed to create dataset of 2D labeled images, accompanied by box locations and labels for the target objects. The completed Blender/Python API was used to augment image qualities such as respective camera positions, visual, and lighting effects. After the computer vision model was trained, a series of tests were conducted to evaluate the performance of the model, strategies were explored to investigate whether the systems' accuracy could be refined.

[1] Data for Computer Vision

The volume of machine learning research has increased over the past five years, which has led to an increased availability of software, theories, and many resources for advancing machine learning systems are readily available [1]. Large public datasets such as Imagenet (image-net.org) or COCO (cocodataset.org/), have been used widely in computer vision research, but these resources do not include marine imagery that is specific to the project goals.

The Nature Conservancy and a collection of international partners have assembled a marine dataset for machine learning applications to enhance the management of fisheries. While a majority of the marine footage is captured from an aerial platform, the purpose of the database and the purpose of the project do not match. This mismatch is a problem of topical diversity within the dataset, where many examples represent one subset of activities (shark fishing) but offer few examples of other subsets of activities (sharks in recreational settings).

There are many instances where data sources do not include a sufficient number of images, with a clearly defined subject, in a variety of poses. Other factors that have limited the availability of quality imagery are privacy, the amount of time to collect data, and the cost of producing a labeled dataset [22]. Similar shortages are reported in a range of computer vision research, including work with thermal-infrared visual tracking [2] and pose estimation [3]. In more complex applications, the sheer volume of imagery needed makes machine learning nearly impossible. For example, computer vision researchers have noted that training a self-driving car to an acceptable level of performance might require the data generated by 100 cars driving 365 days per year, 24 hours, every day for 12 years to capture enough data [4].

[2] Synthetic Data

Synthetic imagery is generated by either encoding sample images using computation methods or by using animated, 3D models to generate 2D images of the subject to be identified. Examples of computation encoding methods are Generative Adversarial Networks (GANs) and Autoencoders. Such methods encode and process a collection of images and decode the data with features changes, a system that is capable of generating unique photo-realistic images based on the original samples. A GAN consists of two collaborative networks: a generator that composes an image, and a discriminator that

[1]Jonathan Adams is with the School of Information, Florida State University, Tallahassee, FL., 32306 USA (corresponding author, e-mail: jladams@fsu.edu).

evaluates the quality of the synthetic images [6]. These two networks cyclically create-and-review images, which enhances the performance of the generator until it consistently configures photorealistic synthetic images [7]. Auto encoders use a single neural network to encode or compress data into a latent space that describes the image. New features are introduced by altering weights and bias in decoding [21].

Blender is an open-source, three-dimensional modeling software with a Python application programming interface 3D animation is often used in a synthetic image pipeline [24]. A pipeline that employs this strategy starts with a human artist who creates a static model or a short, animated scene [8]. The artistic representations are manipulated using a Python script that controls rendering by using Blender's Python (bpy) interface. The processing script adjusts lighting, adds effects and positions the camera dynamically in order to quickly produce images that include a variety of scenes. The techniques are similar to what has been accomplished by other researchers using Blender [23] but do not appear to be reproduced otherwise with the Unreal game engine tools that can generate virtual worlds based entirely on synthetic imagery [9].

The pipeline developed for generating synthetic imagery has a number of related benefits. For example, the processing script can include functions that automatically capture the bounding box of the 3D model and apply an annotation. Error-free boxing and labeling by itself presents an enormous advancement in machine learning. Synthetic imagery solves other problems that plague computer vision training as well, including the ability to circumvent privacy regulations, and reduce dependency on large commercial datasets. Research has also demonstrated that using synthetic images to support training improves accuracy by as much as 10% [1], [10].

Fig. 1 Example of a synthetic image

Data management is a labor-intensive task associated with supervised machine learning. Because hundreds of thousands of images may be needed for training, data collection and management alone may take weeks or months. Once the data collection has been completed, images are segregated into sub-datasets. Then each unlabeled image must be examined and 'captured' with a bounding box and annotated with a label. This step in the process is time-consuming and is prone to human error. For example, in a recent study conducted at MIT, researchers discovered that about 6% of images contained in visual datasets are mislabeled or boxed improperly [5].

Data preparation activities lead to the accumulation of high project costs and high failure rates that have been noted to be as high as 51% for large enterprises and 74% for small enterprises [11]. Synthetic data production reduces cost, mitigates risk, dramatically reduces data management, and eliminates error in each of the data management tasks because data preparation tasks can be automated. Synthetic data offer a manner by which to circumvent issues associated with preparing data for training, thereby reducing time, effort, and risk.

[3] Unmanned Aerial Search and Rescue

The advantages of using unmanned aerial vehicles (UAVs) as a platform for computer vision have been recognized as having great potential in marine search and rescue (SAR). Oftentimes marine searches encompass areas as large as 16,000 square miles [13]. It is understandable that human fatigue plays an important mitigating factor in such situations, making it difficult to find people or crafts lost in the ocean. The use of manned aircraft is costly and oftentimes are not readily available. Remote unmanned aircraft also offer safety advantages in such operations, by reducing the number of people in the field. Most importantly, UAVs have the potential to deploy in emergencies in a shorter period of time [12].

Experiments have demonstrated effective use of aerial cameras to identify and track objects in real time [13], during daylight and night operations using thermal cameras [14]. In recent times there has been an increase in demonstration projects that use artificial intelligence. It has been noted that many recent experiments are designed in simulated environments, and as such are somewhat limited in accounting for aircraft dynamics, or environmental conditions that are likely to affect performance in real-time applications [15].

[4] Purpose of Study

This study evaluates a synthetic dataset production pipeline and reports subsequent performance testing using YOLOv4. The intention is to encompass an end-to-end process of manipulating 3D artwork, managing the training and validation dataset, and evaluating the performance of YOLOv4 when training is enhanced with synthetic data. A number of related research studies have demonstrated an increase in accuracy when training is enhanced with synthetic imagery [1]. The present research, then, focuses on the implications of establishing a synthetic data production pipeline to train a computer vision model.

The synthetic images are imported, manipulated and saved using a Python algorithm developed for the study. Two species of sharks (Great White and Hammerhead) were chosen as subjects for training. The project focuses on producing images to train YOLO to detect sharks from an aerial platform. While deployment of the algorithm is not within the scope of the study, such a system is intended to provide rescue workers the ability to avoid or manage close encounters between sharks and

people.

[5] II. PROCEDURES

While the research is focused on synthetic data, authentic images are still needed to train a computer vision model. The combination of authentic and synthetic imagery provides indistinguishable samples for the computer to learn from and strengthens predictions. Videos that featured sharks, captured from drones and helicopters, were collected from public sources. Individual frames were exported from the video at 6 frame intervals. Using this technique, 550 authentic images of Hammerhead sharks and 650 images of Great White Sharks were organized. From this pool images were set aside for testing and validation. The training and testing images were then individually labeled.

The synthetic dataset was created by rendering animated 3D models. Sharks breathe by moving through the water to keep oxygen circulating through their gills. To capture this movement with a synthetic model, an armature is added to the 3D object. An armature is composed of bones and acts as a skeleton for a model. The bones are paired with the skin of the object, called the mesh, to synchronize their movements and produce a moving model. Each time the model is set in a new position, a keyframe is set. A keyframe is a time marker that saves a place in an animation cycle where the user would like to save the objects' position. The animation that results from stringing the keyframes together makes the shark model appear to swim as the body and torso swing side to side. Lines of code were added to randomly select one of these keyframes for each render to add variation in training data.

A production specification was designed to provide a Blender artist with instructions to adjust the quality of the imagery. The processing script controlled the playback head, camera coordinates, object location, object texture, object position and lighting. The production specification detailed qualities necessary for error-free processing when the 3D model is processed. For example, the 3D object should be centered, and needs to have a base color with an added texture overlay that is bright enough to distinguish the texture from the background. The animation did not have to loop seamlessly as long as it captured the full range of motion. These specifications are optimized for training.

The processing script included several requirements, but none was more important than the camera positions. Camera perspectives are crucial for creating realistic, varied data for training an object detection algorithm. With the 3D model positioned at Blender's origin (0,0,0), the algorithm for generating equidistributed points on the surface of a sphere with regular placement was created to position the camera, to ensure adequate coverage of the object [17].

$$
\begin{aligned}
&Set\ N_{count} = 0.\\
&Set\ a = 4\pi r\text{^}2/N\ and\ d = \sqrt{(a.)}\\
&Set\ M\_\vartheta = round[\pi/d].\\
&Set\ d\_\vartheta = \pi/M\_\vartheta\ and\ d\varphi = a/d\_(\vartheta.)\\
&For\ each\ m\ in\ 0{:}\,(M\_\vartheta - 1)\ do\{\\
&\quad Set\ \vartheta = \pi(m + 0.5)/M\_\vartheta\\
&\quad Set\ M\varphi = round[2\pi sin(\vartheta/d\varphi)]\\
&\quad For\ each\ n\ in\ 0{:}\,(M\varphi - 1)\ do\{\\
&\qquad Set\ \varphi = 2\pi n/M\_\varphi\\
&\qquad x = rsin\vartheta cos\varphi\\
&\qquad y = rsin\vartheta sin\varphi\\
&\qquad z = rcos\vartheta\\
&\qquad N\_count += 1\\
&\quad \}\\
&\}
\end{aligned}
$$

Fig. 2 Algorithm for generating equidistributed points on the surface of a sphere with regular placement.

The camera orientation was adjusted to mimic video frames captured from an aerial platform. Camera positions ranged 0 to 2*π, with φ set to generate downward viewing images. Further, implementing a regular method to place the camera at different angles around the shark allowed each angle to be utilized equally. This strengthened the synthetic dataset by introducing more images that include a diverse set of poses. The complete rendering process was neatly packed in the leopardi library [20].

Once the 3D model has been rendered into a 2D image, a truth background is selected randomly from a separate directory holding several such images, and merged with the image.

Each training session in YOLO requires the training images with their corresponding annotation files, a class text file, a data file, a training file, a testing file, a configuration file, and a convolutional weight file. The class text file lists the target domains in order, so the predictions are labeled with the correct name. For this experiment, the class file only contains the shark label class. The training and validation text files each contain a list of image pathways to be fed through the neural network (NN). The configuration file sets up the NN parameters, such as the batches, subdivisions, image resizing, learning rate, and learning rate decay. The data file contains the pathway to the class, training, and test files as well as the backup directory where training weights are stored after every 100 iterations. This file is called along with the convolutional weight file to run darknet's training command.

Two YOLOv4 models were trained with the same configuration; however, one model was trained on 10000 images and the other was trained on 3000 images. This was done to evaluate whether the *quality of characteristics* contained within the imagery can improve training. In both cases, the synthetic and authentic data were mixed together, in a ratio of 10:1, for training to optimize the model's results, which is consistent with research findings [1].

Training iterations were set to match the number of images in the training dataset [16]. After training, the final weights are stored in a backup directory. These weights are used to test the model on video frames unknown to the model.

The validation set proved crucial to the mean average precision (mAP) calculation set to occur at every epoch. The last 10% of the training data proved not to be varied enough to use as a benchmark, so a script was written using the Numpy library's random sampling function. 1,000 authentic images were randomly sampled from the training pool and used as a new validation set. This change increased testing accuracy by

approximately five percent.

Training and tests were performed on a 16 core Intel i7, with 256 GB of RAM, and an NVIDIA 2080 GPU with 8GB of RAM.

[6] III. Results

The model's best weights, the ones resulting in the highest mAP, were used for testing on shark videos. Two models were trained with the same configuration; however, one model was trained on 10000 images and the other was trained on 3000 images. The learning rate was .001, the learning rate decay was .0005, the batch size was 24, and the image input size was 608x608 pixels.

The mosaic feature and batch normalization were defaulted on the YOLOv4 configuration file as well. The adversarial learning rate feature was added with a value of 0.05. A validation set of 1000 randomly sampled authentic images were used to calculate the mAP value at each epoch. In this study, the model trained on 3000 images performed better; it had a higher mAP value and reduced the number of false positive detections.

The two figures below show the training loss (blue line) and validation mAP (red line). Fig. 3 resulted from training the model on 10000 images. The loss steadily decreased; however, the mAP oscillated throughout training. Although the mAP was 97% at the end of training, the model made numerous false positive detections during the testing phase. The loss value was not a reliable way to measure the accuracy of the model, rather how well the bounding boxes fit the object, whether it was the right object or not.

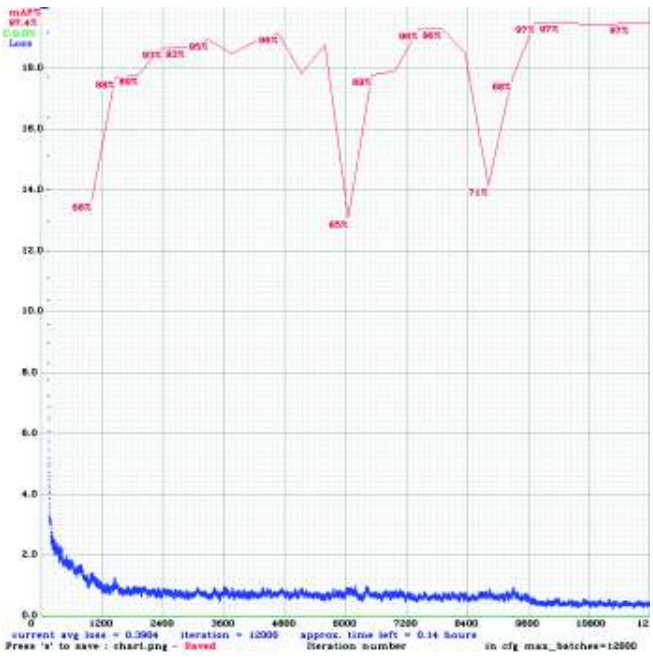

Fig. 3 Training loss and validation mAP after trained on 10000 images

Fig. 4 shows the model's loss and mAP after training the model on 3000 images. The loss value decreased more gradually when compared to Fig. 3, and the training finished with a higher loss value. The mAP values are much more stable throughout training and much higher on average, finishing training with a mAP value of 99%. There were fewer labeling errors during the testing phase with this model.

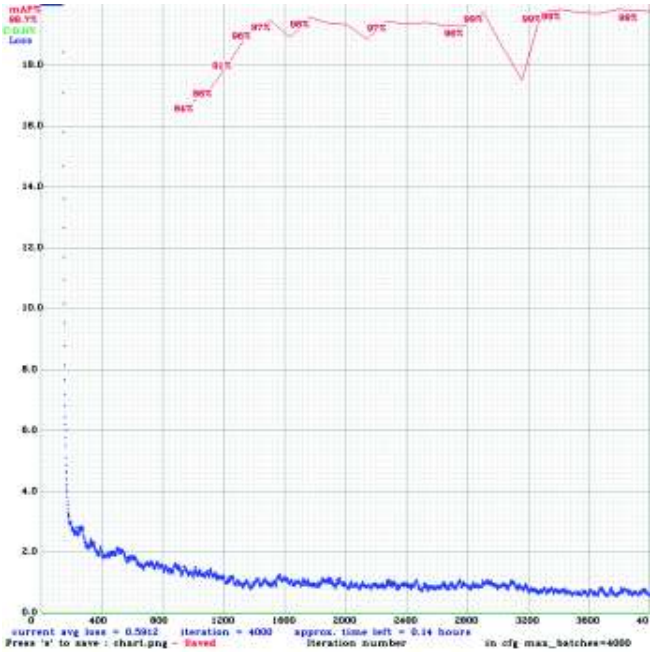

Fig. 4 YOLOv4 training loss and validation mAP after trained on 3000 images

[7] IV. Discussion

Synthetic data plays an important role in machine learning. During the course of this study, finding the "right kind" of authentic images was problematic. The synthetic imagery served to enrich the authentic data with a wide variety of poses, scale and truth backgrounds. Having the ability to produce images suitable for machine learning also allows researchers to manipulate the qualities of the data being presented to the model, and by doing so, improve the performance of the model.

At the outset, our strategy was to generate thousands of images to introduce to YOLO. However, we discovered that in reality, when training a computer vision model, more is not better. This changed the amount of time required to generate images and training substantially. Because fewer images are needed for training, training time decreased from 20 hours to 6, a substantial improvement. We have observed that presenting images that features, textures and other characteristics are enlarged appears to enhance the accuracy of the model.

To evaluate whether further performance enhancements might be achieved, YOLO's batch size, the learning rate, and the learning rate decay were evaluated. YOLOv4's Bag of Freebies was also utilized to evaluate the adversarial learning rate, label smoothing, mosaic, and DropBlock features. The results of these tests did not coincide with current research [18]. Current research literature suggests that there is also no definitive way to choose or optimize the model's hyperparameters, as the tools have been noted as being context-

sensitive, suggesting the necessity to be aware of how these hyperparameters may affect performance. This study focused on how the model's inputs affect training [19].

In the beginning of this study, it was assumed more images would result in a more accurate model due to previous studies suggesting more data would fix overfitting. However, the model appeared to overfit to the 10000-image dataset by the end of training. To remedy this, a smaller dataset composed of 3000 images was used to train the model. This resulted in a higher, more stable mAP and a model that made significantly less mistakes during testing. Therefore, the quality of the images is more important than the size of the dataset. By using synthetic data, a dataset composed of "good" data can be assembled in mere hours. The model also required less training time since there were less images to look through. Training time decreased by 30%.

[8] V. Conclusion

This study focused on creating an end-to-end production pipeline that uses synthetic data in order to speed production without sacrificing the performance of the model. The inclusion of synthetic data was key to filling in the dataset collected for the current research, thereby providing a greater variety of poses.

The 3D renders required several production cycles and tests before the media was working well with the algorithm. Once the algorithm was configured and optimized using a single 3D model, a production specification outlined how to produce the textures, lighting, and animation features for the remaining 3D models. This strategy allowed the researchers to evaluate how well the synthetic media performed based on their specific qualities. For example, it appears that synthetic images perform best when scaled up to fill a larger percentage of the image canvas. It appears that the magnification of edges and features has an impact on training, making it possible to reach acceptable performance standards with fewer images, and subsequently less time.

A set of production tools was developed that was necessary to structure and manage the training, testing, and validation datasets. It is often necessary to track different collections of images that comprise a training dataset. For example, naming conventions can be used to identify different images characteristics such as how images were sourced, quality markers, or domains. A tool is authored to rename batches of files and their accompanying annotation files. A function to translate YOLO annotations to VOC format was also developed as some datasets are managed by one labeling system or the other. Finally, another tool critical to managing datasets is a script that will segregate percentages of images into subsets for training and validation.

Finally, the researchers investigated tuning hyperparameters in order to enhance the model's performance. It should be noted that the most consistent finding in the research literature is that consistent, reliable methods to tune hyperparameters tend to be case-specific. Evaluating hyperparameter adjustments requires time-consuming training cycles and stepwise evaluation. While such adjustments are considered key to optimizing an algorithm's performance, most are considered too advanced to be practical [24]. These specifications provide data with clearly defined features and edges with specific use cases in mind. For this study, the camera angle was a crucial variable because there were a limited number of shark images taken from an aerial perspective. Using synthetic data also provides more opportunity for variety in a shorter amount of time than collecting real data. Synthetic imagery fills in the gaps where authentic imagery is insufficient in a variety of poses. Capturing images of animals is much more difficult than inanimate objects because there is more variety in body positions, and they are able to interact with their environment.

This study focused on optimizing input data to minimize overfitting and build confidence. The input data determine how "good" a model will be when tested in the field. A model must be able to generalize well, so it does not underperform beyond lab testing. Synthetic data are the solution to the lack of available, clean data for machine learning.

VI. Limitations

This study is limited by many factors. There are a limited amount of aerial shark images and videos. Many of the authentic images that are available are too small, where many examples of visible sharks underneath the surface of the water were 16x16 pixels or smaller in size. The researchers used public video to source training samples, therefore, many of the authentic images extracted from video feeds had similar qualities (i.e., background, textures, color). This has the benefit of extracting the full range of motion of the sharks but has the disadvantage of the training and validation sets containing video frames that look very similar.

Acknowledgment

The authors graciously thank Arcvale for providing expertise on three-dimensional rendering and specifications. We also thank Florida State University for providing laboratory space for conducting this research.

References

[9] J. Adams, E. Muphy, J. Sutor, A. Dodd. "Assessing the qualities of synthetic visual data production." Proceedings of the ICIET 2019: 7th International Conference on Information and Education Technology Okayama, Japan March 27-29, 2021, Association for Computing Machinery New York NY United States, 2019.

[10] L. Zhang, A. Gonzalez-Garcia, V.J. Weijer, M. Danelljan, M., & F. S. Khan, "Synthetic data generation for end-to-end thermal infrared tracking." *IEEE Transactions on Image Processing,* vol. 28 no. 4, pp. 1837-1850. 2019.

[11] A. R. Khadka, M. Oghaz, W. Matta, M. Cosentino, P. Remagnino, V. Argyriou, "Learning how to analyse crowd behaviour using synthetic data." in *CASA '19: Proc. of the 32nd Int. Conf. on Comp. Animation and Social Agents,* Paris, France, July 2019, p 11-14

[12] N. Kalra, S. M. Paddock, "Driving to safety: How many miles of driving would it take to demonstrate autonomous vehicle reliability?" in *Transportation Research Part A: Policy and Practice,* vol. 94, RAND Corporation Santa Monica, CA. 2016, pp. 182-193,

[13] C.G. Northcutt, A. Athalye, J. Mueller, "Pervasive label errors in test sets destabilize machine learning benchmarks." Preprint in review. Retrieved June 1, 2021 from https://arxiv.org/pdf/2103.14749.pdf.

[14] T. Xu, P. Zhang, Q. Huang, H. Zhang, Z. Gan, X. Huang, X. He, "AttnGAN: Fine-Grained Text to Image Generation with Attentional

Generative Adversarial Networks," *IEEE/CVF Conference on Computer Vision and Pattern Recognition*, Salt Lake City, UT, USA June 2018. pp. 1316-1324.

[15] Google Developers (2019, October 08). Overview of GAN structure | Generative Adversarial Networks. Retrieved Jan. 10, 2021, from https://developers.google.com/machine-learning/gan/gan_structure

[16] K. Lee, D. Moloney, "Evaluation of synthetic data for deep learning stereo depth algorithms on embedded platforms." *4th International Conference on Systems and Informatics (ICSAI),* Hangzhou, China, Nov. 2017.

[17] W. Qiu, F. Zhong, Y. Zhang, S. Qiao, Z. Xiao, T. S. Kim, Y. Wang, "UnrealCV: Virtual worlds for computer vision." In: Hua G., Jégou H. (eds) *Computer Vision – ECCV 2016 Workshops*. European Conference on Computer Vision, Lecture Notes in Computer Science, vol. 9915.pp. 909–916.

[18] P. S. Rajpura, M. Goyal, H. Bojinov, R. S. Hegde, "Dataset Augmentation with synthetic images improves semantic segmentation." In Rameshan R., Arora C., Dutta Roy S. (eds) *Computer Vision, Pattern Recognition, Image Processing, and Graphics.* NCVPRIPG 2017. Communications in Computer and Information Science, vol 841. Springer, Singapore.

[19] A. Komarraju, "Unfortunately, commercial AI is failing. Here's why." In *Analytics Insight: Artificial Intelligence Latest News,* Feb. 13, 2021. Retrieved June 5 2021, from https://www.analyticsinsight.net/unfortunately-commercial-ai-is-failing-heres-why/

[20] S. Yeong, L. King, S. Dol, "A review on marine search and rescue operations using unmanned aerial vehicles." *International Journal of Marine and Environmental Sciences*, vol 9, no 2, pp 396 – 399, 2015.

[21] P. Nousi, I. Mademlis, I. Karakostas, A. Tefas and I. Pitas, "Embedded UAV real-time visual object detection and tracking," *2019 IEEE International Conference on Real-time Computing and Robotics (RCAR)*, pp. 708-713, 2019.

[22] C. Burke, P. R. McWhirter, J. Veitch-Michaelis, O. McAree, H. Pointon, S. Wich, S. Longmore, "Requirements and limitations of thermal drones for effective search and rescue in marine and coastal areas." *Drones*. Vol. 3 no. 4, 2019.

[23] F. A. de Alcantara Andrade, A. Reinier Hovenburg, L. Netto de Lima, "Autonomous unmanned aerial vehicles in search and rescue missions using real-time cooperative model predictive control." *Sensors.* 21 no. 4, Sep 20, 2019.

[24] A. B. Alexey, "Darknet." Unpublished. Retrieved on June 12, 2021 from https://github.com/AlexeyAB/darknet/blob/master/README.md.

[25] M. Deserno, How to generate equidistributed points on the surface of a sphere. Unpublished. Sept. 28 2004, Retrieved on Jan. 18, 2021 from https://www.cmu.edu/biolphys/deserno/pdf/sphere_equi.pdf.

[26] F. Hutter, H. Hoos, K. Leyton-Brown, "An efficient approach for assessing hyperparameter importance." In ICML, pages 754–762, 2014.

[27] Yu, Tong, and Hong Zhu. 2020. "Hyper-parameter optimization: A review of algorithms and applications." http://search.ebscohost.com.proxy.lib.fsu.edu/login.aspx?direct=true&db=edsarx&AN=edsarx.2003.05689&site=eds-live&scope=site.

[28] Sutor, J. (2021, May 25). *johnsutor/leopardi*. GitHub. https://github.com/johnsutor/leopardi.

[29] P. Baldi, "Autoencoders, Unsupervised Learning, and Deep Architectures." in *Proceedings of Machine Learning Research.* Proceedings of ICML Workshop on Unsupervised and Transfer Learning, vol. 27 pp. 37-49, 2012.

[30] K. Mason, S. Vejdan, S. Grijalva, "An 'On the Fly' Framework for Efficiently Generating Synthetic Big Data Sets" *IEEE International Conference on Big Data (Big Data),* pp. 379-338, 2019.

[31] S. Reitmann, L. Neumann, B. Jung, "BLAINDER-A Blender AI Add-On for Generation of Semantically Labeled Depth-Sensing Data." *Sensors.* 21, no. 6, Mar 18, 2021.

[32] L. Li, "Why Does No One Use Advanced Hyperparameter Tuning?" *Determined AI.* Oct. 08, 2020, Retrieved from https://www.determined.ai/blog/why-does-no-one-use-advanced-hp-tuning

Robust Keypoint Detection with Contrastive Learning and Compositional Modeling

Anonymous

***Abstract*—**As one of the tasks in deep learning, keypoint detection has many applications and it is essential for autonomous driving. For keypoint detection, it could be divided into two approaches based on the usage of an object's spatial constraints. One approach leverages spatial constraints among all the keypoints to make final prediction, but it is easily affected when some of the keypoints are occluded. The other approach doesn't use any spatial constraints in order to make it robust under occlusion. However, the latter one does not perform so good under occlusion as it assumes, because after getting rid of spatial geometry of an object, position of one keypoint may get attracted to another location if two places share similar textures. To get over this problem, based on a keypoint detection structure "CoKe", which uses contrastive learning and does not concern any spatial relations, this paper combines CoKe with Compositional model, adding a soft spatial constraint to the model. The result shows that such intermediate combination performs on par with previous models without occlusion, and performs much better under stronger occlusion.

***Keywords*—**Compositional model, deep learning, keypoint detection, occlusion.

Haoyuan Deng is with the Beijing University of Posts and Telecommunications, China (e-mail: ccdv2@bupt.cn).

Physical Modelling of 1-D Liquefaction Tube with Cyclic Load to Understanding Mechanism of Flow Liquefaction on Palu Mw 7.5 Earthquake 2018

Dandung Sri Harninto

***Abstract*—** The Palu Mw 7.5 earthquake on 28 September 2018 significant building damage a tsunami caused by a submarine landslide, and also large-scale flow liquefaction. In one of area affected, flow movement was more than 100 meters and in other areas exceeded 1,000 meters. Such large flow distances imply unusual geological conditions. The geological formations below Palu city are related to a young alluvial fan from mountains to the west of the city. The formation is dominated by loose non-cohesive material, and fully saturated due to the very shallow ground water table. Sedimentation has formed layers with variety of density and hydraulic properties. Moreover, weathering has modified the materials and could be responsible for forming a series of layers with low permeability referred to locally as silt seams. In order to determine influence of the presence of silt seam layers, 1-D liquefaction physical modeling has been built to knowing behavior of developing build of excess pore water pressure and its released. Two meters transparent tube with 14-cm diameter was filled with fully saturated loose sand with several combination of silt seam layer has been liquefied by series of cyclic load. This research has been accomplishment to learn mechanism void re-distribution/water film phenomena beneath each silt seam layers, which probably become the most factor such a big flow liquefaction occurred on site just after shaking ceased. This research will also analysis of effective stress approach to explore mechanism of flow liquefaction occurred.

***Keywords*—** 1-D physical modelling, effective stress, liquefaction, Palu earthquake, silt seam layers.

Dandung Sri Harninto is with the Indonesia University, Indonesia (e-mail: dandung.sri@gmail.com).

Gas Behavior Modeling Inside the Drilling Wellbore by Accounting for Taylor Vortices and Real-time Parameters: Adjusting the Traditionally Used Single Bubble Model

Z. Al Marhoon, Saudi Aramco; H. Al Ramis, University of Oklahoma.

Abstract

The first step toward an accountable drilling operation is ensuring the safety of the people at the wellsite, especially the rig floor crew. Well control response is a shielding measure that takes place to protect the lives of people in the case of unplanned flow. Gas kicks are one of the major concerns in well control because of the expanding gas. The most used model for gas well control is the single bubble model. This model has been used historically to estimate the pressure surrounding the kick system to enable circulating out the kick. The purpose of this paper is to expand the study of the single bubble model by accounting for parameters and physical phenomena that are not usually included in this model. This will allow for a larger operational window with the latest technologies that were not possible before the model was established. The research process started with quantitative data analysis of kicks in an industry-grade well. The well was 6,000 feet in depth and 5 1/2 inches in diameter (width). An enhanced model of the kick migration to the surface was applied by accounting for variations of operational parameters such as well inclination, drilling fluid rheology, and kill rates. The results were validated with the literature. The second phase of the research explored the effect of the physical phenomenon of Taylor vortices. The Taylor effect describes a pattern of fluid flow in between two cylindrical pipes (drilling pipe and the casing). The presence of Tylor vortices changes the path at which fluid flows inside the casing annulus. The activation of these vortices depends on drilling fluid density, viscosity, and the geometry of the well. The results of the VBA-based model that accounts for the above-mentioned operational parameters were in agreement with previous literature on single bubble model research. The behavior of the gas migrating up the well was less likely to behave as a single bubble. The gas was shown to break down throughout the depth of the well depending on the pressure targeted point. The level gas dispersion has an inversely proportional relationship with well inclination, mud rheology, and kill rates. Taylor vortices occur above a critical speed of drillpipe

rotation. This critical speed of rotation depends on mud density, mud apparent viscosity, and well geometry. Literature investigation on Taylor vortices on hole cleaning and kick situation simulations showed that these vortices might be aiding gas bubble breakage. All of these results suggest a combination of optimizing the gas behavior is a vertical well inclination, low mud rheology, low kill rate, and a drillpipe rotation above the critical speed.

Introduction

The single bubble model, although used in most well control methods calculations, is believed to need more accuracy. The bubble is more likely to break into smaller bubbles and distribute throughout the well as it migrates upwards. The purpose of this chapter is to address the factors that aid or hinder gas distribution; this is divided into two sections. First, we analyze the gas distribution of the full scale tests with different operational variations and cross validating the results with the published literature. Second, we review the effect of pipe rotation on fluid flow through the discussion of a fluid flow phenomenon known as Taylor vortices. These vortices are speculated to increase the gas distribution and breaking the gas into smaller bubble.

The LSU #2 real scale experiments results and literature were cross validated with (Rommetveit and Olsen 1989; Spoerker, Gruber, and Brandstaetter 2012) in regards to factors affecting gas distribution. The gas distribution (i.e. higher gas breakage effect) has been shown to increase with the following factors: 1) less well inclination 2) lower mud rheology 3) lower kill rates

Furthermore, a phenomenon known as Taylor vortices which takes place above a certain critical speed of rotation was proposed to aid to the gas mixing and breakage of the bubble. The Taylor vortices occurrence has been established for the case of liquid flow in-between two pipes with the inner pipe rotating(Taylor 1923). Although the gas mixing has not been experimentally researched for a non-Newtonian fluid with cases similar to a gas kick in the wellbore, evidence from literature supports the hypothesis of Taylor vortices aiding the mixing of gas in the wellbore and furthering the breakage of the gas (Spoerker, Gruber, and Brandstaetter 2012; Lockett, Richardson, and Worraker 1993).

It is vital to discuss the gas distribution because the distribution of gas and maximum casing pressure are closely related. Fig 1 shows the correlation between surface gas void fraction and maximum casing pressure from the DEA project data. The surface gas void fraction is defined as the fraction of the wellbore occupied by the gas when gas reaches the surface. Lower void fraction infers higher bubble breakage and higher gas distribution. As can be seen in

the figure, the gas surface void fraction is highly correlated with maximum casing pressure. The void fraction is dependent on several factors including flow rate, mud properties and type.

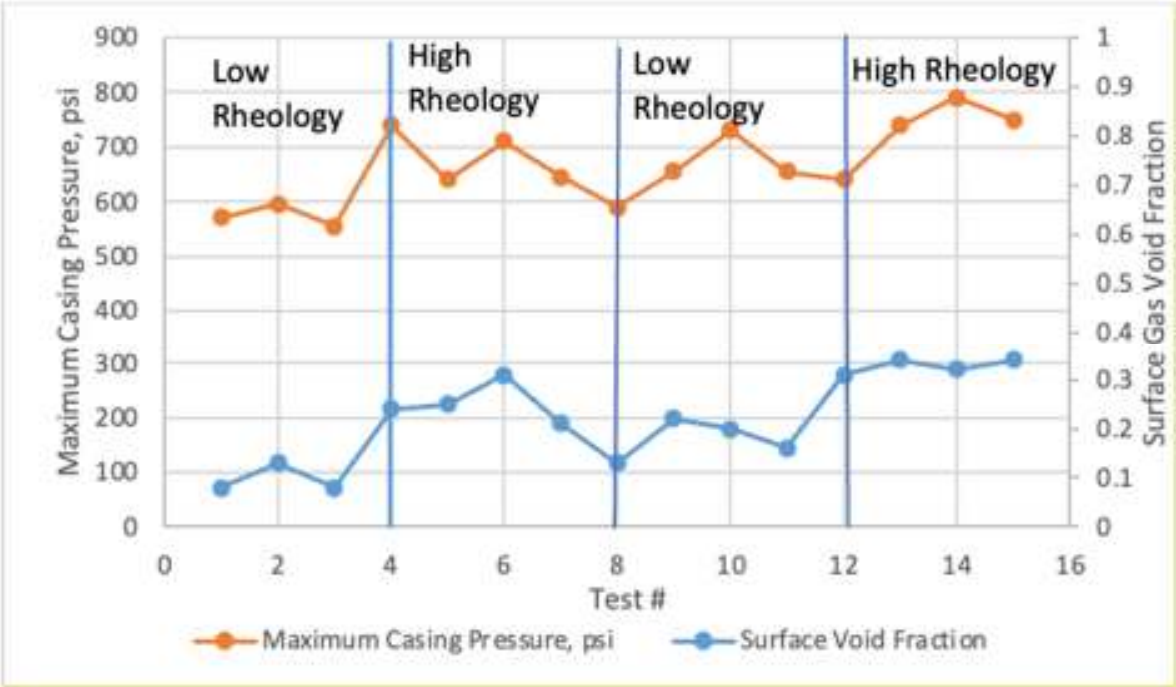

Figure 1: Correlation between surface gas void fraction and Maximum Casing Pressure

Gas Kick Distribution in Wellbore

Well inclination effect on gas distribution. A team of researchers from the university of Leoben, performed a simulation using the VOF (Volume of fluid) multiphase modeling method. The simulation only models 10 meters of the well because the depth to annulus width is too high to graphically represent the behavior. Unlike most well control models of proposing a single bubble of gas moving upward, the vertical well model clearly illustrates that there is a streaking behavior of that gas and only a portion of gas stays as a single elongated bubble as in Fig 2 (Spoerker and Tuschl 2010). This streaking behavior is of an agreement with the results of the DEA tests because the results report a different gas void fraction at the bottom than at the top. When the inclination of the well was slightly altered, the behavior of the gas took a slightly different pattern. The inclination has induced a more consolidated bubble towards the upper facing side of the annulus (Fig 3). As the inclination increases, the gas has a tendency to stay in one bubble.

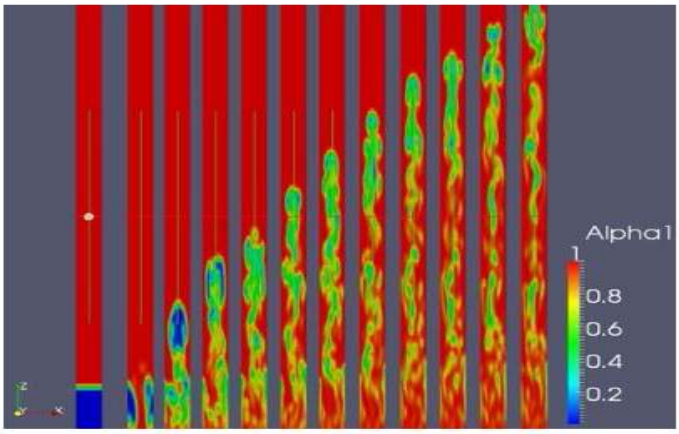

Fig.1: Percolation of gas through liquid across 10 m interval in vertical open hole

Figure 2: Gas bubble flow in mud in vertical open hole over 3 min(Spoerker and Tuschl 2010).

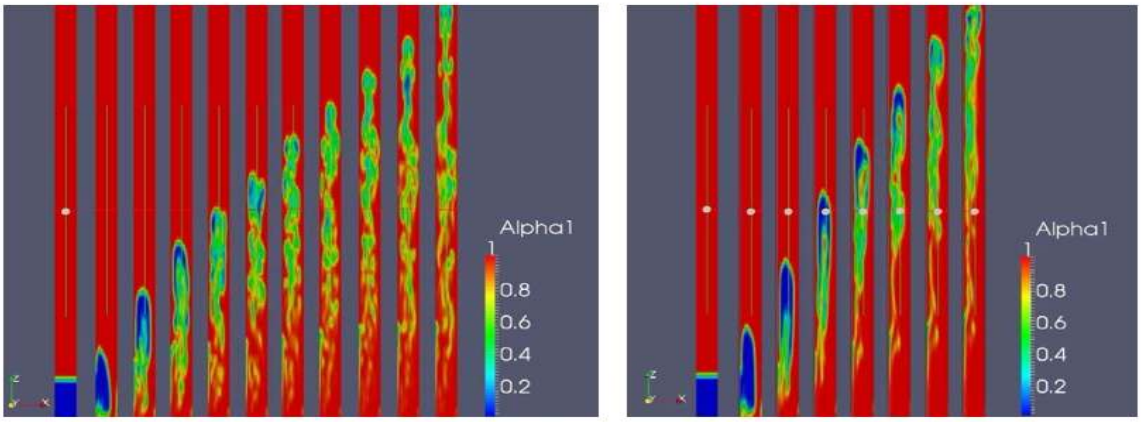

Fig.2: Percolation of gas through liquid across 10 m interval in 1° (left) and 10° (right) open hole

Figure 3: Gas behavior with 1□ inclination (left) and 10□ inclination (Right) over 3 min (Spoerker and Tuschl 2010).

Mud flow rate effect on gas distribution. Experiments of gas distribution coming out of a full size well found in the literature indicate that the lower the rate of the kill operation for water based mud, the more dispersed the gas is (Rommetveit and Olsen 1989). Similarly, DEA project data analysis of the void fraction of gas at surface showed that the lower the kill rate, the more distributed the gas is in the wellbore. The data illustrates that gas distribution at surface increases as the kill flow rate increases as in Fig 4. For each set of tests, mud properties, kick size, and circulation rates are the same.

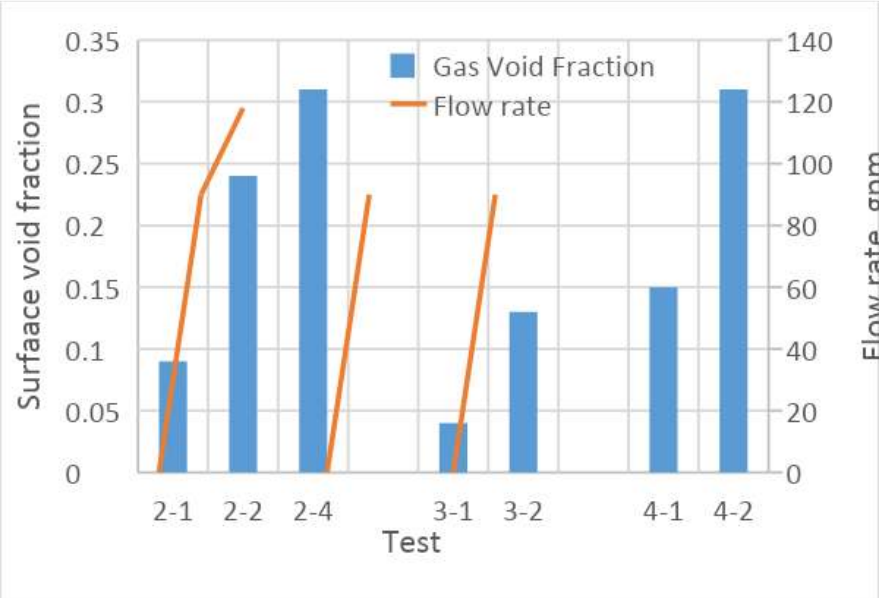

Figure 4: Effect of kill rate on gas distribution ("DEA Project 7" 1986).

Mud viscosity effect on gas distribution. Using the DEA project data, for the similar gas distributions at the bottom and same circulation rate, the increased mud viscosity induces a higher gas concentration at the surface. Fig 5 shows the difference of gas void fraction at surface with all other parameters kept the same except mud rheology. The higher the rheology, the higher the gas void fraction and, hence, the lower the distribution of gas. The low mud rheology in the figure refer to a range of plastic viscosity (μ_p) of 7-19 eq cp and a yield stress (τ_y) of 2-4 lbf100ft^2 ,whereas the high mud rheology refer to a range of plastic viscosity (μ_p) of 25-33 eq cp and a yield stress (τ_y) of 12-9 lbf100ft^2.

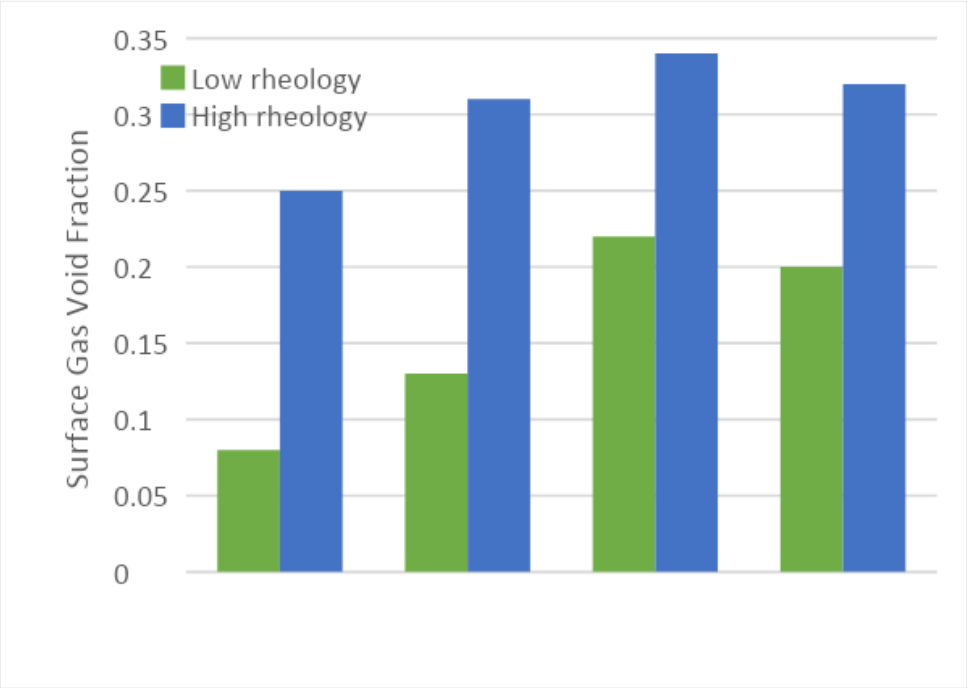

Figure 5: Mud rheology effect on gas distribution

Based on the above mentioned factors, optimum combination of the increased gas distribution and lower casing pressure therefore is low kill rate, low mud rheology and vertical well orientation. However, the only parameter that can be controlled at the time of the operation is the kill rate.

Pipe Rotation Effect on Gas Distribution. In this section, a fluid flow phenomenon known as Taylor vortices is proposed and is speculated to aid in the gas mixing. When these vortices occur, the gas bubble is suggested to break into smaller bubbles that is more likely to compromise the single bubble model.

Overview of Taylor Vortices. In 1915, Taylor has concluded an interesting behavior for the fluid flow in between two concentric cylinders. He studied the effect of rotation for both the inner and outer cylinders. He found that behavior of fluid flow changes when the inner cylinder is in rotation. This is similar to the setup of inner drill pipe rotating inside a casing or open hole. Before Taylor's work, most flow was studied under a Couette flow, which entails that the fluid flow between two cylinders can be approximated by the azimuthal velocity parallel to the direction of pipe rotation. The highest velocity vector is at the inner pipe and lowest is at the outer pipe as in Fig 6. Taylor then found that this is only applicable within a certain range of fluid viscosity and angular velocity of the inner pipe.

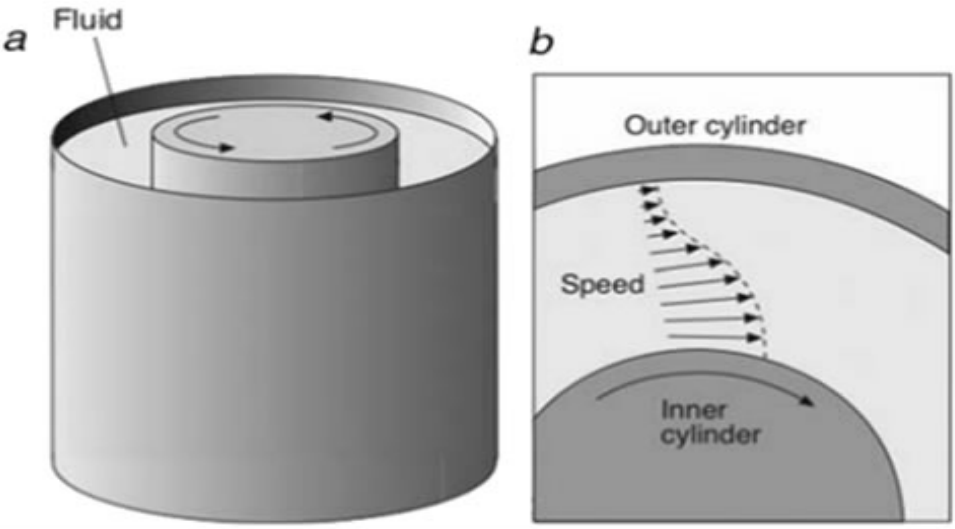

Figure 6: Couette flow illustration (Ball 2009).

After a certain threshold, the fluid starts to take an interesting direction caused by the centrifugal forces coupled with the azimuthal velocity of the pipe. When the centrifugal forces overcome the viscous forces of the fluid, the flow takes a different direction. It produces what is known as Taylor vortices. These vortices are a circular flow perpendicular to the walls of the cylinder as illustrated in Fig 7.

The flow characteristics at which these vortices form depend on speed of rotation, liquid density, liquid viscosity and geometry. A dimensionless number known as Taylor number is defined.

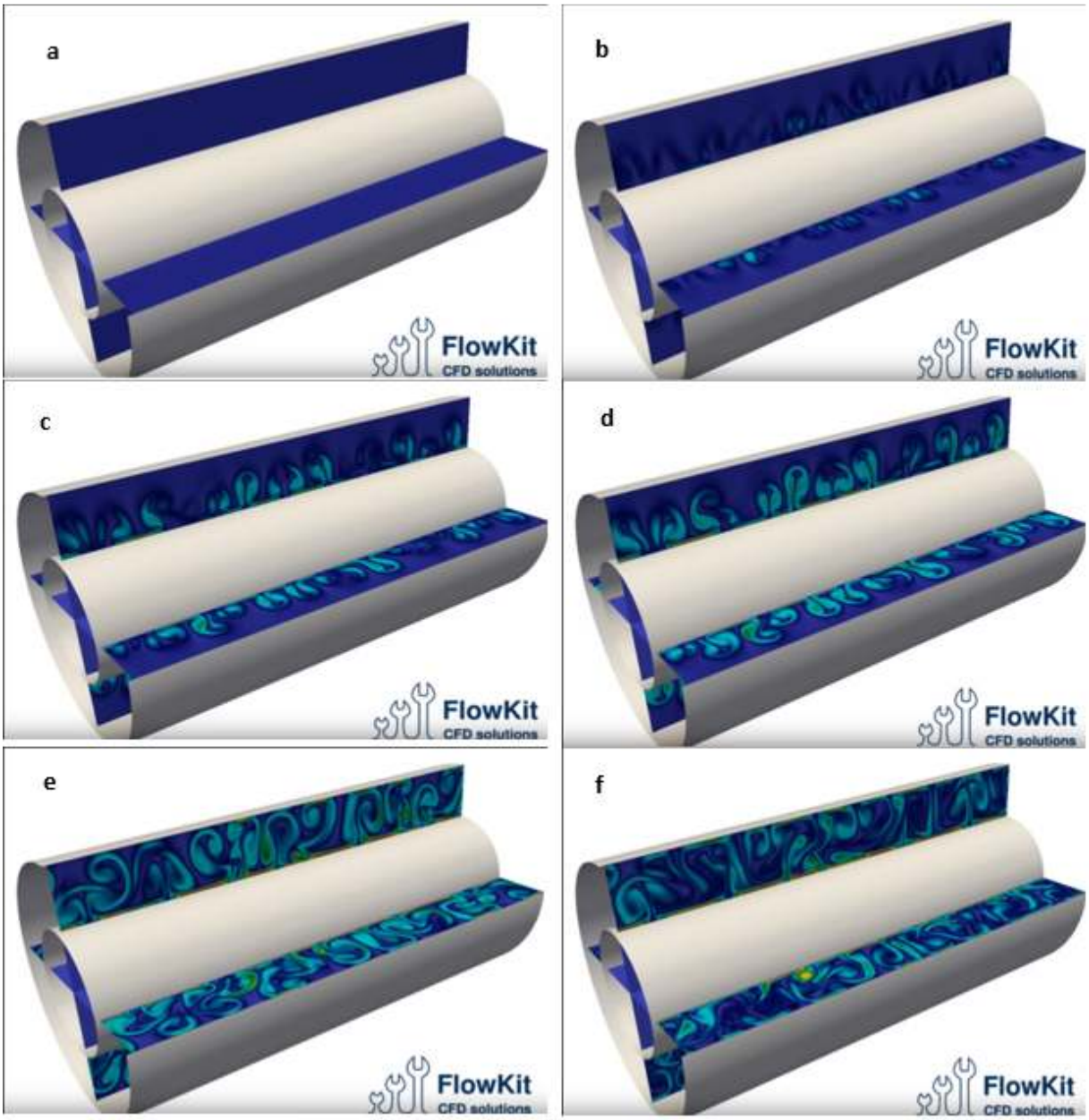

Figure 7: Taylor Vortices Illustration. Snapshots a through f show the time-lapse of the formation of the Taylor vortices with the rotation of the inner Cylinder (FlowKit 2016).

Since the fluid we are dealing with is non-Newtonian shear thinning, the apparent viscosity changes with increased axial and radial velocity (pipe rotation). Ahmed presented a method at which the apparent viscosity can be estimated (Ahmed and Miska 2008)

Critical Taylor number. The critical Taylor number is a number after which Taylor vortices appear. This number has been an area of study in itself. Taylor has defined the critical number to be 1708. Other studies such as Meksyn,

Chandrasekhar, DiPrima, Duty, Watanabe, Harris, and Ried found a range of Critical Taylor number between 1075 to 2255 (Drazin and Reid 2004; Watanabe, Sumio, and Ogata 2006; Walowit 1966). Further studies accounting for fluid rheology model, Soundalgekar et al found the critical Taylor number for stationary outer cylinder in an isothermal system to be 3389.9 (Soundalgekar, Takhar, and Smith 1981). In this analysis, the Taylor critical number used is 3400.

Critical rotation example. An example of a high rheology mud is plotted to find the Taylor number for each rotational speed. In Fig 8, the rotation speed is plotted against the Taylor number for a mud rheology presented in Erge's paper (Erge et al. 2015). The mud flow rate was set at 90 gpm. The point of intersection between critical Taylor number (3400) and the curve gives the highest rotation speed after which the vortices start to appear (Critical rotation). It is observed from Fig 8, the increase in Taylor number is not linear with the increase in pipe rotation. This is due to the shear thinning properties of the fluid. The rotation speed is inversely proportional to the apparent viscosity and proportional to the Taylor number. The geometry used for these graphs are LSU#2's.

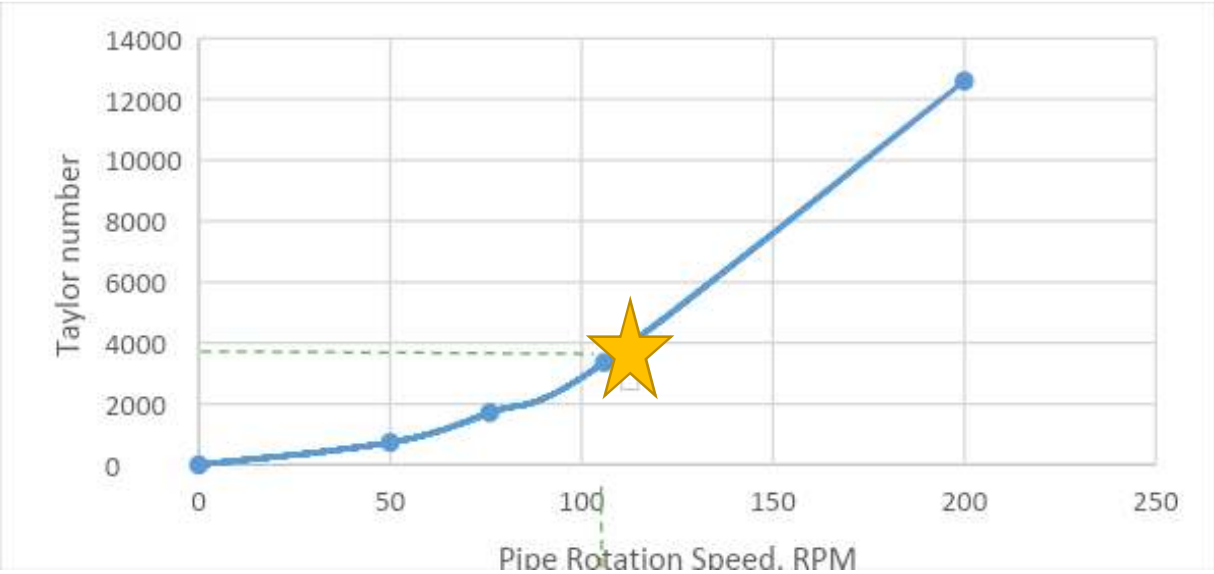

Figure 8: Taylor number increase with increased rotation speed for mud1 at 90 gpm

The process was done for two more mud properties (Table 1). Fig 9 shows the critical speed of rotation for each mud rheology with the increase in flow rate. The observation from Fig 9 shows a decrease in the value of the critical rotation speed with the increase in flow rate because the apparent viscosity decreases. This is caused by the shear thinning properties of the mud.

Table 1: Mud rheology models.

Mud	y, Pa	K, Pa.sm	m	Critical speed of rotation at 90 gpm, RPM
WN6 (Test 1-2 & 1-5)	1.2	.01	1	4
WN20 (Test 4-2)	2.85	.2	0.74	27
Mud1 (literature)	9.65	3.33	0.31	106
Mud2 (literature)	7.1	1.09	0.4	60

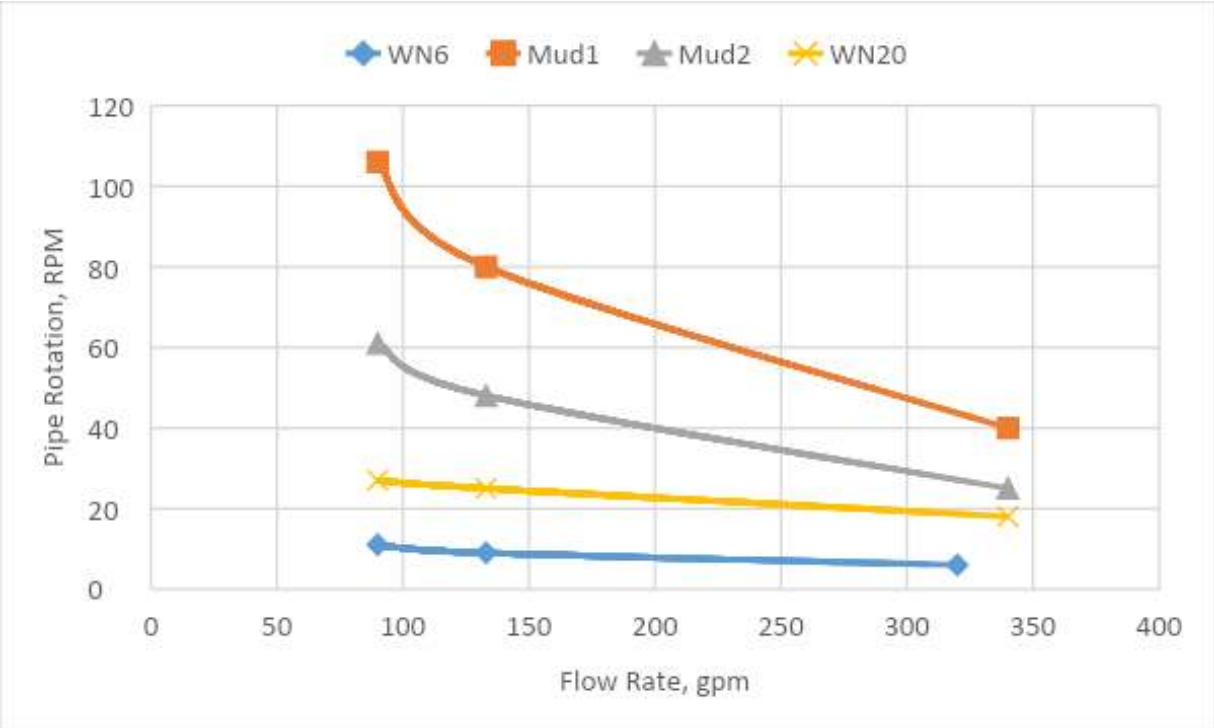

Figure 9: Critical rotation speed

Effectiveness of Taylor vortices in breaking the gas bubble. Although the Taylor vortices criteria is speculated to break the bubble into smaller gas droplets, and consequently compromise the single bubble model, the vortices implications on drilling application were further discussed in the literature. These vortices were studied in reference to hole cleaning, influence on frictional pressure with pipe rotation, experimental two phase flow with rotating cylinder in Newtonian fluids, and numerical simulation of two phase flow with non-Newtonian fluid for kick purposes (Lockett, Richardson, and Worraker 1993; Ahmed and Miska 2008; Shiomi et al. 1992; Spoerker, Gruber, and Brandstaetter 2012). Details on Taylor vortices discussion in regards to hole cleaning and numerical kick simulation with rotation are presented.

Lockett has conducted numerical simulations to understand the path that the particle takes with both pipe rotation and axial flow in a vertical well. The two phase (solid and liquid) investigation of Locket may aid in the understanding of gas path with the introduction of pipe rotation. He found that depending on the density ration between the fluid and the solid particles, the path of the particle is decided. The simulation results show that as long as the solid density to liquid density ratio is 2.4 or lower, the Taylor vortices produced by the rotation is able to suspend the particles at place. It is concluded that after the Taylor vortices are formed, the fluid has the ability to capture the particle and rotate it along the axis of the vortex (Lockett, Richardson, and Worraker 1993).

A computational fluid dynamics simulation using the volume of fluid method to understand the two phase flow of non-Newtonian fluid and gas kick interaction in a wellbore, specifically at the bottom of the well. Fig 10 shows the volume fraction of gas (red) to mud (blue). The figures are numbered representing their positions from the bottom of the well. It can be observed that as the gas bubble moves upward, the phase mixing (bubble breakage) is more evident, potentially caused by pipe rotation (120 RPM in the simulations) (Spoerker, Gruber, and Brandstaetter 2012). The pattern in (Fig 10 (2)), visibly illustrates the Tylor vortices phenomena.

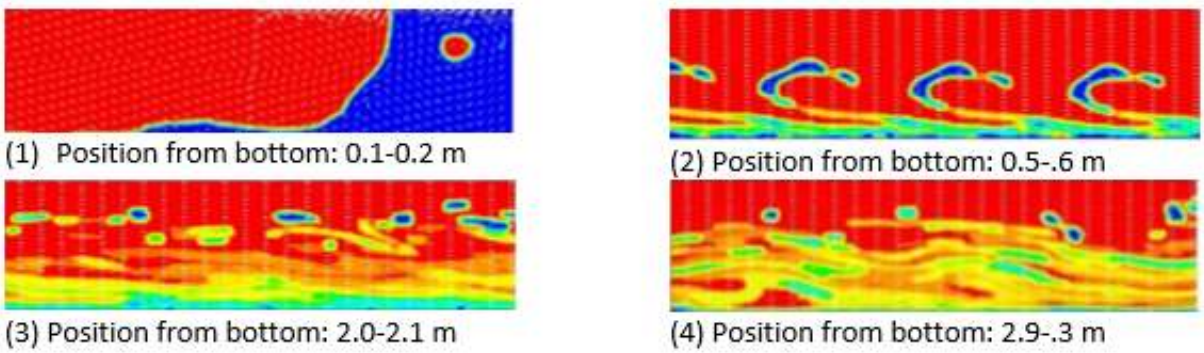

Figure 10: A simulated gas disrubution as kick moves upward in non_Newtanian mud (Spoerker, Gruber, and Brandstaetter 2012).

The work of (Spoerker, Gruber, and Brandstaetter 2012; Lockett, Richardson, and Worraker 1993) discusses a two phase observation with pipe rotation. It is proposed with the presence of Taylor vortices, their trajectory is able to aid to the gas mixing as they help in solid- mud interaction and gas-mud interaction as shown by the above mentioned simulations. The axial flow is forcing the gas and mud to move upwards, while Taylor vortices move fluid from inner pipe to outer pipe in a circular motion.

Conclusion

Evidence from the analysis of the real scale experiments casing pressure and the gas void fraction shows a clear relation between gas dispersion and reducing the surface pressure. If gas stays in one single bubble, the casing pressure is maximized which is an undesirable outcome as it puts the surface equipment and downhole formations near the casing shoe in jeopardy and increases the risk on the crew. Coupling the real scale data analysis with literate has presented that, in many cases, the single bubble model is invalid for a kick situation with non-Newtonian mud. Low kill rate, low mud rheology and vertical well inclination are all among the factors that can aid to the breakage of gas into smaller gas bubbles dispersed in the mud. Furthermore, a fluid flow phenomenon known as Taylor vortices that is known to occur above a critical speed of drill pipe rotation is reviewed. This critical speed of rotation depends on mud density, mud apparent viscosity, and geometry. Further literature investigation on Taylor vortices (hole cleaning and kick situation simulations) showed that these vortices might be a factor into aiding to gas mixing and breaking the single bubble. Therefore, all these results suggest that optimum combination for breaking the gas bubble are a vertical well inclination, low mud rheology, low kill rate and a drill pipe rotation above the critical speed. However, the only operational parameters that can be controlled after taking a kick is the kill rate and pipe rotation speed.

References

Ahmed, Ramadan, and Stefan Miska. 2008. "Experimental Study and Modeling of Yield Power-Law Fluid Flow in Annuli with Drillpipe Rotation." In *IADC/SPE Drilling Conference and Exhibition*, 13. Orlando: Society of Petroleum Engineers.

Ball, Philip. 2009. *Flow*. Oxford University Press.

Drazin, P.G., and W. H. Reid. 2004. *Hydrodynamic Stability*. Cambridge University Press.

Erge, Oney, Evren M Ozbayoglu, Stefan Z Miska, Mengjiao Yu, Nicholas Takach, Arild Saasen, and Roland May. 2015. "The Effects of Drillstring-Eccentricity, -Rotation, and -Buckling Configurations on Annular Frictional Pressure Losses While Circulating Yield-Power-Law Fluids." *SPE Drilling & Completion* 30 (3): 257. doi:10.2118/167950-PA.

FlowKit. 2016. "FlowKit Ltd.: Taylor-Couette Flow - Vorticity Field." *Youtube*. https://www.youtube.com/watch?v=uCutXG9WK70.

Lockett, T J, S.M. Richardson, and W.J. Worraker. 1993. "The Importance of Rotation Effects for Efficient Cuttings Removal During Drilling." In *SPE/IADC Drilling Conference*, 861–69. Amsterdam: Society of Petroleum Engineers.

Rommetveit, R, and T.L. Olsen. 1989. "Gas Kick Experiments in Oil-Based Drilling Muds in a Full-Scale, Inclined Research Well." In *SPE Annual Technical Conference and Exhibition*, 14. San Antonio: Society of Petroleum Engineers.

Shiomi, Yoichi, Hiroaki Kutsuna, Koji Akagawa, and Mamoru Ozawa. 1992. "Two-Phase Flow in an Annulus with a Rotating Inner Cylinder (Flow Pattern in Bubbly Flow Region)." *Nuclear Engineering and Design* 141: 27–34.

Soundalgekar, V M, H S Takhar, and T J Smith. "Effects of Radial Temperature Gradient on the Stability of Viscous Flow in an Annulus with a Rotating Inner Cylinder." *Warme- Und Stoffubertragung* 15 (1981): 233–38.

Spoerker, H F, and T Tuschl. 2010. "Behavior and Shape of Gas Kicks in Well Bores." In *IADC/SPE Drilling Conference and Exhibition*, 7. New Orleans: Society of Petroleum Engineers.

Spoerker, H.F., C Gruber, and W. Brandstaetter. 2012. "Dynamic Modelling of Gas Distribution in the Wellbore During Kick Situations." In *ADC/SPE Drilling Conference and Exhibition*, 9. San Diego: Society of Petroleum Engineers.

Taylor, G. I. 1923. "Stability of a Viscous Liquid Contained between Two Rotating Cylinders." *Philosophical Transactions of the Royal Society of London* 223 (A): 289–343. doi:10.1098/rsta.1923.0008.

Walowit, J A. 1966. "The Stability of Couette Flow Between Rotating Cylinders in the Presence of a Radial Temperature Gradient." *A.I. Ch.E Journal* 12 (1): 104–9.

Watanabe, Keizo, Shu Sumio, and Satoshi Ogata. 2006. "Formation of Taylor Vortex Flow of Polymer Solutions." *Journal of Fluids Engineering* 128 (1): 95–100. doi:10.1115/1.2137350.

"DEA Project 7." 1986. Baton Rouge.

Finite Element Inverse Analysis for Soft Soil Subgrade Settlement Considering Creep Behavior

Serges Mendomo Meye*[a, b, c], Li Guowei [a], Shen Zhenzhong [b, c], Gan Lei [b, c]
Xu Liqun [b, c]

a) State Key Laboratory of Safety for Geotechnical and Structural Engineering, College of Civil Engineering and Transportation, Hohai University, Nanjing—Jiangsu, P.R China

b) State Key Laboratory of Hydrology-Water Resources and Hydraulic Engineering, Hohai University, Nanjing—Jiangsu, P.R China

c) College of Water Conservancy and Hydropower Engineering, Hohai University, Nanjing—Jiangsu, P.R China

Abstract: The finite element inversion analysis method, allowing for describing the creep behavior of soft soil, is presented for simulating the subgrade settlement. The finite element analysis software, ABAQUS, is embedded into an improved whale algorithm (SWAO) based on information entropy by MATLAB, thus the calculation parameters of soft soil can be obtained quickly and accurately. The modified Drucker-Prager and time hardening creep model are used to simulate the subgrade settlement and deformation. To test the reliability of the proposed method, the finite element inversion model is built for a highway subgrade crossing soft soil and the deformation of the subgrade is simulated during the whole construction period. The simulation results indicate that the subgrade deformation obtained by the inversion analysis agreed well with the measured data. In addition, the post-construction settlement is also predicted and the settlement is within 10cm in ten years after construction, which may provide good theoretical guidance for the operation and management of highways.

Keywords: finite element method; inverse analysis; soft soil creep; subgrade settlement

1. Introduction

The settlement deformation of soft soil subgrade under self-weight stress includes elastic deformation and creep effect caused by filling material, which directly affects

* The corresponding author
Serges Mendomo Meye
Email: _mendomos@hhu.edu.cn
Phone number: +86-15261410840

the stability and bearing capacity of highways. Therefore, how to accurately predict the settlement of soft soil foundation and ensure the safe operation of highways not only has important theoretical research value but also has strong engineering guiding significance. FE analyses and analytical solution based tools are widely used in geotechnical engineering [1], such as predicting the bearing capacity of foundations [2], calculating the safety factor of slopes [3], predicting the ground settlement of embankments (e.g., [4, 5]) or tunnel, and predicting the deformation of retaining wall during excavation. For all these cases, a common requirement is to adequately obtain the soil properties and the design parameters from laboratory or field tests measurements [6, 7, 8]. However, this parameter acquisition method has certain limitations and cannot accurately reflect the overall soil properties of subgrades, which leads to the limited accuracy of the calculation results. Therefore, based on the measured data, the intelligent analysis method is needed to inverse the soil mechanical parameters, which provides a new method for obtaining the soil calculation parameters.

In recent years, several more effective back-analysis methods have been developed. These methods primarily achieved improved back-analysis effectiveness by using intelligent optimization algorithms and intelligent computing techniques or a combination thereof [6]. Intelligent optimization algorithms can accelerate the soil parameter optimization and thus avoid unnecessary fitness value calculations. Intelligent computing techniques calculate the fitness values faster than the FEM [9, 6]. However, the results of intelligent optimization algorithms are affected by the initial parameter values, and a local minimum or premature convergence is often obtained [9, 6]. Intelligent computing techniques also require many FEM calculations for training, which consume a considerable amount of time [6]. Furthermore, the results of intelligent computing techniques are affected by the training process, and the solution is sometimes unstable.

Recently, a parallel algorithm was used in geotechnical engineering back-analyses [6]. For example, Ledesma et al. [10] estimated parameters in geotechnical back analysis based on a maximum likelihood approach. Cheng et al. [11] utilized a hybrid approach for handling pile driving back analysis. Yu et al. [12] used artificial neural networks (ANN) for displacement back analysis of earth-rockfill dams. Hashash et al. [13] used optimization-based inverse analysis for excavation response. The soil parameters of the Malutang II CFRD were back-analyzed by Jia & Chi [6] using an intelligent parallel algorithm back-analysis method, in which the soil parameters were optimized by mutation particle swarm optimization. Fang [14] proposed and applied a new improvement of PSO in the inverse analysis for mechanical parameters of a mass concrete arch dam. Li Zheng et al. [15] used BP neural network to invert the mechanical parameters of soft soil foundation, and then predicted the settlement of the project.

Based on the displacement back analysis method of an evolutionary neural network, Li [16] predicted the differential settlement of subgrade before and after the expansion of two expressways. To analyze the rules of soft foundation settlement, Shen et al., [17] used the BP neural network to fit and optimize the settlement data of an expressway project. Taking advantage of the strong non-linear mapping and learning ability of BP neural network, Yi et al. [18] proposed a method to predict soft foundation settlement based on BP neural network model. Li et al. [19] used the measured settlement data of soft ground, then came up with the prediction method of soft ground settlement based on the BP artificial neural network in the MATLAB simulation environment.

Most of the above-mentioned methods adopt semi-empirical and semi-theoretical methods to analyze the settlement and deformation of highways soft foundation. The phenomenon of deformation and settlement of rock and soil layer of highways soft foundation embankment is highly complex, and there are large errors in the practical application of these methods. In geotechnical engineering, we wish to create the most ideal results with the available resources. In the increasingly competitive world, we cannot simply be satisfied with just acceptable solutions or performance. Rather we have to be looking to design the best systems [20]. While designing new models in any field, we must use design tools that provide the desired results in a timely and economical manner [21, 22]. With in□depth research in the field of optimization, the recent literature shows that WOA has a tremendous capability of solving complex engineering optimization problems [23]. Its evident advantages such as simplicity, flexibility, fast convergence speed, and stochastic nature gained outstanding attention among the current research community in multiple disciplines. Some of the striking features of WOA are its balanced implementation of the exploration (global search) and exploitation (local search) strategies of searching, and its successful execution even with a lesser number of parameters [24, 25, 26]. Moreover, it can also inherit the efficient function of an evaluation-based algorithm combining crossover and mutation processes within its structure. Resultantly, it builds a very strong framework exploiting a better convergence rate. Unlike other meta-heuristic algorithms, WOA tends to have some drawbacks. As per the existing literature, the power of the original WOA lies in its global exploration phase, but sometimes it may get trapped into local optima and fails to apply the global search exhaustively [23]. These limitations encourage the researchers to modify and hybridize it with other methods or metaheuristics for solving high-dimensional problems.

Given the limitations of the original WAO in local optimum and low convergence accuracy in complex optimization problems, based on the fundamental WAO, an improved algorithm (SWAO) based on information entropy is proposed. The information entropy itself is an uncertain measure. It is used to control the range of

whale searches in path selection. It can overcome the shortcomings of the basic WAO and can improve the global convergence speed of the algorithm. At the same time, the obtained results of SWOA are compared to those of the traditional PSO.

Furthermore, since the creep effect of soft soil is an important factor that cannot be ignored in the prediction of the long-term settlement deformation of soft soil subgrade, this paper puts forward the back analysis method of subgrade surcharge preloading considering the creep effect of soft soil and constructs a FE back analysis system based on SWAO. Through the embedment of ABAQUS FEA software with SWAO by MATLAB language, the calculation parameters of the soft soil stratum are obtained quickly and accurately. So that the subsequent FEA results more accurately reflect the settlement and deformation of the subgrade soil. To verify the reliability of this method, a FE model of an expressway subgrade across the soft soil area is constructed, and the deformation of the subgrade during the whole construction period is simulated. The obtained results may provide good theoretical guidance for the operation and management of highways.

2. Inverse analysis method of subgrade considering creep

2.1 Constitutive model of coupled creep effect

2.1.1 Soil stress state

Linear Drucker Prager yield criterion hardening model [27] is adopted in this paper, and its governing equation is as follows:

$$\sigma_1 - \sigma_3 + \frac{\tan\beta}{2+\frac{1}{3}\tan\beta}\left(\sigma_1+\sigma_3\right) - \frac{1-\frac{1}{3}\tan\beta}{1+\frac{1}{6}\tan\beta}\sigma_c^0 = 0 \tag{1}$$

Where σ_1 and σ_3 represent the first and third principal stresses respectively; β is the slope angle of linear yield surface, $\tan\beta = \frac{6\sin\varphi}{3-\sin\varphi}$; the initial yield stress $\sigma_c^0 = 2c\frac{\cos\varphi}{1-\sin\varphi}$, where φ is the internal friction angle and c is the cohesion.

2.1.2 Calculation of creep process

ABAQUS provides power law and hyperbolic sine law to describe creep characteristics. The former includes time hardening and strain hardening. In this paper, the widely used time hardening creep model is used to calculate the deformation of subgrade [27, 28]:

$$\dot{\varepsilon}^{cr} = A\left(\bar{\sigma}^{cr}\right)^n t^m , \tag{2}$$

where $\dot{\varepsilon}^{cr}$ is the equivalent creep strain rate $\dot{\varepsilon}^{cr} = \frac{\Delta\varepsilon}{\Delta t}$; A is the parameter reflecting the creep rate, soil composition, and structure of the soil; $\bar{\sigma}^{cr}$ is the equivalent creep stress. Performing the time integration on both the left and right sides of Eq. (2) at the same time, we get:

$$\varepsilon = \frac{A}{m+1}\left(\bar{\sigma}^{cr}\right)^{n} t^{m+1}, \tag{3}$$

Then the logarithms of the two sides are obtained:

$$\ln\varepsilon = \ln\frac{A}{m+1} + n\ln\bar{\sigma}^{cr} + \left(m+1\right)\ln t, \tag{4}$$

in Eq. (4), strain ε is the strain of soil at any time t; n refers to the power function in the ε-σ relationship curve; m+1 refers to the power function in the ε-t relationship curve in the data analysis, it is found that m+1 is a value between 0 and 1, that is, the value of m is between −1 and 0. In theory, A=ε(t,σ), A/(m+1) is the strain when σ=1, t=1, ln(A/(m+1)) can be obtained by intersecting the axis extending through the ln ε-lnσ relationship curve to ln σ =0. From Eq. (3), it can reflect the constitutive relationship of the three parameters *m*, *n*, and *A* of the creep characteristics of the soil. These three parameters also represent different meanings e.g., *m* is the parameter controlling the effect of time on creep, *n* is the effect of stress on creep, and *A* is the rate of soil creep, which reflects the characteristics of soil composition and structure to a certain extent.

2.2 Construction principle of inversion model based on displacement monitoring data

Material parameters mainly include self-property parameters, elastic mechanical parameters, plastic parameters, creep parameters, etc. The parameters to be inverted can be expressed as:

$$X = \left[x_1, x_2 \ldots x_m\right]^T, \tag{4}$$

where *m* is the total number of parameters to be inverted.

The displacement value obtained through actual monitoring or experimental measurement can be expressed as:

$$U^0 = \left(u_1^0, u_2^0, \ldots, u_n^0\right), \tag{5}$$

where $u_1^0, u_2^0,$ and u_n^0 are the measured displacement values at the measuring points; *n* is the number of measuring points.

The soil displacement variable U is a function of the parameters to be inverted, and its function relationship is

$$U = f\left(x_1, x_2, \ldots x_n\right). \tag{6}$$

Given the initial value of the parameter to be calculated $X = \left[x_1, x_2, \ldots x_m\right]^T$, the displacement value of each measuring point can be obtained

$$U = \left[u_1, u_2, \ldots u_n\right]^T, \tag{7}$$

where u_1, u_2,..., u_n are the displacement values of each measuring point.

The following fitness functions are constructed to find the best fitness to minimize the error between the calculated results and the actual monitoring results

$$\begin{cases} \varphi\left(x_1, x_2, \ldots x_m\right) = \sum_{i=1}^{n}\left(u_i^0 - u_i\right)^2 \\ \varphi\left(X^*\right) = \min \sum_{i=1}^{n}\left[u_i^0 - u_i\left(X\right)\right]^2 \end{cases}, \tag{8}$$

Where, X^* is the soil mechanical parameter corresponding to the best fitness; $u_i(X)$ is the displacement value calculated by the FE when the soil mechanical parameter is X^*.

2.3 WAO and its program implementation

This article studies a new algorithm that mimics the behavior of whales. The strangest thing about whales is the way they hunt. Their foraging behavior is called bubble-net feeding. Seyde and Samaneh [29] found two movements, namely positive upward and double cycle.

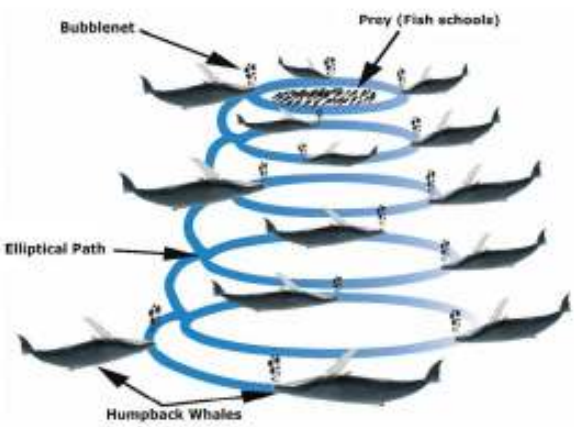

Fig. 1 Bubble-net feeding behavior of humpback whales [30]

Applying this to the algorithm includes three stages: (1) In the stage of encircling

prey, whales are uncertain about the food location, and they need to cooperate in groups to obtain food location information. (2) To achieve the local optimization of whales, the action of whales to prey and spit bubbles through the contraction and spiral update position is designed (Fig. 1). This is called the bubble-net attack stage. (3) The individual selection of reference whales is random, which is designed as the stage of searching for food.

2.3.1 Encircling prey

Whales can identify the location of their prey and surround them. However, the location of the optimal design of the search spatial for whales is unknown. WOA assumes that the current candidate solution is the target location or close to the target location. The best candidate solution appears after the definition of the best search agent, which is updated according to the location.

This behavior is expressed as:

$$\vec{D} = \left|\vec{C} \cdot \vec{X}^*(t) - \vec{X}(t)\right|, \tag{9}$$

$$\vec{X}(t+1) = \vec{X}^*(t) - \vec{A} \cdot \vec{D}, \tag{10}$$

where: t represents the current iteration; $\vec{A}$, $\vec{D}$ represents the vector coefficient; $\vec{X}$ represents the position vector; $\vec{X}^*$ represents the local optimal solution; "||" is the absolute value; "$\cdot$" is dot multiplication.

$$\vec{A} = 2\vec{a} \cdot \vec{r} - \vec{a}, \tag{11}$$

$$\vec{C} = 2\vec{r}, \tag{12}$$

where: $\vec{a}$ decreases linearly from 2-0 in the iterative process; $\vec{r}$ is a vector composed of [0, 1] random numbers. In each iteration, $\vec{X}^*$ is updated when there is an optimal solution.

2.3.2 Bubble-net attacking method (exploitation phase)

This stage simulates the spiral movement of the whale and establishes the spiral equation between the position of whales and the position of the prey.

$$\vec{X}(t+1) = \vec{D}' e^{bl} \cdot \cos(2\pi l) + \vec{X}^*(t), \tag{13}$$

$$\vec{D} = \left|\vec{X}^*(t) - \vec{X}(t)\right|, \tag{14}$$

in the formula: b is expressed as a constant defining the shape of the logarithmic spiral; l is expressed as a random vector of [-1,1].

2.3.3 Search for prey (exploration phase)

Whales search randomly based on each other's location, so a random value is used to make it greater or less than 1, and then force the search agent value to move away from the reference whale. On the contrary, in the development phase, the position of the search agent in the exploration phase is updated until it is found based on the randomly selected search agent instead of the best search agent.

The mathematical model is as follows:

$$\vec{D} = \vec{C} \cdot \vec{X}_{rand} - X(t), \tag{15}$$

$$\vec{X}(t+1) = \vec{X}_{rand} - \vec{A} \cdot \vec{D}, \tag{16}$$

2.4 Algorithm improvement

2.4.1 Improvement based on entropy

Like other intelligent algorithms, WAO has some disadvantages, such as low convergence accuracy, easy to fall into local optimal solution, and so on. It can be seen from Eqs. ((10), (13), and (16)) that the selection of whales' search direction and the control of range size affect the efficiency of predation and slow the convergence speed of the algorithm. We know that information entropy is uncertain. In this paper, the information entropy is introduced into the predation range of whales, and the search range of whales is optimized through the difference between the fitness value in the early and late stages. From the path of the bubble-net attack stage, α is introduced to expand the search range of whales; On the other hand, the optimal candidate solution of whales in the encircling predation stage is adjusted to find food more quickly. Finally, the algorithm can jump out of the local optimum and improve the convergence speed.

Entropy, as a physical concept, was first proposed by Clausius (1850) in thermodynamics. After more than half a century of development and evolution, the probability measure entropy used to describe the state of the system has been updated. The entropy of discrete random variables is as follows:

$$H(x) = -\sum_{i=1}^{n} p_i \ln p_i, \tag{17}$$

where: p_i is the probability of occurrence of each state, $p_i \geq 0$, $\sum_{i=1}^{n} p_i = 1$.

Information entropy is used to measure the amount of information needed to eliminate uncertainty, which refers to the measurement of the amount of information

contained in unknown events. There is a certain uncertainty in the occurrence of any event. The main fields of application of entropy theory are: (1) weight determination; (2) other theories are introduced as a measure of uncertainty; (3) as a new dimension of complexity evaluation; (4) as the algorithm's stopping judgment criterion.

The entropy function of discrete random variables has the following properties: (1) Function symmetry; (2) non-negativity; (3) certainty; (4) scalability; (5) additivity; (6) extreme value; (7) convexity.

Using the characteristics of information entropy, the shortcoming of randomness is avoided in the selection of the initial population. Then, the range of whale feeding is regulated, the local optimal problem no longer exists, and the adaptive adjustment of the algorithm is realized. The emergence of a certain required value makes the algorithm output the optimal solution, and the search is ended.

Because the path of whales' predation is uncertain, and the information entropy itself can measure the uncertainty of event occurrence, the information entropy is introduced into WAO, and the value of information entropy is used to disturb the parameters so that the whale individuals are evenly distributed in the search space.

Information entropy is defined as:

$$E(n) = |n \ln|, \tag{18}$$

where: n = [0,1] is a random vector.

The fitness value is defined at the initial stage of population search, and the fitness value is updated following the population iteration. The direction of the whale prey search is similar to the information entropy value. According to this situation, the population fitness value is updated by the iteration change, and *fitnescz1* and *fitnescz2* are determined, and then the prey behavior is divided into *c1* and *c2* paths.

There is:

$$H_{\max} = -0.5 \cdot \ln(0.5), \tag{19}$$

$$H = -c1 \cdot \ln(c1) - c2 \cdot \ln(c2), \tag{20}$$

The adjustment parameters are as follows:

$$\alpha = \frac{H_{\max} - H}{H_{\max}}, \tag{21}$$

$$\beta = 1 - \frac{H_{\max} - H}{2H}, \tag{22}$$

where: α is the probability of optimal path selection; β is the proportion of whales that can be selected in an appropriate small range; H_{max} is the maximum entropy value, and the maximum entropy value is when t=0.5.

Substitute β into Eq. (9) and modify it to get:

$$\vec{D} = \left| \beta \cdot \vec{X}^*(t) - \vec{X}(t) \right|, \tag{23}$$

Substitute α into Eq. (2) and modify it to get:

$$\vec{X}(t+1) = \vec{X}^*(t) - \alpha \cdot \vec{D}, \tag{24}$$

In the early stage of WAO, the population size is small, and the individual distribution of whales' population is uneven, scattered in the initial solution space. In the later stage, with the iteration, the search range of the whale is expanded, the local search ability is increased, and the premature is well controlled. For β, its value is large at the beginning of the algorithm operation, which ensures that the optimal solution is found as much as possible; In the later stage, with the change of entropy, the search process decreases, and the size of α and β changes due to the change of information entropy, which increases the search process and avoids premature. In the whole process of whale prey, the emergence of information entropy changes the size of α and β, the search efficiency of the algorithm is improved, and the adaptive adjustment of the algorithm runs flexibly.

The principle of self-adaptive adjustment is to realize the self-regulation of the algorithm operation process through the cooperation of α, β, and $\vec{D}$ and $\vec{A}$, and adjust the search process by the change of α and β to overcome the defects of WAO, such as easy to fall into prematurity.

2.4.2 Optimization process

Step 1: initialize the parameters. The probability of optimal path selection is α, the proportion of whales allowed to be selected in an appropriate small range is β, the number of iterations is t, the maximum number of iterations is t_{max}, $E(n)$ is a random number between [0,1], the number of whales is N;

Step 2: calculate the fitness $\{f(X_i), i = 1, 2, ..., N\}$ of an individual whale and record the current optimal whale position;

Step 3: update the parameters α, β, $E(n)$ of each search agent;

Step 4: determine the information entropy value. If $E(n)<E(0.5)$, then make $|A|<1$ judgment, if so, update the position of the next generation according to Eq. (24), otherwise update the position of the next generation according to Eq. (16);

Step 5: if $E(n)>E(0.5)$, update the position of the next generation according to Eq. (13);

Step 6: judge the conditions of the end of the loop, and meet the requirements, that is, end the algorithm and output the target value; Otherwise, return to the above steps and continue the loop.

2.4.3 Improved algorithm flow chart

SWAO optimizes the whales' prey behavior from two aspects. On the one hand, the optimal path selection probability α is used to measure the spiral equation of the bubble-net attack stage, so that whales can obtain the best global optimal solution. On the other hand, the optimal candidate solution in the predation stage is adjusted by selecting the proportion of whales β in an appropriate small range. The flow of SWAO is shown in Fig. 2.

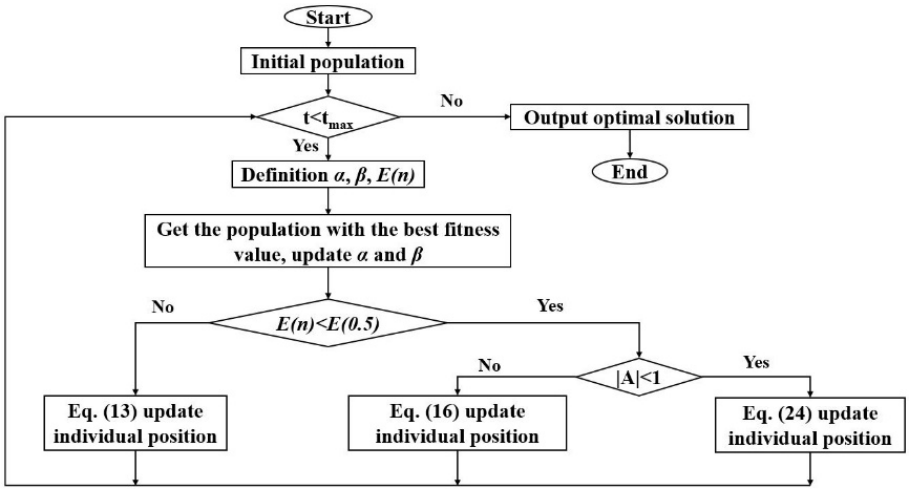

Fig. 2 Flow chart of the improved algorithm

To sum up, the flow of finite element analysis of soft soil foundation settlement based on the improved WOA algorithm is shown in Fig. 3.

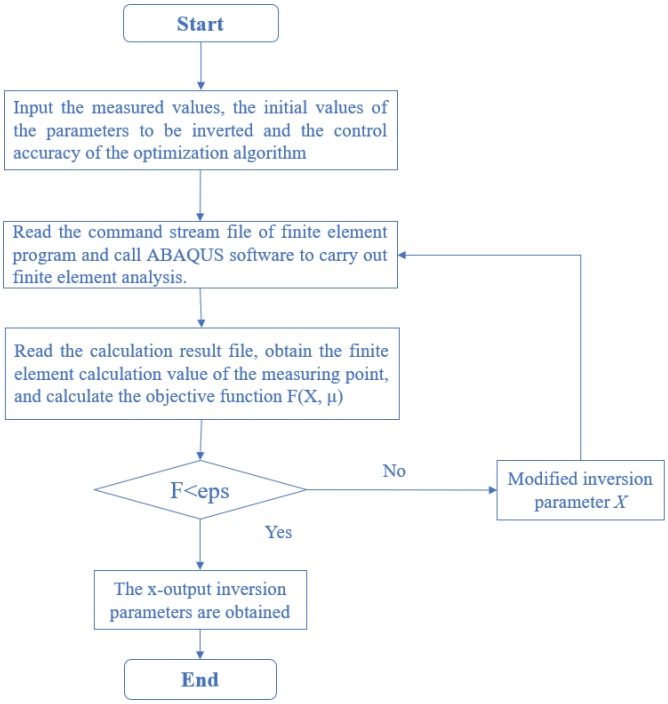

Fig. 3 Flowchart of the finite element inverse method

3. Calculation and analysis of consolidation and creep settlement of soft soil subgrade

3.1 Overview of the calculation model

This paper relies on the numerical simulation of an expressway crossing a soft soil area, and its subgrade section is depicted in Fig. 4. The pavement structure is an asphalt pavement structure. The model is 0.69m asphalt pavement, 4m embankment, 0.5m sand cushion, and 19.5m silty clay from the surface to the bottom. The groundwater level is 1m below the ground. The embankment and pavement are graded according to 1∶1.5. Three deformation monitoring instruments are buried at the measuring points 1, 2, and 3 to monitor the deformation of the foundation during construction.

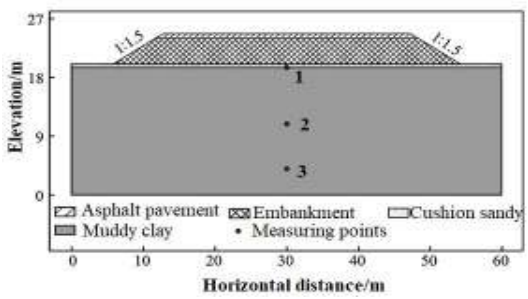

Fig. 4 Design profile of the subgrade

3.2 Finite element model

The finite element model established in this paper is mainly used to obtain the settlement deformation of soft soil subgrade. The mesh of the model is shown in Fig.

5, and the mesh size is 0.75 ~ 1m. The boundary conditions of the model are shown in Table 1.

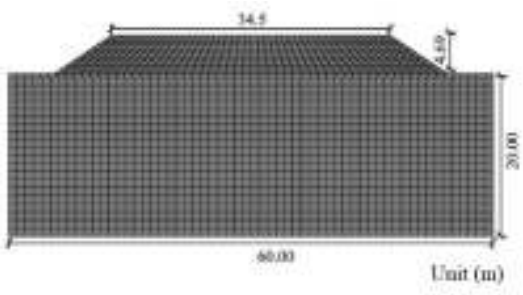

Fig. 5 Finite element mesh of the subgrade model

Table 1 Setting of the subgrade model boundary conditions

Boundary position	Boundary type
Subgrade surface	Free drainage boundary
Left and right side of the subgrade	Horizontal constraint
At the bottom of the foundation	Undrained fixed boundary

3.3 Inversion interval of model calculation parameters

There are seven parameters to be inverted, including elastic modulus E, Poisson's ratio μ, slope angle β of linear yield surface, initial yield stress σ_c^0 and creep parameters *a*, *m*, *n*. The range of values is given in Table 2. For WOA, the maximum number of iterations is set to 150, the population size is 30, and the logarithmic spiral shape constant is 1.

Table 2 Ranges of the unknown inversion parameters

Model parameters to be inverted		Inversion interval
Elastic modulus E/kPa		[3 000,5 000]
Poisson's ratio μ		[0.2,0.4]
Slope angle β of the linear yield surface		[20,40]
Initial yield stress σ_c^0/kPa		[30,80]
Creep parameters	A	[1e 6,2e 6]
	m	[-1,0]
	n	[1,3]

4. Result analysis

The measured settlement data of survey points 1, 2, and 3 on the 210th day of the construction period are used as the basic data to construct the fitness function for parameter inversion analysis. Fig. 6 depicts the convergence curve of the fitness function of the inversion analysis based on the traditional particle swarm optimization (PSO) and SWOA. It can be seen from the figure that the fitness value of SWOA has

not changed in the 38th generation, indicating that the calculation has converged. At this time, the fitness function value is 2.5e□ 5. PSO does not change the fitness at the 75th generation, and the value of the fitness function after convergence is 4.7e 2. It can be seen that SWOA has faster convergence speed, stronger optimization ability, and higher optimization accuracy than PSO. Therefore, the inverse analysis method based on the improved algorithm proposed in this paper cannot only ensure the high-precision calculation results but also greatly save the calculation time.

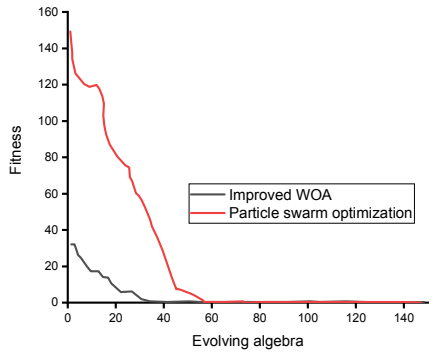

Fig. 6 Optimization curve of the algorithm

Table 3 Comparisons between the inversion parameters and the design parameters

Model parameters		Parameters obtained by inversion	Design parameters
Elastic modulus E/kPa		4 200.0	3 300.0
Poisson's ratio μ		0.36	0.25
Slope angle β of the linear yield surface		35.3	22
Initial yield stress σ_c^0/kPa		57.0	45
Creep parameters	A	1.2e 6	1.5e 6
	m	-0.99	-0.95
	n	2.0	1.5

After inverse analysis, the constitutive model calculation parameters of the foundation are obtained, as given in Table 3. It can be seen that the values of model parameters obtained from inversion analysis are quite different from those of design parameters.

Using the model parameters obtained from the inverse analysis to perform FE calculation, the vertical displacement cloud chart of the subgrade just after construction and 10 years after the completion of the construction are depicted in Fig. 7(a) and Fig. 7(b), respectively. It can be seen from the figure that the contour of the vertical

displacement of the subgrade is approximately elliptical, and the maximum settlement area is in the center of the foundation surface.

By comparison, it is found that the displacement cloud chart just after the completion of the construction and the displacement cloud chart 10 years later is quite different. This indicates that the highway on the soft soil subgrade will undergo obvious later creep deformation. Therefore, to accurately calculate and predict the deformation of highways, the creep effect cannot be ignored.

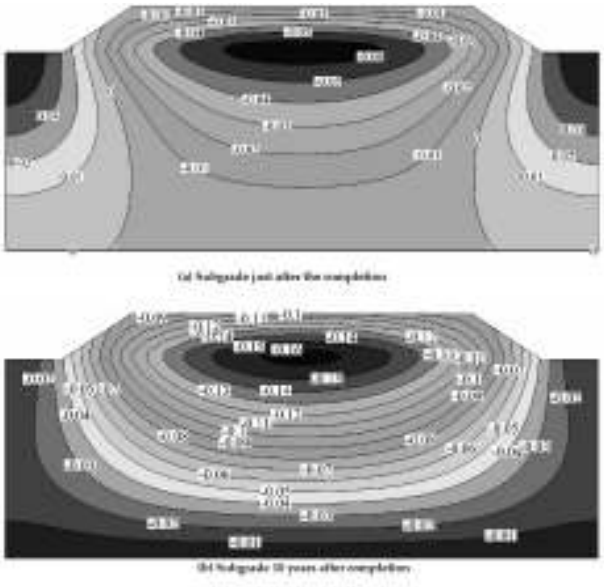

Fig. 7 Contour of the vertical displacement of the subgrade

The calculation results of the whole construction period using the inversion parameters and design parameters are depicted in Fig. 8. It can be seen from the figure that although the trend of the results calculated based on the inversion parameters and the design parameters is the same, as time goes by, the gap between the two gradually increases. The fitting effect between the results of the inversion analysis and the measured values is better. This shows that after inversion analysis, the accuracy of deformation calculation can be greatly improved, which verifies the reliability of the method proposed in this paper.

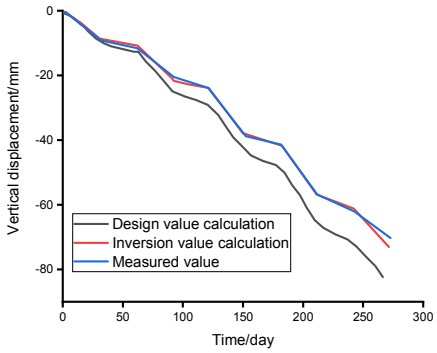

Fig. 8 Comparisons between the calculated and the measured results of the settlement

The vertical settlement changes of the pavement center point and the road shoulder over time are calculated, as depicted in Fig.9(a). It can be seen from the figure that there is continuous settlement deformation after the completion of the highway, and the settlement at the center of the pavement is significantly greater than that at the shoulder, and the deformation rates of both show a trend from fast to slow. After 10 years of construction, the settlement of the pavement is less than 10cm, which meets the requirements of highways subgrade design specifications.

The difference value of settlement between the pavement center and the pavement shoulder (i.e., uneven settlement) is calculated over time, as depicted in Fig. Fig.9(b). It can be seen that with time, about 5 years after the completion of the construction, the uneven settlement value gradually stabilizes and is controlled at about 16mm.

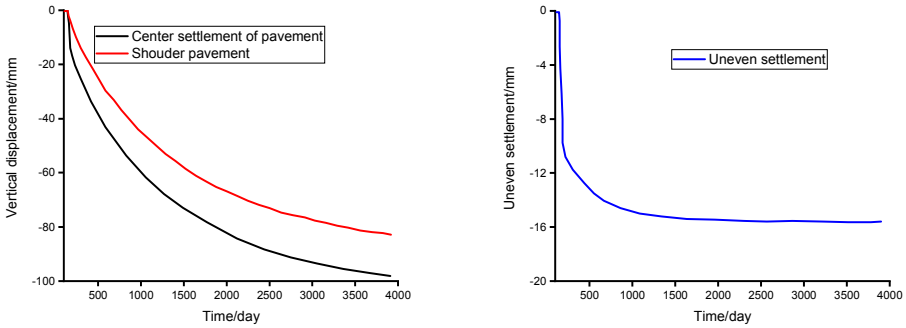

(a) Pavement and shoulder settlement (b) Subgrade deformation

Fig.9 Subgrade settlement time-varying trend

5. Conclusion

Based on the improved WOA algorithm, an inversion analysis model for subgrade settlement that can consider the creep effect of soft soil is proposed, and a numerical

simulation study is carried out relying on a highway crossing a soft soil area. The foundation model parameters of the project are obtained through inversion analysis, and the results show that the improved algorithm has higher optimization speed and accuracy than the traditional particle swarm optimization algorithm. Through the comparative analysis with the measured data, it can be known that the subgrade deformation obtained by the inversion analysis has a high consistency with the measured value, which verifies the reliability and rationality of the method proposed in this paper. On this basis, the calculation parameters obtained from the inversion analysis are used to predict the settlement of the subgrade and pavement in 10 years after construction, which provides good theoretical guidance for the operation and management of highways. At the same time, the research results in this paper may provide a good reference value for similar projects.

Data Availability

The data used to support the findings of this study are included in the article.

Declaration of competing interest

The authors declare that they have no known competing financial interests or personal relationships that could have appeared to influence the work reported in this paper.

Acknowledgments

This work was supported by the Natural Science Foundation of Jiangsu Province (520042711) and Special Project for Free Exploration of Basic Research Funds for the Central Universities (B200203039).

References

[1] Z. Yin, Y. Jin, J. S. Shen and P. Hicher, "Optimization techniques for identifying soil parameters in geotechnical engineering: Comparative study and enhancement," *Int J Numer Anal Methods Geomech,* p. 2018;42:70–94, 2018.

[2] . D. Loukidis and R. Salgado , "Effect of relative density and stress level on the bear ing capacity of footings on sand," *Géotechnique,* p. 61(2):107 119, 2010.

[3] . D. Griffiths and . P. Lane, "Slope stability analysis by finite elements," *Géotechnique,* p. 49(3):387 403, 1999.

[4] S. Shen , L. Ma , Y. Xu and . Z. Yin, "Interpretation of increased deformation rate in aquifer IV due to groundwater pumping in Shanghai," *Can Geotech J,* p. 50(11):1129 1142, 2013.

[5] H. Wu , . S. Shen, L. Ma , Z. Yin and . S. Horpibulsuk, "Evaluation of the strength increase of marine clay under staged embankment loading: a case study," *Mar Georesour Geotechnol,* p. 33(6):532 541, 2015.

[6] Y. Jia and . S. Chi, "Back-analysis of soil parameters of the Malutang II concrete face rockfill dam using parallel mutation particle swarm optimization," *Computers and Geotechnics,* p. 65 (2015) 87–96, 2014.

[7] W. H. Xiao , . J. S. Tong and D. F. Wang , "Finite element analysis of consolidation deformation of pre-loading in expressway soil roadbed," *Highway （in Chinese）,* pp. 2012（5）：79-82, 2012.

[8] H. M. Zhang , "Numerical analysis of settlement and treatment of soft soil subgrade under highway," *Journal of Water Resources and Architectural Engineering,* pp. 5（6）：211-215, 2017.

[9] Y. Yu, B. Zhang and . H. Yuan, " An intelligent displacement back-nalysis method for earth-rockfill dams," *Comput Geotech,* p. 34(6):423–34, 2007.

[10] . A. Ledesma, A. Gens and E. Alonso , "Estimation of parameters n geotechnical backanalysis—I. Maximum likelihood approach," *Comput Geotech ,* p. 18(1):1–27, 1996.

[11] Y. Cheng , L. Li , . Y. Sun and S. Au , "A coupled particle swarm and harmony search optimization algorithm for difcult geotechnical problems," *Struct Multidiscip Optim,* p. 45(4):489–501, 2012.

[12] Y. Yu , . B. Zhang and . H. Yuan, "An intelligent displacement back-analysis method for earth-rockfll dams," *Comput Geotech,* p. 34(6):423–434, 2007.

[13] Y. Hashash , S. Levasseur , A. Osouli , R. Finno and Y. Maleco, "Comparison of two inverse analysis techniques for learning deep excavation response," *Comput Geotech,* p. 37(3):323–333, 2010.

[14] W. Fang , "Back-analysis Improved Particle Swarm Optimization Algorithm on Mechanical Parameters of Divisional Geotechnical Engineering Material," *Applied Mechanics and Materials,* pp. 182-183 (2012) pp 1647-1653, 2012.

[15] Z. Li, D. Meng and B. Li, "Application of neural network to settlement prediction of soft soil foundation," *Journal of Northwest A&F University,* pp. 35（7）：219-222, 2007.

[16] L. Lifeng, "Prediction of differencial settlement of widened subgrade based on displacement back analysis," *Journal of Highway and Transportation Research and Development,* pp. 32（1）：57-63, 2015.

[17] Q. Shen, Y. Li and C. Peng, "Analysis and Prediction of Soft Foundation Settlement for Expressway Based on BP Neural Network," 2016.

[18] X. Yi , . Z. Cao and S. Liu, "The Application of BP Neural Network in Settlement Prediction of Highway Soft Foundation," *Advanced Materials Research,* pp. 250-253 (2011) pp 3440-3443, 2011.

[19] S. Li, S. He, X. Wang, S. Chen and X. Guo, "Prediction of Soft Ground Settlement by BP Neural Network," *Applied Mechanics and Materials,* pp. 608-609 (2014) pp 825-828, 2014.

[20] Z. Li, D. Meng and B. Li, "Application of neural network to settlement prediction of soft soil foundation," *Journal of Northwest A&F University,* pp. 35（7）：219-

222, 2007.

[21] L. Lifeng, "Prediction of differencial settlement of widened subgrade based on displacement back analysis," *Journal of Highway and Transportation Research and Development,* pp. pp. 32（1）：57-63, 2015.

[22] J. Zhao, L. Liu and G. Wang, "Deformation monitoring and inversion analysis of surrounding rock mechanics parameters for metro construction with mining method in Dalian," *Journal of Disaster Prevention and Mitigation Engineering,* pp. 32(1) 57-63, 2015.

[23] Y. Zhou , . Y. Ling and Q. Luo , "Levy flight trajectory-based whale optimization algorithm for global optimization," in *IEEE Access 1:1*, 2017.

[24] T.-K. Dao , T.-S. Pan and J.-S. Pan , "A multi-objective optimal mobile robot path planning based on whale optimization algorithm," in *In: IEEE 13th International Conference on Signal Processing (ICSP)*, IEEE, 337–342, 2016.

[25] S. Li , "The art of clustering bandits," in *Universita` degli Studi dell'Insubria*, 2016.

[26] S. Li , . A. Karatzoglou and C. Gentile , "Collaborative filtering bandits," in *In: Proceedings of the 39th international ACM SIGIR conference on research and development in information retrieval*, ACM, pp 539–548, 2016.

[27] S. Mendomo and Z. Shen, Hydraulic Structures Eng. & Geotechnical Eng. with ABAQUS: A concrete process of modeling, problem solving & post-processing Part I, LAMBERT Academic Publishing, 2020.

[28] Z. Wu, T. Chen and W. Ma, "Creep analysis of plain fill embankment at permafrost regions along Qinghai-Tibet Railway under train dynamic load," *Rock and Soil Mechanics,* pp. 32（Sup 2）：83-87, 2011.

[29] M. B. Seyed and . Y. Samaneh, "IWOA: An improved whale optimization algorithm for optimization problems," *Journal of Computational Design and Engineering,* pp. 6（03）:243-259, 2019.

[30] R. Nadim , S. A. L. Muhammad , M. A. Shafi'i and C. Haruna , "Whale optimization algorithm: a systematic review of contemporary applications, modifications and developments," *Neural Computing and Applications,* p. 32:16245–16277, 2020.

Pre-Training Strategy for Learning Representations of Engineering Materials

Reshinth Adithyan, Jothikrishna Balakrushnan, Roakesh Kalaimamani

***Abstract*—** Material Property Prediction and Material Discovery are few areas of Material Science wherein in Machine Learning plays a key role of accelerating. These applications generally have learning from scratch as the learning strategy. While in other applications of Machine Learning, pre-training has started to show a significant differentiation. This study proposes a pre-training strategy for learning unified representations of Engineering Materials. The study stresses the importance of learning unified representations of Engineering Materials, and shows that learning unified representation from unsupervised learning strategy improves the model's performance significantly. The research systematically studies the improvements of the pre-training in various benchmarking datasets focusing on the tasks of Material Discovery and Material Property prediction. The study amends the researcher's pre-training strategy with different Encoders like Transformer and Graph Neural Networks, both of which are well known to capture structural information. This research finally conducts an ablation study which prevails the different results obtained.

***Keywords*—** graph neural networks, material property prediction, transformers, unsupervised pre-training.

Reshinth Adithyan is with the Sri Manakula Vinayagar Engineering College, India (e-mail: reshinth.adith@outlook.com).

Generative Adversarial Networks for Generation of Synthetic High Entropy Alloys

Christian Eike Precker, Andrea Gregores-Coto, Santiago Muíños-Landín

Abstract—High-performance materials are a key tool for several reasons. On the one hand, their use brings obvious progress in the performance of the pieces where they are used in fields such as aeronautics, construction, or biotechnology. On the other hand, high-performance materials also allow more efficient use of energy in industrial processes where the use of such energy becomes intensive with its consequences in terms of environmental and economic sustainability. For these reasons, the emergence of high-performance materials such as high entropy alloys (HEAs) has captured the attention of industry and researchers within the last years. However, the development of these materials requires a large amount of time and money invested in the design, synthesizability evaluation, construction, and characterization of such compounds. The use of artificial intelligence for the design of materials, even in its current infancy status, provides a valuable tool to accelerate the initial phases of materials design and HEAs, where the high number of combinations brings a perfect scenario for the deployment of Machine Learning techniques. In this work, a Generative based approach is used, namely Generative Adversarial Networks (GANs) to generate synthetic HEAs for highly intensive industrial processes. The architecture model of a GAN involves two neural networks. The first one is a generator model for generating chemical compositions of candidate alloys to form the HEAs. The second one is a discriminator model for classifying the generated samples coming from the generator in real or fake compositions. The discriminator learns from a specific data structure that contains data from real samples to classify the generated samples. A GAN extension that conditionally generates the synthetic outputs by the addition of extra inputs was used. This so-called conditional tabular generative adversarial network (CTGAN) was developed to be used with tabular datasets as input. Such data is normally composed of a mix of continuous and discrete columns, making some deep neural network models fail in performing a properly modeling for this kind of inputs. In the present approach, the generated realistic synthetic data was based on the conventional parametric design parameters used for HEAs, i.e., atomic size difference δ, mean atomic radius a, average melting temperature T_m, mixing enthalpy ΔH_{mix}, mixing entropy ΔS_{mix}, electronegativity χ, valence electron concentration (VEC), mean bulk modulus K, and the standard deviation for most of them. As conditioned input data, the chemical composition of the alloys and their phase has been considered. The phase was classified in four classes, namely amorphous, intermetallic, solid solution, and solid solution + intermetallic, which can be used as an indicator for their applicability. The CTGAN provides as output candidates of HEAs, the expected parameters mentioned above, and corresponding phase. The generated data is compared with the calculated data and a verification of novel generated compositions is done in open materials databases available in the literature. Finally, a specific data structure for the CTGAN training and results of the performance of this approach is provided, which was developed in the framework of the European project ACHIEF for the discovery of novel materials to be used in industrial processes.

C. E. Precker, A. Gregores-Coto, and S. Muíños-Landín are with the AIMEN Technology Centre, Smart Systems and Smart Manufacturing–Artificial Intelligence and Data Analytics Laboratory, PI. Cataboi, 36418 Pontevedra, Spain. e-mail: christian.precker@aimen.es.

Manuscript received August 18, 2021; revised August 24, 2021.

Keywords—Artificial Intelligence, High Entropy Alloys, Generative Adversarial Networks, Intensive Energy Processes.

I. Introduction

TECHNOLOGICAL advances lead humans to search for new possibilities in all fields of science. One example was the development of high-entropy alloys (HEAs) by two independent research groups in 2004 [1], [2], which is a class of materials containing multiple principal chemical elements in near-equiatomic proportions. These kinds of materials are of interest to many fields due to their remarkable physical properties, such as superior hardness, strength, and great wear resistance [3]. Before the HEAs, the common alloying approach consisted of using a primary element, e.g., iron, followed by the addition of small amounts of secondary elements, e.g., chromium, to increase corrosion resistance, and carbon to increase the strength. This primary element method makes the combination space of elements limited, whereas, in the case of HEAs, many exploitable combinations are still open for discovery, with improved mechanical and thermodynamic performance.

In HEAs, the presence of multiple chemical elements in near-equiatomic proportions (composed of five or more principal elements, with each of them possessing between 5 and 35 atomic percentage) increases sufficiently the entropy of mixing, overcoming the enthalpy formation of the compounds, giving rise to stable solid solution formations, rather than intermetallic compounds [1]. HEAs can also be defined in terms of the calculated mixing entropy ΔS_{mix} by the equation

$$\Delta S_{\text{mix}} = -R \sum_{i=1}^{n} c_i \ln c_i, \tag{1}$$

where c_i is the stoichiometric ratio of the i-th component in the alloy, and R is the gas constant [4]. The mixing entropy can be written in terms of the gas constant R, and HEAs defined when a composition has $\Delta S_{\text{mix}} \geq 1.5\,R$. For $1\,R \leq \Delta S_{\text{mix}} \leq 1.5\,R$ the compounds are defined as medium entropy alloys (MEAs) and for $\Delta S_{\text{mix}} < 1\,R$, low entropy alloys (LEAs) [5]. From Eq. (1) it is possible to see that with the increase of the number of elements, the entropy also increases, e.g., an alloy containing five and six equiatomic elements has $\Delta S_{\text{mix}} = 1.61\,R$ and $1.79\,R$ respectively.

The high entropy effect in HEAs is important because it can enhance the formation of phases. Among the phases in which HEAs can be found, the alloys can be classified as solid-solution (SS), intermetallic (IM), amorphous (AM), or a mixture of them. The SS phase means a significant or

complete mixing of all constituent elements in the structures of body-centered cubic (BCC), face-centered cubic (FCC), or hexagonal close-packed (HCP). IM phases mean stoichiometric compounds with specific Strukturbericht designation, such as B2 (for example NiAl) and $L1_2$ (for example Ni_3Al) [3], [5]. The phase is an important parameter for HEAs since it determines the physical properties. For example, to achieve high hardness, the SS is indicated, for better elasticity, the AM, and for great wear resistance, IM [6], [7].

With the graphic processor unit (GPU) developments using parallel processing for imaging, e.g., in video games, video processing, and simulations, in 2009, a window was opened to make use of GPUs in neural networks [8]. Since then, artificial intelligence applications have had significant growth in applications in all fields, such as in medicine, identifying metastatic breast cancer tumors, or in transport, with autonomous cars. Furthermore, artificial intelligence and machine learning methods can also be used in the field of materials science to speed up discoveries, saving time and money when compared to traditional methods [9], [10], [11].

In this work, artificial intelligence is used to generate synthetic data based on real HEAs found in the literature, and calculated parameters data, providing as output candidates of possible new alloys and corresponding parameters. For that, a dataset containing a large amount of HEAs and specific calculated design parameters [12] was used in a generative model, called conditional tabular generative adversarial network (CTGAN) [13].

II. Methodology

In this section, the methodology used will be discussed, i.e., how the generation of the dataset used in this work was done, as well as the explanation about the Deep Learning methods addressed. Fig. 1 shows a sketch of the workflow, where the dataset containing the phases feeds the generative model, creating new candidates o HEAs, and finally verified in density functional theory (DFT) based open materials databases.

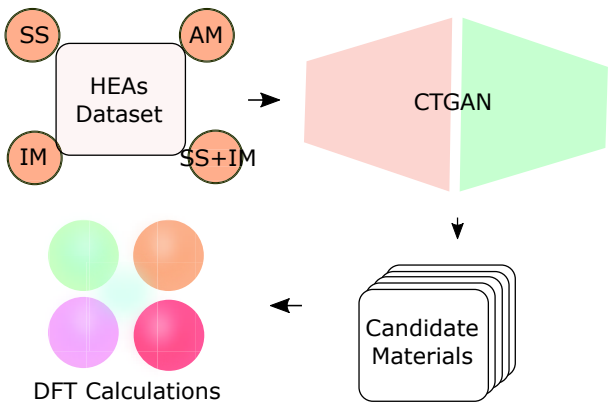

Fig. 1. The approach followed in this work to obtain synthetic HEAs compositions. A specific dataset has been developed and made accessible for this purpose, containing a large amount of HEAs data. The data feeds the CTGAN network architecture, where the Discriminator is used to classify the Generator outcomes until the synthetic compounds become realistic considering real data. Candidate materials that come out from the CTGAN are evaluated via DFT calculations to consider its synthesizability for a real case.

TABLE I
Design parameters.

Parameter	Equation
Mixing entropy	$\Delta S_{mix} = -R\sum_{i=0}^{n} c_i \ln c_i$
Mixing enthalpy	$\Delta H_{\text{mix}} = 4\sum_{i\neq j} c_i c_j H_{ij}$
Standard deviation of mixing enthalpy	$\sigma_{\Delta H} = \sqrt{\sum_{i\neq j} c_i c_j \left(H_{ij} - \Delta H_{mix}\right)^2}$
Mean atomic radius	$a = \sum_{i=0}^{n} c_i r_i$
Atomic size difference	$\delta = \sqrt{\sum_{i=0}^{n} c_i \left(1 - \frac{r_i}{a}\right)^2}$
Electronegativity	$\chi = \sum_{i=0}^{n} c_i \chi_i$
Electronegativity standard deviation	$\Delta\chi = \sqrt{\sum_{i=0}^{n} c_i \left(\chi_i - \chi\right)^2}$
Valence electron concentration (VEC)	$VEC = \sum_{i}^{n} c_i VEC_i$
Standard deviation of VEC	$\sigma_{VEC} = \sqrt{\sum_{i=0}^{n} c_i \left(VEC_i - VEC\right)^2}$
Mean bulk modulus	$K = \sum_{i=0}^{n} c_i K_i$
Standard deviation of bulk modulus	$\sigma_K = \sqrt{\sum_{i=0}^{n} c_i \left(K_i - K\right)^2}$
Averege melting temperature	$T_m = \sum_{i=0}^{n} c_i T_{mi}$
Standard deviation of melting temperature	$\sigma_{T_m} = \sqrt{\sum_{i=0}^{n} c_i \left(1 - \frac{T_{mi}}{T_m}\right)^2}$

A. Data Collection

For this work, a dataset containing several HEAs was prepared. The HEAs were collected from works available in the literature and merged [7], [11], [14], [15], [16]. After filtering and removing duplicated compounds, the given dataset ended with 1117 entries [12]. The phases were used as conditional training parameters, and because this information for some

compounds was unknown, they were also removed, and the dataset used to train the CTGAN model had at the end 1103 entries, composed of 195 AM, 362 IM, 350 SS, and 196 SS+IM.

Previous studies on predicting HEAs phases have used parametric approaches, based on the Hume-Rothery rules, which concern the mutual solubility at high temperatures [3], [11], [17], [18], [19]. Based on these works, 13 design parameters were chosen, calculated, and included in the dataset, i.e., the mixing entropy ΔS_{mix}, where $R = 8.314$ J·K^{-1}·mol^{-1} is the gas constant, and c_i is the stoichiometric ratio of the i-th component in the alloy, the mixing enthalpy ΔH_{mix}, its standard deviation $\sigma_{\Delta H}$, where H_{ij} is the binary mixing enthalpy in the liquid phase, the mean atomic radius a, where r_i is the atomic radius of the i-th component in the alloy, the atomic size difference δ, the Pauling electronegativity χ, its standard deviation $\Delta\chi$, the valence electron concentration VEC, its standard deviation σ_{VEC}, the mean bulk modulus K, its standard deviation σ_K, the average melting temperature T_m, and its standard deviation σ_{T_m}, listed in Table I. Finally, columns containing the chemical elements and their corresponding fraction in the alloy were included and used as conditional training parameters.

B. CTGAN

A neural network (NN) can be fed with a dataset, so that it will learn the relationship between the features present in that dataset, i.e., what characterizes an output and classify it accordingly. But would a NN be able to create synthetic data that is very close to the real data? That's exactly what the generative adversarial networks (GANs) do, turning the world's attention to them in the last years due to their ability to generate realistic fake content. A GAN is a generative model first used to create images [20], but now the scope is extended to create other contents, e.g., furniture designs for 3D printing [21].

The GANs work with two NN models, one competing against the other. One of the models is called generator (G), responsible for generating synthetic data from a noisy entry z (a bunch of random values, e.g., randomized values from a normal distribution between 0 and 1), which tries to generate a synthetic sample as close as possible to a real one. The other model is called discriminator (D), which is trained with both real and fake data, learning the difference between them and classifying the data from the generator as real or fake. The results from the discriminator's classification are used as input for the Generator, which learns from these results and calibrates its weights to generate samples that look closer to the real samples. After the generator improves its generated data, the discriminator is also improved, being updated by the new bunch of samples coming from the generator, calibrating its weights, working as a loop, where the discriminator tries to become better at differentiating the generated from the real data.

In this work, the conditional tabular generative adversarial network (CTGAN) [13] was used, one member of the large family of GANs (DCGAN, WGAN, etc.). This specific kind

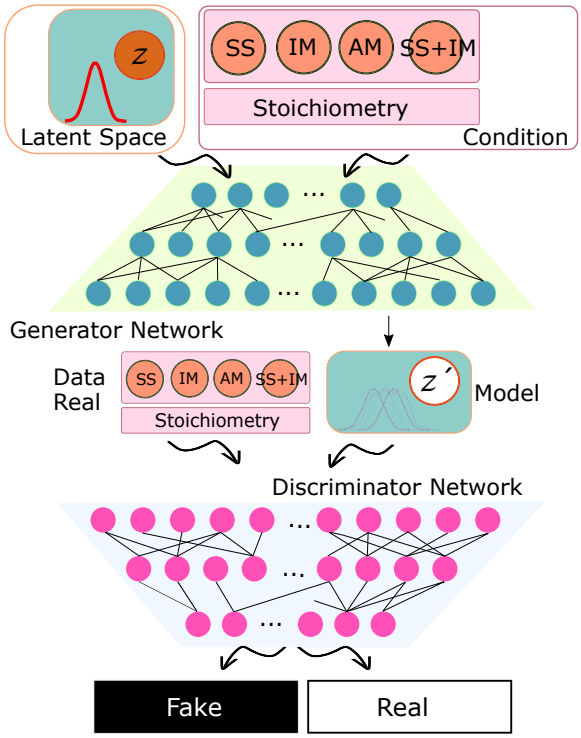

Fig. 2. The main structure of a CTGAN. Random vector and conditions feed the Generator Network, whose outcome feeds the discriminator to classify using also real data to distinguish between real and fake compounds. The architecture of the Networks is described in the main text. The conditions are based on the phases of the compounds and their stoichiometry.

of GAN gives solutions to data problems such as mixed data types, non-Gaussian distributions, multi-modal distributions, learning from sparse one-hot-encoded vectors, and highly imbalanced categorical columns, which normal GANs don't address. Since our HEAs dataset comprises mixed types of data, containing discrete and continuous values, the CTGAN addresses the needs imposed by the dataset, and it can be used to generate new synthetic tabular data.

The CTGAN can be conditioned on some extra information y, which can be any kind of auxiliary information, feeding the network with an additional input layer, e.g., class labels or data from other modalities. In a conditional GAN, the networks G and D are trained and optimized in an adversarial learning framework, called objective function, as follows [22]

$$\min_G \max_D V(D,G) = E_{x\sim p_{data}(x)}[\log D(x|y)] + E_{zp_z(z)}[\log(1 - D(G(z|y)))], \tag{2}$$

where x represents the real data. In the conditional training, the CTGAN encodes the conditioned tabular data columns and categorical variables in condition vectors, using these vectors as generator inputs. This architecture uses recent GAN approaches where the quality and stability of the generated data are improved, e.g., it uses the discriminator of the PacGAN [23], and the loss function of the WGAN-GP [24], defined as

$$L = E_{G(z\sim P_g}[D(G(z))] - E_{x\sim P_r}[D(x)] + \lambda E_{\hat{x}\sim P_{\hat{x}}}[(\|\nabla_{\hat{x}} D(\hat{x})\| - 1)^2], \tag{3}$$

where the two first terms are the original loss of the WGAN [25] and the last term the gradient penalty loss, implemented to control the discriminator's gradient for random samples $\hat{x} \sim P_{\hat{x}}$. $\hat{x}$ represents samples that are interpolated by the real data, λ is the gradient coefficient penalty, and the distribution of the real and generated data are represented by P_r and P_g.

Fig. 2 shows the CTGAN's architecture sketch, comprised of the generator and discriminator models with the conditional entries used in this work, i.e., the phases and stoichiometry to obtain the desired modes from the trained model. Table II summarizes the used architecture. The following parameters were used in both G and D neural networks models: Adam optimizer with a learning rate of 2×10^{-4}, and weight decay of 1×10^{-6}. For G, the ReLU activation was used in the input and hidden layers, and a tanh activation function in the output. For D, the LeakyReLU activation was used in the input and hidden layers and the sigmoid activation function in the output.

TABLE II
CTGAN STRUCTURE USED IN THIS STUDY.

	Generator		Discriminator	
Layer	Type	Dimension	Type	Dimension
Input	Latent + Cond.	90	Features + Cond.	71
Hidden 1	Dense layer	256	Dense layer	256
Hidden 2	Dense layer	128	Dense layer	128
Output	Dense layer	71	Dense layer	1

III. DISCUSSION

In this section, the obtained results using the structure shown in Table II and details mentioned in the previous section are discussed.

A. Generation of Data

The CTGAN was fed with real HEAs data as input, containing the stoichiometry, the phase, and 13 design parameters. The loss function for G and D versus the training epochs is showed in Fig. 3. The convergence of the loss function in both G and D occur at approximately epoch 50, which means that from this point, the model reached a limit where G and D stopped to evolve.

Once the model was trained, synthetic data based on the knowledge acquired during the training process was generated. The outputs provided by the CTGAN were the same 71 parameters used as inputs, i.e., the 13 design features, the 4 phases, and the columns containing the chemical elements fraction. Some of the generated compounds were identical to compounds provided in the input dataset, e.g., the compounds AlCo and $TiZrNbMoV_2$. All generated features were compared with the features in the initial dataset. As result, the values were identical, indicating that the generated data respects the knowledge acquired from the input data.

Within the generation, new compositions were also delivered by the CTGAN. Between the generated compounds, an experimentally known HEA that was not included in the initial dataset was generated, the TiZrCuNiBe, and the correct phase AM was attributed [26], which means that this method really opens the possibility of generating real

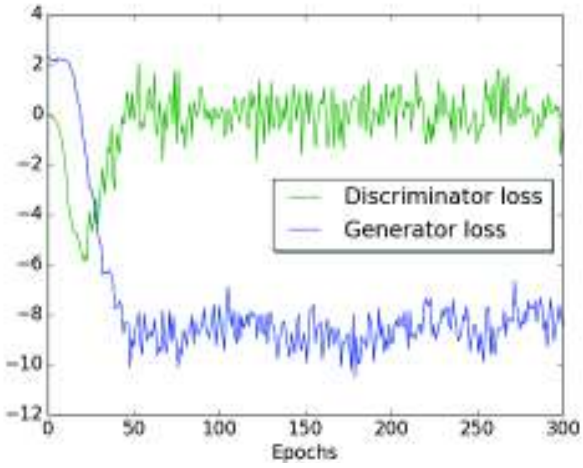

Fig. 3. Generator and Discriminator loss of the CTGAN training progress. The convergence after epoch 50 means that one of the models stopped evolving, and consequently the second model also stops to evolve, since it's a competition between generating fake samples that look real and discriminating these samples as real and fake.

HEAs. Some other examples of possible HEAs candidates (experimentally not proved) are $TiAl_{0.75}CrCo_7Ni$, B_2CoGa_2VZr, $Al_{0.5}BCoCr_{6.3}FeMn$, $AlCoNdNi_{10}Ti$, and $CoCuFeSn_3TiZn_{0.5}$.

The evaluation metrics used to get the score of the model were CSTest, KSTest, KSTestExtended, and ContinuousKL-Divergence, which are statistical metrics found in the ecosystem of libraries of the synthetic data vault (SDV) [27]. The average score value obtained from all these metrics together reached a value of 93 %.

Some of the present compounds in the initial dataset and some generated compounds were taken for evaluation in DFT-based open databases for materials, the Open Quantum Materials Database (OQMD) [28], [29], and Automatic-FLOW for Materials Discovery (AFLOW) [30]. Fig. 4 shows on the upper part four aleatory selected compounds from the HEAs dataset (real compounds), and at the bottom, four compounds selected from the CTGAN generation (synthetic compounds). They are classified according to their phase, i.e., the real phase for the dataset compounds and the expected phase attributed by the CTGAN for the generated compounds. The bars inside the phase areas compare the mixing enthalpy ΔH for the real compounds (in the case of the dataset, calculated from Table I) and synthetic with the mixing enthalpy calculated from the OQMD. When compared, the values are in good agreement in both cases for the real and synthetic data. Note that for comparison purposes, the mixing enthalpy modulus $|\Delta H|$ was used in Fig. 4. Other generated compounds were found in the database of AFLOW, e.g., AlCuTi, $Al_{0.5}CuV$, AlFeNi, and AlCrNiTi, which once more validates the CTGAN as a generative candidate model for the discovery of novel HEAs.

IV. CONCLUSION

With a specific database containing experimentally proved HEAs, a study using the generative model CTGAN was performed to generate new HEAs candidates. The CTGAN

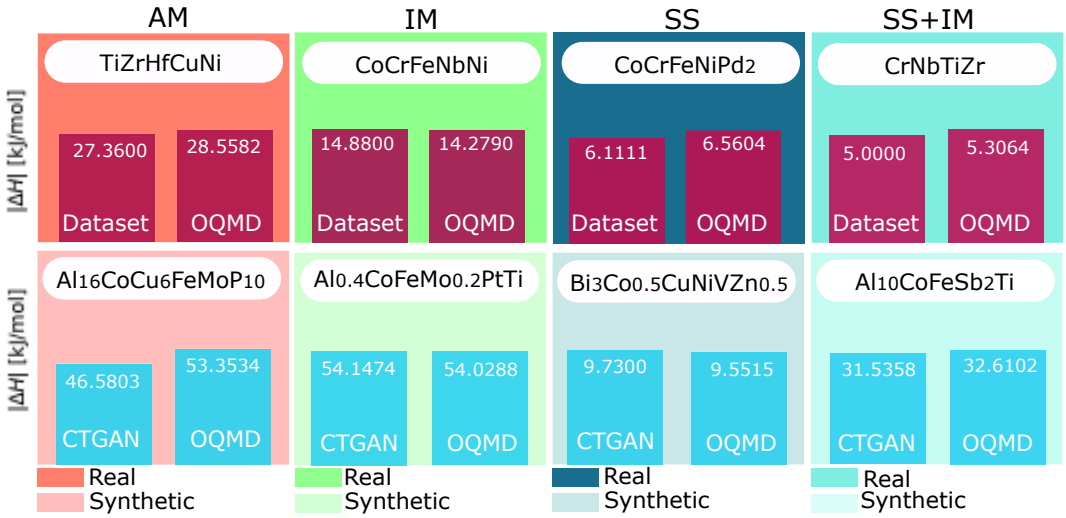

Fig. 4. Main results from the generative approach. Comparison of real values of ΔH for HEAs and those generated by our CTGAN. The figure shows results for the four different phases, AM, IM, SS, and SS+IM, separated in columns. Note that absolute values are shown (all the obtained values for ΔH are negative). The dark boxes contain compounds and ΔH values from real compounds (dark red columns), while those contained in the faded color boxes (blue columns) have been obtained with the CTGAN. The values of ΔH from the dataset and also those generated by the CTGAN are compared with the calculations performed using OQMD.

proved to be a tool that suits this purpose since it can generate experimentally proved compounds. To improve the ability to generate novel HEAs, some filters can be taken into account, e.g., a phase-oriented training, but in that case, more data would be necessary to train the model. Data validation was done using DFT-based open databases, e.g., comparing the mixing entropy calculated by the OQMD and the CTGAN generated values, and finding out that some of the generated compounds were also found in the AFLOW database. The use of artificial intelligence in the materials science field has the potential to improve the industrial sector, e.g., in the case of intensive energy processes by providing alloys with improved thermo-mechanical properties, such as a material with higher strength at high temperatures, being more agile and cost-friendly when compared with traditional methods as trial and error.

Acknowledgment

This research has received funding from the European Union's Horizon 2020 research and innovation programme under the project ACHIEF with Grant Agreement 958374.

The authors want to thank the comments and fruitful discussions with all the members of the Artificial Intelligence and Data Analytics Lab (AIDA-Lab) of the Smart Systems and Smart Manufacturing (S3M) department of AIMEN.

References

[1] J. W. Yeh, S. K. Chen, S. J. Lin, J. Y. Gan, T. S. Chin, T. T. Shun, C. H. Tsau, and S. Y. Chang, *Nanostructured High-Entropy Alloys with Multiple Principal Elements: Novel Alloy Design Concepts and Outcomes*, Advanced Engineering Materials, 2004, vol. 6, no 5, pp. 299-303, DOI: https://doi.org/10.1002/adem.200300567.

[2] B. Cantor, I. T. H. Chang, P. Knight, A. J. B. Vincent, *Microstructural development in equiatomic multicomponent alloys*, Materials Science and Engineering: A, 2004, Vol. 375–377, pp. 213-218, DOI: https://doi.org/10.1016/j.msea.2003.10.257.

[3] X. Wang, W. GUO, Y. FU, *High-entropy alloys: emerging materials for advanced functional applications*, Journal of Materials Chemistry A, 2020, vol. 9, pp. 663-701, DOI: https://doi.org/10.1039/D0TA09601F.

[4] J. W. Yeh, *Physical Metallurgy of High-Entropy Alloys*, JOM 67, 2015, pp. 2254–2261, DOI: https://doi.org/10.1007/s11837-015-1583-5.

[5] J. W. Yeh, *Alloy Design Strategies and Future Trends in High-Entropy Alloys*, JOM 65, 2013, pp. 1759–1771, DOI: https://doi.org/10.1007/s11837-013-0761-6.

[6] Z. Wang, S. Guo, C. T. Liu, *Phase selection in high-entropy alloys: from nonequilibrium to*, Jom, 2014, vol. 66, no 10, p. 1966-1972, DOI: https://doi.org/10.1007/s11837-014-0953-8.

[7] M. H. Tsai, R. C. Tsai, T. Chang, W. F. Huang, *Intermetallic Phases in High-Entropy Alloys: Statistical Analysis of their Prevalence and Structural Inheritance*, Metals, 2019, vol. 9, 247, DOI: https://doi.org/10.3390/met9020247.

[8] R. Raina, A. Madhavan, A. Y. Ng, *Large-scale Deep Unsupervised Learning using Graphics Processors*, ICML '09: Proceedings of the 26th Annual International Conference on Machine Learning, 2009, pp. 873-880, DOI: https://doi.org/10.1145/1553374.1553486.

[9] Y. Dan, Y. Zhao, X. Li, et al. *Generative adversarial networks (GAN) based efficient sampling of chemical composition space for inverse design of inorganic materials*, npj Comput Mater, 2020, vol. 6, 84, DOI: https://doi.org/10.1038/s41524-020-00352-0.

[10] Kaufmann, K., Maryanovsky, D., Mellor, W.M. et al., *Discovery of high-entropy ceramics via machine learning*, npj Comput Mater 6, 42 (2020), DOI: https://doi.org/10.1038/s41524-020-0317-6.

[11] Zhou, Z., Zhou, Y., He, Q. et al., *Machine learning guided appraisal and exploration of phase design for high entropy alloys*, npj Comput Mater 5, 128 (2019), DOI: https://doi.org/10.1038/s41524-019-0265-1.

[12] C. E. Precker, A. Gregores Coto, and S. Muíños-Landín, *Materials for Design Open Repository. High Entropy Alloys*, Zenodo, 2021, DOI: https://doi.org/10.5281/zenodo.5155149.

[13] L. Xu, M. Skoularidou, A. Cuesta-Infante, and K. Veeramachaneni, *Modeling Tabular data using Conditional GAN*, NeurIPS, 2019, Available: https://arxiv.org/abs/1907.00503v2.

[14] D. B. Miracle, O. N. Senkov, *A critical review of high entropy alloys and related concepts*, Acta Materialia, 2017, Vol. 122, pp. 448-511, DOI: https://doi.org/10.1016/j.actamat.2016.08.081.

[15] S. Gorsse, M. H. Nguyen, O. N. Senkov, D. B. Miracle, *Database on the mechanical properties of high entropy alloys and complex con-*

centrated alloys, Data in brief, 2018, vol. 21, p. 2664-2678, DOI: https://doi.org/10.1016/j.dib.2018.11.111.

[16] M. Vaidya, G. M. Muralikrishna, B. S. Murty, *High-entropy alloys by mechanical alloying: A review*, Journal of Materials Research, 2019, vol. 34, pp. 664–686, DOI: https://doi.org/10.1557/jmr.2019.37.

[17] W. Huang, P. Martin, H. L. Zhuang, *Machine-learning phase prediction of high-entropy alloys*, Acta Materialia, 2019, vol. 169, pp. 225-236, DOI: https://doi.org/10.1016/j.actamat.2019.03.012.

[18] Y. Zhang, X. Yang,P. K. Liaw, *Alloy Design and Properties Optimization of High-Entropy Alloys*, JOM, 2012, vol. 64, pp. 830–838, DOI: https://doi.org/10.1007/s11837-012-0366-5.

[19] Y. Zhang, Y. J. Zhou, J. P. Lin, G. L., Chen, P. K. Liaw, *Solid-Solution Phase Formation Rules for Multi-component Alloys*, Advanced Engineering Materials, 2008, vol. 10, issue 6, pp. 534-538, DOI: https://doi.org/10.1002/adem.200700240.

[20] I. J. Goodfellow, J. Pouget-Abadie, M. Mirza, B. Xu, D. Warde-Farley, S. Ozair, A. Courville, Y. Bengio, *Generative Adversarial Networks*, 2014, Available: https://arxiv.org/abs/1406.2661.

[21] C. González-Val, S. Muíños-Landín, *Generative design for Social Manufacturing*, Proceedings of the Workshop on Applied Deep Generative Networks, 2020, 2692, DOI: https://doi.org/10.5281/zenodo.4597558.

[22] M. MIRZA, S. OSINDERO, *Conditional generative adversarial nets*, 2014, Available: https://arxiv.org/abs/1411.1784.

[23] Z. Lin, A. Khetan, G. Fanti and S. Oh, *PacGAN: The Power of Two Samples in Generative Adversarial Networks*, IEEE Journal on Selected Areas in Information Theory, 2020, vol. 1, no. 1, pp. 324-335, DOI: 10.1109/JSAIT.2020.2983071.

[24] I. Gulrajani, F. Ahmed, M. Arjovsky, V. Dumoulin, A. C. Courville, *Improved training of Wasserstein GANs*, 2017, Available: https://arxiv.org/abs/1704.00028.

[25] M. Arjovsky, S. Chintala, and L. Bottou, *Wasserstein GAN*, 2017, Available: http://arxiv.org/abs/1701.07875.

[26] H.Y. Ding, K.F. Yao, *High entropy Ti20Zr20Cu20Ni20Be20 bulk metallic glass*, Journal of Non-Crystalline Solids, 2013, vol. 364, pp. 9-12, ISSN 0022-3093, DOI: https://doi.org/10.1016/j.jnoncrysol.2013.01.022.

[27] N. Patki, R. Wedge, K. Veeramachaneni, *The Synthetic Data Vault*, 2016 IEEE International Conference on Data Science and Advanced Analytics (DSAA), 2016, pp. 399-410, DOI: https://doi.org/10.1109/DSAA.2016.49.

[28] J. E. Saal, S. Kirklin, M. Aykol, B. Meredig, C. Wolverton, *Materials Design and Discovery with High-Throughput Density Functional Theory: The Open Quantum Materials Database (OQMD)*, JOM, 2013, vol. 65, pp. 1501-1509, DOI: https://doi.org/10.1007/s11837-013-0755-4.

[29] S. Kirklin, J. E. Saal, B. Meredig, A. Thompson, J. W. Doak, M. Aykol, S. Rühl, C. Wolverton, *The Open Quantum Materials Database (OQMD): assessing the accuracy of DFT formation energies*, npj Computational Materials 1, 2015 15010, DOI: https://doi.org/10.1038/npjcompumats.2015.10.

[30] S. Curtarolo, W. Setyawan, G. L. W. Hart, M. Jahnatek, R. V. Chepulskii, R. H. Taylor, S. Wang, J. Xue, K. Yang, O. Levy, M. J. Mehl, H. T. Stokes, D. O. Demchenko, D. Morgan, *AFLOW: An automatic framework for high-throughput materials discovery*, Computational Materials Science, 2012, vol. 58, pp. 218-226, ISSN 0927-0256, DOI: https://doi.org/10.1016/j.commatsci.2012.02.005.

Study on Temperature Distribution throughout the Continuous Casting Process of Copper Magnesium Alloys

Paweł Strzępek, Małgorzata Zasadzińska, Szymon Kordaszewski, Wojciech Ściężor

***Abstract*—** The constant tendency toward the materials properties improvement nowadays creates opportunities for the scientists, and furthermore the manufacturers all over the world to design, form and produce new alloys almost every day. Considering the fact that companies all over the world look for alloys with the highest values of mechanical properties coexisting with a reasonable electrical conductivity made it necessary to develop new materials based on copper, such as copper magnesium alloys with over 2 wt. % of Mg. Though, before such new material may be mass produced it must undergo a series of tests in order to determine the production technology and its parameters. The presented study is based on the numerical simulations calculated with the use of finite element method analysis, where the geometry of the cooling system, the material used to produce the cooling system and the surface quality of the graphite crystallizer at the place of contact with the cooling system and its influence on the temperatures throughout the continuous casting process is being investigated. The calculated simulations made it possible to propose the optimal set of equipment necessary for the continuous casting process to be carried out in laboratory conditions with various casting parameters and to determine basic materials properties of the obtained alloys such as hardness, electrical conductivity and homogeneity of the chemical composition.

The authors are grateful for the financial support provided by The National Centre for Research and Development – Research Project No. LIDER/33/0121/L-11/19/NCBR/2020.

***Keywords*—** CuMg alloys, continuous casting, temperature analysis, finite element method.

Paweł Strzępek, Małgorzata Zasadzińska, Szymon Kordaszewski, Wojciech Ściężor are with the AGH University of Science and Technology, Faculty of Non-Ferrous Metals (e-mail: strzepek@agh.edu.pl).

Response of Scented geranium (*Pelargonium graveolens* L.) to iron and zinc chelate nano fertilizers

Mohammad Ali Bahmanyar, Hossein Gholami Varmezabadi, Vahid Akbarpour

***Abstract*—** Scented geranium (Pelargonium graveolens) is a valuable and medicinal plant that contains essential oil, phenol, flavonoid and antioxidant and is used in various industries. In order to investigate the effect of nano-iron and zinc chelate fertilizers on morphological characteristics and some phytochemical attributes of Pelargonium graveolens, a factorial research performed with two factors of spray of nano–iron chelate fertilizer and spray of nano–zinc chelate fertilizer on each five levels (0, 1.5, 2.5, and 3.5 mg.l-1) in a completely randomized design with three replications. Morphological traits including plant height, number of leaves per plant, number of lateral branches, main stem diameter, and petiole length were investigated. Phytochemical traits including chlorophyll content, carotenoid, antioxidant activity, amount of phenolic compounds and total flavonoid were also studied.Analysis of variance showed that the interaction effect of foliar application of iron and zinc nano chelate on morphological traits was significant at leaf number and petiole length at 5% level and at main stem diameter, height, leaf length and number of lateral branch at 1% level and in physiological traits of chlorophyll a, chlorophyll b, total chlorophyll and carotenoid as well as phytochemical traits of phenolic, flavonoid and antioxidant activity were significant at the 1% level. According to the results, the highest number of leave and lateral branch were observed in the treatment (Fe0.5 Zn2.5). Also, the highest stem diameter was observed in the treatments (Fe0 Zn0.5) and (Fe3.5 Zn0) and the highest plant height in treatment (Fe0.5Zn3.5). The highest pellet length was obtained in the treatment (Fe2.5 Zn2.5) and the longest petiole length in the treatments (Fe1.5 Zn0), (Fe2.5 Zn2.5) and (Fe3.5 Zn3.5). Rate of Chlorophyll a, total chlorophyll and carotenoids were highest in treatment of (Fe0.5 Zn1.5) with means 6.48, 7.44 and 410.28 mg/g fresh weight, respectively and Fe0 Zn1.5 was the most effective treatment for chlorophyll b with average of 1.21 mg.g-1 fresh weight. The highest amount of total antioxidant in the treatment (Fe3.5 Zn1.5) was 86.87% as well as the total flavonoid content in the treatment (Fe1.5 Zn0) was 2.86 mg quercetin per gram of dry matter. The control (Fe0 Zn0) had the highest total phenol content compared to other treatments with 1.66 mg gallic acid per gram of dry matter. The results show that the use of low concentrations of nano-iron and zinc chelate fertilizer can increase the yield components and biochemical traits of the Pelargonium graveolens, which suggests suitable or low concentrations of these nano-iron and zinc chelated fertilizers. basil.

***Keywords*—** Antioxidant, Nano fertilizer, Pelargonium graveolens, Photosynthetic pigment

Mohammad Ali Bahmanyar is with the Department of Soil Sciences, Faculty of Crop Sciences, Sari Agricultural Sciences and Natural Resources University, Sari, Iran (e-mail: mali.bahmanyar@gmail.com).

Hossein Gholami Varmezabadi, is Graduated M.Sc. Student of Medicinal Plants, Sana Institute of Higher Education, Sari, Iran (e-mail: y_valiollahi@yahoo.com).

Vahid Akbarpour, is with the Horticultural Sciences and Engineering Department, Faculty of Crop Sciences, Sari Agricultural Sciences and Natural Resources University, Sari; (e-mail: v_akbarpour60@yahoo.com).

Yield Response of Pepper (Capsicum Frutescence) to Source of P Application in Anyigba, Kogi State, Nigeria

Charles Iledun Oyewole

***Abstract*—** The use of both organic and inorganic manures have been reported to enhance soil productivity, increase the soil organic carbon content, soil micro-organism, improve soil and enhance crop yield. The superiority and richness of combination of organic manures and mineral fertilizers over single manure applications have been confirmed in other studies. The study evaluates effect of P - source (as NPK 15:15:15 or cow dung manure) on the growth and yield of pepper (Capsicum frutescence) in Anyigba (latitude 7o151N and 7o291N and longitude 7o111E and 7o321E with altitude of 420m above sea level). The treatment components were a control: 60 kg and 120 P/ha (applied as cow dung) as well as 60 kg and 120 kg P/ha (applied as NPK 15:15:15) in addition to 60 kg and 120 kg P/ha as equal split between NPK 15:15:15 and cow dung.in a Randomized Complete Block Design (RCBD) with three replications. Data on growth and yield components were taken at 2, 4, 6, and 8 weeks after transplanting (WAT). Generally nutrient source did not differ significantly relative to plant height, leaf number and stem girth. Nutrient addition however indicate better significant performance when compared with the control. Regarding crop yield application of 120 kg P /ha in split equal doze of NPK 15:15:15 + Cow dung gave the best yield result.

***Keywords*—** Plant height, NPK fertilizer, Number of leaves, Organic fertilizer, Stem girth.

Charles Iledun Oyewole is with the Kogi State University Anyigba, Nigeria (e-mail: oyewole.ci@ksu.edu.ng).

Microfluidic Based Chips for SERS Ultrasensitive Detection

Sergio Gómez-Graña,[a] Daniel García-Lojo,[a] Isabel Pastoriza-Santos[a] and Jorge Perez-Juste[a]

a Departamento de Química Física y Centro Singular de Investigaciones biomédicas (CINBIO) Universidade de Vigo 36310 Vigo (Spain)

Microfluidic platforms allow generating a highly-ordered assembly of uniform gold nanoparticles inside their microchannels through the pervaporation of the solvent (Figure 1A).[1] Furthermore, the microfluidic approach enables the fabrication of uniform assemblies of any dimension or morphology studied by SAXS.

Surface-enhanced Raman spectroscopy, SERS, is an advanced analytical technique that can be used for the ultra-sensible detection of analytes since it offers orders of magnitude increases in Raman signals. It occurs at the surface of a plasmon surface mainly due to the presence of strong electromagnetic fields generated after the plasmon excitation. Moreover, this effect could be more intense in the case of hierarchical nanoparticles assemblies due to an antenna effect as demonstrated by recent simulations.[2] While the plasmonic substrates made by drop-casting show poor uniformity that limits their potential plasmonic applications, the microfluidic approach gives rise to platforms with highly uniform and intense SERS activity (being both key parameter to achieve quantitative analysis and low detection limits (LOD). Herein this study will show the fabrication and characterization of plasmonic platforms fabricated using Au octahedral nanoparticles synthesized through a wet chemical method. Besides, the sensing capabilities of the platforms will be analyzed by investigating the SERS efficiency using different Raman active analytes. For instance, experiment performed with Crystal Violet showed a LOD of 100 zM, which is several orders of magnitude lower than those found in the literature. Additionally, by assembling a 3D silica super-crystal before the 3D plasmonic super-crystal the study demonstrated its potential applicability as microfluidic liquid chromatography-chip with SERS-based sensing capabilities. [3]

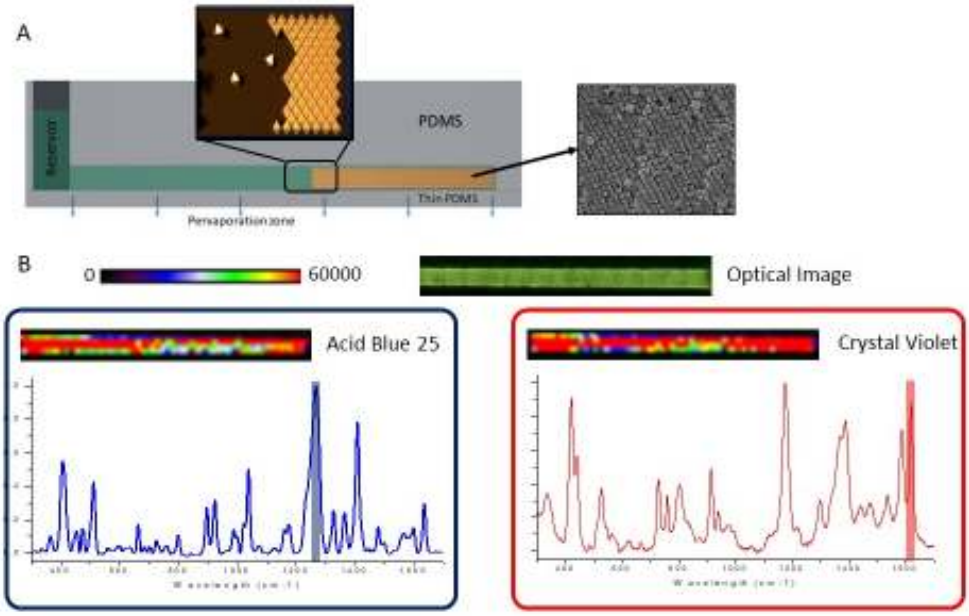

Figure 1: (A) Schematic illustration of the evaporated microfluidic system used for self-assembled Au nanoparticles with a SEM micrograph of the nanoparticles assembly. (B) Raman optical image and SERS spectra and mapping at 1270 cm^{-1} for acid blue 25 and 1618 cm^{-1} in the presence of a mixture of 10^{-7} M of each analyte.

References

(1) Gómez-Graña, S., et al. Gold Nanooctahedra with Tunable Size and Microfluidic-Induced 3D Assembly for Highly

Uniform SERS-Active Supercrystals. *Chem. Mater.* **2015**, acs.chemmater.5b03620.
(2) Solís, D. M., et al. Toward Ultimate Nanoplasmonics Modeling. *ACS Nano* **2014**, *8* (8), 7559–7570.
(3) García-Lojo D. Integrating plasmonic supercrystals in microfluidic for ultrasensitive, label-free, and selective Surface Enhanced Raman Spectroscopy detection. *ACS Appl. Mater & Interf.* **2020** (41) 46557-46564

A Public Health Approach to Emotional Intelligence

Michael G. Schwab

***Abstract*—**Many emotions are associated with health and disease at a personal and collective level. In public health, they form a part of the web of causation that underlies problems as diverse as diabetes, depression and violence. For example, frustration, anger, pride and greed all contribute to violence, which is a major cause of death and disability. Emotional intelligence (EI) is a critical element of interventions designed to address violence and has gained traction in some populations. A public health approach would address not only 'EI-deficiency' as a risk factor for violence, but also the factors that contribute to that deficiency (for example, poor education, lack of access to care, racism, violent media). It would explore not only social and emotional learning as a remedy, valuable though these are, but also actions to address the underlying conditions. This would necessarily involve collaboration across sectors, across industries and across disciplines.

***Keywords*—**Public Health, Emotional Intelligence, Violence Prevention,

Dr. Michael Schwab is with the College of Health Sciences, Walden University (phone: 505-670-3408; e-mail: michael.schwab@mail.waldenu.edu

Correlative Look at Relationship between Emotional Intelligence and Effective Crisis Management in Context of Covid-19 in France and Canada

Brittany Duboz-Quinville

***Abstract*—** Emotional Intelligence (EI) is a growing field, and many studies are examining how it pertains to the workplace. In the context of crisis management several studies have postulated that EI could play a role in individuals' ability to execute crisis plans. However, research evaluating the EI of leaders who have actually managed a crisis is still lacking. The COVID-19 pandemic forced many businesses into a crisis situation beginning in March and April of 2020. This study sought to measure both EI and effective crisis management (CM) during the COVID-19 pandemic to determine if they were positively correlated. A quantitative survey was distributed via the internet that comprised of 15 EI statements, and 15 CM statements with Likert scale responses, and 6 demographic questions with discrete responses. The hypothesis of the study was: it is believed that EI correlates positively with effective crisis management. The results of the study did not support the studies hypothesis as the correlation between EI and CM was not statistically significant. An additional correlation was tested, comparing employees' perception of their superiors' EI (Perception) to employees' opinion of how their superiors managed the crisis (Opinion). This Opinion and Perception correlation was statistically significant. Furthermore, by examining this correlation through demographic divisions there are additional significant results, notably that French speaking employees have a stronger Opinion/Perception correlation than English speaking employees. Implications for cultural differences in EI and CM are discussed as well as possible differences across job sectors. Finally, it is hoped that this study will serve to convince more companies, particularly in France, to embrace EI training for staff and especially managers.

***Keywords*—** crisis management, emotional intelligence, empathy, management training.

Brittany Duboz-Quinville is with the IAE Lyon, France (e-mail: brquinville@gmail.com).

Post-Covid 19 Pandemic Economy: Corporate Governance and Performance of Private Security Firms in Kenya

Sewe Silvanus Odhiambo

***Abstract*—** Globally, many governments have publicly recognized private security firms as essential services providers. The private security firms face a lot of challenges, but the COVID-19 situation also has exacerbated them to another level. This paper locates its relevance in the post-coronavirus era. The COVID-19 pandemic has redefined the world operation which shows a higher impact on the security field. Accordingly, the purpose of the study was to examine the role of corporate governance on performance of private security firms in a post-covid pandemic era in Kenya. The study employed descriptive research design which included quantitative approach and secondary data. The study was carried in the month of July, 2021 from the registered private security firms. After targeting all private security firms, only 54 firms had disclosed their annual report by the time of conducting the study. The results depicted that pandemic has affected performance of private security firms measures unfavorably. Further, boards of director's show a positive association with security firm performance. The study recommends that there is need board of directors to enhance management's risk assessments in the midst of COVID-19; ensure that there are business continuity plans; there is organizational resilience; there is need for development of new digital strategies; enabling the digital workforce in the firms and have effective communication plans with both internal and external stakeholders to deal with uncertainties and develop more post-COVID practices for boards of directors to improve performance of private security firms in Kenya. The practical implications of the study is that the research outcomes might assist regulatory bodies, investors, policymakers and security sector in general in their formulation of public and corporate governance strategies concerning future emergency preparedness and responses. This study also provides a unique contribution to the literature of COVID-19 and security firm performance in emerging economies context.

***Keywords*—** COVID-19,Corporate Governance,Firm Performance,Private Security firms.

Silvanus Sewe is with the Jomo Kenyatta University of Agriculture and Technology, Kenya (e-mail: sewememory@yahoo.com).

Developing a Model for Lifelong Learning within Purchasing and Supply Management

V. Delke, J. te Raa

Purpose**—**Today, purchasing and supply management (PSM) has developed to a knowledge-intensive and fluid field that requires professionals with specific skills. The notions of a divided lifetime, where work follows education, are no longer feasible. Here, the PSM environment changes due to new technologies supporting, replacing, and introducing new purchasing tasks. Scholars often describe this phenomenon as a new industry paradigm called Industry 4.0. Following the assumption of working environment changes and skills, purchasing professionals must be educated and trained continuously. For this reason, this work develops a model for lifelong learning within the field of PSM by combining practitioner training and higher education study programs. Thus this research tries to answer the research question: How to achieve lifelong learning within purchasing and supply management?

Methodology**—**This study utilises a multiple-method approach. First, the current needs within industry and available educational programs are explored by a multiple-case study. The multiple-case study also analyses the purchasing maturity stages and human resource development strategies of 15 firms in the Netherlands. Second, secondary data on available practitioner training and study programs offered are analysed. Here, the content of existing professional training and higher education study programs is explored. Third, a lifelong learning model is developed based on the multiple-case study outcome and higher education experts' experience within PSM. Therefore, the lifelong learning model will be the outcome of this research.

Findings**—**The multiple-case study results show a low maturity level in purchasing for the cases addressed, with little focus on human resource development. A lifelong learning process is necessary to keep up with rapid developments in the current business environment. In contrast to what the literature suggests, financial constraints do not seem to be the reason for missing a personal development policy. Respondents claimed that a structural personal development policy on both individuals and collective level could improve purchasing performances due to greater human resources. Here, findings show a limited supply of purchasing education and training in the Netherlands. Educational institutions such as NCOI, LOI and ISBW offer purchasing education on a basic level. After that, the NEVI offers specialised education that is highly recognised and respected nationally. With NEVI I and NEVI II training, purchasing professional create a strong foundation in terms of competence and knowledge level for the purchasing function. However, from a purchasing maturity perspective, this available purchasing training does not provide skills within purchasing latest developments. Here, universities hold the knowledge of future developments within the field based on their explorative research activities. This research suggests combining practitioner educational programs and higher educational institute teaching to realise lifelong learning for students and the current workforce (see figure 1).

V. Delke is with the University of Twente, Chair Technology Management and Supply, PO Box 217, 7500 AE Enschede, The Netherlands (e-mail: v.f.delke@utwente.nl).

J. te Raa is with the University of Twente, Chair Technology Management and Supply, PO Box 217, 7500 AE Enschede, The Netherlands (e-mail:jordyteraa@hotmail.nl).

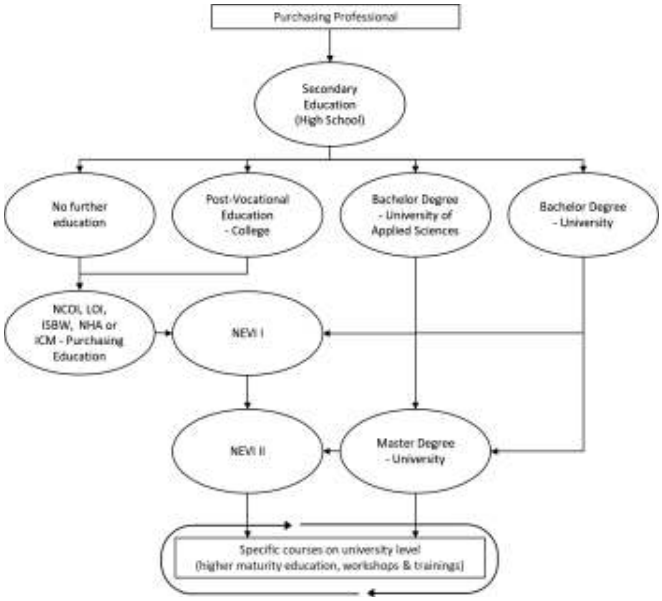

Fig. 1 Suggested model for lifelong learning in PSM

Contribution**—**This work contributes by providing a lifelong learning model within PSM. The model provides a guideline for an organisation to increase purchasing maturity by implementing a bottom-up approach, starting with sophisticated human resource development strategies. Here, the study suggests creating competence profiles (or job profiles) which can be used to identify competence gaps among purchasing employees. With the help of job- or competence profiles, organisations can create a standard policy to determine each individual's further education.

Further, an assessment to identify skill requirements and competency gaps should be performed regularly. The assessments are key to this concept, which stimulates continuous learning. This approach meets the demands of purchasing professionals towards a structural collective and individual approach to a personal development plan. Thus, the model ensures individuals (and therefore also organisations) meet the purchasing function's future needs. The lifelong learning model is especially supported by the specific courses which are organised on a university level. Professional can attend these courses to obtain current and future-oriented skills, realising continuous improvement.

Tactile Strategies for the Education of Tensile Membrane Structures using a Full-Scale Membrane Teaching Kit: Case Study of the University of Surrey

Dr Alireza S. Behnejad, Saajan Bassi

***Abstract*—**Accelerated development in structural membrane technology and practice since the 1950s has increased the difficulty for fledglings to contribute to the field [1]. Thus, educational strategies should be employed to increase student understanding of membrane structures at undergraduate level.

This research focuses on the importance and effectiveness of tactile teaching methods in the education of tensile membrane structures at undergraduate level. Students gaining membrane construction experience and improving their understanding about tensile membrane structure design have been identified as key learning outcomes. The selection of these objectives is supported by the works of Lewis [2] and Adriaenssens [3].

The DAD Project requires students to deliver the Design, Assembly and Dismantling of a full-scale lattice structure, with a teaching kit comprised of prefabricated tubular steel members and connectors. Group participants develop and construct designs using the available kit (Figure 1), focussing on health and safety as well as honing creative and management skills.

Figure 1: Example of a structure constructed by first-year undergraduate students in June 2016.

Figure 2: The new full-scale membrane teaching kit constructed by undergraduate students in April 2021.

The full paper will present a new case study – a full-scale teaching kit utilised in workshops at the University of Surrey for the DAD Project (Figure 2), as well as other educational schemes using tactile strategies such as those from the University of Belgrade and Sadjad University of Technology.

***Keywords*—**Education, Membrane, Structural Membrane, Tactile Teaching.

***References*—**

[1] Huntington, G. C. (2013) Tensile Fabric Structures: Design, Analysis, and Construction. Reston, VA: American Society of Civil Engineers. doi: 10.1061/9780784412893 (Accessed: 01 June 2021).

[2] Lewis, W. J. (2003) Tension structures: form and behaviour. London: Thomas Telford.

[3] Adriaenssens, S. et al. (2015) 'A Project-Based Approach to Learning Form Finding of Structural Surfaces', International Journal of Space Structures, 30, pp. 297–306. doi: 10.1260/0266-3511.30.3-4.297. (Accessed: 10 June 2021).

Dr Alireza S. Behnejad is with the Department of Civil and Environmental Engineering at the University of Surrey, Guildford, Surrey GU2 7XH, United Kingdom, Email: a.behnejad@surrey.ac.uk.

Saajan Bassi is with the Department of Civil and Environmental Engineering at the University of Surrey, Guildford, Surrey GU2 7XH, United Kingdom, Email: sb01124@surrey.ac.uk.

The Smart City: A New Solution to Urban Shrinkage? Evidence from China

Zixuan Han, Kangjun Peng, Jianing Mi, Bin Li

***Abstract*—** Urban shrinkage is a prevalent challenge with a marked feature of population loss. By revisiting current global solutions of urban shrinkage, we find notable drawbacks that are required to be resolved and grounded presume that the smart city strategy which constitutes a dominant vision for cultivating a more sustainable future for urban economy and living quality could be a complementary recipe. As China's national smart city pilot projects in 2013 contained 34 prefecture-level pilot cities facing urban shrinkage, the study takes the pilot projects as a quasi-experiment to verify the presumption and answer how smart cities could bring a brighter future for shrinking cities. By difference-in-difference method based on propensity score matching (PSM-DID), the study finds significant effects of smart city strategies on shrinking cities in catalysing sustainable economic growth by upgrading and diversifying local industries, promoting economic growth, and providing better quality of life for citizens through improved wages and quality of urban environment, and enhanced public service. By clarifying the generalizability of theories, policies and intervention strategies, the study also implicates policy significance to other countries.

***Keywords*—** Shrinking cities,smart cities,policy response,pilot project,difference-in-difference,China.

Zixuan Han is with the Harbin Institute of Technology, China (e-mail: hithanzx@gmail.com).

The Impact of Socio Political Conflicts on Young Children and Their Education System at Sebha City, Libya

Fatimah Ali

***Abstract*—** 1.1 Overview:

This study was made because we had comprehended that the war had effect in everything in our daily life, universally here in our city SEBHA. Since 2011,till, 2015 students have had seen a lot of actions which effect in their environment, education system , their learning habits, their thinking ability and that effects the students while learning the English language, the researcher investigate about How the English language can be effected by the war, Why it was effected? What was the things that help this problem to take time ? and what's the solution for this problem? Moreover all of that is important for the students future and that what we try to clarify in the coming study . There is little doubt that wars cause stagnation of many development programs, including education. Writing from the Ethiopian civil war experience, Rowley (1998, 482) reveals that, "the civil war with Eritrea and the time of the 'Dreg' impacted schools and families". The civil wars have been very costly and they have crippled social infrastructures including education and other basic and necessary social services (Waal and Vines 1992; Malecela 1999). The civil wars have not only been causing inestimable cost in the war zones but also in the neighboring countries, which suffer the effects of civil wars directly and indirectly. As Goulding (1999, 157-159) puts it:

***Keywords*—** war conflicts, society, education, children.

Fatimah Ali is with the Sebha University, Libya (e-mail: tame.tame313@gmail.com).

Comparison of Use of Typical and Atypical Antipsychotics in the Development of Obsessive-Compulsive Symptoms in Patients with Schizophrenia

Afshan Niknafs,

Department of Psychology,University of Tehran,Tehran,Iran afshan.niknafs@ut.ac.ir

***Abstract*— Objective**: In this study, the effect of typical and atypical antipsychotics in the development of obsessive-compulsive symptoms in patients with schizophrenia was compared. **Method**: In a descriptive-comparative study, 64 patients with schizophrenia (32 patients in the group of typical antipsychotics and 32 patients in the group of atypical antipsychotics) were studied. All patients who received a definitive diagnosis of schizophrenia based on a structured clinical interview for DSMV (SCID-I) Axis I Disorders, underwent two Yale–Brown Obsessive Compulsive Scale (YBOCS) and a Brief Psychiatric Rating Scale (bprs) tests at baseline, three weeks and six weeks after treatment. The obtained data were analyzed by descriptive statistics, repeated measures analysis of variance and t-test. **Results**: In the receiving typical antipsychotics group, the mean score of YBOCS test was 2.40, 2.30 and 2.18 before the start of treatment, three weeks and six weeks after it, respectively. In the group of atypical antipsychotics, the mean score of YBOCS test at the beginning of treatment, three, and six weeks after treatment was 4.12, 4.46 and 4.53, respectively. The difference in YBOCS test scores between the two groups receiving typical and atypical antipsychotics before treatment was close to a significant level and was significant in the third and sixth weeks of treatment ($p < 0.05$). In the typical group, one patient with a positive family history showed a decrease in obsessive-compulsive symptoms and in the atypical group, a patient with a positive family history showed an increase in obsessive-compulsive symptoms. **Conclusion:** Atypical antipsychotics can cause obsessive (albeit mild) symptoms in patients with schizophrenia. Despite the importance of family history in clinical manifestations of obsessive-compulsive disorder in users of atypical antipsychotics, the role of this variable in reducing or increasing obsessive-compulsive symptoms was small.

***Keywords*—** typical antipsychotics, atypical antipsychotics, obsessive symptoms, schizophrenia.

Long Term Follow up of Single Incision Laparoscopic Cholecystectomy Compared to Conventional Laparoscopic Cholecystectomy

Hayder Shabana, Abdul-Karim Abbas, Darragh Grace, Jeremy Kay Hock Lee, Colm J O'Boyle

***Abstract*—** Purpose: Conventional Laparoscopic Cholecystectomy (CLC) is the "gold standard" approach for patients with gallstones. Single-incision Laparoscopic Cholecystectomy (SILC) was an alternative technique, purportedly offering several postoperative benefits over CLC. Studies comparing short-term postoperative outcomes of SILC versus CLC have yielded conflicting results. Our paper aims to compare the long-term postoperative outcomes of patients undergoing SILC and CLC with a minimum follow up of seven years.

Methods: A comparative retrospective study between SILC and CLC was conducted among 118 patients undergoing cholecystectomy from October 2008 to December 2010 (SILC=67/CLC=61). An initial retrospective chart review was performed. We later surveyed the patients who had undergone cholecystectomy by telephone interview at a mean(sd) of 4(0.75) years, and at 8(0.75) years. Postoperative outcomes were evaluated.

Results: No significant difference between SILC and CLC groups for daily pain scores ($p = 0.45$ and 0.97, for day 1 and 2, respectively), daily narcotic requirements ($p = 0.09$ and 0.85, for day 1 and 2, respectively), and time to return to normal activity ($p = 0.11$). The mean(sd) operative time was greater in SILC group [52(2.0) mins versus 36(2.3) mins; $p < 0.05$]. There was a shorter mean(sd) length of stay postoperatively in the SILC group [2(0.11) days versus 3(0.32) days; $p < 0.05$]. The SILC group had a higher median(sd) cosmetic satisfaction score (IQR) than the CLC group at both the intermediate-term [10(10) versus 9(8 to10); $p < 0.05$] and long-term [10(10) versus 9(9to10); $p < 0.05$] follow up.

Conclusion: SILC is associated with higher patient cosmetic satisfaction than CLC. However, the procedure is more technically challenging and associated with increased operating time and costs. The marginal cosmetic benefit at the expense of increased operative time and economic costs will likely mean that the choice of procedure will be largely patient rather than physician driven.

***Keywords*—** Conventional laparoscopic cholecystectomy, Cosmetic satisfaction, Long-term follow up , Single-incision laparoscopic cholecystectomy.

Hayder Shabana, Darragh Grace, Colm J O'Boyle are with the Bon Secours Hospital of Cork, Cork, Ireland.

Abdul-Karim Abbas is with the Sahlgrenska Academy, University of Gothenburg, Gothenburg, Sweden.

Jeremy Kay Hock Lee is with the College of Medicine and Health, University College Cork, Ireland (Tel: +353 0831817939; e-mail: j-lee95@hotmail.com).

Classification and Hierarchical Cluster Analysis of Principal Romanian Bottled Mineral Waters

Zsolt Bodor, Katalin Bodor, Alexandru Szep, Robert Szep, Agnes Keresztesi

***Abstract*—** In the present study, 53 commercially available mineral water brands were collected from the Romanian market and have been analyzed based on the chemical, mineral content as labeled by manufacturers. The selected chemical parameters were, from the cations: Ca^{2+}, Mg^{2+}, Na^{+}, K^{+}, from the anions: HCO-3, Cl-, SO2-4 , and fixed residue at 180ºC. The Spearman correlation showed that cations (Ca^{2+}, Mg^{2+}, Na^{+}, K^{+}) had positive correlation with the , the correlation coefficients were 0.90, 0.83, and 0.75. The mineral content varied between a large spectrum. According to the fixed residue, the distribution of low, medium, and rich mineralized water was 43.9%, 41.46%, and 14.63%, respectively. Based on ion composition mineral waters can be classified as: bicarbonate-, calcium-, magnesium-sodium waters with 34%, 26.4%, 24.5%, and 18.9%, respectively. The Hierarchical Cluster Analysis (HCA) resulted in two different clusters and five sub-clusters; cluster 1 had three mineral and bicarbonate grads (1.1-low, 1.3-medium, and 1.2-high), and the average Ca2+/Mg2+ ratios varied between 3.61-5.71. The mineral water brands with very high mineral and bicarbonate content belonged to cluster 2. The differences in chemical composition of the bottled waters can be mainly attributed to the host rocks geology, underground residence time and physico-chemical parameters as well.

***Keywords*—** bottled mineral water, fixed residue, mineral content, Romania.

Zsolt Bodor is with the Sapientia Hungarian University of Transylvania, Romania (e-mail: bodorzsolt@uni.sapientia.ro).

Environmental and Nutritional Challenges with Down's Syndrome

L. Aljerf

***Abstract*— Background:** Down's syndrome patients are suffering from such gastrointestinal and metabolic complications which affect their prolongation for survival and this could be attributed to the malnutrition system. To reduce the risk factors for mortality, the paper has focused on the assessment of the socioeconomic, clinical, physical, biophysiological, and biochemical characteristics of them which can be affected by the type of nutrition system, toxicity, and ecological footprint.

Methods: Patients were males with trisomy 21 diagnosed by karyotype test and assessed by clinical examinations. The clinical observations, medical interventions, and oral diseases associated with DS have been defined and oral treatment is explored. Samples collected from different biofluids. The physicochemical analyses of the biomatrix samples were performed and these properties had compared to findings of healthy males and age-matched controls. In specific, trace elements which could be originated from environmental resources were assessed in saliva, blood, urine, and hair.

Results: Duraphat application was proved effective for their oral treatment and saliva was the optimum biomarker for detecting malnutrition. The patients were hypersensitive to Cu while the Mn content in blood and hair was considered an expression to the degree of epileptic condition and chronic seizure development. The ecological footprint was 5.6 gha and carbon footprint was recognised in food poverty habits. These can be reduced by eating more plant-based proteins and fibre-rich foods with low saturated fats and sodium.

Conclusion: The current findings provide an up-to-date reference for expected developmental outcomes in children with DS in terms of biophysicochemistry. The genetically sensitive intervention is affected by heredity factor and sensitivity to toxics. Down's syndrome is encouraged to live green-hipster life. Besides, doctors are recommended to order the physicochemical analyses for early detection of this special intervention.

***Keywords*—** Carbon footprint, Energy metabolism, Nutrition system, Toxicity.

L. Aljerf is with the Department of Basic Sciences, Faculty of Dental Medicine, Damascus University, Damascus, Syria (phone: 963-944-482203; fax: 963-11-2718704; e-mail: envirochrom@hotmail.com).

Microbial Terroir of the Viticultural Nemea Protected Designation of Origin Zone of Greece

Lena Payati, Maria Kazou, Effie Tsakalidou

***Abstract*—** Vitivinicultural microbial "terroir" uncovers the impact of vineyard characteristics, such as grape cultivar, geographical region, climate conditions and applied vitivinicultural practices, on grapes' microbiota suggesting that there is a unique microbial fingerprint associated with the terroir. Until recently, the microbial diversity of grapes and wine has been explored mostly by culture-depended techniques. However, to overcome the limitations of these techniques, culture-independent approaches have been recently developed to study food microbial ecosystems. Among them, high-throughput sequencing, and, in particular, the amplicon-based metagenomics is nowadays the golden standard to elucidate microbial terroir. Agiorgitiko (Vitis vinifera L. cv.) is the most popular indigenous grape variety in Greece, grown in the Protected Designation of Origin (PDO) Nemea zone. Both terrain and climate conditions are quite diverse along the zone, resulting the informal division of the zone into three sub-zones, which impact the maturation process and the microbial ecology as well as the physicochemical characteristics of the grapes. The present study, the first of its kind in Greece, aims at depicting the microbial fingerprint of the sub-zones of Nemea, by examining the grapes' microbial biodiversity over time and space using amplicon-based metagenomics analysis. Towards this, 25 vineyards from four different areas of the Nemea PDO zone were selected, and grape and soil samples were collected at harvest from two consecutive harvest seasons (2019 and 2020). Total DNA was extracted from all samples and the 16S rRNA gene and ITS DNA region were sequenced and analyzed by bioinformatics tools for the identification of the bacteria and yeasts/fungi diversity, respectively, while statistical analyses were also employed. The results revealed that, generally, soil yeasts/fungi biodiversity was higher than that of grapes. Moreover, yeasts/fungi biodiversity varied among the four regions, no matter soil or grapes. In particular, Fusarium, Robillarda, Ascobolus, Alternaria, Truncatella, Geomyces, Leucoagaricus and Cryptococcus dominated in the soil samples, whereas Aureobasidium, Aspergillus, Cladosporium, Alternaria and Penicillium were the prevailing yeasts/fungi genera in grapes, with varying abundances depending on both region and time. On the other hand, bacteria diversity was higher than that of yeasts/fungi, in both grapes and soil, with the genus Acidobacterium dominating in both ecosystems, followed by several other genera, such as Pseudomonas, Rubrobacter, Skermanella, Gemmatimonas, Ohtaekwangia, Microvirga and Sphingomonas with minor abundance differences among the four regions and the harvest seasons. Principal component analysis (PCA) clustered the majority of vineyards together, regardless the yeasts/fungi or bacteria communities, thus, showing a joint microbiota fingerprint for the Nemea PDO zone; a couple of outliers observed might be attributed to variations in cultivation conditions.

***Keywords*—** Agiorgitiko, amplicon-based metagenomics analysis, grape and soil microbiota, Nemea, terroir, Vitis vinifera.

Lena Payati is with the Agricultural University of Athens, Greece (e-mail: lenapagiati@aua.gr).

Microbial Biogeography of Greek Olive Varieties Assessed by Amplicon-Based Metagenomics Analysis

Lena Payati, Maria Kazou, Effie Tsakalidou

***Abstract*—** Table olives are one of the most popular fermented vegetables worldwide, which along with olive oil, have a crucial role in the world economy. They are highly appreciated by the consumers for their characteristic taste and pleasant aromas, while several health and nutritional benefits have been reported as well. Until recently, microbial biogeography, i.e., the study of microbial diversity over time and space, has been mainly associated with wine. However, nowadays, the term 'terroir' has been extended to other crops and food products so as to link the geographical origin and environmental conditions to quality aspects of fermented foods. Taking the above into consideration, the present study focuses on the microbial fingerprinting of the most important olive varieties of Greece with the state-of-the-art amplicon-based metagenomics analysis. Towards this, in 2019, 61 samples from 38 different olive varieties were collected at the final stage of ripening from 13 well spread geographical regions in Greece. For the metagenomics analysis, total DNA was extracted from the olive samples, and the 16S rRNA gene and ITS DNA region were sequenced and analyzed using bioinformatics tools for the identification of bacterial and yeasts/fungal diversity, respectively. Furthermore, principal component analysis (PCA) was also performed for data clustering based on the average microbial composition of all samples from each region of origin. According to the composition, results obtained, when samples were analyzed separately, the majority of both bacteria (such as Pantoea, Enterobacter, Roserbergiella, and Pseudomonas) and yeasts/fungi (such as Aureobasidium, Debaromyces, Candida, and Cladosporium) genera identified were found in all 61 samples. Even though interesting differences were observed at the relative abundance level of the identified genera, the bacterial genus Pantoea and the yeast/fungi genus Aureobasidium were the dominant ones in 35 and 40 samples, respectively. Of note, olive samples collected from the same region had similar fingerprint (genera identified and relative abundance level) regardless of the variety, indicating a potential association between the relative abundance of certain taxa and the geographical region. When samples were grouped by region of origin, distinct bacterial profiles per region were observed, which was also evident from the PCA analysis. This was not the case for the yeast/fungi profiles since 10 out of the 13 regions were grouped together mainly due to the dominance of the genus Aureobasidium. A second cluster was formed for the islands Crete and Rhodes, both of which are located in the Southeast Aegean Sea. These two regions clustered together mainly due to the identification of the genus Toxicocladosporium in relatively high abundances. Finally, the Agrinio region was separated from the others as it showed a completely different microbial fingerprinting. However, due to the limited number of olive samples from some regions, a subsequent PCA analysis with more samples from these regions is expected to yield in a more clear clustering. The present study is part of a bigger project, the first of its kind in Greece, with the ultimate goal to analyze a larger set of olive samples of different varieties and from different regions in Greece in order to have a reliable olives' microbial biogeography.

***Keywords*—** amplicon-based metagenomics analysis, bacteria, microbial biogeography, olive microbiota, yeasts/fungi

Lena Payati is with the Agricultural University of Athens, Greece (e-mail: lenapagiati@aua.gr).

Protective Effect of Lisinopril and Enalapril against Acute Kidney Injury Induced by Doxorubicin in Male Wistar Rats: Involvement of Kim-1 and Heme Oxygenase-1 Rna Expression

Gihan F. Asaad, Azza Hassan, Rasha E. Mostafa

***Abstract*—** Intro: Doxorubicin (DOX) is a standard anticancer agent exerting devastating effects as nephrotoxicity, hepatotoxicity and cardiotoxicity. The purpose of this study was to increase the clinical use of DOX through decreasing its detrimental effects via combination with ACE inhibitors to ameliorate the induced acute kidney injury (AKI). Method: AKI was induced by a single injection of DOX (7.5 mg/kg; i.p.). Group 1: control -ve, Group 2: DOX (7.5 mg/kg; i.p.) single dose, Group 3 and 4: Lisinopril (Lis) (20 mg/kg) and Enalapril (Enal) (40mg/kg) orally for 15 consecutive days after DOX injection. Serum samples were used to measure creatinine and BUN, tissue samples were extracted to determine myeloperoxidase (MPO), malondialdehyde (MDA), total antioxidant capacity (TAC) and kidney injury molecule (KIM-1) using ELISA technique. Heme oxygenase (HO-1) RNA expression was quantified in tissue using real time polymerase chain reaction (PCR). Part of the kidney tissue was kept in formalin for immunohistochemical demonstration of Cleaved Caspase-3 and NF-κβ immune staining and the other part was used for pathological examination. Results: Oral treatment with Lis (20 mg/kg) and Enal (40mg/kg) for 15 consecutive days reversed DOX effects as they reduced the serum creatinine and BUN, kidney levels of MPO and MDA, whereas the drugs showed an increase in the TAC. Drugs also reduced KIM-1 and HO-1 RNA expression. A significant decrease in cleaved caspase-3 and NF-κβ immune stained cells of the rat kidney as well as an impressive improvement in pathological findings. Conclusion: The study concluded that DOX adverse effects can be controlled by Lis and Enal..

***Keywords*—** lisinopril, enalapril, acute kidney injury, doxorubicin, oxidative stress.

Gihan F. Asaad, Rasha E. Mostafa are with the Pharmacology Department, Medical Research Division, National Research Centre, 33 EL Bohouth St., P.O. 12622, Dokki, Giza, Egypt (e-mail: dr_g.asaad@yahoo.com).

Azza Hassan is with the Pathology Department, Faculty of Veterinary Medicine, Cairo University, Giza, Egypt.

In Vivo Evaluation of the Anti-Inflammatory, Analgesic Activities of Crataegus Sinaica Methanol Extract

Rehab F. Abdel-Rahman, H. Handoussa, A. H. El-Desoky, M. R. Meselhy, S. El-Mekkawy, Gihan F. Asaad

***Abstract*—** Objective: The current study aimed to evaluate the in vivo anti-inflammatory and anti-nociceptive properties of Crataegus sinaica methanol extract. Methods: Mass spectrometric analysis of the methanol extract of C. sinaica was done, as well as, metabolites' profiling using UPLC/PDA/ESI-MS. Afterward, the anti-inflammatory and the analgesic activities of C. sinaica at three oral dose levels (50, 100 and 200 mg/kg) were tested. Key findings: Metabolites profiling revealed the presence of several classes to confirm the richness of Crataegus sinaica with phenolic-derived metabolites. The study of anti-inflammatory activity demonstrated that the different examined doses of C. sinaica extract significantly suppressed inflammation in carrageenan-induced rat paw edema compared to the untreated control. Moreover, biochemical analysis of PGE2, TNF-α and MPO levels in paw exudate showed significant reduction compared to the control. The peripheral analgesic activity of C. sinaica extract exhibited inhibition of the abdominal contractions induced by ip injection of acetic acid. Likewise, C. sinaica extract increased the latency time in hot plate test, in the central analgesic activity test, compared to the control. Conclusion: These findings support the traditional use of C. sinaica against several inflammatory ailments.

***Keywords*—** crataegus sinaica, metabolites profiling, inflammation, carrageenan, writhing.

Rehab F. Abdel-Rahman, Gihan F. Asaad are with the Department of Pharmacology, National Research Centre, 33 El Bohouth St., Dokki, Giza, Egypt, P. O. 12622. (e-mail: dr_g.asaad@yahoo.com).

H. Handoussa is with the Department of Pharmaceutical Biology, Faculty of Pharmacy and Biotechnology, German University in Cairo GUC, Egypt.

A.H. El-Desoky is with the Department of Pharmacognosy, National Research Centre, 33 El Bohouth St., Dokki, Giza, Egypt.

M.R. Meselhy is with the Department of Pharmacognosy, Faculty of Pharmacy, Cairo University, Egypt.

S. El-Mekkawy is with the Chemistry of Natural Compounds Department, National Research Centre, El-Behoos St. 33, Dokki-Cairo, 12622, Egypt.

Evaluating Neural Networks in Coronary Plaque Detection on Coronary CT Angiography

Mario Viti, Hugues Talbot, Nicolas Gogin

***Abstract*—** Coronary artery plaques present features of varying nature with corresponding degree of severity and risk for both obstructive and non-obstructive diseases (stenosis) [1]. Though plaque characterization plays the most important role, automatic methods must first localize the plaque on the coronary length. For this work a dataset of 124 coronary CT angiography (CCTA) scans were retrospectively collected. All patients were accepted at triage with minimal to severe coronary artery disease (CAD) suspicion. To perform automated analysis the manual annotation of coronary centerline was used as supervision. The goal of this work is to propose an effective method for plaque localization by performing a frontal comparison of multiple methods using a unified framework and tailored metric for plaque detection/localization. All methods reported are based on a neural network architecture trained on the same Train Set and evaluated on the same Test set. Because of the lack of openly available frameworks for the assessment of non-obstructive diseases we propose to make use of the plaque annotations present in the Rotterdam Coronary Algorithm Evaluation Framework [2] for additional test on 18 patients.

***Keywords*—** Plaque Detection, Computer Aided Diagnosis · Coronary CT Angiography · Deep Learning.

I. Introduction

Coronary plaque classification has been lately approached using machine learning [3]. While coronary calcified plaques detection can be solved quite successfully using deep learning by Agatston Score [4] prediction [5], coronary plaques (especially non obstructive plaques) in CCTA remains a more challenging topic. In [6] the author implemented a pipeline for 2.5d image classification. The model is trained to classify the image as plaque soft, plaque mix, plaque calcified and healthy. The provided input is a multichannel image with two orthogonal views of the coronary CPR-straightened (Curved Plane Reconstruction) volume. Another method [7] proposes a more complex pipeline. Using RCNN the CNN extracts features later to be provided as input to a recurrent neural network with memory units (GRU) to aggregate information along the whole coronary segment. Even more recently in [8] the author claims that Radiomics [9] are better embeddings than CNN extracted features for the same pipeline with GRU units as aggregators for stenosis and revascularization prediction. These methods proved the feasibility of plaque characterization using deep learning however the plaques detection remains unsolved as the measurements shows that discrimination performances are not as high as localization performances (No-plaque vs rest).

II. DATA

A. Test set split

The dataset used in this work includes 124 coronary CT angiography (CCTA) scans, collected and cleaned up during a 2 years period. Each patient underwent both CCTA and anatomical test and has been assigned a CAD-RADS [10] score by trained cardiologist. Each Scan is paired with annotated coronary centerline: to each point of the centerline is assigned a label: 0(no-plaque), 1(calcified plaque), 2(mixed plaque), 3(soft plaque). All annotation is based on clinical reports issued during medical review. The manual annotation has been carried out to match the clinical report and the final annotation was submitted to a trained cardiologist for review.

The Train/Test set split was hand-picked by annotators so that each positive class (calcified plaque, mixed plaque, soft plaque) is uniformly represented. This allows to have the most representative Test set for the problem at hand while keeping a feasible amount of data for training using deep learning. The Test set presents 14 patients with a grand total of 74 plaques: 32 calcified, 20 mixed, 21 softs. Although patients aren't numerous the plaque concentration is higher than the normal population, for example the Rotterdam Coronary Artery Train Dataset includes 15 calcified, 5 mixed and 7 softs among 18 patients.

Table 1. Test set plaque distribution and CAD-RADS

CAD-RADS 0	CAD-RADS 1	CAD-RADS 2	CAD-RADS 3	CAD-RADS 4
1	4	3	2	4
Calcified	Mixed	Soft	Total	Patients
32	20	21	74	14

III. METHODS

A. Task

Automatic Coronary Plaque characterization consists in

Mario Viti GE Healthcare CIFRE engineer, Centrale Supélec Phd Student at CVN INRIA (mario.viti@centralesupelec.fr)
Hugues Talbot Professor at Centrale Supélec, Université Paris-Saclay, researcher at CVN INRIA Phd supervisor (Hugues.talbot@ceteralesupele.fr)
Nicolas Gogin Sr Manager Software Engineer GE Helthcare, Phd research coordinator.(nicolas.gogin@ge.com)

localize any region of the coronary tree that might be interested by plaque and then assess its class among 3 main classes: soft, mixed and calcified [11]. Multiclass issues may impact learning in 3 main ways: the first is inter operator variance among the annotated plaques, while localization of the plaque is unanimous its composition can be contentious (consensus), the second is that plaques of different types may over-lap significantly on different sides of the coronary (overlap), finally the comparison of multiclassification methods is less obvious than the binary case. For these conjoint reasons this work focuses on the most general plaque localization via binary classification task which can be followed by plaque characterization as a downstream task.

B. Vnet

The first method is based on the 3D convolutional **Vnet** architecture arranged as an encoder-decoder fashion with skip connections. To repurpose the architecture for centerline annotations it is applied a cross-sectional pooling layer on the full segmentation to obtain a 1D vector from a 3D stretched-CPR-straightened view of the coronary.

Fig. 1. Vnet model repurposed for Centerline Annotation prediction of coronary plaques, the input is the 3D CPR-straightened view of the vessel, the segmentation is pooled to 1D annotation.

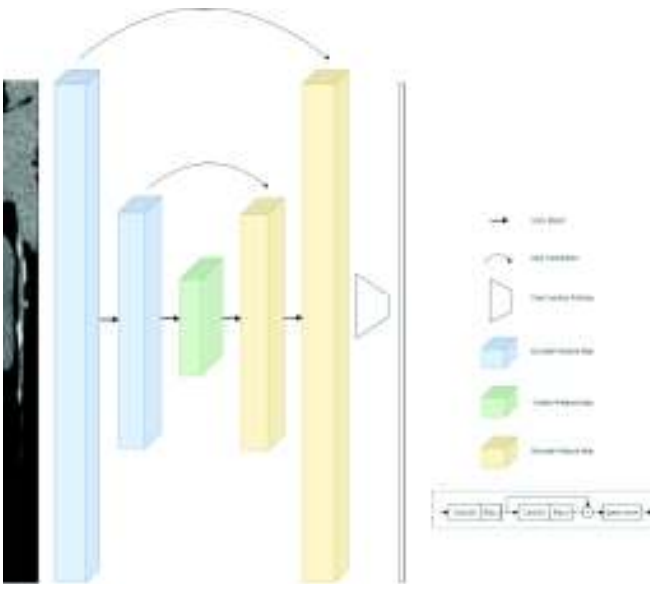

DeepMedic. One out-of-the-box method consists in repurposing the DeepMedic [12] architecture for lesion detection. This model is based on 3D convolutional layers and it has been extensively tested on MRI for brain tumor segmentation. The model implements a dual resolution pathway to capture the context and the details of small lesions. For plaque detection the model takes as input the 3D CPR-straightened view. The output has roughly the same dimension as the input, so cross-section pooling is applied in order to obtain a pointwise centerline prediction (without CRF module).

CNN. One method was to use a simple CNN (3D encoder and fully connected layers in sequence) to classify patches sampled and augmented under affine transformation from the centerline to avoid the distortion caused by the CPR-straightened reconstruction. Patch side was tuned via random search to 28 with anisotropic resolution of 0.33 mm.

Fig. 2. The CNN model is fed isotropic patches sampled around the centerline.

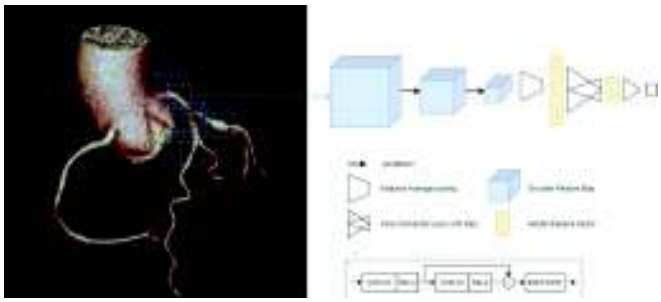

IV. EXPERIMENTS

A. Evaluation using tailored metric

Each model will be compared based on 3 criteria. The binary classification performances (no-plaque, plaque), the multiclass performance (no-plaque, soft, mix, calcified) and finally time of inference and computational requirements. The third criterium is necessary for a full costs/benefit analysis. The multi class evaluation aims to decide whether the method can encode the variety of plaques and distinguish them from the healthy (no-plaque) segments. In order to carry out this evaluation one can design tailored metrics.

The Per Plaque Recall measures the overlap of prediction and annotation over a contiguous annotated plaque, each overlap is normalized with respect to the length of the plaque making the Per Plaque Recall invariant to plaque length thus focusing on hit/miss ratios.

Binary Classification Performances. The simplest approach is to measure the global performances over the whole Test-set in terms of binary classification performance metrics. This method however gives a partial view as class imbalance highly affects results.

Table 2. Binary classification measurement

Model	Accuracy	F1-score	Recall	Precision
CNN	0.929	0.692	0.563	**0.898**
Vnet	**0.943**	**0.700**	**0.883**	0.580
DeepMed	0.814	0.411	0.286	0.732

Fig. 3. A representative example of how the prediction is evaluated. True positives overlap 90% of each of the 4 contiguous plaque annotations. The contiguous empty segments <1.5 mm accounts for most of the inter annotation segments in this case the far-left prediction will count as false positive in this context.

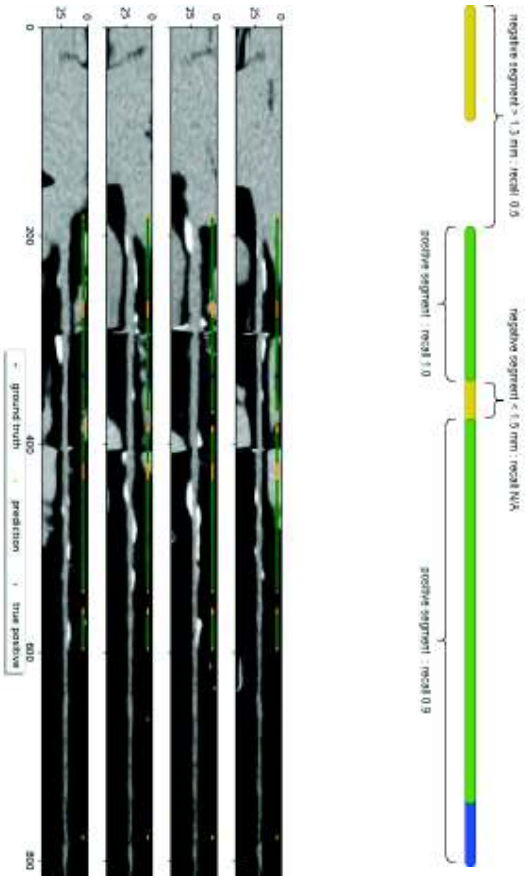

Table 3. Multiclass Per Plaque Recall measurement

Model	No-Plaque	Calcified	Mixed	Soft
CNN	0.846	**0.985**	**0.985**	**0.676**
Vnet	**0.989**	0.729	0.689	0.118
DeepMedic	0.812	0.936	0.881	0.352

Table 4. F1 | Class means that the evaluation is conditional to the Class (only the positives of the corresponding class are used as target). Multiclass F1 measurement agrees with the measurement done with the Multiclass Per Plaque Recall

Model	F1 | Calcified	F1 | Mixed	F1 | Soft	Avg
CNN	**0.990**	**0.993**	**0.787**	**0.923**
Vnet	0.866	0.837	0.222	0.641
DeepMedic	0.967	0.904	0.482	0.784

Time of inference and computational requirements. The final criterium is re-ported in order to assess the cost/benefits of each method, the time of inference refers to the CPU (Intel(R) Xeon(R) Silver 4114 CPU @ 2.20GHz) time per patient (all coronaries) while CPR-straightened indicates a larger memory footprint.

Table 5. Requirements and Costs, Coronary-Points column indicate if the model needs points sampled from the coronary and Time of inference is avg+-std sec per patient (all coronaries). Note that inference time do not consider CPR reformation.

Model	Coronary-Points	CPR-straightened	Time of inference (CPU)
CNN	yes	**no**	30.35 +- 5 sec
Vnet	yes	yes	**10.5 +- 1 sec**
DeepMed	yes	yes	40.3 +- 7 sec

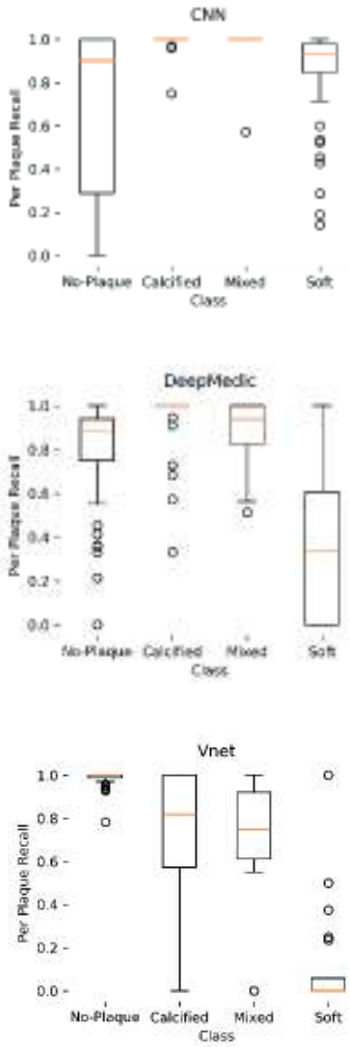

Fig. 4. Per Segment Recall Box Plot of each model

B. Rotterdam Coronary Artery Dataset

Coronary Plaque detection algorithms can be tested on the Rotterdam Coronary Algorithm Evaluation Framework. While the test data and evaluation backend focused on lumen segmentation and stenosis prediction the train data contains annotated coronary plaque information. For this study additional evaluation "in the wild" is performed on the Rotterdam Train set annotated centerline plaque information. This dataset includes 18 CCTA thin slice scans with coarse axial resolution (0.35-0.42 mm) with 238 annotated coronary segments. These segments present 7 soft plaques, 5 mixed plaques, 16 calcified plaques. For this analysis the same Per Plaque Recall measurement is adopted.

Table 6. Rotterdam Data set.

Dataset	Patients	Segments	Calcified	Mixed	Soft
Rotterdam	18	238	16	5	7

Table 7. Multiclass Per Plaque Recall measurement on Rotterdam Coronary Artery train set.

Model	No-Plaque	Calcified	Mixed	Soft
CNN	0.722	0.9100	0.948	0.515

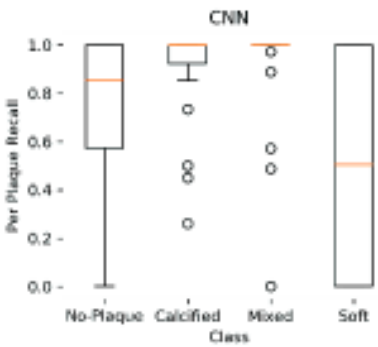

Fig. 5. Per Segment Recall Box Plot on the Rotterdam Train set

C. Robustness of CNN approach

One of the major concerns about this method is the robustness to the centerline extraction quality. Centerline can be extracted automatically but CPR-straightened view can be affected by reconstruction and distortion noise due to the noise induced by the reformation in correspondence of bifurcation or because of high tortuosity. In order to test whether this method can be invariant to the centerline quality, the model is trained using augmented inputs under affine random transform and evaluated under centerline coordinates noise augmentation to measure the impact on the inference as noise increases. Each coordinate point p around the centerline is perturbed by a uniform noise $u \sim U(-s, s)^3$. Embeddings e_p were extracted at the midpoint of the network after the GAP (global average pooling) layer, the cosine similarity shows how embeddings are perturbed as noise increases.

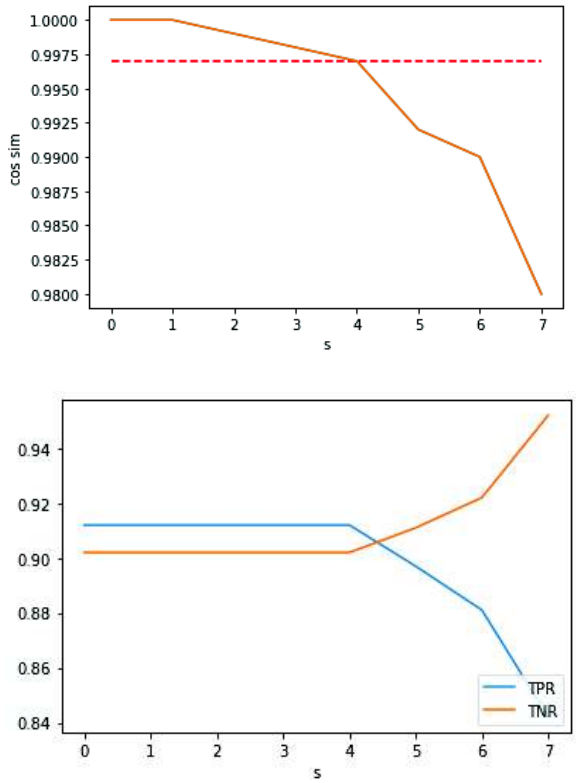

Fig. 6. Noise impact on performances, performance remains unchanged up to s=4 voxels translation shift or 4.5 mm offset (diagonal of a 4 voxels side cube considering an anisotropic voxel of 0.33 mm).

$$cossim(e_p, e_{p+u}) = \frac{<e_p, e_{p+u}>}{\|e_p\|\|e_{p+u}\|} \quad (1)$$

V. Conclusion

We presented a work on coronary plaque detection using deep learning, what arose from the presented results is that most simple approaches might be the best solution to certain problems. We could also extend the CNN approach with a GRU sequence aggregator like [7] [8] but with no significant benefits.

The most challenging issue for this type of tasks is the class imbalance. Imbalanced dataset is an issue that can be tackled in many ways: weighting the loss terms and uniform sampling can help cope with the imbalance. Because of the problems affecting multi-class labelling of coronary segment (consensus and overlap) to simulate the balance apported from a weighted cross-entropy loss each batch is sampled to be uniformly distributed with respect to the 4 classes (no-Plaque, Calcified, Mixed, Soft), by doing so each class contributes to ¼ of the backpropagated features, assuming training is carried out using any variant of stochastic gradient descent, thus achieving the same balance as the multiclass formulation without the downside of consensus and overlap. If the dataset is highly imbalanced uniform sampling may lead to overfitting, it is therefore important to find the correct balance between strictly uniform and random sampling

REFERENCES

[1] M. C. Williams, A. J. Moss and M. Dweck, "Coronary Artery Plaque Characteristics Associated With Adverse Outcomes in the SCOT-HEART Study," *Journal of the American College of Cardiology,* vol. 73, no. 3, pp. 291-301, 2019.

[2] H. Kirişli, M. Schaap and C. Metz, "Standardized evaluation framework for evaluating coronary artery stenosis detection, stenosis quantification and lumen segmentation algorithms in computed tomography angiography.," *Medical Image Analysis,* vol. 17, no. 8, pp. 859-76, 2013.

[3] H. Nils, M. Wolterink Jelmer and van Velzen, "Machine Learning for Assessment of Coronary Artery Disease in Cardiac CT: A Survey," *Frontiers in Cardiovascular Medicine,* vol. 6, p. 172, 2019.

[4] A. Agatston, W. Janowitz and Hildner, "Quantification of coronary artery calcium using ultrafast computed tomography," *Journal of the American College of Cardiology,* vol. 15, no. 4, pp. 827-832, 1990.

[5] G. Santini, D. Della Latta and N. Martini, "An automatic deep learning approach for coronary artery calcium segmentation," *IFMBE proceedings,* pp. 374-377, 2018.

[6] A. Tejero-de-Pablos and e. al., Texture-Based Classification of Significant Stenosis in CCTA Multi-view Images of Coronary Arteries., vol. 11765, Springer, Ed., Medical Image Computing and Computer Assisted Intervention, 2019.

[7] M. Zreik, . W. Hamersvelt and . M. van Wolterink, "A Recurrent CNN for Automatic Detection and Classification of Coronary Artery Plaque and Stenosis in Coronary CT Angiography," *IEEE Trans Med Imaging,* vol. 7, pp. 1588-1598, 2019.

[8] F. Denzinger, M. Wels and N. Ravikumar, "Coronary Artery Plaque Characterization from CCTA Scans using Deep Learning and Radiomics.," *Lecture Notes in Computer Science,* 2019.

[9] M. Kolossváry, M. Kellermayer and B. Merkely, "Cardiac Computed Tomography Radiomics: A Comprehensive Review on Radiomic Techniques.," *Journal of Thoracic Imaging,* vol. 33, no. 1, pp. 26-34, 2018.

[10] R. Cury, S. Abbara, S. Achenbach and A. Agatston, "Coronary Artery Disease - Reporting and Data System (CAD-RADS): An Expert Consensus Document of SCCT, ACR and NASCI: Endorsed by the ACC," *JACC Cardiovascular Imaging,* vol. 9, no. 9, pp. 1099-1113, 2016.

[11] H. Hecht, P. Cronin and M. Blaha, "2016 scct/str guidelines for coronary artery calcium scoring of noncontrast noncardiac chest ct scans: A report of the society of cardiovascular computed tomography and society of thoracic radiology.," *Journal of Cardiovascular,* vol. 11, pp. W54-W56, 2016.

[12] K. Kamnitsas, C. Ledig and V. F. Newcombe, "Efficient multi-scale 3D CNN with fully connected CRF for accurate brain lesion segmentation," *Medical Image Analysis,* vol. 36, pp. 61-78, 2017,.

Preliminary Host Range and Impact Trials of Bikasha Sp. (Coleoptera: Chrysomelidae), a Candidate Agent for Biological Control of Mother-of-Millions, Kalanchoe Delagoensis Eckl. and Zeyh. (Crassulaceae) in Australia

Tahina Ernest Rajaonera, Lala Harivelo Ravaomanarivo, Andrew Mcconnachie

***Abstract*—** Native to Madagascar, Kalanchoe delagoensis (mother-of-millions) was introduced to Australia and was first recorded as a weed in 1940. It has since become invasive throughout New South Wales and Queensland in eastern Australia, where it competes with native biodiversity and is toxic to livestock. Chemical and mechanical control methods exist for K. delagoensis, but they are not always effective and are often cost prohibitive. Biological control (using natural enemies from the country of origin) was therefore considered to be the most cost-effective, sustainable approach to manage this weed in Australia. The flea beetle, Bikasha sp., a newly discovered species, was found on K. delagoensis in southern Madagascar in 2017. After field collection, a laboratory culture of the beetle was established at the University of Antananarivo to evaluate its potential as a biological control agent for K. delagoensis in Australia. Host specificity and impact trials were designed and conducted on species of interest to Australia. Adult no-choice and paired-choice host-specificity trials were conducted on six species of Madagascar Crassulaceae (K. blossfeldianna, K. miniata, K. prolifera, K. daigremontiana, K. pinnata and Echeveria elegans) and one native Australian species (Kalanchoe spathulata). The seven test species were initially included in replicated no-choice trials. Of these, three test species (K. prolifera, K. daigremontiana and E. elegans) tested positive for feeding damage and three species (K. spathulata and K. blossfeldiana, K. pinnata) received feeding damage, oviposition and larval development. These six species were subsequently included in replicated adult paired-choice trials. Results indicated that Bikasha sp. adults didn't show a distinct preference for K. delagoensis over either K. pinnata, K. blossfeldianna or K. spathulatha, with viable larvae and eggs being recorded on all of these species. However, for the remaining three test species (K. prolifera, K. daigremontiana and Eucheveria elegans), significantly less feeding damage, oviposition and larval development was recorded compared to K. delagoensis. To quantify the impact of Bikasha sp. on K. delagoensis, replicated impact trials were conducted using four size classes of plants (<10 cm, 10 - 20 cm, 20-30 cm, 30 - 40 cm) measuring six growth parameters (total wet weight, stem diameter, plant height, number of bulbils and number of phyllodes). Results of the impact trials showed that Bikasha sp. was able to significantly reduce plant weight, number of phyllodes and bulbils. It didn't have a significant impact on stem diameter and plant height. Overall, the impact trial showed a beneficial result in that three of the five growth parameters measured were significantly impacted. However, host range studies revealed the polyphagous nature of this species, especially for the two species (K. spathulata and K. blossfeldiana) which are of concern for Australia. Multiple choice trials could be used to explore the host range of this species further, however, it is unlikely that it would ever be considered safe for consideration as a potential biocontrol agent in Australia.

***Keywords*—** biocontrol, bryohyllum delagoense, flea beetle, host specificity, impact.

Tahina Ernest Rajaonera, Lala Harivelo Ravaomanarivo are with the Department of Entomology, Faculty of Science, University of Antananarivo Madagascar (e-mail: thnrajao@gmail.com).

Andrew Mcconnachie is with the Weed Research Unit, Invasive Species Biosecurity New South Wales, Department of Primary Industries, Orange, NSW, Australia.